INDRAPRASTHA INSTITUTE OF INFORMATION TECHNOLOGY, DELHI

DOCTORAL THESIS

Viscoelastic Subdiffusive Flows: Modelling, Analysis and Computation

---

Author:
Tanisha CHAUHAN

Supervisor:
Dr. Sarthok SIRCAR

A thesis submitted in fulfillment of the requirements
for the degree of Doctor of Philosophy

to the

Indraprastha Institute of Information Technology Delhi

January 27, 2025

.

Certificate

This is to certify that the thesis titled "Viscoelastic Subdiffusive Flows: Modelling, Analysis and Computation" being submitted by Tanisha Chauhan to the Indraprastha Institute of Information Technology Delhi, for the award of the degree of Doctor of Philosophy, is an original research work carried out by her under my supervision. In my opinion, the thesis has reached the standards fulfilling the requirements of the regulations relating to the degree.

The results contained in this thesis have not been submitted in part or full to any other university or institute for the award of any degree/diploma.

Sarthok Sircar

January, 2025
Dr. Sarthok Sircar

Indraprastha Institute of Information Technology Delhi
New Delhi 110020

Declaration

This is to certify that the thesis titled "Viscoelastic Subdiffusive Flows: Modelling, Analysis and Computation" being submitted by Tanisha Chauhan to the Indraprastha Institute of Information Technology Delhi, for the award of the degree of Doctor of Philosophy, is a bonafide work carried out by me. This research work has been carried out under the supervision of Dr. Sarthok Sircar. The study pertaining to this dissertation has not been submitted, in part or in full, to any other university or institute for the award of any other degree or diploma.

Tanisha

January, 2025
Tanisha Chauhan

Indraprastha Institute of Information Technology Delhi
New Delhi 110020

INDRAPRASTHA INSTITUTE OF INFORMATION TECHNOLOGY, DELHI

Abstract

Doctor of Philosophy

Viscoelastic Subdiffusive Flows: Modelling, Analysis and Computation

by Tanisha CHAUHAN

This thesis explores the rheodynamics of viscoelastic subdiffusive fluids and highlights the potential of fractional calculus in modelling these types of fluids. A novel fractional model is developed to investigate the regions of spatiotemporal instability. Direct numerical simulations are used to capture the macrostructures within the flow, utilizing a new structure tensor, which is physically realizable, contributing to a deeper understanding of this complex fluid dynamics phenomenon. The seven chapters are described as follows:

- Chapter 1 lays the foundation by introducing subdiffusive fluids and delving into the historical backdrop of fractional models applied to viscoelastic flows. This chapter surveys past analytical outcomes, numerical strategies, and experimental findings, exhibiting a wide range of applications in various fields.

- In Chapter 2, the fundamental groundwork is established, including a thorough explanation of several types of instability: convective, absolute, and evanescent modes. This chapter elucidates numerical methods, especially finite difference schemes, designed to handle various equation components such as advection and diffusion terms and also discusses the different fractional derivatives and their corresponding numerical approximations.

- Chapter 3 embarks on a comprehensive investigation of temporal and spatiotemporal linear stability analyses within the viscoelastic subdiffusive plane Poiseuille flow. The Fractional Upper Convected Maxwell model is derived and explored under low to moderate Reynolds numbers (Re) and Weissenberg numbers (We) to uncover regions of topological transition in advancing flow interfaces. The relation between the exponent in the time scale of the microscale models (t^{α}) and fractional order (α) in stress constitutive equations is derived. Using Brigg's method of analytic continuation, insights into instability modes as fractional derivative order changes are discussed. The stability studies are limited to two exponents: monomer diffusion in Rouse chain melts, $\alpha = 1/2$, and in Zimm chain solutions, $\alpha = 2/3$. The presence of a non-homogeneous environment with hindered flow is revealed by the discovery of an abnormal region of temporal stability at high fluid inertia, highlighting the potential of the model to accurately capture some experimentally observed flow-instability transitions in subdiffusive flows.

- Chapter 4 presents a theory to quantify the development of the spatiotemporal macrostructures for viscoelastic sub-diffusive flows by decomposing the polymer conformation tensor into the so-called structure tensor. Our method bypasses the traditional arithmetic decomposition's fundamental flaw, which is that the fluctuating conformation tensor fields might not be positive definite and, as a result, lose their physical significance. By defining and building a geodesic via the inner product on its tangent space, the space of positive definite matrices is converted into a Riemannian manifold using some well-proven results in matrix analysis. Three scalar invariants of the structure tensor are defined by means of this geodesic. The maximum amount of time that the perturbative solution's evolution may be accurately predicted by linear theory along the Euclidean manifold is found.

- Chapter 5 introduces a novel family of time-asymptotically stable, implicit-explicit, adaptive, time integration methods (denoted with the θ-method) for the solution of the fractional advection-diffusion-reaction equations. The computationally explicit L1 method is generalised by this class of temporal integration techniques. For a specific range of Peclet numbers, the dispersion relation analysis of the method which takes into account the group velocity and the phase speed, indicates a favorably large region. The one-dimensional fractional diffusion equation is used to validate the method's correctness and effectiveness.

- Chapter 6 includes the direct numerical simulations of viscoelastic, subdiffusive, plane Poiseuille flow in the regime of low to moderate Reynolds number and low Weissenberg number. These simulations successfully capture the flow structures by offering (i) a better resolution of the instantaneous regions of elastic shocks (which are the alternating regions of expanded and compressed polymer volume, in comparison with the volume of the mean conformation tensor), and (ii) a higher resolution to identify areas where the mean conformation tensor tends to diverge significantly from the instantaneous conformation tensor, supporting the experimentally observed transition of subdiffusive flows into flow instability.

- Chapter 7 summarizes the real-life applications involving viscoelastic subdiffusive fluids, focusing on their rheological properties. Fractional models, although instrumental in comprehending intricate phenomena with non-local and memory-dependent behaviour, do present certain limitations. To wrap up, this chapter points out the main challenges in understanding these flows and emphasizes potential future problems that need serious attention in this new category of complex fluids

Acknowledgements

As I stand at the end of this journey, I would like to thank all who have been involved in ensuring I reach my destination. I extend my deepest gratitude to my supervisor, Dr. Sarthok Sircar, for his invaluable guidance, support, and encouragement throughout the course of my Ph.D. His profound knowledge, thoughtful insights, and consistent mentorship have been instrumental in shaping this research and ensuring its successful completion.

I sincerely thank Dr. Subahshree Mohapatra and Dr. Kaushik Kalyanaraman for their constructive feedback and support during my academic journey. I would also like to acknowledge Dr. Abhijit Deshpande and Dr. Priyanka Shukla from IIT Madras for his insightful comments and suggestions, which have significantly contributed to refining my research. I sincerely thank IIIT Delhi and CSIR for their financial support and for providing the resources and amenities essential for the successful completion of my research work.

My heartfelt thanks go to my senior, Dr. Diksha Bansal, for being my unwavering supporter. Her constant encouragement and companionship have made this challenging journey more manageable and enriching. I am grateful to my friends Shivangi Tayal, Pooja Yadav, Heena Valecha, and Shweta Sharma for their steadfast friendship and encouragement. I also express my gratitude to my colleagues Dr. Dipa Ghosh, Archana Arya, Dr. Shivani Goel, Madhu Bhatt, and Ishani Chaudhary for their companionship, which provided much-needed moments of joy and motivation during late-night walks and heartfelt conversations.

I deeply thank my grandparents, parents, and family for their unconditional love, patience, and encouragement throughout this journey. A special acknowledgement to my brother, Yatin Chauhan, and my husband, Rajat Pattenwal, for their continuous motivation, understanding, and unwavering support. Their belief in me has been my source of strength and determination.

Lastly, I thank the Almighty for granting me the strength, perseverance, and wisdom to complete this work.

Tanisha Chauhan

Contents

List of Figures

List of Abbreviations and Symbols

ω_i^{Temp}	Temporal Growth Rate
ω_i^{Cusp}	Absolute Growth Rate
V_g	Group Velocity
Re	Reynolds Number
We	Weissenberg Number
$\mathbf{v}$	Fractional Velocity
λ^{α}	Relaxation Time
ρ	Density
p	Isotropic Pressure
$\boldsymbol{\tau}$	Elastic Stress
η_s	Solvent Viscosity
η_p	Polymeric Contribution to the Shear Viscosity
η_0	Total Viscosity $(= \eta_s + \eta_p)$
ν	Viscous Contribution to the Total Viscosity
$\boldsymbol{A}$	Polymer Stress Tensor
$\boldsymbol{D}$	Rate of Strain Tensor
Ω	Vorticity
ψ	Streamfunction
$\mathscr{C}$	Instantaneous Conformation Tensor
$\overline{\mathscr{C}}$	Mean Conformation Tensor
$\mathscr{C}'$	Fluctuating Conformation Tensor
$\mathscr{G}$	Instantaneous Structure Tensor
$\mathscr{G}'$	Fluctuating Structure Tensor
$\boldsymbol{F}$	Instantaneous Deformation Gradient Tensor
$\overline{\boldsymbol{F}}$	Mean Deformation Gradient Tensor
$\mathscr{L}$	Fluctuating Deformation Gradient Tensor
$\boldsymbol{GL}_n$	Set of all $n \times n$ Invertible Matrices
$\boldsymbol{SO}_n$	Set of all $n \times n$ Special Orthogonal Matrices
$\boldsymbol{PS}_n$	Set of all $n \times n$ Positive Definite Matrices
N_c	CFL number
Pe	Peclet number
Da	Damköhler number

Dedicated to my parents
Mr. Pawan Chauhan and Mrs. Lokesh Chauhan

Chapter 1

Introduction and Review of Literature

This chapter provides an overview of historical findings and the theoretical, experimental and numerical study of viscoelastic subdiffusive flows with a motivation of understanding their importance in the real world. Subdiffusive viscoelastic fluid research seeks to understand the underlying mechanisms, characterise their behaviour, and build reliable models to describe and forecast their properties. This chapter focuses on the use of fractional models for viscoelastic flows, their analytical results, numerical and computational schemes to solve them, and experimental findings in the available literature. Subdiffusive viscoelastic fluids refer to complex fluids that exhibit both subdiffusion and viscoelastic behaviour. Section 1.1 provides a brief description of subdiffusive viscoelastic flows and their properties. It reviews the literature related to the concept of subdiffusion and various models already there for viscoelastic flows. However, these models were insufficient to explain the features of the viscoelastic flows across a wider range, and that is when fractional calculus emerged as a viable method for precisely defining the rheological behaviour of viscoelastic materials. Section 1.2 describes in greater detail, the evolution of fractional calculus and its relation to viscoelasticity. Several studies have been undertaken to investigate the exact solution for fractional viscoelastic flows in various geometrical domains. Section 1.3 discusses numerous studies providing analytical results for fractional viscoelastic flows. On the other hand, experimentation is also useful in capturing viscoelastic behaviour since it aids in the development of theoretical constitutive models that can be used to mimic realistic behaviour. Section 1.4 provides the detail of various experimental findings that demonstrate that fractional models may be employed for the best fit of diverse viscoelastic fluids over a wide frequency range. Having an experimental validation of the theoretical results for fractional viscoelastic flows is of great importance, but when it comes to solving a problem, analytical results sometimes cannot be used immediately, and therefore, the fractional differential operators are solved using a variety of numerical techniques. Section 1.5 is about numerical studies on subdiffusion problems and fractional viscoelastic models. The understanding of the analysis, experiments and numerics has significance in a variety of domains, including materials science, biology, and industrial processes where complicated fluid behaviour is important. Finally, in section 1.6, several real-world applications of subdiffusive viscoelastic flows are discussed.

1.1 Subdiffusive Viscoelastic Flows and their Properties

The subject of anomalous diffusion, especially in viscoelastic flows, has received tremendous attention over the last half-century, ranging from physics (Goychuk, Kharchenko, and Metzler, 2017; Goychuk and Pöschel, 2020; Goychuk and Pöschel, 2021), biology (Lai et al., 2009) to quantitative finance (Coffey, Kalmykov, and Waldron, 2004). The existence of internal microstructure, such as polymer networks hinders molecular movement, leading to subdiffusive transport. To examine the complicated dynamics and properties of these fluids, experimental techniques such as rheology, microscopy, and particle tracking methods, as well as theoretical modelling and simulations, are used. Various applications accounting for this fluid behaviour are outlined in section 1.6. The observed (anomalous) sub-diffusion often combines features of an ergodic fractional Brownian motion (reflecting viscoelasticity) and the nonergodic jumplike non-Markovian diffusional processes (reflecting disorder) (Fricks et al., 2009; Morgado et al., 2002). The combination of subdiffusion and viscoelasticity in fluids can have various implications. For example, in polymeric systems, subdiffusive viscoelastic behaviour can affect the transport of macromolecules, the rheological properties of the fluid, and the overall mechanical response of the material. It is also relevant in biological systems, where viscoelastic fluids are present in tissues, extracellular matrices, and cell cytoplasm, and their subdiffusive behaviour can impact cellular processes and transport phenomena.

Rheology, defined as the science of material deformation, employs mathematical models to accurately describe the material behaviour. This makes material comparison and classification easier, as well as prediction, which can subsequently help in engineering design decisions and enhance production processes. The molecular theory of viscoelasticity provides a good account of the material's properties, but a subsequent study is underway to investigate viscoelastic fluids at the continuum level. Given the seeming intricacy of any microscopic theory, it is logical to start with a coarser level of description in order to establish the overall phenomenology and mathematical structure of the governing equations at the continuum level. Using the relationship between average microscopic motion and macroscopic viscoelastic response, a range of experimental techniques for measuring this average motion can be used to derive the rheology of complex fluids. Viscoelasticity refers to the combined properties of viscosity and elasticity, where the material displays both viscous (flows under stress) and elastic (deforms and returns to its original shape) characteristics. In contrast to Newtonian fluids, the relationship between strain rate and stress tensor for viscoelastic fluids is much more complex. Due to this complexity, these fluids have crucial properties and are essential to study. For a detailed study, refer to these books (Bird, 1987; Phan-Thien and Mai-Duy, 2017; Chhabra, 2010). Though the classical Navier Stokes equations are highly significant in pure mathematics, the rheology of complex fluids such as blood and heavy oils was inadequately predicted using the classical theory, and thus, the theory for viscoelastic fluids has developed over time. To solve the issue of a more precise description of material qualities observed, a number of mechanical models were put forth, developed, and generalised using the mathematical tools at hand. Historically, Maxwell pioneered this methodology in his

1863 study on viscoelasticity. Fluids are complicated, hence there are several constitutive equations, modelling non-Newtonian fluids. Maxwell, Kelvin-Voigt, Zener and Burgers models are examples of classical models for linear viscoelasticity named after researchers who made substantial contributions to the subject (Flügge, 1975). The models satisfied the requirements for a sufficient description of the material's response to applied stresses and strains by using two main elements, spring (elastic component) and dashpot (viscous component), connected in series and/or parallel.

The theory of linear viscoelasticity (Gemant, 1936) is a popular method for analysing experimental data that results in a well-defined mathematical description of the stress-strain-time relationship, also known as a constitutive relationship. Using such mathematical tools, it is feasible to extract parameters that uniquely describe a given material and predict the evolution of stress and strain within the material under arbitrary loading situations (Flügge, 1975). Elastic susceptibility is one of the fundamental properties one wants to study about viscoelastic fluids, which can be characterized by the Complex shear modulus, $G^*(\omega)$. It determines the stress induced in a material upon application of an oscillatory strain at frequency ω. Over a long period of time, viscoelastic fluids have been characterized by two functions that demonstrate the fluid's elastic and viscous properties, respectively called the storage modulus, $G'(\omega) = \mathscr{R}(G^*(\omega))$ (real part of $G^*(\omega)$), defined as the ratio of elastic component of stress to strain and loss modulus, $G''(\omega) = \mathscr{I}(G^*(\omega))$, (imaginary part of $G^*(\omega)$) defined as the ratio of the viscous component of stress to strain. The storage modulus represents the energy that is stored in the fluid when it is deformed elastically, and the loss modulus represents the energy that is dissipated in the fluid due to viscous losses. Different types of biological tissues exhibit a wide range of mechanical responses, leading to the development of numerous experimental approaches to mechanical testing (Figure 1.1).

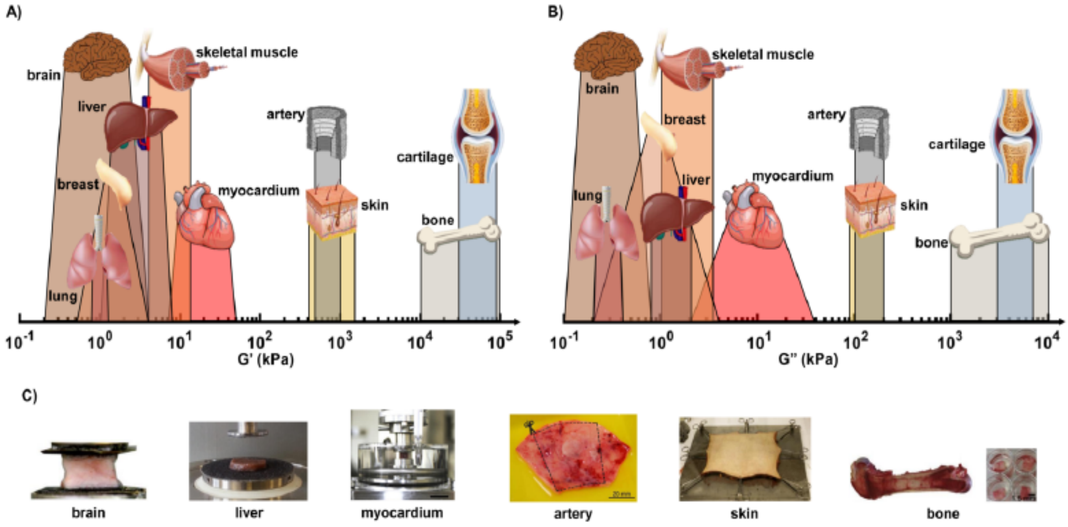

FIGURE 1.1: Comparison of (A) Storage modulus and (B) Loss modulus for common biomaterials, (C) Examples of tissues in rheological testing (Source: Zhang, Capilnasiu, and Nordsletten (2021)).

Among different models for capturing viscoelasticity, one of the most basic spring-dashpot sets is the Linear Maxwell model. It is made up of a spring connected in series with a dashpot. Under this model, if the material is subjected to constant strain, the stresses gradually relax. When a material is subjected to constant stress, the strain has two components: an elastic component that appears instantly and relaxes immediately upon stress release and a viscous component that develops with time as long as the stress is applied. This model is applicable to soft solids, fresh concrete, and a variety of metals at temperatures near their melting points. While Maxwell did not develop his model for polymeric liquids, he recognised that the body has a means of storing energy and a means of dissipating energy, with the former characterising the fluid's elastic response and the latter characterising its viscous nature. Another is the Kelvin-Voigt model, which uses spring and dashpot in parallel. In this, stress is the sum of two components, one of which is proportional to the strain, and the other is proportional to the rate of shear. The model produces satisfactory results for modelling creep in materials. However, it is substantially less precise when simulating relaxation. When the stress is not too high, this model can be used for organic polymers, rubber, and wood. The Zener model, or the standard linear solid model, is made up of two springs and a dashpot. It is the simplest model that accurately represents the creep and stress relaxation characteristics of a viscoelastic material. Burger's model is made up of a spring and a dashpot connected in series with another spring and dashpot connected in parallel (Burgers, 1935). A generalised Maxwell model is made up of n Maxwell components connected by a spring at the n^{th} element. The Wiechert model, or the Generalised Maxwell model, is the most general form of the viscoelastic linear model. It takes into account that relaxation does not happen all at once but rather over a period of time (Macosko, 1994) (refer Figure 1.2).

The models governing linear viscoelasticity are used in many industrial and engineering applications. At the same time, non-linear viscoelasticity typically occurs when deformations are substantial or when the material's characteristics vary as a result of deformations. Non-linear viscoelasticity (Kremer and Grest, 1990) also explains observed phenomena in viscoelastic fluids, such as normal stresses, shear thinning, and extensional thickening. Some of the nonlinear viscoelastic models are the Upper Convected Maxwell model, Oldroyd-B model, Linear Phan-Thien Tanner model, Wagner model etc. The Maxwell model is one of the most basic types of models for accounting for the rheological effects of viscoelastic fluid. However, one limitation of the model is that it does not adequately explain the normal relationship between shear rate and shear stress for subdiffusive flows; it was not feasible to produce appropriate results confirming the experimental data across the whole frequency range. Two testing paradigms for viscoelastic materials are relaxation tests (in which a constant strain is applied and stress is recorded) and creep tests (in which continuous stress is applied and strain is recorded). Traditionally, these properties were studied using experiments that require litres of material, which presents a severe difficulty when studying living materials. While many materials used in industry can be sampled in litres, biological fluids such as mucus and cytoplasm simply cannot be sampled in this manner. Also, because these processes were mechanical, these experimental results were applied to a limited range. However, the development of molecular theory for viscoelastic fluids proved to be extremely useful (Doi and Edwards, 1986; Rubinstein and Colby, 2003).

The study of polymer dynamics has received significant experimental and theoretical attention. To obtain the velocity field on the molecular level, the Generalized

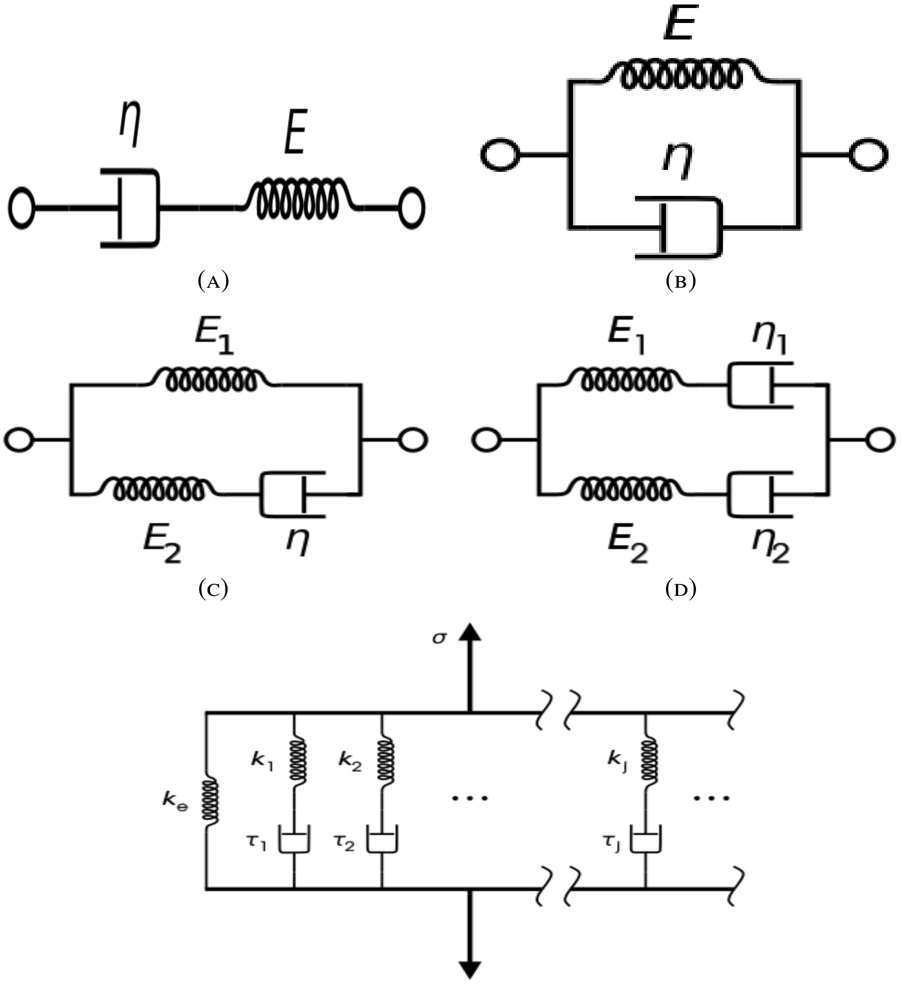

(A) (B)

(C) (D)

(E)

FIGURE 1.2: Different models based on spring and dashpot. (A) Maxwell model, (B) Kelvin Voigt model, (C) Zener model, (D) Burger's model and (E) Generalized Maxwell model

Langevin equation (Goychuk, 2012) is used, which incorporates a dissipative memory kernel to account for viscoelasticity. The generalized Langevin equation is a modification of the classical Langevin equation that includes memory effects and non-Markovian dynamics. One of the most significant studies in this field was done by Mason and Weitz (Mason and Weitz, 1995; Mason, Gang, and Weitz, 1996; Zwanzig and Bixon, 1970), which can infer viscoelastic properties for a wider range of fluids. They used the Generalized Langevin equation to find a relation between the statistics of the probe particle given by the mean square displacement to the bulk fluid property, i.e. storage and loss moduli. A novel experiment using Dynamic light scattering was proposed to evaluate the complex shear modulus. Mason considered three completely different types of materials: colloids in concentrated suspensions, colloids in entangled polymer solutions, and droplets in concentrated emulsions. Subsequently, Gittes et al. (Gittes et al., 1997) and Schnurr et al. (Schnurr et al., 1997) also employed laser microscopy techniques to estimate rheological modulus by measuring the motions of individual particles. More details on the molecular developments in the theory of viscoelastic fluids can be found in literature (Adelman, 1976; Santamaría-Holek, Reguera, and Rubí, 2001; Santamaría-Holek, Rubí, and Pérez-Madrid, 2005; Santamaría-Holek et al., 2008; Hohenegger, Durr, and Senter, 2017; Hohenegger and McKinley, 2018; Brader, 2010).

The subdiffusive object is considered primarily as being elastic and structurally robust, although it requires ‘fluidity’ and flexibility besides its elasticity for proper functioning, e.g., consider a viscoelastic nanoscaled polymer drop armed with a rigid backbone that can take on different macroscopic conformations (Vainstein, Lapas, and Oliveira, 2008). Subdiffusion refers to the slower-than-linear random motion or transport of particles within the fluid. It has been actively explored in recent years due to its importance in comprehending a variety of processes. It has been observed in polymers, porous media, and biological transport processes within cells. Many viscoelastic fluids are formed as a result of interactions between suspended microstructures in a viscous background fluid. Complex fluids, in general, comprise colloidal structures that partially store and partially dissipate energy when deformed by perturbative shear, making them viscoelastic materials. These colloidal structures suspended in fluid exhibit subdiffusive motion as the elasticity increases. Due to the presence of elastic forces and molecular motors, the dynamics of the Brownian particles become anomalous. Mucus, for example, is a water-like fluid suspension of oligomeric mucin proteins, whereas blood is a plasma suspension with red blood cells. As a result, biological fluids have recently gained a lot of interest. The mean square displacement of the particle’s position scales sublinearly with time, which is the most prevalent feature of such fluids, and hence, looking at the mean square displacement of the particles is the best way to investigate sub-diffusive dynamics (McKinley, Yao, and Forest, 2009; Vainstein, Lapas, and Oliveira, 2008). Anomalous diffusion is characterized by a non-linear relationship between the mean squared displacement, $\langle r^2(\mathscr{T})\rangle$, and time (Vainstein, Lapas, and Oliveira, 2008). This behaviour is opposed to the usual diffusion process, in which the mean square displacement is a linear function of time (i.e., $\langle r^2(\mathscr{T})\rangle = 2dD\mathscr{T}$, where d is the number of dimensions, and D is the diffusion coefficient). Whereas, a power law describes anomalous diffusion, $\langle r^2(\mathscr{T})\rangle = K_\alpha \mathscr{T}^\alpha$ where K_α is the so-called generalized diffusion coefficient and $\mathscr{T}$ is the elapsed time (Metzler et al., 2014). The exponent α classifies the type of diffusion: for normal diffusion, $\alpha = 1$; for subdiffusion, $\alpha < 1$; and for superdiffusion, $\alpha > 1$ (refer to Figure 1.3). It has been discovered that equations describing diffusion can not characterize complicated diffusion processes. Subdiffusive processes have gained prominence in recent decades as a result of accumulated experimental evidence of subdiffusive behaviour in complex systems, particularly biological systems. The intricacies of the dynamics differ between different physical conditions that contribute to subdiffusion. These distinctions are what allow us to theoretically reconstruct the underlying physics from observational data. More details on subdiffusive mechanisms can be found in a study by Meroz et al. (Meroz and Sokolov, 2015). However, the introduction of fractional calculus proved to be quite valuable for the modelling of subdiffusive viscoelastic fluids, as explained in the next section.

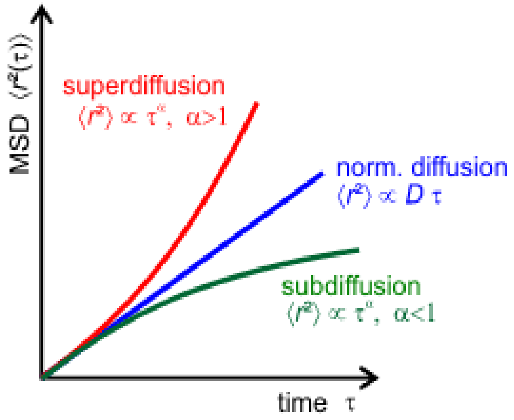

FIGURE 1.3: Mean squared displacement for different types of anomalous diffusion

1.2 Fractional Calculus and its Application to Viscoelastic Flows

Fractional calculus can be used to precisely describe slow relaxation (subdiffusion) as well as fast relaxation (superdiffusion) of viscoelastic materials. It is a non-trivial extension of regular calculus. The origin of fractional calculus can be seen back in 1695 (Figure 1.4) when Leibniz wrote to L'Hopital and asked the following question: “Can the meaning of derivatives with integer order be generalized to derivatives with non-integer orders?". L'Hopital was intrigued by the aforementioned query and responded with another simple one to Leibniz.: “What if the order will be 1/2?". Leibniz replied: “It will lead to a paradox, from which one day useful consequences will be drawn.". This subject sought major attention from Euler. In 1730, he wrote: “When n is a positive integer, and p is a function of x, the ratio of $d^n p$ to dx^n can always be expressed algebraically. But what kind of ratio can then be made if n be a fraction?" Laplace utilised an integral to define fractional derivative in 1812, and this concept first appeared in a text by Lacroix in 1819. The concept of fractional-order differentiation and integration, their relationship, and the realisation that fractional-order differentiation and integration are the same generalised operation order may all be found in one of Niels Henrik Abel's early publications published in

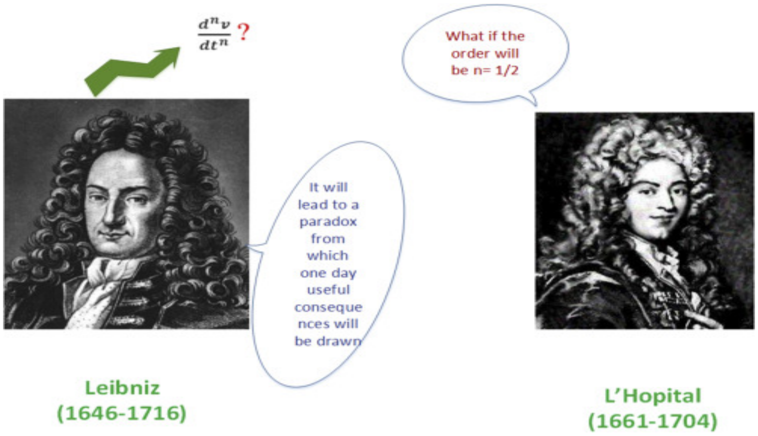

FIGURE 1.4: Origin of Fractional Calculus (1695)

1823 (Podlubny, Magin, and Trymorush, 2017). Abel thought about the Tautochrone problem's integral equation solution. He discovered that the answer could be achieved via an integral transform, which could be expressed as a semi-derivative. Separately, Liouville set the groundwork for the issue in an 1832 paper. He provided the first definition for fractional derivatives, but it was only applicable to a subset of functions. Then he presented the second formula. In order to generalise a Taylor series, Riemann devised a new formulation in 1853 that included a definite integral and was applicable to power series with non-integer exponents (Ross, 1977; Bertram, 1977).

The paper by N. Ya. Sonin (Sonin, 1869), in 1869 appears to be the earliest work that eventually led to what is now known as the Riemann-Liouville definition, where he used Cauchy's integral formula as a starting point to approach differentiation with arbitrary index. A few years later, in 1872, A. V. Letnikov expanded on Sonin's concept. Almost concurrently, Grunwald and Letnikov established the foundation for another concept of fractional derivative, which is still widely used today. Caputo revised the more "classic" definition of the Riemann-Liouville fractional derivative to employ classical beginning conditions, which are required by integer order differential equations. Riemann and Liouville's study is of great significance in generalised differentials, but it was Heaviside who used them more extensively in his operational calculus. Oliver Heaviside developed the practical application of fractional differential operators in electrical transmission line analysis in 1890 (Bertram, 1977). More details on the evolution of the theory for fractional calculus can be found in the following references (Ross, 1977; Mainardi, 2010; Mainardi, 2018). The theory and applications of fractional calculus improved significantly over the nineteenth and twentieth centuries, and various authors defined fractional derivatives and integrals (Valério, Machado, and Kiryakova, 2014; Jacob, Priya, and Karthika, 2020). Many applications of fractional calculus in the real world can be found in these references (Hilfer, 2000; Sun et al., 2018a; Failla and Zingales, 2020; Patnaik, Hollkamp, and Semperlotti, 2020).

As experimental results began to accumulate, revealing behaviours went beyond the available models mentioned above in the previous section, and then fractional calculus came into the picture. Advancements in mechanical testing hardware have revealed that many materials with complex microstructures have a distinct power-law signature in their creep, relaxation, and spectral behaviour. Traditional viscoelastic models can mimic power-law behaviour with a large number of model parameters, which substantially complicates physical interpretation. Traditional approaches are frequently abandoned in order to overcome this restriction. This resulted in the invention of fractional viscoelasticity, a novel formalism for simulating viscoelastic materials. Nutting's early observations are regarded as the parent of this new technique (Nutting, 1921). He showed that the stress relaxation process might be modelled using fractional powers of time. Gemant (Gemant, 1936; Gemant, 1938) attempted to analyse experimental results pertaining to the behaviour of elasto-viscous bodies. It was demonstrated that relaxation trials agree with the deduced transient equation. They showed the typical behaviour of fractional differential quotients and found that the stiffness and damping properties of viscoelastic materials appear to be proportional to the fractional powers of frequency. In 1947, Scott-Blair proposed to use fractional order time derivatives, which modelled Nutting and Gemant's observations concurrently. He approached the problem from the ground up by revisiting a fundamental aspect. He came up with the idea of considering a single element capable of representing the material's viscous and elastic properties at the same time. This method used the concept of fractional derivatives to modify the balance of viscous and elastic properties while staying simple and applicable to a wide range of materials (Scott-Blair, 1944; Scott-Blair, 1947; Rogosin and Mainardi, 2014). To precisely and compactly express the power-law response found in genuine industrial materials, Scott Blair proposed writing the stress response to an induced deformation in terms of a fractional derivative. This type of material response can be represented by the response of a spring-pot mechanical element, also known as the Scott Blair element. Bagley and Torvik conducted a comprehensive investigation of fractional applications to viscoelasticity (Bagley and Torvik, 1983; Bagley and Torvik, 1986). They established a link between molecular theories that describe the macroscopic behaviour of certain viscoelastic media and an empirically developed fractional calculus approach. They discovered that the outcomes of these molecular theories are identical to constitutive relationships expressed in fractional calculus. They concluded that fractional calculus models of viscoelastic materials are consistent with the physical principles governing their behaviour because (i) they provide accurate descriptions of the frequency-dependent shear and loss modulus of materials (ii) the fractional equation formulations are well-posed problems with closed-form solutions.

Fractional calculus emerged as a useful technique for analysing slow relaxation phenomena such as stress-strain relationships in polymeric materials (Friedrich, 1991; Metzler et al., 1995). In the past, fractional viscoelastic models were proposed by simply replacing first-order derivatives with fractional-order derivatives. In general, this formal replacement results in the best fit of experimental results. However, this procedure should be used with caution because the resulting expressions are not always physically reasonable. The fractional Zener model, which relates stress and strain, was discovered by Nonnenmatcher et al. (Nonnenmacher, 1991; Glockle and Nonnenmacher, 1991). Friedrich et al. (Friedrich, Schiessel, and Blumen, 1999) hypothesised that fractional order models can be constructed from mechanical analogies of components with behaviour ranging from pure spring to pure dashpot. This method yields a set of fractional-order models that accurately describe complex viscoelastic fluids. Schiessel et al. (Schiessel and Blumen, 1993) concentrated on the generalised dashpot and generalised Maxwell models, displaying the related arrangements. These models offer a transparent interpretation of the parameters that enter the fractional equations and indicate that the internal dynamics are hierarchically limited. The sequence of fractional differentiation can be changed by modifying the structure of the arrangement and the material constants of the spring and dashpots (Schiessel and Blumen, 1995; Schiessel et al., 1995). Friedrich et al. demonstrated the evolution of fractional versions of the Maxwell model, Zener model, Kelvin-Voigt model, and Poynting-Thomson model using different fractional element arrangements (Friedrich, Schiessel, and Blumen, 1999). The relaxation patterns of these models can be used to fit the experimental results for large classes of materials. Polymeric materials with ramified structures (such as cross-linked polymers) or whose dynamics are characterised by cooperativity (such as glasses) are particularly notable options. The capacity of fractional calculus to characterise the influence of non-localities as well as the memory effect, has been identified as the main contribution of the fractional-order systems method. Since then, the discipline has expanded, especially as biomedical applications have become more precise. Several approaches to material balancing between viscous and elastic properties have been developed in the past. The next section focuses on the analytical methods and results found in the literature for fractional viscoelastic flows, with a few listings of the stability results for viscoelastic channel flows.

1.3 Analytical Results

Analytical solutions for fractional viscoelastic models are still an active area of study, with new results being published consistently. These findings can help engineers in materials science and biomedical engineering by providing insights into the behaviour of viscoelastic materials. Publications focusing on analytical solutions for constitutive equations governing fractional viscoelastic flows are more likely to use the Laplace or Fourier transform approach. Plethora of research conducted to date examines the exact solution for the flow in various geometrical domains. With the Fractional Maxwell model, much earlier research has focused on the unsteady flow between two parallel plates when a rapid motion in the wall triggers the flow. The flows produced by one of the plates' periodic oscillations were investigated by Wenchang et al. (Wenchang and Mingyu, 2002; Wenchang, Wenxiao, and Mingyu, 2003). The authors brought to light that the effect of fractional orders in the constitutive relationship on the flow field is important and that for small periods, there are appreciable viscoelastic effects on shear stress at the plate, whereas, for large durations, the viscoelastic effects become negligible. Hayat et al. (Hayat, Nadeem, and Asghar, 2004) emphasised the importance of fractional constitutive models in the development of theory for non-Newtonian fluids. They applied Fourier transforms to establish a generic solution for three types of unidirectional flows: flow induced by periodic oscillations of a rigid plate, flow produced by periodic oscillations of the lower plate when the upper plate is at rest, and flow produced by periodic oscillations of the lower plate when the upper plate is free to move. Tong and Liu (Tong and Liu, 2005) studied unsteady rotational flows in an annular pipe using a fractional model for an Oldroyd-B fluid. The exact solutions were obtained using Hankel transform and Laplace transform for fractional derivatives. They showed that their model could have the Navier Stokes fluid and the Maxwell fluid as limiting cases. In a further study, Tong (Tong, 2005) investigated four problems using fractional models: Poiseuille flow due to a continuous pressure gradient, Poiseuille flow as a result of both a continuous pressure gradient and a longitudinal constant shear, as well as axial Couette flow in an annulus owing to a longitudinal constant shear. For a unidirectional oscillating flow in an infinite straight pipe, Yin and Zhu (Yin and Zhu, 2006) compared the linear Maxwell model and the Fractional Maxwell model. They used the Fourier transform to provide precise solutions in both the time and frequency domains. They discovered that while the findings of both models were similar, there were several significant discrepancies. However, they did not address whether using fractional models produces more accurate results. Shaowei et al. (Shaowei and Mingyu, 2006) conducted an investigation that demonstrated that the decaying of the unsteady section of a generalised Maxwell fluid exhibits power law behaviour with scale invariance. They derived the exact solution in terms of the Mittag Lefler function using the Laplace and Weber transform for an unstable Couette flow with a fractional model. The limiting instances include the Newtonian as well as the Classical Maxwell model. Qi and Jin (Qi and Jin, 2006) investigated the viscoelastic fluid flow with the Fractional Maxwell model between two coaxial cylinders induced by a simple harmonic motion or an impulsively rotating motion of the outer cylinder. Weber transform and the inverse Laplace transform were used to find exact solutions. They inferred that the propagation of motion increased with α (the fractional order of the time-derivative) in the vicinity of the outer cylinder, but the opposite is true in the vicinity of the inner cylinder.

Later in 2007, Qi and Xu (Qi and Xu, 2007) obtained exact solutions for arbitrary pressure gradients using the Laplace transform and the finite Fourier cosine transform. They considered the Fractional Maxwell model for an unsteady viscoelastic flow and confirmed that the properties of the viscoelastic fluid could be better examined by the fractional model rather than the classical integer order model. Vieru et al. (Vieru, Fetecau, and Fetecau, 2008) discovered accurate solutions for the velocity field for the Fractional Maxwell model when the flow is constrained between two side walls perpendicular to a plate. The flow was caused by an endless plate sliding in its plane with a constant velocity field. Fourier sine and Laplace transforms were used to derive the solutions in terms of generalised Mittag-Leffler functions. To circumvent the time-consuming calculations of residues and contour integrals, the discrete inverse Laplace transform approach was utilised to compute the velocity distribution. In the absence of side walls, all solutions obtained reduce to those corresponding to motion across an infinite plate. Jia and Hua (Jia and Hua, 2008) investigated the oscillating flow of viscoelastic fluids in an endless pipe using the Fractional Maxwell model, and the exact solution in series form for the velocity fields was obtained. They studied the time-velocity profiles of silicon gel and discovered that the flow behaves like the Newton fluid for low oscillating frequencies and reverses for high oscillating frequencies. In a follow-up study, Qi and Xu (Qi and Xu, 2009) used a Fractional Oldroyd-B model to study unsteady unidirectional flows; plane Poiseuille and plane Couette flow. They obtained analytical solutions using finite Fourier sine transforms and showed that some well-known solutions for the generalised second-grade fluid, the generalised Maxwell fluid, and the ordinary Oldroyd-B fluid may be revived as limiting instances of the current results. In a study by Fetecau et al. (Fetecau et al., 2009), the unsteady flow of an incompressible generalised Oldroyd-B fluid in a somewhat different geometry was presented. A rapid movement caused the flow in a plate located between two side walls perpendicular to the moved plate. The general solution for the velocity field was found as the sum of Newtonian and non-Newtonian contributions, the effect of fractional parameters on the velocity field and the influence of side walls on fluid motion were highlighted.

Significant research has been conducted that compares the analytical results with experiments and shows that the fractional model produces more appropriate results. One study that shows the importance of fractional order for the flow of Fractional Maxwell fluid was done by Wang and Xu (Wang and Xu, 2009). They investigated unstable axial Couette flow of fractional second-grade and Fractional Maxwell fluids between two indefinitely long concentric circular cylinders. They obtained the analytical solutions for the velocity fields by decomposing them in two parts, steady and unsteady, with the use of the Laplace transforms and Weber transforms, generalized Mittag Leffler function and H-fox function. The unstable flow of a viscoelastic fluid between two indefinitely long concentric circular cylinders was studied by Khan et al. (Khan, Hyder Ali, and Qi, 2009a), utilising a fractional equivalence. They solved Burger's model by using the Laplace transform with the Weber transform. They concluded that the integer order models require more time as the velocity approaches the steady state than the fractional ones. They also demonstrated that the velocity profiles for fractional models are smaller in magnitude and more stable than those for integer-order models. In another study, Khan et al. (Khan, Hyder Ali, and Qi, 2009b) derived accurate results for the velocity field of the accelerated flows for a viscoelastic fluid governed by the fractional Burgers' model using the Fourier sine transform and fractional Laplace transform. They looked at two situations: flow caused by a plate that was accelerating continuously and flow caused by a plate that was accelerating inconsistently. Mittag Leffler functions were used to present the solutions in series form. They also discussed the effect of fractional order on the flow's shear-thinning and shear-thickening properties. Even in seepage mechanics, the fractional calculus approach is used. The rheological properties of heavy oil are found to be viscoelastic. Wang and Tong (Wang and Tong, 2010) developed a three-dimensional viscoelastic fluid relaxation model for various unstable flows in an infinite reservoir. The Laplace transform and the Fourier sine and cosine integral transform were used to find accurate results. The pressure transient behaviour of a non-Newtonian viscoelastic fluid was investigated using the Stehfest numerical Laplace transform inversion method and the Gauss-Laguerre numerical integral equations. As limiting examples, the solutions for the Fractional Maxwell model, classical Maxwell, and classical Oldroyd-B models could be found. Hyder et al. (Hyder Ali Muttaqi Shah and Qi, 2010) solved the flow of a viscoelastic fluid analytically in an annular pipe using fractional Burger's equation and concluded that the fractional constitutive relationship model is more flexible than the conventional model in describing the properties of viscoelastic fluids. They used the Laplace transform and the Weber transform for two types of flows: one with a constant pressure gradient and one with a constant velocity of the outer cylinder. Yang et al. (Yang and Zhu, 2010) investigated a unidirectional start-up flow of a viscoelastic fluid in a pipe caused by a constant pressure gradient described by a Fractional Maxwell's model. They used the variable-separable method and Heaviside operational calculus to produce the exact solution, which was then used to examine the flow characteristics.

During the last decade, Jamil et al. (Jamil, Fetecau, and Fetecau, 2012) conducted a study for an incompressible fluid in the annular region between two infinite coaxial circular cylinders, where the inner cylinder produced the motion. They derived exact solutions in series form for velocity and shear stress using Laplace and finite Hankel transform. They compared three types of fluid: Newtonian, Maxwell, and Fractional Maxwell, and concluded that Newtonian fluid is the fastest in the vicinity of the inner cylinder, whereas Fractional Maxwell fluid is the slowest. Sahu et al. (Sahu and Govindarajan, 2012) published a paper that found the analytical solution for the time-fractional Navier-Stokes equation. To explore double-diffusive channel flow, they provided a simple and efficient strategy based on a modified, reduced differential transform method and a novel iterative Elzaki transform method. The results revealed that at $Re \sim 100$, absolute instability develops quickly, but this instability is much weaker in single solute fluids. The study of magnetohydrodynamic viscoelastic flows also requires a strong understanding of fractional calculus. The paper by Zheng et al. (Zheng, Liu, and Zhang, 2012) investigated the magnetohydrodynamic flow of an incompressible generalised Oldroyd-B fluid driven by an accelerating plate and including slip boundary conditions. They used discrete Laplace transforms to find the closed-form solutions for velocity and shear stress in terms of H-fox function. The solutions for magnetohydrodynamic flows are significant not only because they are solutions to specific flows of technical value but also because they can be used to assess the accuracy of experimental, numerical, and asymptotic approaches. Another study of magnetohydrodynamic flows was demonstrated in Maqbool et al. work (Maqbool et al., 2016). Three different classes of magnetohydrodynamic incompressible flows of a Burgers fluid, flow originated by general periodic oscillation, Poiseuille flow, and periodic flow in a parallel plate channel with electrically non-conducting boundaries, were analysed. Because of the applicability of electro-osmosis in micro- and nano-devices, it has long been an important research area. The electrolytic solution moves relative to the pipe because an electric field is applied externally to the electrolytic solution. Ming et al. (Ming et al., 2016) employed a modified variable-separable technique to convert a fractional order partial differential equation, which included terms for spatial diffusion, time-fractional diffusion, and reaction terms, into a set of fractional partial differential equations. Using Mikusiski-type operational calculus, they obtained the exact solution of the equation in terms of Mittag Leffler functions. They claimed that their equation could model generalised viscoelastic Oldroyd-B fluid and Burger's fluid. Wang and Liu (Wang and Liu, 2016) used a modified, reduced differential transform method and a novel iterative Elzaki transform method to get the exact analytical solution for the time-fractional Navier Stokes Equation. Laghari et al. (Laghari, Abro, and Shaikh, 2017) explored the helical effects of three types of fluid, including fractional and ordinary Maxwell fluid, in a helically moved cylinder. Hankel and discrete Laplace transforms were used to obtain exact solutions. Jaber and Ahmad (Jaber and Ahmad, 2018) employed the residual power series approach to construct a power series solution of the nonlinear time-fractional Navier-Stokes equation in two dimensions. They demonstrate that their method requires less computation than traditional methods for solving linear and nonlinear fractional partial differential equations.

In recent work, Gritsenko and Paoli (Gritsenko and Paoli, 2020) discovered the generalisation of the exact analytical solutions for fractional viscoelastic flow in a circular pipe. The authors described velocity profiles and shear stresses for a variety of fractional models, including Fractional Maxwell, Kelvin-Voigt, Zener, Poynting-Thomson, and Burgers models, and showed that the same form of the solution is applicable to all of them. Su et al. (Su, Yao, and Xu, 2020) discovered yet another formulation of fractional models by constructing a transfer function connecting two selected limiting viscoelastic models and showed that the numerical and analytical solutions could be derived with this transfer function method. However, this transfer function was different for different materials. An et al. (An et al., 2022) investigated the unsteady slip flow of an incompressible viscoelastic fluid in a microchannel with combined electro-osmotic and pressure gradient forcings. They used Debye-Hackel linearization, the Laplace transform, and the residue theorem to discover analytical solutions for velocity and potential distributions.

Numerous studies have been conducted on the stability of parallel flows of viscoelastic fluids, including plane Poiseuille and Couette flow. The stability of plane Poiseuille flow of viscoelastic fluid at low Reynolds numbers was investigated (Teh and Morton, 1977; Lee and Finlayson, 1986; Wilson, Ren ardy, and Renardy, 1999), and the flow was shown to be stable. For high Reynolds number viscoelastic Poiseuille flow, the stability problems have been studied by many authors (Teh and Morton, 1977; Kundu, 1972; Sureshkumar and Beris, 1995; Tackels and Crochet, 1973; Tlapa and Bernstein, 1970), and their findings concluded that the resulted instability is due to the non-Newtonian parameter. It has been discovered that the flow of viscoelastic fluids in plane Couette flow is identically stable at low Reynolds numbers. Sureshkumar et al. (Sureshkumar and Beris, 1995) investigated the linear stability studies for viscoelastic Poiseuille and Couette flow at high Re utilising the Upper Convected Maxwell model, Oldroyd-B model, and Chilcott-Rallison models. To obtain the extremal eigenvalues of a non-Hermitian matrix, they used Amoldi-orthogonalization. They observed the oscillatory decay of finite disturbances in the full parameter range investigated for Couette flows, both in the inertial and elastic regimes. In a further study (Sureshkumar, 2001), smaller values of the channel wall amplitude and frequency were considered so that separated flow regions did not exist and domain perturbation analysis gave a convergent solution to the base state. In 2002, Atalik et al. (Atalik and Keunings, 2002) used a fully-spectral method with a stream-function formulation to examine the non-linear analysis of the temporal evolution of finite, two-dimensional disturbances in plane Poiseuille and Couette flows of viscoelastic fluids. Upper-convected Maxwell, Oldroyd-B, and Giesekus models were taken into account. Even under conditions of linear stability, it was discovered that a temporary increase of misfit disturbances occurs under the influence of the Reynolds and Weissenberg numbers. In a recent study, Chaudhary et al. (Chaudhary et al., 2021; Khalid et al., 2021) studied the stability formulation for viscoelastic pipe Poiseuille flow subjected to infinitesimal amplitude axisymmetric disturbances. A modal stability analysis showed that the pressure-driven pipe flow of an Oldroyd-B fluid is linearly unstable to axisymmetric perturbations, in stark contrast to its Newtonian counterpart, which is linearly stable at all Reynolds numbers.

1.4 Experimental Results

This section focuses on various experimental findings that show how fractional models are better for approximating the subdiffusive viscoelastic behaviour. The enormous potential of fractional-order viscoelastic models for capturing the natural features of materials has long been recognised and experimentally proved. Experimental testing is important in capturing viscoelastic behaviour since it helps in the development of theoretical constitutive models that can be used to simulate accurate behaviour. To determine the derivative at an instant, the fractional derivative operators consider the entire history of the system. Viscoelastic materials have infinite memory, which means that the past influences their current mechanical response. Experiments have been done, taking into consideration the previous deformations of the subdiffusive material. When the analytical results reflect the system dynamics predicted by fractional calculus, experiments and measurements on viscoelastic materials can offer light on the meaning of fractional order operations. Fractional calculus allows us to start separating contributions to physics from the underlying model dynamics, geometry, system component interactions, and physical barriers. Polymer melts, and solutions deform, resulting in chemical and mechanical interactions that can only be explained by physically intuitive yet, challenging constitutive equations. To characterise the rheological properties of polymer melts, an adequate mathematical constitutive equation is critical. To thoroughly parameterize the flow behaviour, experimentalists must select appropriate experiments to identify the behaviour of fluid in diverse flow circumstances with various forms of deformation history. Complex modulus measurements at various frequencies, followed by relaxation spectra calculation, may provide some insight into these processes.

During the 20th century, Laun (Laun, 1978) demonstrated that rheological measurements could completely determine the memory function using a Weissenberg Rheogoniometer Model R 12/15. In another work (Laun, 1986), he used several rheometers to assess transient and steady-state stresses in polyethylenes, polypropylenes, polystyrene, polyamide 6, and a PIB solution. Theoretical and experimental findings were contrasted. He discovered that the degree of recoverable stresses measured after unloading orientated polymers increased with flow rate. These elastic strains must be considered in polymer processing since they affect product characteristics and shape. Historically, experiments were used to determine the complex modulus of viscoelastic fluids. Nonnenmatcher. (Nonnenmacher, 1991) conducted experiments on polyisobutylene and natural rubber and compared the results to the analytical solutions derived in terms of H-fox functions for the fractional Zener model. A comparison with experimental relaxation data showed good agreement with theoretical predictions, supporting the fractional model, which incorporated the Fractional Maxwell rheological law as a particular instance. An in vivo investigation by Eldred et al. (Eldred, Baker, and Palazotto, 1995) used two wholly different materials, one similar to tyre rubber, with a springy response across a wide frequency range and an acrylic core foam, utilised for dampening purposes, to compare the integer and fractional models. They employed three constitutive equations and discovered that a four-parameter fractional model improves accuracy in materials with significant glassy regions, followed by a three-parameter fractional model that provides significantly better results over a much larger bandwidth. Finally, the integer order Kelvin-Voigt scheme was shown to be adequate in only a few frequency ranges. Field et al. (Field, Swain, and Phan-Thien, 1996) performed one such test based on tiny amplitude random squeezing between parallel plates to generate the complex modulus spectrum of small volumes of fluid with a wide variety of viscosities and frequencies. The equipment and fluid sample were regarded as a dynamic system, and transfer functions were computed from measurements of relative plate motion and the fluctuation of the associated normal force. The gadget could be utilised as a novel "Fourier micro-rheometer" with pathological applications.

Subsequently, Hernandez et al. (Hernández-Jiménez et al., 2002) conducted an experimental study to examine stress relaxation in samples of polymers PMMA and PTFE (polymethylmethacrylate and polytetrafluorethylene). They found that contrary to what the classic Maxwell model predicts, there are two relaxation time distributions rather than just one. They made this discovery using a fractional model. They concluded that by implementing a constant strain following the first deformation process, the stress and the value of the elastic deformation are decreased. Viscoelastic materials are useful for vibration-controlling devices, including isolators, dynamic vibration neutralisers (also known as dynamic vibration absorbers), sandwich panels, and structural connections. The storage and loss modulus of the material must be known in order to make good use of such devices. The fractional order stress-strain element is a widely utilized mathematical model for describing the viscoelastic properties of the red blood cell membrane, other cell membranes, and multilayered tissue such as cartilage or the artery wall in a simple manner. Kiss et al. (Kiss, Varghese, and Hall, 2004) conducted an in vitro investigation on canine liver tissue specimens utilising an EnduraTEC ELF 3200, a dynamic testing system for assessing the mechanical properties of canine liver tissue specimens over a frequency range of 0.1 to 400 Hz. The load response of normal tissues and thermal lesions generated by radiofrequency ablation was studied after uniaxial compression with Plexiglas platens. The acquired data agreed quite well with the fractional Kelvin Voigt model, especially at frequencies less than 100 Hz. Espindola et al. (De Espindola, Da Silva Neto, and Lopes, 2005) presented a novel experimental approach to measure dynamic modulus with a single mass attached to a vibrating string. To calculate the viscoelastic properties of materials, the vibrating beam approach and the direct complex stiffness method were combined with a fractional model. Lu (Lu, 2006) compared the frequency-dependent complex moduli of automobile elastomers calculated using a fractional derivative model to experimental results obtained with different durometers and a dynamic mechanical analyzer. The experimental results were found to be very close to the projected results.

Later in 2010, Meral et al. (Meral, Royston, and Magin, 2010) examined viscoelastic materials, which are fractional order material models for soft tissue, to enhance the diagnostic potential of Magnetic Resonance Elastography, which is a fractional calculus application used to solve surface waves analytically. They tested two different soft tissue-mimicking phantoms with varied elastic and viscous properties but in the same viscoelastic range as biological tissues. A noncontact Laser Doppler Vibrometer was used to monitor surface wave vibration. This research compared fractional and integer order models to describe the behaviour of the tissue-imitating materials CF-11 and gelatin under harmonic mechanical pressure. Therefore, in order to establish an autonomous testing platform for assessing viscoelastic material models that may eventually be used in Magnetic Resonance Elastography reconstruction techniques, surface waves were investigated both conceptually and experimentally. Magin (Magin, 2010) conducted another experimental study that demonstrated that the fractional order model best fits electrical and mechanical measurements made on living tissue using three examples: the electrical impedance of the electrode-tissue interface, the stress-strain behaviour of arterial, and the bulk elastic properties of normal and cancerous breast tissue. They remarked that the multiscale patterns found in muscle fibres, tendons, and nerve fibres were efficiently recorded in fractional order processes, and the resulting dynamics were represented using fractional order differential equations. Craiem and Magin (Craiem and Magin, 2010) reviewed different fractional models to analyze the viscoelasticity of red blood cell membranes.

Many experimental findings have been made to validate the results for linear fractional constitutive equations, and it has been demonstrated that fractional models may be employed for the best fit of diverse viscoelastic fluids over a wide frequency range. However, little experimental research has been conducted to characterise the behaviour of non-linear viscoelastic materials. Experiments on polymer melts have revealed that such materials have non-linear behaviour. Muller et al. (Müller et al., 2011) developed a fractional order model that can simulate both long-term (relaxation tests) and short-term (tensile tests) material behaviour at varied strain rates. They validated their model using polymeric material Polypropylene experiments. The strain rate was then calculated using relaxation tests in which a constant strain level was introduced to the specimen, and a set of uniaxial simulations were run and compared with experimental data to determine the model's applicability. Paola et al. (Di Paola, Pirrotta, and Valenza, 2011) wrote a paper that validates the fractional theory governing viscoelastic characteristics. To thoroughly confirm the fractional model, two alternative chemical and physical attributes were investigated, labelled Aerstop CN 20 and Aerstop VX 5. The tests were carried out with varying amplitudes, and the theoretical relaxation and creep functions always overlapped the experimental data, resulting in the conclusion that the fractional model is capable of fully capturing the visco-elastic behaviour, encompassing a wide range of materials. Sasso et al. (Sasso, Palmieri, and Amodio, 2011) conducted a series of studies on styrene-butadiene rubber and polypropylene plastic specimens. They explored compression and tension testing, as well as cyclic loading for a variety of frequencies, assuming modest deformations and linear viscoelastic material. Choudhary et al. (Choudhury et al., 2012) investigated the spreading of a potato starch gel between two glass plates with a constant weight on the upper plate. They created a fractional model to investigate rheology and spreading. Their results demonstrated how the fractional calculus approach may be used to analyse the interesting phenomena of oscillatory spreading of a starch gel on glass. Paola et al. (Di Paola et al., 2014) conducted various tests using commercial epoxy resin (SP106) samples at two distinct rates of deformation to show that the stress history during the relaxation test is significantly influenced by the initial ramp of deformation., confirming that the correct way to characterise viscoelastic properties is through the use of fractional calculus, which also reduces the long duration of the experimental tests. Kontou et al. (Kontou and Katsourinis, 2016) conducted another in vivo work to demonstrate the capabilities of the fractional Zener model to represent the time and frequency-dependent response of two polymeric materials with distinct structures, a thermosetting epoxy resin and a biodegradable polymer and its nanocomposite.

More recently, Ding et al. (Ding et al., 2017) received rock samples for their experimental research from the Changqing oilfield in China, which is a key hub of tight gas production. They discovered that tight sandstone is viscoelastic in nature, and they used a Fractional Maxwell model to obtain the constitutive equation in order to anticipate the long-term deformation behaviour of tight sandstone. Their research would aid in the creation of a tight gas reservoir development plan. Lorenzo et al. (Di Lorenzo et al., 2017) presented a non-linear fractional model for capturing the non-linear trend of polymer melt shear viscosity as a function of shear rate. They contrasted the results for the fractional model with the results of the classical integer order models. The comparison of the experimental data and the theoretical model demonstrated good agreement, highlighting that the fractional model is appropriate for analysing viscoelasticity even when the material exhibits non-linear behaviour.Biofilms derived from electro-active bacteria are being studied as potential biocatalysts for green chemistry, with applications in waste remediation, energy production, and chemical compound and nanomaterial synthesis. One significant work demonstrating that the incorporation of fractional time derivatives in linear viscoelastic equations is a necessary technique for modelling the rheological properties of biomaterials over a wide variety of time and frequency scales, done by Majumdar et al. (Majumdar et al., 2017). They conducted a study on the rheology of biological viscoelastic materials and an aqueous gel of the synthetic clay Laponite using the bacterial biofilms Staphylococcus epidermidis, Pseudomonas aeruginosa, and Bacillus subtilis. They compared their experimental findings for complex visco-elastic modulus, creep compliance, and complex viscosity modulus to theoretical results for integer and fractional order models. For laponite gels, the fractional models utilised were the Boltzmann model and the three-element fluid model for biofilms. A microfluidic electrochemical system was used by Zarabadi et al. (Zarabadi, Charette, and Greener, 2018) to properly modulate hydrodynamic conditions while measuring changes in biofilm pH. They discovered that increasing flow rates could, in fact, minimise biofilm acidification, but only at high turnover concentrations, which are commonly used in research studies. Using the Caputo derivative and Mittag Leffler functions, Nandagopalan et al. (Nandagopalan et al., 2018) investigated the instability mechanism of such fuels by subjecting them to shear flow in a cone-plate rheometer. The rheological investigation yielded two distinct results: the presence of elastic instability in the secondary flow due to normal stress in the low We regime and the maximum extension beyond which the polymer breaks down as the applied shear rate increases in the high We regime.

The most recent results include the study by Liu and Li (Liu and Li, 2020). They presented an improved fractional model for studying rock rheology. They compared the findings of a series of experiments employing sandstone, salt-rock, and mudstone to validate their model and detail the mechanical behaviour of accelerating creep. Based on a fractional order theory, Chen et al. (Chen et al., 2021) conducted an experimental study to analyse the properties of blood flow in the fractal network of blood vessels. Their study results demonstrated that blood flow alters as time-fractional order changes. It was determined that time-fractional order influences blood distribution and exhibits variable velocity field characteristics under various flow Reynolds numbers, pulse frequencies, time, and pulse pressures.

1.5 Numerical and Computational Results

The last few decades have seen a growing trend towards using fractional order derivatives to numerically explain various models in the broad subject of engineering and biological modelling. The fractional operators and the accompanying integero-differential equations are commonly used for their memory effect. However, theoretical solutions are rarely applicable to the provided circumstances when it comes to solving a mathematical problem derived from a real-life fractional model; therefore, a number of numerical methods are found to solve the fractional differential operators. There are several kinds of fractional derivatives; Riemann–Liouville derivatives, Grunwald–Letnikov derivatives, Caputo derivatives and Riesz derivatives. For these different kinds, there are numerous methods to approximate fractional derivatives and fractional differential equations; the fractional versions of the rectangular formula, Trapezoidal rule, Newton Cotes formula, Linear multistep methods, Grunwald Letnikov approximation, Euler method, Weighted difference, Adams methods, L1, L2 and L2C methods.

Although analytical solutions for fractional differential equations have been established or can be generated using various transform techniques, they are typically expressed in terms of multinomial Mittag-Leffler functions, which are exceedingly complex and difficult to evaluate. Using numerical methods to solve these equations is preferable, especially in circumstances where analytical solutions are unavailable. More recent attention has focused on providing numerical schemes to space-time fractional or time-fractional equations.

At the start of the 21st century, Schmidt and Henningson (Schmid and Henningson, 2001) used the Grunwald and modified Grunwald approximations to extend the fractional model to three-dimensional situations, distinguishing between the hydrostatic and deviatoric portions. They demonstrated using finite element formulation that fractional derivatives arise in non-local operators that offer the 'fading memory' trait recognised from viscoelastic media. Many researchers have focused on fractional convection or diffusion equations using mainly Caputo or Riemann Liouville derivatives. Time-fractional diffusion equations are used in an attempt to explain transport processes with long memory, when the rate of diffusion is not consistent with the classical Brownian motion model. In 2005, Yuste and Acedo (Yuste and Acedo, 2005) devised a novel approach for solving the fractional diffusion equation by combining the central space method with the Grunwald Letnikov temporal discretization. Yang et al. (Yang et al., 2006) constructed efficient higher-order schemes by modifying coefficients of the upwind schemes and analyzed that their technique preserves the theoretically anticipated features. They used the new methods for the linear scalar equation, Burgers equation and the hyperbolic system of conservation laws to study the Rayleigh–Taylor instability. Meerschaert et al. (Meerschaert, Scheffler, and Tadjeran, 2006) resolved a class of fractional partial differential equations with variable coefficients that are two-dimensional initial-boundary value problems on a finite domain using realistic alternating directions implicit approach. Using the Grunwald Letnikov formula, Liu et al. (Liu et al., 2007) offered an implicit-explicit technique for solving the space-time fractional advection-dispersion equation. They investigated these methods' numerical stability and convergence. Two decisive algorithms, namely; the Adomian decomposition method and variational iteration method, were proposed by Momani et al. (Momani and Odibat, 2008) to find numerical solutions to the space-time fractional advection-dispersion problem in the form of a quickly converging series with easily estimable components. The fractional derivatives were described in the Caputo sense. Using the Grunwald Letnikov finite difference approximation, Zhang (Zhang, 2009) provided an implicit unconditionally stable difference method for fractional convection-diffusion equations. The spectral approach was used by Li and Xu (Li and Xu, 2009) to discretize the temporal and spatial derivatives of the time-fractional subdiffusion equation. They noted that because the spectral technique is precise in both space and time, the storage need may be lowered, and the process can be simulated over a longer time period. Su et al. (Su, Wang, and Xu, 2010) used an unconditionally stable weighted average finite difference approach to solve the space-fractional advection-dispersion equation.

Later on, researchers have seen that, since fractional models incorporate memory effects, the amount of information to be stored is extremely heavy, and the process of computing is large. Standard finite difference methods with fixed timesteps typically require a very long calculation time to solve fractional differential equations. Furthermore, the solutions to these issues frequently entail vastly diverse time scales, resulting in numerical errors. Adaptive numerical methods, in which the size of the timesteps is selected based on the behaviour of the solution, are a logical way to handle these challenges. The efficiency of the adaptive algorithm used to dynamically set the size of each timestep is a major element of these approaches. Many researchers have begun to use time adaptive systems to model the long-term behaviour of fractional viscoelastic flows. Brunner et al. (Brunner, Ling, and Yamamoto, 2010) introduced the time-adaptivity-based algorithm to simulate a subdiffusion-convection equation. Wang and colleagues (Wang and Wang, 2011) devised a rapid characteristic finite difference approach for solving the space-fractional advection-dispersion problem. They demonstrated that the method produces more accurate solutions than typical implicit methods, even with far bigger time steps and spatial meshes. Sweilam et al. (Mahdy, Sweilam, and Khader, 2012) solved the linear time-fractional diffusion problem with Caputo's fractional derivative using the Crank-Nicolson finite difference method. Zeng et al. (Zeng et al., 2013; Zeng et al., 2015) employed a fractional linear multistep method to approximate time derivatives for the time-fractional subdiffusion equation with Dirichlet boundary conditions. They also presented a corresponding scheme with the Neumann boundary conditions as well. Chen et al. (Chen et al., 2014) introduced the numerical simulation of the three-dimensional fractional subdiffusion equation. They proposed a scheme called fractional alternating direction implicit scheme, which is uniquely solvable and proved to be convergent. Birajdar (Birajdar, 2014) used the Adomian decomposition approach to solve the time fractional discrete Navier-Stokes equation. The graphical representation of the answer provided by the MATLAB program was compared to the actual solution and the integer order case. Ercan and Kavvas (Ercan and Kavvas, 2016) presented a numerical approach based on finite differences to solve the time-space fractional governing equations of a one-dimensional unsteady/non-uniform open channel flow process. Hao et al. (Hao et al., 2016) investigated semi-linear space-fractional diffusion equations with a fixed time delay using a quasi-compact finite difference scheme. They employed the shifted Grünwald-Letnikov formula to estimate the space-fractional derivatives, which can accomplish a fourth-order approximation under particular smoothness assumptions of the solution. Feng et al. (Feng et al., 2016) illustrated two finite element methods for solving space-time fractional diffusion equations using the Riemann-Liouville space fractional derivative. Because of the rising prevalence of boundary layer flow and heat transfer research in industry, fractional partial differential equations are of tremendous practical importance. Zhao and Liu (Zhao et al., 2016) explored natural convection heat transfer via the Maxwell viscoelastic fluid in an unstable boundary layer across a vertical plate. They demonstrated how to solve a nonlinear coupled equation model with mixed time-space derivatives in the convection terms using a newly developed finite difference method in conjunction with an L1 algorithm. They discovered that fractional order thickens velocity and reduces the effect of natural convection and heat conduction. Santos et al. (Yuste and Quintana-Murillo, 2016) proposed two adaptable strategies that make use of the step-doubling method. These methods allow for the establishment of a tolerance threshold for numerical errors, which turns out to be a good predictor of the actual errors, and are stated to be substantially faster than the related standard method with fixed timesteps. Cao et al. (Cao et al., 2016a) used the finite difference approach and the L1 scheme to examine the magnetohydrodynamic flow and heat transfer of a Fractional Maxwell viscoelastic nanofluid across a moving plate. Yu et al. (Yu, Perdikaris, and Karniadakis, 2016) conducted research using three-dimensional fractional constitutive equations to analyse artery wall mechanics. They used a rapid convolution method with a high-order backward differentiation to describe the continuous relaxation features of soft tissue and simulate flow structure interactions for patient-specific brain aneurysms. They showed that fractional calculus may be used effectively to represent complex material behaviour in realistic 3D time-dependent issues if efficient methods are correctly devised to overcome the extra memory requirements and computing complexity.

More recently, one of the works of Ferras et al. (Ferrás et al., 2017) addressed the Fractional Maxwell model, which interpreted that the model might be reduced to the suitable limitations of a Hookean solid, a Newtonian fluid, and the classical Maxwell Viscoelastic fluid. They compared their findings to earlier analytical findings, indicating that using fractional models for rheological data yields better results. Xu et al. (Xu, Jiang, and Yu, 2017) numerically solved the space fractional Navier-Stokes equations with Riesz fractional derivatives in place of the Laplacian operator. They used the finite difference approach of fractional differential equations to investigate a pressure-driven flow between two parallel plates. In addition, they presented the Levenberg-Marquardt approach for estimating model parameters. Sin et al. (Sin et al., 2017) explored the unsteady flow of a viscoelastic fluid between two parallel plates caused by the bottom plate's impulsively accelerated motion. The unidirectional flows were simulated using Fractional Maxwell and Fractional K-BKZ models and finite difference techniques, with exact solution validation. Their findings revealed that viscoelasticity rapidly fades in Fractional Maxwell fluid. Takeuchi et al. (Takeuchi, Yoshimoto, and Suda, 2017) presented finite difference algorithms with second-order accuracy for fractional equations with Dirichlet boundary conditions. Carrera et al. (Carrera et al., 2017) proposed a Fractional Maxwell model with a non-linear term that incorporated the non-Newtonian viscosity behaviour and derived expressions for the storage and loss moduli in terms of frequency and amplitude of the shear strain excitation signal. They extracted three examples from the previous in vivo studies; Aeromonas gum in an aqueous solution, Lebanese locust bean gum in an aqueous solution and double emulsion stabilized by protein-polysaccharide complexes. They obtained a numerical solution to their problem and compared their results for storage and loss moduli with the available experimental findings, confirming the ability of the Fractional Maxwell model to describe experimental data for a variety of complex fluids found in food and pharmaceutical industries. Ding et al. (Ding and Li, 2018) employed higher-order numerical schemes to approximate the space-fractional convection equations with the Riemann-Liouville derivatives. Liu et al. (Liu et al., 2018) discussed the Galerkin finite element method with a second-order temporal discretization scheme to approximate a nonlinear time-fractional diffusion equation. They compared their computational results with the previously predicted theory and also confirmed the stability of the scheme. Dehgan et al. (Dehghan and Abbaszadeh, 2018) proposed a novel numerical scheme based on finite element and finite difference method to study fractional diffusion wave equation. Zhang and Wang (Zhang and Wang, 2018) in their study investigated a $2-\alpha$ order accurate numerical scheme to solve time-fractional Navier Stokes Equations, using finite differences for time and Legendre spectral method approximation for space. Ferras et al. (Ferrás et al., 2018) studied the pure tangential annular flow of fractional viscoelastic fluids. They established a numerical method based on finite differences to solve coupled fractional differential equations for velocity and stress. They reported the numerical convergence of the method and its application to simulate the rheological reaction of complex fluids in a real concentric cylinder rheometer. One of the applications of fractional viscoelastic flows is to study the Chemical species reaction because of its importance in combustion, biochemical systems and catalysis. Rasheed and Anwar (Rasheed and Anwar, 2018) explored the velocity and concentrations profile of chemically reacting species for various physical parameters. To capture a wide range of physical and chemical processes, they considered unequal diffusivities of chemical species. They used finite difference techniques along with the L1 algorithm for the discretization of equations. Another study by Rasheed et al. (Rasheed and Shoaib Anwar, 2019) used finite element and finite difference methods for the numerical estimation of velocity and concentration of chemical species in the viscoelastic flow regime.

In recent years, Xie and Feng (Xie and Fang, 2019) investigated a second-order accurate numerical technique for fractional equations based on the traditional Crank-Nicolson method. A unique time and space-fractional heat conduction equation was analysed to study the heat and mass transport of a Maxwell viscoelastic nanofluid across a moving flat plate to model Brownian diffusion and thermophoresis by Zhang et al. (Zhang et al., 2019). They concluded that for a bigger order of fractional derivatives, one could have a stronger memory characteristic that exhibits fractional derivative's physical meanings. Using the Riesz derivatives, Sayevand et al. (Sayevand, Machado, and Moradi, 2019) dealt with the fractional Navier–Stokes equations using a novel non-standard finite difference method to obtain the pressure driven by the flow between two parallel plates. They also discussed the stability and convergence of the method. Prakash et al. (Prakash, Prakasha, and Veeresha, 2019) studied an unstable, unidimensional viscous fluid motion caused by a constant pressure gradient in a long circular pipe that was initially at rest. They employed Caputo derivatives to numerically solve the Fractional Navier Stokes using a combination of the q-homotopy analysis technique and the Laplace transform. Feng et al. (Feng, Liu, and Turner, 2019) suggested a new fractional equation with a specific time-space coupled derivative to analyse mixed diffusion on convex domains. They considered the finite element approach and the mixed L schemes for discretisation. In addition, they investigated the temporal fractional mixed diffusion equation on a circular domain and a generalised Oldroyd-B fluid in a magnetic field. Many computational, theoretical, and experimental studies of naturally convecting and radiating flow of viscous fluids in vertical cylinders, channels, and across an infinite plate have been conducted. For example, Hamid et al. (Hamid et al., 2019) used a fractional technique to examine unsteady naturally convecting and radiating flow in an open-ended vertical channel. The Crank-Nicolson method with a finite difference scheme was used to obtain numerical solutions. Yang and Jiang (Yang and Jiang, 2019) employed the L1 finite difference scheme for the temporal derivatives and the Legendre spectral method for the spatial derivatives to approximate a numerical solution for the two-dimensional fractional Stokes' problem. They also included numerical experiments to verify theoretical predictions.

The rotating electro-osmotic flow of Fractional Maxwell fluid through a parallel plate microchannel was recently explored by Wang et al. (Wang, Xu, and Qi, 2020) utilizing the finite difference method to solve the governing equations of the velocity distribution. The results were compared with the analytical results of the Newtonian fluid. Liu et al. (Liu et al., 2020a) characterized the distributed order time fractional equations that govern the heat flow. L1 and L2 schemes are used to discretize the fractional derivatives. They also obtained the exact solution and compared the numerical results to verify the correctness. Because the computation cost for solving fractional differential equations is very high, Nikan et al. (Nikan and Avazzadeh, 2021) proposed a localised scheme that is based on dividing the domain into smaller subdomains using kernel approximation and allows one to simplify the system to have a small condition number. To describe heat flow in memory materials, they employed a second-order finite difference scheme to discretize the temporal derivatives and a local radial basis function partition of unity technique for the spatial ones. Using the Caputo fractional derivative, Hanif (Hanif, 2022) suggested a Crank-Nicolson-based L1-algorithm to solve two-dimensional boundary layer flow and heat transfer of Fractional Maxwell fluid with constant heating. They also reported that at the maximum value of the temporal relaxation parameter, the thickness of the velocity boundary layer grows. Janelli (Jannelli, 2022) used adaptive mesh refinement procedures to solve fractional differential equations numerically. The results with the double-stepping procedure were compared with the classical ones to ensure the efficiency and accuracy of the procedure.

1.6 Applications of Subdiffusive Viscoelastic Flows

Fractional viscoelastic models have a lengthy history of applications. The last half-century has seen that some of the most significant and profoundly published experimental results are better rationalized within the viscoelastic subdiffusive approach in random environments such as in dense colloidal suspensions (Kremer and Grest, 1990), crowded complex fluids and polymer solutions (Levine and Lubensky, 2001), the cytosol and the plasma membrane of biological cells (Rubenstein and Colby, 2003), and single-file diffusion in colloidal systems (Kou and Xie, 2004). Kohandel et al. studied the dynamic moduli of the brain tissue using the Fractional Zener model (Kohandel et al., 2005). Various applications of sub-diffusion in biology in the cell nucleus, plasma membrane and cytoplasm, ultra-cold atoms, harmonic spring-mass systems, ion channels in the plasma membrane, and moisture transport in cement-based materials have made anomalous diffusion a considerable subject of interest (Lai et al., 2009). Following are some significant research demonstrating the viability of modelling real-world situations using fractional constitutive equations.

Lewandowski et al. (Lewandowski and Chorążyczewski, 2010) investigated an important application of fractional viscoelastic models. They demonstrated how to use these models to report on the dynamic behaviour of viscoelastic dampers. These dampers are widely used in aerospace and machine structures; they aid in the management of aircraft vibrations. These are also used in civil engineering to reduce excessive earthquake oscillations in buildings. The quality of these dampers is mostly determined by the viscoelastic substance utilised. Lewandowski presented an identification approach using the Fractional Maxwell and Fractional Kelvin-Voigt models so that instead of obtaining the complex modulus empirically, the fractional models can adequately reflect the damper's properties.

Recent experimental results indicate that fractional-order models provide a new flexible approach fitting biological tissue data. This is due to their intrinsic capacity that, with only the fractional order α of the time-derivative, one can manage the interaction between elastic energy storage and viscous dissipation. Because of their simplicity, these models have been employed to represent artery wall viscoelasticity in various 1D blood flow experiments. Perdikaris et al. (Perdikaris and Karniadakis, 2014) used the fractional viscoelastic model in a one-dimensional blood flow solver and investigated their behaviour with an in-silico analysis on a large patient-specific cranial network. They created a fast parallel algorithm that supports the fractional wall models, allowing them to investigate viscoelasticity's effect on pulse wave propagation in depth.

Palomares et al. (Palomares-Ruiz et al., 2015) compared the classical viscoelastic models with the fractional ones. They aimed to determine the fractional order of the time-derivative which can characterize the mechanical stress-strain relation and the stress relaxation of these models for biological soft tissues, specifically a femoral artery. They also framed a real-world blood flow pulse and provided a numerical adjustment to determine the displacement response for the pulse load application.

Among the key fractional rheological models examined by Wagner et al. (Wagner et al., 2017) are the Fractional Maxwell model and the fractional Jeffreys model. They looked into how well these models could simulate the viscoelastic responses of different liquid food solutions, both linear and nonlinear. Using fractional rheological models, they looked into the nonlinear rheological response of human saliva, various plant extracts, and viscoelastic liquid meals.

Mahiuddin et al. (Mahiuddin et al., 2018) presented yet another use of fractional viscoelastic models. The viscoelastic properties of food materials change dramatically during drying, which must be taken into account when forecasting the physical qualities of food products using mathematical models. Classical methods such as the Maxwell model and the Burgers model were used to predict the viscoelastic properties of fresh food samples. However, these models are unable to effectively parameterize numerous viscoelastic properties since conditions are always changing. In this regard, they proposed the fractional viscoelastic model as a new way to forecast the precise viscoelastic behaviour of food components with experimental validation. It is found that whereas the stiffness varies in a third-order polynomial manner, the fractional order of the time-derivative increases exponentially with moisture content. It is interesting to note that the material behaviour is strain rate dependent when a monotonic compression load is applied to a fresh apple tissue under various constant strain rates.

Mechanical properties of particularly soft tissues, such as the brain, liver, and kidney, have piqued the interest of medical scientists due to their numerous applications in medicine, including hydrocephalus, surgical operation planning, and traumatic brain damage. A recent study found that fractional models approximate biomechanics in the liver. Zhang et al. (Zhang et al., 2020) simulated fractional viscoelasticity in soft tissues using a previously performed experiment on ex vivo bovine liver tissue. Additionally, they introduced a numerical technique for the finite element approximation of fractional nonlinear viscoelastic materials. This technique has the potential to greatly simplify the application of fractional viscoelastic models in general and pave the way for the effective simulation of intricate biomechanical systems through the use of viscoelastic soft tissue models.

Food is processed by passing the liquid through a permeable surface for a sufficient amount of time to guarantee that the fluid flow is fully developed. Meng et al. (Meng et al., 2021) used permeability parameters, generalised Reynolds number, and generalised Schmidt number to report the impact on the velocity and concentration boundary layers with regard to time. They discovered that when the fractional order of the spatial derivative increases, horizontal velocity decreases, confirming the effectiveness of anomalous diffusion on fluid mass transfer.

A recent study by Huang et al. (Huang et al., 2022) looked into the dead-end capillary tube, which is a typical residual oil capillary structure. Their physical model contained a capillary with a length of 500 microns and a dead-end capillary with a depth of 100 microns in the middle, which was filled with leftover oil. Using a Fractional Maxwell model and the traditional momentum equation, the process of viscoelastic fluid flooding the residual oil in the dead end was investigated. Further, the flow control equation for fractional-order viscoelastic fluids was solved semi-analytically, and simulation for the oil-repelling process was done. The results demonstrated that the fractional order time derivative has a considerable effect on polymer solution properties, and increasing fluid elasticity can improve oil-repelling efficiency greatly. The fractional order time-derivative α and relaxation time can accurately characterise the fluid's degree of elasticity when compared to the Newtonian fluid flow model. The smaller the α, the more effective it is at repelling oil.

This chapter 1 has reviewed the literature on fractional viscoelastic flows, the models governing such flows, the numerical schemes involved in evaluating these models and the enormous practical implications connected with them. Chapter 2 provides a thorough review of (i) the local instabilities in free shear flows, (ii) finite difference schemes applicable to advection and diffusion terms of a differential equation and (iii) fractional calculus: the different types of fractional derivatives, and the numerical schemes used for its discretization. Chapter 3 establishes a comprehensive picture of the stability of the two-dimensional, viscoelastic, subdiffusive, fully developed Poiseuille flow. The temporal and spatiotemporal instabilities of these channel flows are discussed. Chapter 4 explores a novel theory to quantify the formation of spatiotemporal microstructures (or the non-homogeneous regions of high viscosity at moderate to high fluid inertia) for viscoelastic sub-diffusive flows by introducing a mathematically consistent decomposition of the polymer conformation tensor. Chapter 5 includes the development, analysis and applicability of a novel family of spatiotemporal discretization methods for the numerical solution of the one-dimensional and two-dimensional fractional advection diffusion reaction systems. Chapter 6 entails the description of direct numerical simulations for sub-diffusive viscoelastic plane Poiseuille flow under the conditions of low to moderate Reynolds numbers and low Weissenberg numbers. Chapter 7 concludes the limitations and the potential for future work.

Chapter 2

Mathematical Concepts

This chapter lays down the essential groundwork. It is crucial to comprehend the hydrodynamic stability and transition of viscoelastic solutions in order to fully understand the basic theory of viscoelastic liquids and the practical uses of these materials. The study of spatiotemporal stability is concerned with how minor perturbations to the flow behave and whether they increase or decay through time and space. Reynolds and Weissenberg numbers are two non-dimensional numbers that govern the stability of fluids. The Reynolds number is a key metric in fluid mechanics that is used to anticipate the onset of turbulence in a variety of fluid systems, such as pipelines, channels, and boundary layers. The ratio of inertial and viscous forces, known as the Reynolds number, aids in the prediction of flow behaviour. When viscous forces prevail at low Re, the flow is smooth, referred to as laminar flow, and when inertial forces dominate at high Re, the flow tends to create chaotic eddies, vortices, and other instabilities. The Weissenberg number is an important factor to consider while researching non-Newtonian fluids. The elastic forces are weaker than the viscous forces when the We number is low, and the fluid then acts like a Newtonian fluid. But when the We number increases, the elastic forces also increase, leading to complex flow behaviour such as flow instabilities, flow patterns, and vortex formation (Alexander and Saarloos, 2007).

Researchers have utilised linear stability analysis to explore the start of instability in viscoelastic flows within various geometries, such as straight channels, curved channels, and circular flows. The emergence of complex spatiotemporal patterns in viscoelastic flows, such as oscillations, travelling waves, and chaos, has also been studied using nonlinear stability analysis and numerical simulations. Understanding the stability qualities of viscoelastic flows can aid in the design of industrial processes involving complex fluid transport, such as polymer manufacturing and oil recovery. Research has shown that mathematical models and numerical simulations are precise methods to examine the spatiotemporal stability of viscoelastic flows. Section 2.1 demonstrates the different types of local instabilities encountered in a flow and the details of the Briggs method, which we use to classify regions of temporal stability, absolute and convective instabilities and evanescent modes. Section 2.2 describes the methodology for the evaluation of temporal and spatiotemporal modes. Section 2.3 includes the numerical methods, mainly finite difference methods used to discretize temporal and spatial derivatives in the integer-order partial differential equations. In section 2.4, we will first cover fractional calculus (fractional integration and fractional differentiation). There are at least six types of definitions for fractional derivatives. They are not equal, though. We outline the most popular fractional integrals, derivatives, and several numerical techniques for approximating them.

2.1 Instability Analyses: Local vs. Global

It is important to initially assume that streamwise changes of the mean flow are slow throughout a typical instability wavelength because in many flows of interest, the mean-velocity profile is not uniform in the streamwise direction. This makes it difficult to discern between local and global instability features. The instability of the local velocity profile and the overall flow field are then referred to as being "local" and "global," respectively. The local impulse response of the system inside the parallel-flow approximation at each streamwise station will be further described in this chapter.

A brief review of the traditional hydrodynamic instability description of open flows is discussed. Numerous controlled studies have been carried out to ascertain the responsiveness of different stimulation frequencies since several spatially evolving shear flows are known to be particularly sensitive to external noise. As a result, it has been a common practice to depict the downstream development of vortical structures as a collection of spatially increasing instability waves of various frequencies (for a review of previous investigations of mixing layers using this method, refer to the work by Ho and Huerre (Ho and Huerre, 1984)). In other words, the findings of local spatial stability calculations on the recorded time-averaged mean velocity profiles at each streamwise station (with provided real frequency and unknown complex wave number) have generally been compared with experimental observations. In forced experiments, this method has been somewhat successful in characterising the development of vortices. The reader is directed to the references (Crighton and Gaster, 1976; Gaster, Kit, and Wygnanski, 1985) for instances of this type of analysis. However, a significant portion of the literature on hydrodynamic stability has been devoted to temporal theory, where it is implicitly assumed that the flow develops from a specific beginning condition (with a given real wave number and unknown complex frequency). The fundamental justification for choosing a spatial theory point of view in many open shear flows might thus be questioned. Here, it is argued that in certain open flows (homogeneous mixing layers, flat-plate wakes, and uniform-density jets), the concepts of local "absolute/convective" instability offer a rigorous rationale for choosing spatial theory. The application of these ideas to additional open flows, such as hot jets and bluff body wakes, leads to the conclusion that real frequency-based local spatial theory is inappropriate. Both wave number and frequency must be taken into account as complex quantities, and a global temporal instability may develop whereby the entire nonparallel mean flow admits self-sustained global modes with clearly defined complex frequencies.

Such ideas appear to have had a considerably more recent influence on the research of fluid-mechanical instabilities. Early on, Gaster et al. (Gaster, Kit, and Wygnanski, 1985) developed a spatiotemporal description of Tollmien-Schlichting wave packets in boundary layers and proposed a general formal methodology without explicitly introducing a clear distinction between the absolute or convective nature of the instability mechanism. The method recommended by Briggs (Briggs, 1964) has been used numerous times to examine the susceptibility of compressible shear flows to sonic stimulation. In a two-layer model of baroclinic instability, Thacker (Thacker, 1976)) and Merkine (Merkine, 1977) identified the change from absolute to convective instability. In the past fifty years, the description of hydrodynamic instabilities in spatially developing shear flows has gained popularity. The distinction between absolute and convective instability appears to have been made for the first time in a broad setting in the writings of Twiss (Twiss, 1952) and Landau (Landau and Lifshitz, 1959). It is important to note that plasma physicists have contributed significantly to the theoretical underpinnings of these ideas and have used them to examine a variety of plasma instabilities. The reader is directed to the works of Sturrock (Sturrock, 1958), Briggs (Briggs, 1964), and Lifshitz (Lifshitz and Pitaevskii, 1981) for systematic developments of these concepts. For an up-to-date summary of theoretical efforts in the description of spatiotemporal plasma instabilities, the thorough and understandable review of Bers (Bers, 1983) is especially advised. Absolute/convective instabilities have been a common topic in the literature on plasma physics; the fundamental concepts are presented in the book by Clemmow et al. (Clemmow and Dougherty, 1969).

The concepts of absolute/convective instability and local/global instability offer the essential theoretical framework for categorising various open shear flows in accordance with the qualitative characteristics of their dynamic behaviour. For instance, the velocity profile is considered to be absolutely unstable in the local sense if the localised disturbances propagate upstream and downstream and contaminate the entire parallel flow. Shear flows that exhibit localised convective instability everywhere, such as mixing layers and flat-plate wakes, primarily exhibit extrinsic dynamics; in contrast, shear flows that exhibit a sufficiently large pocket of absolute instability, such as bluff-body wakes and hot or low-density jets, exhibit intrinsic dynamics that are similar to those found in the corresponding closed-flow systems. Although fluid particles are still transported downstream, there may be globally expanding temporal modes. These flows exhibit oscillatory behaviour; the increase of initial disturbances over time, rather than their spatial amplification, determines how vortices evolve. Additionally, the streamwise distribution of global modes is synchronised. A nonlinear dynamical systems method of the kind used in closed systems is especially well adapted to this class of open flows. If deterministic chaos arises in these systems, it is likely to be well defined: A limit cycle (the global mode) should bifurcate into a low-dimensional strange attractor in an orderly manner. On the other hand, it is much more challenging to distinguish between low dimensional chaos resulting from the flow dynamics and spatially amplified random noise since convectively unstable flows are sensitive to outside noise. There is also a third class of flows that are only marginally globally stable, where the local velocity profiles are strictly speaking locally convectively unstable throughout the field but are beginning to exhibit absolute instability at a streamwise station. When this occurs, global modes are frequently only weakly damped in time, and external forcing applied close to the global mode frequency can be used to destabilise them selectively. (Additional information about this last case is provided in section 2.1.3). This section is organized as follows. In section 2.1.1-2.1.3, we explore the concepts of Temporal Instability, Absolute / Convective Instability and the concept of Evanescent modes, respectively. A fundamental comprehension of the branch/pinch point and the Cusp-Map diagram is created in order to identify between each of these instabilities in section 2.2.1 and section 2.2.2, respectively. Section 2.2.3 explains how to categorise the flow-material factors that contribute to the aforementioned stability-instability regimes using the Briggs' Contour Integral Method., and section 2.2.4 further explains this technique with an example.

2.1.1 Temporal Instability

A given fundamental flow $U(y;Re)$ is the focus of the classical linear stability theory of parallel shear flows, which examines how tiny perturbations evolve in space and time. In the follow-up, the streamwise direction, the cross-stream direction, and the time are denoted by x,y, and t, respectively. The only element of the fundamental flow in the x-direction is $U(y;Re)$. The base state is supposed to be parallel and independent of x. Typically, fluctuations are broken down into plane wave instability of the type $\phi(y;\alpha)exp[i(\alpha x-\omega t)]$, where α is the complex wave number and ω is the complex frequency. The cross-stream distribution $\phi(y;\alpha)$ is then demonstrated to satisfy an Orr-Sommerfeld-type ordinary differential equation typically. An eigenvalue problem results from the application of the proper boundary conditions, and the eigenfunctions $\phi(y;\alpha)$ only exist if α and ω are required to satisfy a dispersion relation of the form,

$$D[\alpha,\omega,\boldsymbol{M}]=0. \tag{2.1}$$

where the vector of material and fluid parameters is called **M**. This relation can be determined clearly for straightforward fundamental flows. It is generated by numerically integrating the Orr-Sommerfeld equation for more accurate velocity profiles. Situations where the complex frequency ω is determined as a function of real wave number α are referred to as *temporal modes* $\omega(\alpha,Re)$. In contrast, when the value of the parameter ω is supplied in real, *spatial branches* $\alpha(\omega;Re)$ are derived by solving for the complex wave number α. We purposefully disregard changes in the cross-stream direction y in this section and only take into account the spatiotemporal evolution of instability waves in the (x,t)-plane. Without sacrificing any of the crucial aspects of instability, this projection dramatically simplifies the presentation of the core ideas. A dispersion relation (2.1) in spectrum space is thus associated with an integro-differential operator known as $D[-i(\partial/\partial x),i(\partial/\partial t);\boldsymbol{M}]$ in physical space (x,t), such that fluctuations $u(x,t)$ satisfy,

$$D\left[-i\frac{\partial}{\partial x},i\frac{\partial}{\partial t};\boldsymbol{M}\right]u(x,t)=0 \tag{2.2}$$

The associated receptivity problem for the aforementioned equation is resolved by introducing an impulse response of the flow, denoted by $G(x,t)$, defined as

$$D\left[-i\frac{\partial}{\partial x},i\frac{\partial}{\partial t};R\right]G(x,t)=\delta(x)\delta(t) \tag{2.3}$$

with δ standing for the source of the Dirac delta function. Consequently, if the base flow exhibits linear stability

$$\lim_{t\to\infty}G(x,t)=0 \text{ along all rays } x/t= \text{ constant} \tag{2.4}$$

likewise, if it is linearly unstable, then

$$\lim_{t\to\infty}G(x,t)=\infty \text{ along at least one ray } x/t= \text{ constant.} \tag{2.5}$$

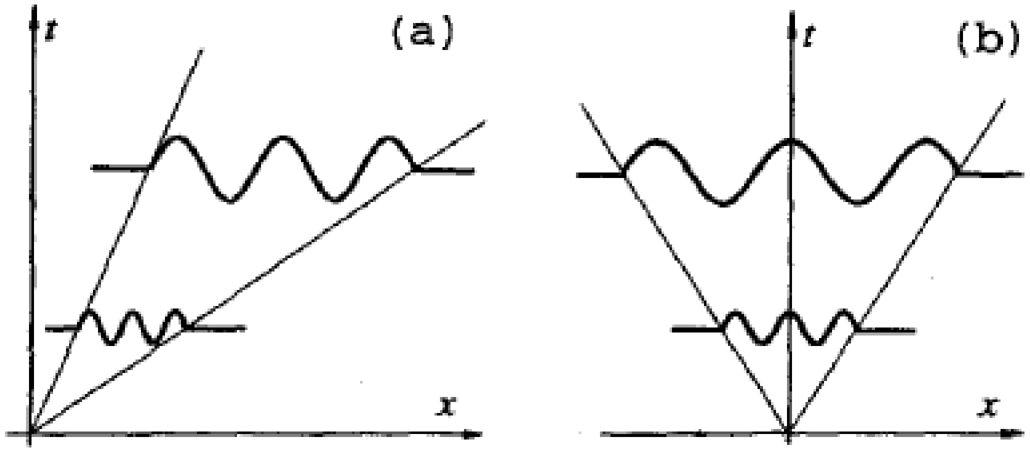

FIGURE 2.1: (a) Convective instability, (b) Absolute instability (Source: Schmid and Henningson (2001))

2.1.2 Spatiotemporal Instability: Absolute vs. Convective

When one introduces an impulse excitation locally in a flow and watches how the disturbance develops, spatial-temporal analysis is often pertinent. One must further distinguish between two kinds of impulse responses among linearly unstable flows: the base flow is convectively unstable if,

$$\lim_{t\to\infty} G(x,t) = 0 \text{ along the ray } x/t = 0 \tag{2.6}$$

and it is absolutely unstable if,

$$\lim_{t\to\infty} G(x,t) = \infty \text{ along the ray } x/t = 0, \tag{2.7}$$

as shown in Figure 2.1. The linearized Ginzburg Landau model can be used to illustrate the aforementioned definitions. The operator D then takes the form,

$$D\left[-i\frac{\partial}{\partial x}, i\frac{\partial}{\partial t}; \boldsymbol{M}\right] u(x,t) = \frac{\partial \Psi}{\partial t} + V_g \frac{\partial \Psi}{\partial x} \quad \frac{i}{2} V_{gg} \frac{\partial^2 \Psi}{\partial x^2} + i V_{gr} (R \cdot R_{\mathrm{e}}) \Psi = 0 \tag{2.8}$$

where V_g is a real positive constant group velocity, V_{gg} and V_{gr} are complex constants, with $V_{gg.i} < 0$.

Physically, convectively unstable flows produce wave packets that eventually leave the medium undisturbed after moving away from the source. In contrast, a point-source input gradually contaminates all absolutely unstable flows. It is also required to look at the long-term behaviour of the wave number α_0 seen along the ray $x/t = 0$ at a fixed spatial point in order to differentiate between convective and absolute instabilities. By definition, this complex α_0 has a zero group velocity, that is,

$$\frac{\partial \omega}{\partial \alpha}(\alpha_0) = 0, \tag{2.9}$$

where the equivalent absolute frequency is known as $\omega_0 = \omega(\alpha_0)$. Then, $\omega_{0,i} = \text{Imag}(\omega(\alpha_0))$ is used to represent the absolute growth rate. In other words, the temporal evolution of the wave number α_0 recorded at a fixed station in the limit $t \to \infty$ is characterised by the absolute growth rate $\omega_{0,i}$. In contrast, after the peak of the wave packet, the maximum growth rate $\omega_{i,max}$ is seen. The sign of $\omega_{0,i}$ determines the flow's absolute/convective character, much as the sign of $\omega_{i,max}$ indicates how unstable or stable the flow is. Therefore, one is directed to the following standard:

$$\begin{aligned} &\omega_{0,i} > 0 \qquad \text{absolutely unstable flow,} \\ &\omega_{0,i} < 0 \qquad \text{convectively unstable flow.} \end{aligned} \tag{2.10}$$

2.1.3 Evanescent Modes

According to Pierce (Pierce, 1981), three separate types of modal wave fields—acoustic, vorticity, and entropy waves—can all coexist in a flow field governed by the Navier-Stokes equations. Except for at boundaries or perhaps at direct resonances, these modal fields are uncoupled under the linear approximation. If two or more of these modes converge in a physical system that permits more than one wave mode, this is referred to as a direct resonance. We will focus on the coalescence of modes of the same wave type in this inquiry, particularly the coalescence of vorticity modes. Direct resonance can be a rather potent selection mechanism leading to an algebraic growth for small times or short distances if there are no or only very weak instabilities. The corresponding potentially large amplitudes may start the nonlinear solution much earlier than the exponentially growing mode.

According to Akylas (Akylas, 1982) and Benny (Benny and Gustavsson, 1981), the stability of locally parallel shear flows and the creation of waves by wind are both significantly impacted by the idea of direct resonance. (Refer to these references (Gustavsson and Hultgren, 1980; Gustavsson, 1981; Hultgren and Gustavsson, 1981; Akylas and Benney, 1980; Akylas and Benney, 1982) for detail on a weakly nonlinear theory of waves at direct resonance). The resonant forcing of the vertical vorticity (and consequently the horizontal velocity components) by the vertical velocity has been investigated in the aforementioned publications on the stability of parallel shear flows with the aim of clarifying the laminar-turbulent transition process.

This indicates a direct resonance between a vertical vorticity, also known as the "Squire" mode, and an Orr-Sommerfeld. Extensive research has been conducted on this process, known as the Benney-Gustavsson resonance, and it shows great promise. The kind of singularity in the dispersion relation at the mode coalescence point determines the nature of a direct resonance. Usually, it is ascertained by examining how a point source responds in both space and time. For instance, this category includes the 'cut-off' phenomena that separates propagating from evanescent acoustic waves in a hard-walled duct in a linear neutrally stable system (Aranha, Yue, and Mei, 1982).

The associated singularity is of double pole type if the two coalescing modes are caused by waves travelling in the same direction, as in the case of a convectively unstable flow. Linear theory predicts that such a disturbance will eventually decay. Nonetheless, the system may reach a nonlinear state due to the short-term algebraic development linked to this type of double pole. The damping rate determines if this

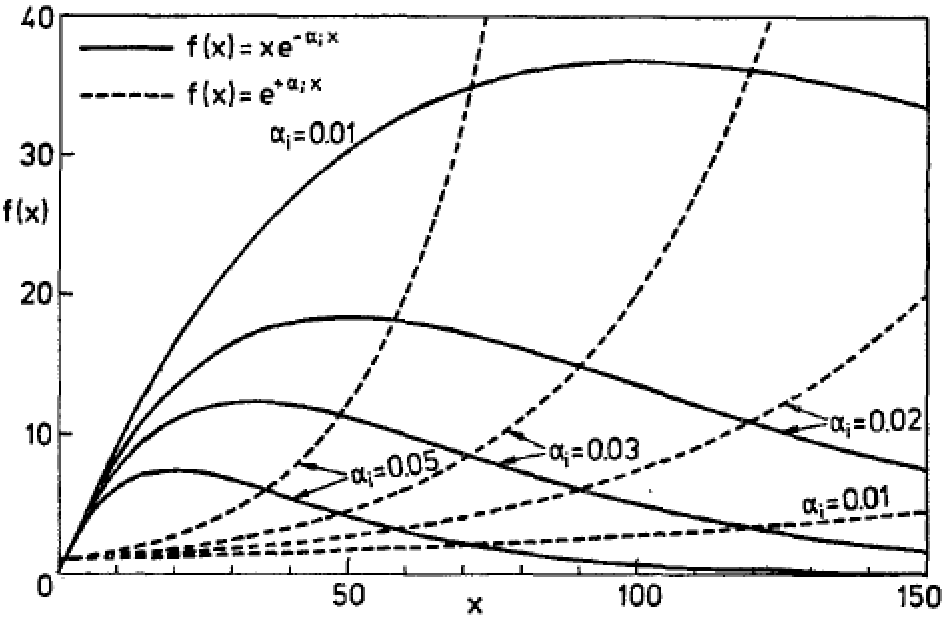

Figure 2.2: Impact of direct resonance on the growth of amplitude (Source: Koch (1986))

is physically feasible. Such resonances are significant in some linear optimisation problems if the damping rate is high (a paper by Cremer (Cremer, 1953) for ducts with acoustically absorbing walls provides an example). The related damping rates are relatively small if the coalescing modes are almost neutral, and the algebraic growth may locally outweigh the exponential decay. Benny et al. (Benny and Gustavsson, 1981) and the current study of plane Poiseuille and boundary-layer type mean flows—two common instances of convectively unstable flows—address this issue.

In order to get the idea of evanescent mode, let's look at a function example $f(x) = \exp(-\alpha_i x)$ This is demonstrated in figure 2.2 by plotting the functions $x\exp(\alpha_i x)$ and $\exp(-\alpha_i x)$ for various $\alpha_i = \mathrm{Im}(\alpha)$. For large α_i high amplitudes $f(x)$ are quickly reached by the exponentially growing mode $\exp(\alpha_i x)$. Nevertheless, this growth is exceedingly slow if α_i is very small. In this case, high amplitudes can be produced considerably faster via a direct resonance producing mode $x\exp(-\alpha_i x)$. The locally large amplitudes may initiate towards a nonlinear state, even though these modes ultimately decay in accordance with linear theory. To ascertain whether this is feasible for a particular flow, we need to figure out (i) the circumstances in which direct resonances occur and (ii) the magnitude of the corresponding damping rates.

2.2 Evaluation of Instability Modes

We give a thorough description of the methods used in this section for the analytical and numerical assessment of the modes described in sections (2.1.1- 2.1.3).

2.2.1 Branch Points and Pinch Points

The following can be used to explain why a branch point in the ω-plane and a pinch point in the α-plane occur simultaneously. The complex α-plane's α^{pinch}, pinch points are a particular type of saddle point that satisfy the relation

$$D\left(\alpha^{pinch},\omega^{Cusp}\right)=0 \quad \frac{\partial D}{\partial\alpha}\left(\alpha^{pinch},\omega^{Cusp}\right)=0 \quad \frac{\partial^2 D}{\partial\alpha^2}\left(\alpha^{pinch},\omega^{Cusp}\right)\neq 0 \tag{2.11}$$

The dispersion relation in the neighbourhood of the singularity $(\alpha^{pinch},\omega^{Cusp})$ is then expanded using a Taylor series to get

$$0=\left.\frac{\partial D}{\partial\omega}\right|_0\left(\omega-\omega^{Cusp}\right)+\frac{1}{2}\left.\frac{\partial^2 D}{\partial\alpha^2}\right|_0\left(\alpha-\alpha^{pinch}\right)^2+\mathscr{O}\left(\left(\omega-\omega^{Cusp}\right)^2,\left(\alpha-\alpha^{pinch}\right)^3\right) \tag{2.12}$$

The neighbourhood of ω^{Cusp} in the ω-plane and the neighbourhood of α^{pinch} in the α-plane are related by this expression. A square root singularity for the local map between the ω and α planes results from the local map between these two planes being quadratic.

We are dealing with absolute instability if the corresponding branch point in the ω-plane lies above the imaginary ω-axis, which happens if the contour deformation technique produces a pinch point in the α-plane. It is evident from the definition of absolute instability that the presence of an unstable wave with zero group velocity is necessary for such instability to occur. The group velocity, V_g, at an unstable pinch/branch point is such that,

$$V_g=\frac{\partial\omega}{\partial\alpha}=\frac{\partial D}{\partial\alpha}/\frac{\partial D}{\partial\omega}=0. \tag{2.13}$$

2.2.2 The Cusp Map

We have shown that the asymptotic space-time evolution of a linear instability in the complex α-plane, which is found by analytic continuation of the Laplace inversion contour into the bottom half of ω-plane, is determined by the placement of pinch points. The dispersion relation for the spatial wavenumber α as a function of the frequency ω must be solved in order to use this technique. This seems unfortunate because, for the most part, it is considerably simpler to compute ω as a function of α. This section presents a mapping from the α-plane to the ω-plane as the only means of finding absolute instabilities. Kupfer et al. (Kupfer, Bers, and Ram, 1987) invented this method, which they call the 'cusp map' in the complex-frequency plane.

The stability problem in Fourier-Laplace space will be tackled first. Upon employing equation (2.3) for the Fourier and Laplace transforms and formally returning to the physical space, we obtain

$$G(x,t)=\frac{1}{4\pi^2}\int_L\int_F\frac{\exp[i(\alpha x-\omega t)]}{D(\alpha,\omega,\boldsymbol{M})}d\alpha d\omega \tag{2.14}$$

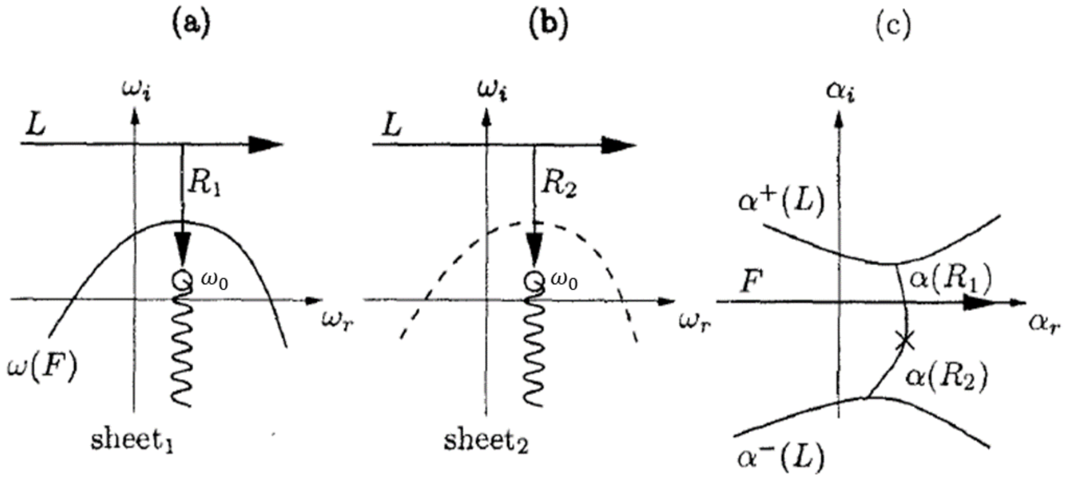

FIGURE 2.3: An illustration of the cusp map technique (Source: Kupfer, Bers, and Ram (1987)).

where the inversion contours in the Fourier α-plane and the Laplace-ω-plane are denoted by L and F, respectively. We study the mapping between the ω and α planes. Dispersion relations are typically higher order polynomials in the wave number α or even transcendental functions; as a result, the mapping from the F-contour to the ω-plane has several values. Let $\omega(F)$ represent the image of F in the ω-plane. n branches $\alpha_k(\omega(F))$ will arise from the reverse mapping of $\omega(F)$ back into the α-plane, where n represents the highest order of α in the dispersion relation. However, one of the n branches recovers the original contour F. We create n Riemann sheets in the complex ω-plane and associate the n contours in the multi-sheeted ω-plane with the n branches $\alpha_k(\omega(F))$ in the α-plane in order to make the mapping of the F-contour into the ω-plane single-valued. The dispersion relation $D(\alpha,\omega)=0$ controls the map between the ω and α-plane. We have the extra limitations for a pinch point in the complex α-plane, given by

$$\frac{\partial D(\alpha,\omega)}{\partial \alpha}=0 \quad \frac{\partial^2 D(\alpha,\omega)}{\partial \alpha^2}\neq 0 \tag{2.15}$$

There are only $n-1$ image points in the complex α_0 plane for a point ω_0 in the ω-plane that satisfies the constraints stated above for a corresponding α_0. Put otherwise, at this precise position ω_0, two sheets in the ω-plane connect. Now, we'll focus on these two sheets. Now let us insert a vertical ray that goes from the point ω_0 (see figure 2.3) to the contour L in each of the two sheets. These rays will be denoted as R_1 and R_2. They will assist us in establishing whether a pinch point α_0 in the α-plane and a point ω_0 in the ω-plane correspond: The branch point at $\omega=\omega_0$ corresponds to a pinch point in the α-plane if and only if the images of the rays R_1 and R_2 in the complex α-plane, i.e., $\alpha(R_1)$ and $\alpha(R_2)$ in figure 2.3, originate on two separate sides of F. We must conclude that at least one of the pictures $\alpha(R_1)$ and $\alpha(R_2)$ crosses F if they begin on different sides of F and link at a single point, α_0, which is not on F. If there are many crossings, both images' total crossing counts must be odd.

The cusp map procedure is based on this criterion: We may ascertain whether the branch point ω_0 corresponds to a pinch point in the α-plane by counting the number

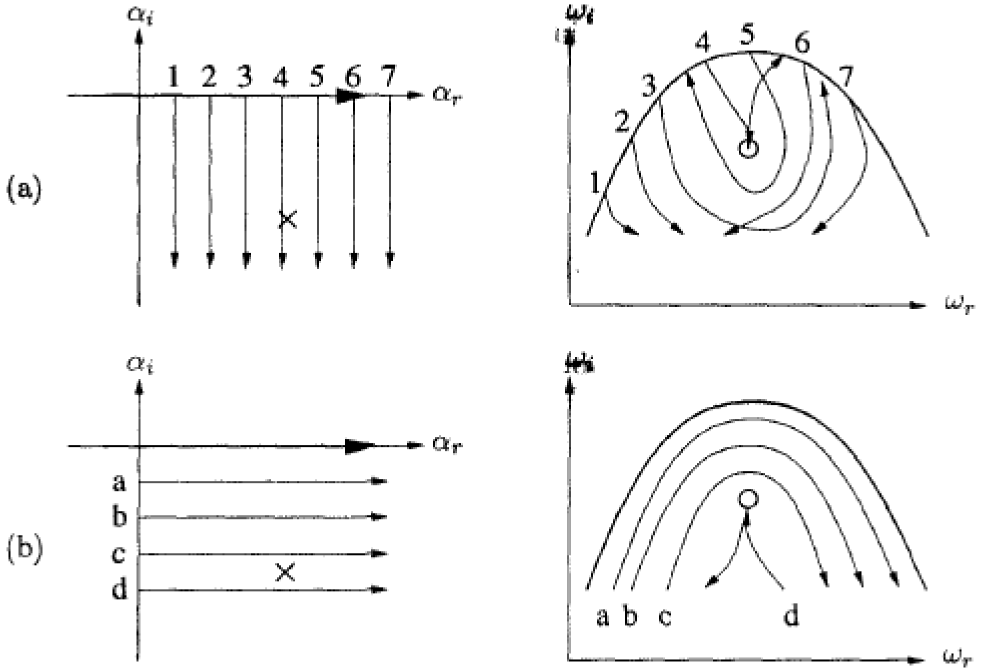

FIGURE 2.4: A description of the numerical procedure utilised in the cusp map approach to find branch points in the ω-plane (Source: Kupfer, Bers, and Ram (1987)).

of times each vertical ray, R_1 and R_2, meets the contour $\omega_k(F)$. Any dispersion relation's stability properties can be ascertained in a similar manner. The process entails projecting a portion of the α-plane onto a designated area below $\omega(F)$. The ω-plane is mapped onto a collection of vertical rays that span the range of unstable wave numbers. These rays may have intersecting images, suggesting a branch point, while being initially parallel in the α plane. The local map of the singularity exhibits the property of angle doubling. Figure 2.4 illustrates this situation, with the branch point nestled at the edge of a trajectory resembling a cusp. One obtains a mapping consistent with the multi-sheeted structure predicted by the contour $\omega(F)$ if one takes a branch cut downhill from the singularity. Since $\omega(F)$ covers the branch point only once in this instance, it resembles a pinch point. In many cases, it is easier to use a collection of horizontal contours that represent deformations of the Fourier integral path in place of the vertical rays seen in figure 2.4. These contours will move from the map $\omega(F)$ downward in the ω-plane, forming a cusp as they get closer to the singularity (see figure 2.4). Once more, the angle-doubling (or tripling, etc.) attribute of its local map is used to determine the branch point. A systematic generalisation of this process to dispersion relations with numerous unstable branches is possible.

2.2.3 Briggs' Method

Next, we shall derive the mathematical criteria for categorising instabilities as absolute or convective based on the singularity structure of the dispersion relation in the complex ω and α-planes. Finding pinch points in the complex plane is an important

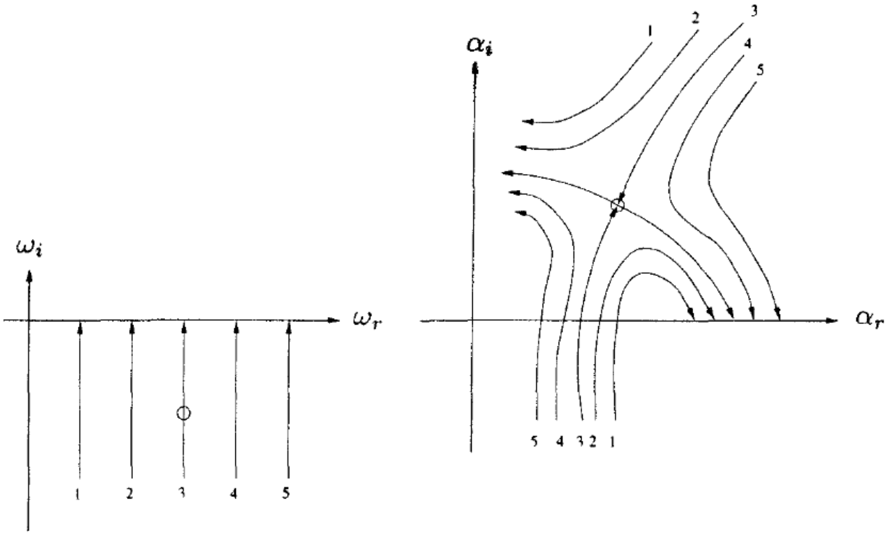

FIGURE 2.5: An example of the Briggs' method's numerical process for finding saddle points in the α-plane (Source: Schmid and Henningson (2001)).

step in detecting absolute instability. Briggs (Briggs, 1964) offered a methodical approach to this, in which we iteratively solve for the spatial branches of the dispersion relation for frequencies ω provided along predetermined paths in the complex ω-plane. We select straight lines parallel to the imaginary ω-axis for simplicity's sake. The spatial branches of the dispersion relation linked to the specified temporal branches in the ω-plane are traced out by mapping points along these ω trajectories onto the α-plane. We gradually visualise the map of the ω-plane onto the α-plane under the dispersion relation $D(\alpha,\omega) = 0$ by adjusting the real part of the ω lines. Locating saddle points in the α-plane should thus be rather easy. One crucial constraint to remember is that the saddle point can only be composed of spatial branches that originate in different half-spaces. In the α plane, a saddle point is evidently formed when the ω lines are adjusted correspondingly. Briggs' criterion indicates that the equivalent branch point in the ω-plane, represented by a circle along the third ray (see figure 2.5), does not represent an absolute instability because it is located below the real ω-axis.

While it is possible to determine the Fourier-Laplace integral (2.14) for all x and t, the dispersion relation's complexity points to a time-asymptotic solution for the integral. Furthermore, evaluating the Fourier-Laplace integral (2.14) requires an asymptotic technique because convective and absolute instability are defined as limited processes for large times. The modification of the integration contours in the complex α and ω planes will be required for the time-asymptotic assessment of the integral expression for Green's function. The time-asymptotic behaviour can be assessed using the method of steepest descent by deforming the integration path through a saddle point in the plane. According to the definition, the flow under consideration is deemed absolutely unstable if this evaluation produces a divergent integral. The flow is convectively unstable if the asymptotic limit yields a convergent integral, or even a zero integral. When using the steepest descent method, extra caution must be used. Later on, we shall revisit this matter. Briggs provided a method for carefully evaluating the time-asymptotic behaviour of the Fourier-Laplace integral (2.14). The approach used by Briggs (Briggs, 1964) selects the wave number integral first.

$$\tilde{G}(x,\omega) = \frac{1}{2\pi}\int_F \frac{\exp[i\alpha x]}{D(\alpha,\omega,\boldsymbol{M})}d\alpha \tag{2.16}$$

which is followed by the ω-inversion

$$G(x,t) = \frac{1}{2\pi}\int_L \tilde{G}(x,\omega)\exp[-i\omega t]d\omega \tag{2.17}$$

The original L-contour is deflected using the analytic continuation method in an effort to bring it below the real ω-axis (see figure 2.6). If this is accomplished, the exponent in the $\omega-$inversion integral (2.17) forces the integrand to vanish as $t \to \infty$; if not, the greatest discrete singularity in the ω-plane governs the time-asymptotic discrete response. If there is a singularity above the real ω-axis, lowering the ω-contour could not work. This singularity in the ω-plane will have an associated singularity in the α-plane due to the connectivity via the dispersion relation.

The real α-axis is first selected to be used as the inversion contour for the spatial part. This integration path maps to a curve in the ω-plane, $\omega(F)$, using the dispersion relation. To ensure causality, the temporal inversion contour must be above this curve: The integrand of the ω integral (2.17) must be analytic in the ω-half-space: maxIm($\omega(F) < 0$). This means that the integration route for $t < 0$, which involves closure in the upper half-plane, cannot encompass any singularities. It is also possible to map the temporal contour L back into the α-plane, yielding the branches $\alpha^-(L)$ and $\alpha^+(L)$. The dynamics downstream (upstream) of the origin are linked to the spatial branch above (below) the real axis. We shall attempt to lower the ω inversion contour below the real axis by use of analytical continuation. The ω-contour's image in the α-plane will also deform when we deform it. The original ω-contour will eventually need to be reshaped because the original α-contour will eventually be squashed between the two branches. We can reach a state where the spatial inversion contour is squeezed between the two spatial branches, preventing any further deformation without crossing singularities, by continuously modifying the inversion contours and their maps onto the corresponding plane. If this happens, a branch point in the ω-plane forms, making it impossible to reduce the temporal inversion contour any more.

When two eigenmodes combine, an absolute instability eigenmode is created. Because the merged eigenmode has ω_i> 0, its occurrence can, therefore be intuitively seen as a type of resonance between the modes—a resonance that promotes growth. The modal interaction related to the merging occurs physically over the perturbation source. The reason for this is that the modes that are involved originate from both the downstream $(x_1 > 0)$ and upstream $(x_1 < 0)$ sides of the source. As a result, the instability is confined to the source's position and with time, it encircles a progressively larger area surrounding the source of perturbation. A shear flow with a sizable pocket of absolute instability may display the dynamic characteristics of a closed-flow (compact) system. These unstable flows behave like an oscillator. A convectively unstable mode, on the other hand, has been shown to be associated with a sinusoidal wave that grows in amplitude as it travels away from the source, from which it also derives its frequency. A convectively unstable mode is essentially a driven mode. It

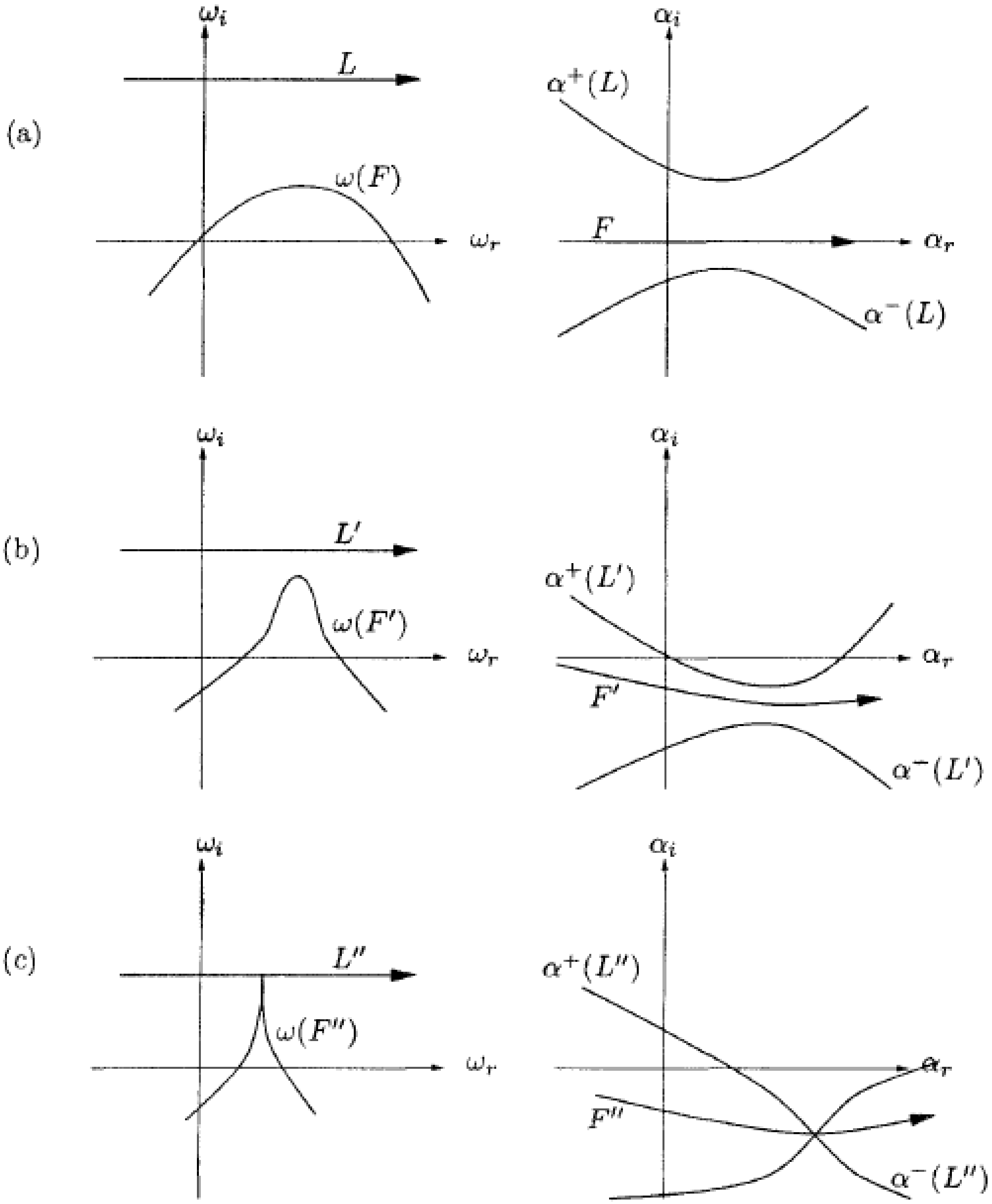

FIGURE 2.6: An illustration of the Briggs' method's contour deformation technique. Complex ω-plane on the left, complex α-plane on the right (Source: Schmid and Henningson (2001)).

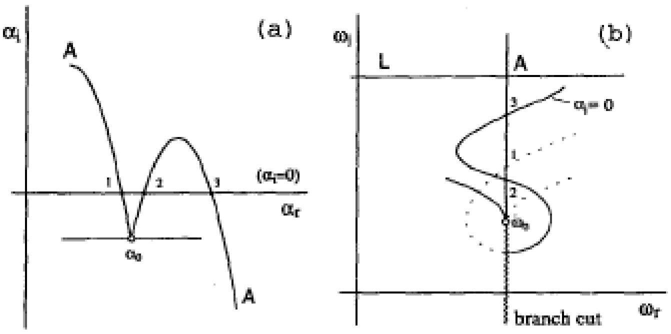

FIGURE 2.7: An illustration of an absolute instability in the schematic is given by two α-roots intersecting with three crossings of the α_r-axis ($\alpha_i = 0$). In the double-sheeted ω-plane, the vertical ray from ω_0 cuts the $\alpha_i = 0$ contour in three locations. (Source: Yeo, Khoo, and Zhao (1996)).

decays to zero with time when the driving source is turned off, whereas an absolutely unstable mode is more akin to a self-sustaining temporal mode and has been termed as such by Bers (Bers, 1983).

A probable absolute instability is suggested when $(\omega_o)_i > 0$. Nevertheless, confirmation that the intersection results from roots coming from the opposing half of the α-plane is still required. At least one of the α-roots must cross the α_r-axis of the α-plane at least once in order for such an intersection to be possible. An α-root crosses into its original half of the α-plane with an even number of crossings, and into the opposite half with an odd number. For it to be a true pinch point, the total number of crossings must be odd. By drawing a straight line from the suspected cusp point vertically upward (ω_r = constant) and counting the number of times this ray intersects the image of the α_r-axis ($\alpha_i = 0$) in the ω-plane (a double or multisheeted Riemann surface), it is possible to determine whether this requirement is met. This is because, as the ω_i is varied with the lowering of the L contour, every crossing of the α_r-axis in the α-plane by the α-roots is reflected by a corresponding crossing of the image of the α_r-axis ($\alpha_i = 0$) in the ω-plane by the vertical ray (which represents variation in ω_i) in one of the Riemann sheets of the co-plane. A schematic illustration of applying this criterion to a scenario where the crossing pair of α-roots crosses the α_r-axis three times is shown in Figure 2.7. In this instance, the image of the α_r-axis ($\alpha_i = 0$) is cut three times on the two Riemann sheets by the upward vertical ray that originates from the cusp point. No pinching of F can happen as L is lowered when the Riemann sheets of the branch point ω^{Cusp} correspond to spatial branches situated in the same α-plane for high enough L. The absolute growth rate does not affect the associated branch point in the ω-plane. Therefore, branch-point singularities for spatial branches that originate from different halves of the α-plane must be carefully located. Thus, genuine convective instabilities can be distinguished from evanescent modes using the vertical ray criteria.

The Briggs technique can be summed up as follows: At the saddle point in the α-plane or the branch point in the ω-plane, the vanishing characteristic of the group velocity, V_g, is a required (but not sufficient) condition for the existence of absolute instability. ($V_g = \frac{\partial \omega}{\partial \alpha} = (\frac{\partial D}{\partial \alpha})/(\frac{\partial D}{\partial \omega}) = 0$ such that $\omega = D(\alpha)$). But the group velocity is zero at every saddle point, in particular where the two α-branches meet, independent of whether the branches originate from the same half of the α-plane (i. e., when evanescent modes are detected) or not. To overcome this inadequacy, Briggs (Briggs, 1964) devised the idea of analytic continuation in which the Laplace contour L, in equation (2.14), is deformed towards the ω_r axis of the complex ω-plane, with the simultaneous adjustment of the Fourier contour F in the α-plane to maintain the separation of the α-branches; those which originate from the top half (the upstream modes with $\alpha_i > 0$) from those which originate from the bottom half of the α-plane (or the downstream modes). The deformation of the F contour (while preserving causality) is inhibited, however, when the paths of the two α-branches originating from the opposite halves of the α-plane intersect each other, leading to the appearance of saddle points which are the *pinch point*, $\alpha^{\text{p}inch}$. The concurrent branch point appearance in the ω-plane is the *cusp point*, $\omega^{\text{c}usp}$ (i. e., $D(\alpha^{\text{p}inch},\omega^{\text{c}usp}) = \frac{\partial D(\alpha^{\text{p}inch},\omega^{\text{c}usp})}{\partial \alpha} = 0$ but $\frac{\partial^2 D(\alpha^{\text{p}inch},\omega^{\text{c}usp})}{\partial \alpha^2} \neq 0$). Kupfer (Kupfer, Bers, and Ram, 1987) used a local mapping process to conceptualise this branch point's stability properties. A local Taylor expansion near a "reasonably close" neighbourhood of the pinch point produces a dispersion relation, $(\omega - \omega^{\text{c}usp}) \sim (\alpha - \alpha^{\text{p}inch})^2$, that has a second-order algebraic form in the ω-plane (and which is a first-order saddle point in the α-plane). The cusp is formed when the α_i-contours 'rotate' around ω^{cusp} due to the map's period-doubling characteristic. In the ω-plane, we draw a ray from the cusp point parallel to the ω_i-axis so that it intersects the image of the F-contour (or $\alpha_i = 0$ curve). Then, as indicated in Figure 2.7, we count the number of intersections (that is, the number of times both α-branches cross the α_r-axis before forming a pinch point in the α-plane). The flow dynamics correspond to an evanescent mode if the ray traced from the cusp point crosses the image of the F contour in the ω-plane an even number of times (or if one or both of the α-branches cross the α_r-axis). If not, the observed cusp point in the case of odd intersections is genuine, resulting in a system that is either convectively unstable (in the lower half of the ω-plane) or absolutely unstable (in the upper half); this is assuming that the system is temporally unstable.

2.2.4 An Example

We shall use the Briggs' method and introduce a basic dispersion relation (Kupfer, Bers, and Ram, 1987) to further illustrate this crucial technique. The dispersion relation is purely demonstrative and is a mathematical concept. Because of its simplicity, the positions of the pinch point and branch point can have clear answers. We consider

$$D(\omega,\alpha) = \omega - \left[\frac{1}{3}(\alpha - i)^3 + i - \alpha V\right] \tag{2.18}$$

wherein a parameter V has also been introduced. One can get the pinch and branch points by solving dω/dα = 0, which produces

$$\alpha_{1,2} = i \pm \sqrt{V} \tag{2.19}$$

for the pinch points and

$$\omega_{1,2} = (1 - V)i \mp \frac{2}{3}V\sqrt{V} \tag{2.20}$$

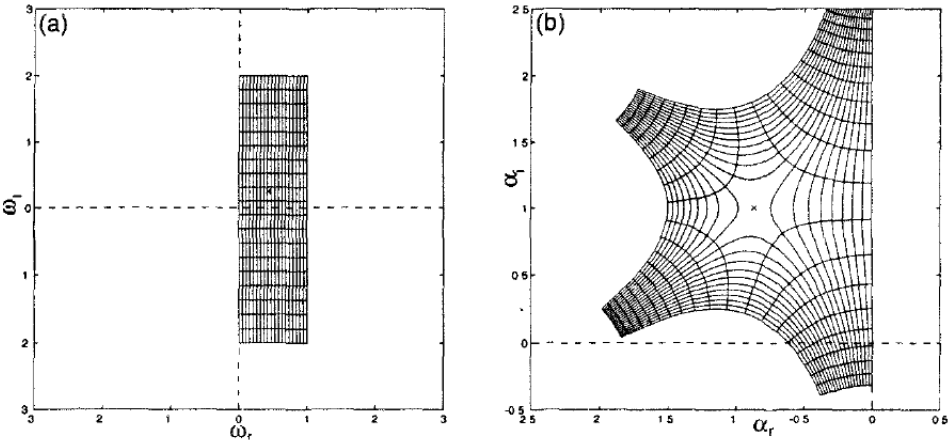

FIGURE 2.8: A schematic of the complex ω-plane under the dispersion relation (2.18) onto the complex α-plane (Source: Schmid and Henningson (2001)).

for the ω-plane's corresponding branch points. Setting V = 0.75, we apply Briggs' approach as previously described. By resolving the cubic dispersion relation (2.18), we shall transfer lines of constant ω into the complex α-plane.

It is evident that, for V = 0.75 (see figure 2.8), a saddle point occurs in the complex α-plane, indicated by a symbol. This saddle point corresponds to the solution of equation (2.19). Its branches originate in different α-plane half-spaces. Additionally noted is the matching branch point in the ω-plane. The branch point can be observed to be distinctly above the actual ω-axis, indicating the presence of absolute instability. This is a really basic example. Nevertheless, it shows how effective Briggs' approach is for identifying absolute instabilities. It is possible to create more complex dispersion relations that test the readers' understanding of analytic function theory.

The steepest descent approach is closely related to the procedure just described for calculating the properties of absolute and convective stability. Branches that originate in separate half-spaces are treated equally by the method of steepest descent. To concentrate on the right kind of saddle points in the α-plane, more examination of the phase function's global topology is required. Actually, the integral representation of the solution for Green's function advises locating the phase function's saddle points and asymptotically calculating the integral using accepted methods. The phase function's global topology must also be taken into account; not all points with $d\omega/d\alpha = 0$ are connected to absolute instabilities. Ignoring the phase function's global topology could lead to erroneous computations and conclusions regarding the instability's absolute or convective character (Huerre and Monkewitz, 1990). The reader is referred to Lingwood (Lingwood, 1997) for a more thorough approach that includes numerical examples.

2.3 Numerical Methods

Numerical methods for solving differential equations are essential tools in various scientific and engineering disciplines where analytical solutions are difficult or impossible to obtain. The computational methods allow us to approximate the solutions of ordinary, partial, and fractional differential equations. Some commonly used numerical methods for differential equations are finite difference methods, which include discretization of the spatial domain and replacing derivatives with finite difference approximations, finite element methods which discretize the domain into smaller subdomains (elements) and approximate the solution within each element using piecewise functions, Finite volume methods focus on the discrete representation of the integral form of PDEs over control volumes (finite volumes) rather than the spatial domain. Spectral methods use basis functions (e.g., Fourier series, Chebyshev polynomials) to approximate the solution. In this section, our focus will be exclusively on finite difference methods, with a particular emphasis on upwind schemes. These numerical techniques are invaluable tools for approximating solutions to differential equations by discretizing the domain and utilizing directional information to simulate the transport and convection processes accurately.

2.3.1 Finite Difference Approximations

In a finite difference technique, approximate finite difference terms are used in place of the differential equations' derivatives. This makes it possible to replace the differential problem with an algebraic system of equations that can be solved by a computer. Let $f(x)$ be a one-variable function that is always regarded as smooth, unless otherwise indicated. This means that each derivative of the function is a bounded function with a well-defined range within an interval that contains x, the specific point of interest.

Forward Difference approximation For a function $f(x)$ and a small step size h, the forward difference approximation of the first derivative $f'(x)$ and second derivative $f''(x)$ at a point x is given by:

$$f'(x) \approx \frac{f(x+h) - f(x)}{h}, \tag{2.21a}$$

$$f''(x) \approx \frac{f(x+2h) - 2f(x+h) + f(x)}{h^2}. \tag{2.21b}$$

Backward Difference approximation For a function $f(x)$ and a small step size h, the backward difference approximation of the first derivative $f'(x)$, and second derivative $f''(x)$ at a point x is given by:

$$f'(x) \approx \frac{f(x) - f(x-h)}{h}, \tag{2.22a}$$

$$f''(x) \approx \frac{f(x) - 2f(x-h) + f(x-2h)}{h^2}. \tag{2.22b}$$

It is important to note that while the forward and backward difference approximation for the first derivatives has an error proportional to h, the forward and backward difference approximation for the second derivatives has an error proportional to h^2.

Central Difference approximation For a function $f(x)$ and a small step size h, the central difference approximation of the first derivative $f'(x)$, and second derivative

$f''(x)$ at a point x is given by:

$$f'(x) \approx \frac{f(x+h)-f(x-h)}{2h}, \tag{2.23a}$$

$$f''(x) \approx \frac{f(x+h)-2f(x)+f(x-h)}{h^2}. \tag{2.23b}$$

The advantage of the central difference approximation lies in its second-order accuracy for both first and second-order derivatives, meaning that the error decreases quadratically as the step size h is reduced.

Truncation Errors Expanding each of the function values of f in a Taylor series about the point x is the typical method for analysing the error in a finite difference approximation. For example

$$f(x+h) = f(x)+hf'(x)+\frac{h^2}{2}f''(x)+\frac{h^3}{6}f'''(x)+O(h^4). \tag{2.24}$$

$$f(x-h) = f(x)-hf'(x)+\frac{h^2}{2}f''(x)-\frac{h^3}{6}f'''(x)+O(h^4). \tag{2.25}$$

This implies that for the forward difference approximation (2.21a),

$$f'(x)-\frac{f(x+h)-f(x)}{h} = -\frac{h}{2}f''(x)-\frac{h^2}{6}f'''(x)+O(h^3). \tag{2.26}$$

Similarly, for the backward difference approximation (2.22a),

$$f'(x)-\frac{f(x)-f(x-h)}{h} = \frac{h}{2}f''(x)-\frac{h^2}{6}f'''(x)+O(h^3). \tag{2.27}$$

We see that the error in the above two equations is proportional to h. Hence, the approximations (2.21a) and (2.22a) are first-order accurate. For central difference approximation (2.23a), we get

$$f'(x)-\frac{f(x+h)-f(x-h)}{2h} = -\frac{h^2}{6}f'''(x)+O(h^4). \tag{2.28}$$

Hence, the error is proportional to h^2, and the method is second-order accurate.

2.3.2 Stability and Convergence

Consider a second-order ordinary differential equation

$$u''(x) = f(x) \text{ for } 0 < x < 1 \tag{2.29}$$

with some boundary conditions $u(0) = \alpha$ and $u(1) = \beta$. We discretize the $x-$domain into $(M+2)$ points, say $u_0, u_1, u_2, \cdots, u_M, u_{M+1}, x_j = jh$ and $h = 1/(M+1)$ such that u_j approximates the exact solution $u(x_j)$. Using central difference approximation, we get

$$\frac{u_{j+1}-2u_j+u_{j-1}}{h^2} = f(x_j) \text{ for } j = 1,2,\cdots,M. \tag{2.30}$$

We have a linear system of M equations for the M unknowns, which can be written in the form $AU = F$, where $U = [u_1, u_2, \cdots, u_M]^T$, and A is a tridiagonal matrix. Solving this system will give us the approximate solution.

Local truncation error (LTE) The LTE, τ_j is defined by replacing u_j by the exact solution $u(x_j)$ in the finite difference formula for $j = 1, 2, \cdots, m$.

$$\tau_j = \frac{u(x_{j+1}) - 2u(x_j) + u(x_{j-1})}{h^2} - f(x_j). \tag{2.31}$$

Using equations (2.24) and (2.25), we get,

$$\tau_j = \left[u''(x_j) + \frac{1}{12}h^2 u''''(x_j) + O(h^4)\right] - f(x_j) = \frac{1}{12}h^2 u''''(x_j) + O(h^4). \tag{2.32}$$

So, $\tau_j = O(h^2)$. We define τ as the vector with components τ_j, then $\tau = A\hat{U} - F$, where $\hat{U}$ is the vector of exact solutions.

Stability Using the two equations $AU = F$, and $\tau = A\hat{U} - F$, we obtain the relation between the local error τ and the global error $E = U - \hat{U}$, given by $AE = -\tau$. Consider the discrete system $A^h E^h = -\tau^h$, where the superscript h indicates that we are on a grid with mesh spacing h. Then $E^h = -\left(A^h\right)^{-1} \tau^h$. Taking norms

$$\left\|E^h\right\| = \left\|(A^h)^{-1}\tau^h\right\| \leq \left\|(A^h)^{-1}\right\| \left\|\tau^h\right\|. \tag{2.33}$$

Now, if $\left\|(A^h)^{-1}\right\| \leq C$ for all h sufficiently small, where C is a constant, then $\left\|E^h\right\| \leq C\left\|\tau^h\right\|$. This implies $\left\|E^h\right\| \to 0$ at least as fast as $\left\|\tau^h\right\|$ (LeVeque, 2007).

Definition 1 *Suppose a finite difference method for a linear boundary value problem gives a sequence of matrix equations of the form $A^h U^h = F^h$ where h is the mesh width. We say that the method is stable if $(A^h)^{-1}$ exists for all h sufficiently small (for $h < h_0$, say) and if there is a constant C, independent of h, such that*

$$\left\|(A^h)^{-1}\right\| \leq C \quad \textit{for all } h < h_0. \tag{2.34}$$

Consistency We say that a method is consistent with the differential equation and boundary conditions if $\left\|\tau^h\right\| \to 0$ as $h \to 0$.

Convergence We say that a method is convergent with the differential equation and boundary conditions if $\left\|E^h\right\| \to 0$ as $h \to 0$. From the above equations, we can see that if a method is consistent and stable, then it is convergent.

2.3.3 Methods for Diffusion Equation

The diffusion equation describes how a quantity (such as heat, concentration, or temperature) spreads or diffuses through a medium over time. Using finite difference methods is motivated by the practical need to analyze and predict diffusion processes in a wide range of applications and allow for the advancement of knowledge in numerous scientific and engineering domains. The choice of spatial and temporal discretization methods, as well as boundary conditions, depends on the specific problem being solved and the desired accuracy and stability of the numerical solution.

Consider the one-dimensional diffusion equation

$$\frac{\partial u}{\partial t} = \frac{\partial^2 u}{\partial x^2} \tag{2.35}$$

with the initial condition $u(x,0) = \eta(x)$, and some boundary conditions if working on a bounded domain. A natural discretization is obtained by using a combination of the forward difference in time and the central difference in space (FTCS). Let u_i^n denote the approximate value of $u(x_i,t_n)$, where $x_i = i\Delta x$ and $t_n = n\Delta t$. The explicit scheme is given by:

$$\frac{u_i^{n+1} - u_i^n}{\Delta t} = \frac{u_{i+1}^n - 2u_i^n + u_{i-1}^n}{(\Delta x)^2}. \tag{2.36}$$

We will see using von Neumann stability analysis that the above method is stable under the condition $\frac{\Delta t}{(\Delta x)^2} \leq \frac{1}{2}$.

Crank-Nicolson method Another one-step method, based on the Trapezoidal method which is much more useful in practice, is the Crank-Nicolson method, given by

$$\frac{u_i^{n+1} - u_i^n}{\Delta t} = \frac{1}{2}\left(\frac{u_{i+1}^{n+1} - 2u_i^{n+1} + u_{i-1}^{n+1}}{(\Delta x)^2} + \frac{u_{i+1}^n - 2u_i^n + u_{i-1}^n}{(\Delta x)^2}\right). \tag{2.37}$$

Using an implicit approach, all of the values u_i^{n+1} can be simultaneously solved by using a tridiagonal system of equations. Any time step $\Delta t > 0$ gives stability for the Crank-Nicolson technique. Of course, if Δt is too large, then it might not be accurate. To get an acceptable solution, we usually have to use $\Delta t = O(\Delta x)$, and this is made possible by the unconditional stability.

Local Truncation Error Let $h = \Delta x$, and $k = \Delta t$. For the discretization given by equtaion (2.36), we have

$$\tau(x,t) = \frac{u(x,t+k) - u(x,t)}{k} - \frac{1}{h^2}\left(u(x+h,t) - 2u(x,t) + u(x-h,t)\right). \tag{2.38}$$

Using the Taylor series expansion about $u(x,t)$, we get

$$\tau(x,t) = \left(u_t + \frac{1}{2}ku_{tt} + \frac{1}{6}k^2 u_{ttt} + \cdots\right) - \left(u_{xx} + \frac{1}{12}h^2 u_{xxxx} + \cdots\right). \tag{2.39}$$

Since $u_t = u_{xx}, u_{tt} = u_{txx} = u_{xxxx}$, we get

$$\tau(x,t) = \left(\frac{1}{2}k - \frac{1}{12}h^2\right)u_{xxxx} + O(k^2 + h^4). \tag{2.40}$$

This method is said to be second-order accurate in space and first-order accurate in time since the truncation error is $O(h^2+k)$. Similarly, the local truncation analyses for the Crank-Nicolson method show that it is second-order accurate in both space and time, and the error is $O(h^2+k^2)$ (LeVeque, 2007).

Stability Analyses We apply Von-Neumann stability analyses to check the stability of equations (2.36) and (2.37). Let $u_j^n = e^{ijh\zeta}$ where $i=\sqrt{-1}$, then the amplification factor $g(\zeta)$ is defined as u_j^{n+1}/u_j^n. Substituting these values in equation (2.36), we get,

$$\begin{aligned} g(\zeta)e^{ijh\zeta} &= e^{ijh\zeta} + \frac{k}{h^2}\left(e^{i(j+1)h\zeta} - 2e^{ijh\zeta} + e^{i(j-1)h\zeta}\right) \\ &= \left(1+\frac{k}{h^2}\left(e^{ih\zeta}-2+e^{-ih\zeta}\right)\right)e^{ijh\zeta} \end{aligned} \tag{2.41}$$

$$g(\zeta) = 1+2\frac{k}{h^2}\left(\cos\left(\zeta h\right)-1\right). \tag{2.42}$$

For any value of ζ, we see that

$$1-4\frac{k}{h^2} \leq g(\zeta) \leq 1. \tag{2.43}$$

For stability, we want $|g(\zeta)| \leq 1$ for all ζ, which implies $\dfrac{k}{h^2} \leq \dfrac{1}{2}$.

For the Crank-Nicolson scheme (2.37), we get

$$g(\zeta) = 1+\frac{k}{2h^2}\left(e^{ih\zeta}-2+e^{-ih\zeta}\right)(1+g(\zeta)). \tag{2.44}$$

$$g(\zeta) = \frac{1+\frac{1}{2}z}{1-\frac{1}{2}z}, \tag{2.45}$$

where $z = \dfrac{k}{h^2}\left(e^{ih\zeta}-2+e^{-ih\zeta}\right) = \dfrac{2k}{h^2}\left(\cos\left(\zeta h\right)-1\right)$. Since $z \leq 0$ for all ζ, $|g(\zeta)| \leq 1$ and the method is stable for any choice of h and k (LeVeque, 2007).

2.3.4 Methods for Advection Equation

The advection equation describes the transport or advection of a quantity within a fluid or medium due to the motion of the fluid itself. Upwind schemes are a valuable class of finite difference methods for solving advection-dominated problems described by the advection equation. They are widely used in computational fluid dynamics, environmental modelling, and other fields where the accurate representation of directional transport is essential for obtaining reliable numerical solutions.

Consider the following one-dimensional linear advection equation

$$\frac{\partial u}{\partial t} + a\frac{\partial u}{\partial x} = 0 \tag{2.46}$$

which describes a wave propagating along the x-axis with a velocity a. The initial value is given by $u(x,0) = \eta(x)$. The first approach for discretization might be using forward difference in time and central difference in space.

$$\frac{u_i^{n+1} - u_i^n}{\Delta t} = -a \frac{u_{i+1}^n - u_{i-1}^n}{2\Delta x} \tag{2.47}$$

where n refers to the time dimension and i refers to the $x-$dimension. This can be rewritten as

$$u_i^{n+1} = u_i^n - \frac{a\Delta t}{2\Delta x}\left(u_{i+1}^n - u_{i-1}^n\right). \tag{2.48}$$

Because of stability concerns, this approach is ineffective in actual application.

Lax-Friedrichs method The Lax-Friedrichs scheme is commonly used for solving first-order hyperbolic PDEs, given by:

$$u_i^{n+1} = \frac{1}{2}\left(u_{i-1}^n + u_{i+1}^n\right) - \frac{a\Delta t}{2\Delta x}\left(u_{i+1}^n - u_{i-1}^n\right). \tag{2.49}$$

This is explicit and first-order accurate in time and first-order accurate in space. This method is stable and convergent provided $\frac{a\Delta t}{\Delta x} \leq 1$.

Lax-Wendroff method Lax-Wendroff scheme is a second-order accurate 3-point method given by:

$$u_i^{n+1} = u_i^n - \frac{a\Delta t}{2\Delta x}\left(u_{i+1}^n - u_{i-1}^n\right) + \frac{a^2(\Delta t)^2}{2(\Delta x)^2}\left(u_{i-1}^n - 2u_i^n + u_{i+1}^n\right). \tag{2.50}$$

This method is stable, and convergent provided $\left|\frac{a\Delta t}{\Delta x}\right| \leq 1$.

Stability Analyses The stability criterion for the Lax-Wendroff method can also be determined using von Neumann analysis. Let $u_j^n = e^{ijh\zeta}$, then $g(\zeta) = u_j^{n+1}/u_j^n$. Let $k = \Delta t$, $h = \Delta x$, $\mu = ak/h$. Substituting these values in equation (2.50), we get,

$$\begin{aligned} g(\zeta) &= 1 - \frac{1}{2} i\mu \left(e^{ih\zeta} - e^{-ih\zeta}\right) + \frac{1}{2}\mu^2\left(e^{ih\zeta} - 2 + e^{-ih\zeta}\right) \\ &= 1 - i\mu \sin(\zeta h) + \mu^2 (\cos(\zeta h) - 1) \\ &= 1 - i\mu\left(2\sin(\zeta h/2)\cos(\zeta h/2)\right) + \mu^2\left(2\sin^2(\zeta h/2)\right). \end{aligned} \tag{2.51}$$

This implies

$$\begin{aligned} |g|^2 &= \left(1 - 2\mu^2 \sin^2(\zeta h/2)\right)^2 + 4\sin^2(\zeta h/2)\cos^2(\zeta h/2) \\ &= 1 - 4\mu^2(1-\mu^2)\sin^4(\zeta h/2). \end{aligned} \tag{2.52}$$

We have $|g| \leq 1$ when $|\mu| \leq 1$. Hence Lax-Wendroff scheme is stable when $\left|\frac{a\Delta t}{\Delta x}\right| \leq 1$ (LeVeque, 2007).

Upwind schemes The upwind scheme, often referred to as upwinding, is a numerical method used in computational fluid dynamics and other areas to discretize and solve partial differential equations involving convection or advection terms. It is particularly effective for problems where the solution propagates in a specific direction.

First order upwind scheme The first order upwind scheme is given by:

$$u_i^{n+1} = u_i^n - \Delta t \left(a^+ u_x^- + a^- u_x^+\right), \tag{2.53}$$

where,

$$a^+ = \max\{a,0\}, a^- = \min\{a,0\}, u_x^- = \frac{u_i^n - u_{i-1}^n}{\Delta x}, \text{ and } u_x^+ = \frac{u_{i+1}^n - u_i^n}{\Delta x}.$$

The upwind scheme is stable if $\mu = \left|\frac{a\Delta t}{\Delta x}\right| \leq 1$.

Second order upwind scheme The second-order upwind scheme uses three data points instead of two and provides a more accurate finite difference stencil for the approximate approximation of spatial derivative. In this scheme u_x^- and u_x^+ in equation (2.53) changes to

$$u_x^- = \frac{3u_i^n - 4u_{i-1}^n + u_{i-2}^n}{2\Delta x}, \text{ and } u_x^+ = \frac{-u_{i+2}^n + 4u_{i+1}^n - 3u_i^n}{2\Delta x}.$$

Third order upwind scheme For the third order upwind scheme u_x^- and u_x^+ in equation (2.53) changes to

$$u_x^- = \frac{2u_{i+1}^n + 3u_i^n - 6u_{i-1}^n + u_{i-2}^n}{6\Delta x}, \text{ and } u_x^+ = \frac{-u_{i+2}^n + 6u_{i+1}^n - 3u_i^n - 2u_{i-1}^n}{6\Delta x}.$$

Modified upwind scheme A modified upwind scheme for equation (2.46) is given by:

$$u_i^{n+1} = u_i^n - \Delta t \left(a \left(\frac{u_{i+1}^n - u_{i-1}^n}{2\Delta x} \right) + q \left(a^+ u_x^- + a^- u_x^+\right) \right), \tag{2.54}$$

where a^+ and a^- are as defined above, and

$$u_x^- = \frac{u_{i-2}^n - 3u_{i-1}^n + 3u_i^n - u_{i+1}^n}{3\Delta x}, \text{ and } u_x^+ = \frac{u_{i-1}^n - 3u_i^n + 3u_{i+1}^n - u_{i+2}^n}{3\Delta x}.$$

It should be noted that the modified formula is only second-order correct for other values of q, while $q = 0.5$ reflects the third-order accurate upwind formula. Additionally, $q = 0$ gives the central difference scheme.

Beam-Warming method For $a > 0$, the Beam-Warming method takes the form:

$$u_i^{n+1} = u_i^n - \frac{a\Delta t}{2\Delta x}\left(3u_i^n - 4u_{i-1}^n + u_{i-2}^n\right) + \frac{a^2(\Delta t)^2}{2(\Delta x)^2}\left(u_i^n - 2u_{i-1}^n + u_{i-2}^n\right). \tag{2.55}$$

For $a < 0$, it takes the form:

$$u_i^{n+1} = u_i^n - \frac{a\Delta t}{2\Delta x}\left(-3u_i^n + 4u_{i+1}^n - u_{i+2}^n\right) + \frac{a^2(\Delta t)^2}{2(\Delta x)^2}\left(u_i^n - 2u_{i+1}^n + u_{i+2}^n\right). \tag{2.56}$$

These methods are stable, provided $\left|\frac{a\Delta t}{\Delta x}\right| \leq 2$, and are second-order accurate.

The CFL condition In general, the following prerequisites must be met for any approach created for the advection equation: If u_j^{n+1} is computed based on values $u_{j+p}^n, u_{j+p+1}^n, \cdots, u_{j+q}^n$ with $p \leq q$ (p and q can be negative), $k = \Delta t, h = \Delta x$, then for the method to be convergent,

$$-q \leq \frac{ak}{h} \leq -p \tag{2.57}$$

The advection equation result is a particular instance of the CFL condition, a much broader principle: Only when the numerical domain of dependence of a numerical method encompasses the genuine domain of dependence of the PDE, at least as k and h approach zero, can the method be considered convergent. The Courant number is frequently denoted by the value $\mu = \frac{ak}{h}$. The approach cannot be convergent if the CFL condition is failed. If it is satisfied, the technique may converge; however, to establish the appropriate stability restriction on k and h, or to verify this, an appropriate stability analysis is needed. For example: consider the Beam-Warming method; if $a > 0$, we have $p = -2, q = 0$. For convergence, $0 \leq \frac{ak}{h} \leq p$. And if $a < 0$, we have $p = 0, q = 2$. For convergence, the necessary condition is $-2 \leq \frac{ak}{h} \leq 0$. For the detailed stability analyses of various finite difference methods, one can refer to the books (LeVeque, 2007; Causon, 2010).

2.4 Fractional Calculus

In the realm of mathematical modelling and computational simulations, the use of fractional calculus has gained significant attention due to its ability to describe and analyze complex phenomena that classical integer-order calculus fails to capture adequately. This section provides an overview of different types of fractional derivatives, including the Caputo derivative, the Riemann-Liouville derivative, and other variants. The numerical methods used for the discretization of fractional derivatives are also discussed. These methods are specifically designed to approximate fractional derivatives of functions discretely. Some of the special functions used in fractional integrals and derivatives are defined below:

Definition 2 *The Gamma function $\Gamma(z)$ is a fundamental mathematical function that generalizes the concept of the factorial to non-integer arguments. For $z \in \mathbb{C}$ such that*

$\mathscr{R}(z) > 0$, $\Gamma(z)$ *is defined as*

$$\Gamma(z) = \int_0^\infty t^{z-1}e^{-t}dt \tag{2.58}$$

The incomplete Gamma function is defined as

$$\Gamma^*(z,x) = \int_0^x t^{z-1}e^{-t}dt. \tag{2.59}$$

Definition 3 *For $z \in \mathbb{C}$, the Mittag Leffler function $E_\alpha(z)$ is defined as the following power series representation:*

$$E_\alpha(z) = \sum_{k=0}^{\infty} \frac{z^k}{\Gamma(\alpha k + 1)} \qquad \alpha > 0, \tag{2.60}$$

and the Generalized Mittag Leffler function $E_{\alpha,\beta}(z)$ is defined as,

$$E_{\alpha,\beta}(z) = \sum_{k=0}^{\infty} \frac{z^k}{\Gamma(\alpha k + \beta)} \qquad \alpha > 0, \beta > 0. \tag{2.61}$$

Definition 4 *Given a function $f(t), t \in (a,b)$, the Riemann Liouville integral with order $\alpha > 0$ is defined as*

$$_{RL}D_{a,t}^{-\alpha} f(t) = \frac{1}{\Gamma(\alpha)} \int_a^t (t-s)^{\alpha-1} f(s)ds, \tag{2.62}$$

where $\Gamma(\dot{})$ is the Gamma function.

Examples of Riemann Liouville fractional integrals

Example 1 Consider $f(t) = t^\mu$, where $\mu > -1$. By definition,

$$\begin{aligned}
_{RL}D_{0,t}^{-\alpha} t^\mu &= \frac{1}{\Gamma(\alpha)} \int_0^t (t-s)^{\alpha-1} s^\mu ds, \\
&= \frac{1}{\Gamma(\alpha)} \int_0^t \left(1 - \frac{s}{t}\right)^{\alpha-1} t^{\alpha-1} s^\mu ds, \\
&= \frac{1}{\Gamma(\alpha)} \int_0^1 (1-u)^{\alpha-1} t^{\alpha-1} (ut)^\mu t du, \left(u = \frac{s}{t}\right) \\
&= \frac{1}{\Gamma(\alpha)} t^{\alpha+\mu} \int_0^1 (1-u)^{\alpha-1} (u)^\mu du, \\
&= \frac{1}{\Gamma(\alpha)} t^{\alpha+\mu} B(\mu+1, \alpha), \text{ where } B \text{ is the Beta function,} \\
&= \frac{\Gamma(\mu+1)}{\Gamma(\mu+\alpha+1)} t^{\alpha+\mu}.
\end{aligned}$$

The above example tells that if k is a constant, $_{RL}D_{0,t}^{-\alpha} k = \dfrac{k}{\Gamma(\alpha+1)} t^\alpha$.

Example 2 Consider $f(t) = e^{at}$, where a is a constant. By definition,

$$\begin{aligned} {}_{RL}D_{0,t}^{-\alpha} e^{at} &= \frac{1}{\Gamma(\alpha)} \int_0^t (t-s)^{\alpha-1} e^{as} ds \\ &= -\frac{1}{\Gamma(\alpha)} \int_{at}^0 \frac{1}{a} \left(\frac{u}{a}\right)^{\alpha-1} e^{at-u} du, (u = a(t-s)) \\ &= \frac{e^{at}}{a^{\alpha}\Gamma(\alpha)} \int_0^{at} u^{\alpha-1} e^{-u} du, \\ &= \frac{e^{at}}{a^{\alpha}\Gamma(\alpha)} \Gamma^*(\alpha, at). \end{aligned}$$

Definition 5 *Given a function $f(t), t \in (a,b)$, the Grunwald Letnikov derivative of order $\alpha > 0$ is defined as*

$$ {}_{GL}D_{a,t}^{\alpha} f(t) = \lim_{\substack{h\to 0 \\ Nh = t-a}} h^{-\alpha} \sum_{j=0}^{N} (-1)^j \binom{\alpha}{j} f(t-jh). \tag{2.63}$$

Definition 6 *The Riemann Liouville derivative with order $\alpha > 0$ of the given function $f(t), t \in (a,b)$ is defined as*

$$ {}_{RL}D_{a,t}^{\alpha} f(t) = \frac{1}{\Gamma(m-\alpha)} \frac{d^m}{dt^m} \int_a^t (t-s)^{m-\alpha-1} f(s) ds, \tag{2.64}$$

where m is a positive integer satisfying $m-1 \le \alpha < m$.

Example 3 Consider $f(t) = t^{\mu}$, where $\mu > -1$. By definition,

$$\begin{aligned} {}_{RL}D_{0,t}^{\alpha} t^{\mu} &= \frac{d}{dt} \left({}_{RL}D_{0,t}^{-(1-\alpha)} t^{\mu} \right), \\ &= \frac{d}{dt} \left(\frac{\Gamma(\mu+1)}{\Gamma(2-\alpha+\mu)} t^{1-\alpha+\mu} \right), \\ &= \frac{\Gamma(\mu+1)}{\Gamma(1-\alpha+\mu)} t^{\mu-\alpha}. \end{aligned}$$

The above example tells that if k is a non-zero constant, ${}_{RL}D_{0,t}^{\alpha} k = \frac{k}{\Gamma(1-\alpha)} t^{-\alpha}$, which is not zero. For more examples of fractional derivatives, one can refer to these references (Miller and Ross, 1993; Podlubny, 1999). Definitions of fractional derivatives that permit the use of physically comprehensible initial conditions, such as $f(a), f'(a)$, etc., are necessary for solving applied issues. Unfortunately, the Riemann Liouville method results in initial conditions at the lower terminal $t = a$ that contain the limit values of the Riemann Liouville fractional derivatives. Such starting conditions have no recognised physical explanation. In order to maintain consistency, Caputo fractional derivative was introduced.

Caputo fractional derivatives are well-suited for modelling initial value problems. The fundamental benefit of Caputo's method is that the initial conditions for fractional differential equations with Caputo derivatives have the same structure as differential equations for integer order. They contain the limit values of integer order derivatives at $t = a$.

Definition 7 *The Caputo derivative with order* $\alpha > 0$ *of the given function* $f(t), t \in (a,b)$ *is defined as*

$$ {}_{C}D^{\alpha}_{a,t} f(t) = \frac{1}{\Gamma(m-\alpha)} \int_a^t (t-s)^{m-\alpha-1} f^{(m)}(s) ds, \tag{2.65}$$

where m *is a positive integer satisfying* $m-1 < \alpha \leq m$.

Another difference between the Riemann Liouville derivative and the Caputo derivative is that the Riemann Liouville derivative of a non-zero constant function is not zero, but the Caputo derivative of a constant function is zero, which is physically more realizable. The definitions of fractional derivative, Grunwald Letnikov derivative, Riemann Liouville derivative or the Caputo derivative are not identical. Assuming that $f(t)$ is adequately smooth, that is, $f \in C^m[a,b]$,

$$ {}_{RL}D^{\alpha}_{a,t} f(t) = {}_{GL} D^{\alpha}_{a,t} f(t). \tag{2.66}$$

The following relation applies to the Riemann Liouville and Caputo derivative of $f(t)$,

$$ {}_{RL}D^{\alpha}_{a,t} f(t) = {}_{C} D^{\alpha}_{a,t} f(t) + \sum_{k=0}^{m-1} \frac{f^{(k)}(a)(t-a)^{k-\alpha}}{\Gamma(k+1-\alpha)}, \tag{2.67}$$

where $f \in C^{m-1}[a,t]$, $f^{(m)}$ is integrable on $[a,t]$, $m-1 < \alpha < m$, and m is a positive integer.

2.4.1 Operator Properties of Fractional Derivatives and Integrals

The following are some characteristics that fractional derivatives and integrals of various orders follow when they are operated upon each other. The proofs for the following propositions can be found in these references (Podlubny, 1999; Miller and Ross, 1993; Li and Zeng, 2015)

Proposition 1 *The Riemann-Liouville fractional integral operators satisfy the following property (for* $\alpha, \beta > 0$*):*

$$ D^{-\alpha}_{a,t} D^{-\beta}_{a,t} f(t) = D^{-\beta}_{a,t} D^{-\alpha}_{a,t} f(t) = D^{-\alpha-\beta}_{a,t} f(t) \tag{2.68}$$

Proposition 2 *The following properties are met by the Riemann-Liouville fractional derivative operators:*

$$ {}_{RL}D^{\alpha}_{a,t} D^{-\alpha}_{a,t} f(t) = f(t), \tag{2.69a}$$

$$ D^{-\alpha}_{a,t} \left({}_{RL}D^{\alpha}_{a,t} f(t) \right) = f(t) - \sum_{j=1}^{m} \left[{}_{RL}D^{\alpha-j}_{a,t} f(t) \right]_{t=a} \frac{(t-a)^{\alpha-j}}{\Gamma(\alpha-j+1)}, \tag{2.69b}$$

where $m-1 \leq \alpha < m$, m *is a positive integer.*

If there are an adequate number of continuous derivatives for $f(t)$, *then* $\left[{}_{RL}D_{a,t}^{\alpha-j}f(t)\right]_{t=a}=0, j=1,2,\cdots m$ *is equivalent to* $f^{(j)}(a)=0, j=0,1,\cdots m-1$.

A more general case for the above proposition is

$$
\begin{aligned}
{}_{RL}D_{a,t}^{\alpha}D_{a,t}^{-\beta}f(t) &={}_{RL}D_{a,t}^{\alpha-\beta}f(t), &\text{(2.70a)}\\
D_{a,t}^{-\beta}\left({}_{RL}D_{a,t}^{\alpha}f(t)\right) &={}_{RL}D_{a,t}^{\alpha-\beta}f(t)-\sum_{j=1}^{m}\left[{}_{RL}D_{a,t}^{\alpha-j}f(t)\right]_{t=a}\frac{(t-a)^{\beta-j}}{\Gamma(1+\beta-j)}, &\text{(2.70b)}
\end{aligned}
$$

where $m-1\leq\alpha<m, n-1\leq\beta<n$, m,n are positive integers.

Proposition 3 *If* $m-1\leq\alpha<m, n-1\leq\beta<n$, *where* m,n *are positive integers,* ${}_{RL}D_{a,t}^{\alpha+\beta}f(t)$ *and* ${}_{RL}D_{a,t}^{\alpha}\left({}_{RL}D_{a,t}^{\beta}f(t)\right)$ *exist, then,*

$$
{}_{RL}D_{a,t}^{\alpha}\left({}_{RL}D_{a,t}^{\beta}f(t)\right)={}_{RL}D_{a,t}^{\alpha+\beta}f(t)-\sum_{j=1}^{n}\left[{}_{RL}D_{a,t}^{\beta-j}f(t)\right]_{t=a}\frac{(t-a)^{-\alpha-j}}{\Gamma(1-\alpha-j)}. \tag{2.71}
$$

Proposition 4 *Let* $\alpha>0$, $n-1<\beta<n$, n *is a positive integer,* $f\in C^{n}[a,b]$. *Then,*

$$
D_{a,t}^{-\alpha}\left({}_{C}D_{a,t}^{\beta}f(t)\right)={}_{C}D_{a,t}^{\beta-\alpha}f(t), \tag{2.72}
$$

where ${}_{C}D_{a,t}^{\beta-\alpha}=D_{a,t}^{\beta-\alpha}$, *if* $\beta<\alpha$. *Especially,*

$$
D_{a,t}^{-\beta}\left({}_{C}D_{a,t}^{\beta}f(t)\right)=f(t)-\sum_{k=0}^{n-1}\frac{f^{(k)}(a)}{\Gamma(k+1)}(t-a)^{k}. \tag{2.73}
$$

Proposition 5 *Assuming that* $f(t)$ *is sufficiently smooth and* $\alpha,\beta>0$, ${}_{C}D_{a,t}^{\beta}D_{a,t}^{-\alpha}f(t)$ *and* ${}_{C}D_{a,t}^{\beta-\alpha}f(t)$ *exist. Then,*

$$
{}_{C}D_{a,t}^{\beta}\left(D_{a,t}^{-\alpha}f(t)\right)=\begin{cases}D_{a,t}^{(\alpha-\beta)}f(t), & \beta\leq\alpha,\alpha<\beta,\alpha\in\mathbb{N}\\ {}_{C}D_{a,t}^{\beta-\alpha}f(t)+\sum_{k=0}^{n-m}\dfrac{f^{(k)}(a)}{\Gamma(k+1+\alpha-\beta)}(t-a)^{k+\alpha-\beta}, & \\ \qquad\qquad \alpha<\beta, m-1<\alpha<m, n-1<\beta<n, m,n\in\mathbb{N}\end{cases} \tag{2.74}
$$

Proposition 6 *Let* $\beta>0$, $n-1<\beta<n$ *and* m *be any non-negative integer. Then,*

$$
\begin{aligned}
{}_{C}D_{a,t}^{\beta}\left({}_{C}D_{a,t}^{m}f(t)\right) &={}_{C}D_{a,t}^{m+\beta}f(t), &\text{(2.75a)}\\
{}_{C}D_{a,t}^{m}\left({}_{C}D_{a,t}^{\beta}f(t)\right) &={}_{C}D_{a,t}^{m+\beta}f(t)+\sum_{j=n}^{m+n-1}\frac{f^{(j)}(a)}{\Gamma(1+j-m-\beta}(t-a)^{j-m-\beta}. &\text{(2.75b)}
\end{aligned}
$$

Proposition 7 Linearity

Fractional integrals and derivatives are linear operators, i.e.,

$$
D^{\alpha}(\lambda_1 f(t)+\lambda_2 g(t))=\lambda_1 D^{\alpha}f(t)+\lambda_2 D^{\alpha}g(t), \tag{2.76}
$$

where D^{α} *represents any fractional derivative or integral.*

Proposition 8 Leibniz Rule for Fractional Derivatives

Given any two functions with derivatives up to n, say $f(t)$ and $g(t)$. Then, the fractional derivative Leibniz rule is given by

$$ {}_{RL}D^{\alpha}_{a,t}(g(t)f(t)) = \sum_{k=0}^{n} \binom{\alpha}{k} g^{(k)}(t) f^{(\alpha-k)}(t) - R^{\alpha}_{n}(t), \tag{2.77} $$

where $n \geq \alpha + 1$, $f^{(\alpha-k)}(t) = {}_{RL}D^{\alpha-k}_{a,t} f(t)$, and

$$ R^{\alpha}_{n}(t) = \frac{(-1)^n (t-a)^{n-\alpha+1}}{n!\Gamma(-\alpha)} \int_0^1 F_a(t,\zeta,\eta) d\zeta d\eta, \tag{2.78} $$

where

$$ F_a(t,\zeta,\eta) = f(a + \eta(t-a)) g^{(n+1)}(a + (t-a)(\zeta + \eta - \zeta\eta)). $$

Proposition 9 Laplace Transform of Fractional Derivatives

The Laplace transform of a given function $f(t)$, (must be of exponential order μ such that for positive constants M and T, $|f(t)| \leq Me^{\mu t}$ for all $t > T$) is defined as:

$$ F(s) = L\{f(t);s\} = \int_0^{\infty} e^{-st} f(t) dt. \tag{2.79} $$

The Laplace transform of the fractional integral is given by

$$ L\{{}_{RL}D^{-\alpha}_{0,t} f(t);s\} = s^{-\alpha} L\{f(t);s\}. \tag{2.80} $$

The Riemann-Liouville derivative operator with order $\alpha, m-1 \leq \alpha < m$ has the Laplace transform given by

$$ L\{{}_{RL}D^{\alpha}_{0,t} f(t);s\} = s^{\alpha} L\{f(T);s\} - \sum_{k=0}^{m-1} s^k \left[{}_{RL}D^{\alpha-k-1}_{0,t} f(t) \right]_{t=0}. \tag{2.81} $$

The Caputo derivative operator with order $\alpha, m-1 \leq \alpha < m$ has the Laplace transform given by

$$ L\{{}_{C}D^{\alpha}_{0,t} f(t);s\} = s^{\alpha} L\{f(T);s\} - \sum_{k=0}^{m-1} s^{\alpha-k-1} f^{(k)}(0). \tag{2.82} $$

2.4.2 Numerical Methods for Fractional Integrals

Suppose that $f(t) \in C(I), I = [0,T]$. Let Δt be the time step, and $t_k = k\Delta t$.

Fractional Rectangular Formula The left fractional rectangular formula is given by:

$$ \left[D^{-\alpha}_{0,t} f(t) \right]_{t=t_n} \approx \sum_{k=0}^{n-1} b_{n-k-1} f(t_k), \tag{2.83} $$

and the right fractional rectangular formula is given by:

$$\left[D_{0,t}^{-\alpha} f(t)\right]_{t=t_n} \approx \sum_{k=0}^{n-1} b_{n-k-1} f(t_{k+1}), \tag{2.84}$$

where

$$b_k = \frac{\Delta t^{\alpha}}{\Gamma(\alpha+1)} \left[(k+1)^{\alpha} - k^{\alpha}\right].$$

The formulae (2.83, 2.84) can be seen as the special cases of weighted fractional rectangular formula, given by

$$\left[D_{0,t}^{-\alpha} f(t)\right]_{t=t_n} \approx \sum_{k=0}^{n-1} b_{n-k-1} \left[\theta f(t_k) + (1-\theta) f(t_{k+1})\right], \quad 0 \leq \theta \leq 1. \tag{2.85}$$

Fractional Trapezoidal Formula On each subinterval $[t_k, t_{k+1}]$, $f(t)$ is approximated by piecewise polynomials with the degree of order one, and the resultant fractional trapezoidal formula is given by:

$$\left[D_{0,t}^{-\alpha} f(t)\right]_{t=t_n} \approx \sum_{k=0}^{n} a_{k,n} f(t_k), \tag{2.86}$$

where,

$$a_{k,n} = \frac{\Delta t^{\alpha}}{\Gamma(\alpha+2)} \begin{cases} (n-1)^{\alpha+1} - (n-1-\alpha) n^{\alpha}, & k = 0, \\ (n-k+1)^{\alpha+1} + (n-1-k)^{\alpha+1} - 2(n-k)^{\alpha+1}, & 1 \leq k \leq n-1, \\ 1, & k = n. \end{cases}$$

For other numerical approximations like fractional Simpson's formula, fractional Newton Cotes formula etc., one can refer to the book by Li and Zeng (Li and Zeng, 2015).

2.4.3 Numerical Methods for Fractional Derivatives

Grunwald-Letnikov Approximation Let $f(x)$ be a suitably smooth function defined on the real line, and let α be a positive real number representing the order of the fractional derivative to be approximated. Then,

$$\left[{}_{RL}D_{0,t}^{\alpha} f(t)\right]_{t=t_n} \approx \frac{1}{\Delta t^{\alpha}} \sum_{j=0}^{n} \omega_j^{(\alpha)} f(t_{n-j}), \tag{2.87}$$

where, $\omega_j^{(\alpha)} = (-1)^j \binom{\alpha}{j}$. This method is convergent for order 1 for any $\alpha > 0$, but it may contribute to unstable numerical schemes for $1 < \alpha < 2$. Although the error might not increase for higher values of Δt, the approach is unstable when Δt is refined (Meerschaert and Tadjeran, 2004).

The shifted Grunwald-Letnikov formula (p shifts, $p \in \mathbb{N}$) is useful for constructing stable numerical schemes and is first-order accurate. It is given by

$$\left[{}_{RL}D_{0,t}^{\alpha} f(t)\right]_{t=t_n} \approx \frac{1}{\Delta t^{\alpha}} \sum_{j=0}^{n+p} \omega_j^{(\alpha)} f(t_{n-j+p}). \tag{2.88}$$

L1 method The classical L1 method is suitable for the case $0<\alpha<1$. For uniform grids, the L1 approximation is given by

$$\left[{}_{RL}D_{0,t}^{\alpha} f(t)\right]_{t=t_n} \approx \frac{f(0)t_n^{-\alpha}}{\Gamma(1-\alpha)} + \sum_{k=0}^{n-1} b_{n-k-1}\left[f(t_{k+1}) - f(t_k)\right], \tag{2.89a}$$

$$\left[{}_{C}D_{0,t}^{\alpha} f(t)\right]_{t=t_n} \approx \sum_{k=0}^{n-1} b_{n-k-1}\left[f(t_{k+1}) - f(t_k)\right], \tag{2.89b}$$

where $t_0 = 0$ and $b_k = \dfrac{\Delta t^{-\alpha}}{\Gamma(2-\alpha)}\left[(k+1)^{1-\alpha} - k^{1-\alpha}\right]$. The above method (2.89a) has the following error estimate,

$$\left| \frac{f(0)t_n^{-\alpha}}{\Gamma(1-\alpha)} + \sum_{k=0}^{n-1} b_{n-k-1}\left[f(t_{k+1}) - f(t_k)\right] - \left[{}_{RL}D_{0,t}^{\alpha} f(t)\right]_{t=t_n} \right| \leq C\Delta t^{2-\alpha}, \tag{2.90}$$

where C is a constant that is positive and depends on α and f.

L2 and L2C methods

- L2 approximation for $1<\alpha<2$ is given by,

$$\left[{}_{RL}D_{0,t}^{\alpha} f(t)\right]_{t=t_n} \approx \frac{f(0)t_n^{-\alpha}}{\Gamma(1-\alpha)} + \frac{f'(0)t_n^{1-\alpha}}{\Gamma(2-\alpha)} + \sum_{k=-1}^{n} W_k f(t_{n-k}), \tag{2.91a}$$

$$\left[{}_{C}D_{0,t}^{\alpha} f(t)\right]_{t=t_n} \approx \sum_{k=-1}^{n} W_k f(t_{n-k}), \tag{2.91b}$$

where the weights W_k are given by,

$$W_k = \frac{\Delta t^{-\alpha}}{\Gamma(3-\alpha)} \begin{cases} 1, & k=-1, \\ 2^{2-\alpha}-3, & k=0, \\ (k+2)^{2-\alpha} - 3(k+1)^{2-\alpha} + 3k^{2-\alpha} - (k-1)^{2-\alpha}, & 1 \leq k \leq n-2, \\ -2n^{2-\alpha} + 3(n-1)^{2-\alpha} - (n-2)^{2-\alpha}, & k=n-1, \\ n^{2-\alpha} - (n-1)^{2-\alpha}, & k=n. \end{cases}$$

- L2C approximation for $1<\alpha<2$ is given by,

$$\left[{}_{RL}D_{0,t}^{\alpha} f(t)\right]_{t=t_n} \approx \frac{f(0)t_n^{-\alpha}}{\Gamma(1-\alpha)} + \frac{f'(0)t_n^{1-\alpha}}{\Gamma(2-\alpha)} + \sum_{k=-1}^{n+1} \hat{W}_k f(t_{n-k}), \tag{2.92a}$$

$$\left[{}_{C}D^{\alpha}_{0,t}f(t)\right]_{t=t_n} \approx \sum_{k=-1}^{n+1} \hat{W}_k f(t_{n-k}), \tag{2.92b}$$

where the weights $\hat{W}_k$ are given by,

$$\hat{W}_k = \frac{\Delta t^{-\alpha}}{2\Gamma(3-\alpha)} \begin{cases} 1, & k=-1, \\ 2^{2-\alpha}-2, & k=0, \\ 3^{2-\alpha}-2^{2-\alpha}, & k=1, \\ (k+2)^{2-\alpha}-2(k+1)^{2-\alpha}+2(k-1)^{2-\alpha}-(k-2)^{2-\alpha}, & 2\le k\le n-2, \\ -n^{2-\alpha}-3(n-1)^{2-\alpha}+2(n-2)^{2-\alpha}, & k=n-1, \\ -n^{2-\alpha}+2(n-1)^{2-\alpha}-(n-2)^{2-\alpha}, & k=n, \\ n^{2-\alpha}-(n-1)^{2-\alpha}, & k=n+1. \end{cases}$$

L2 and L2C method converges with order $O\left(\Delta t^{3-\alpha}\right)$. For more such numerical methods for fractional derivatives, one can refer to these references (Li and Zeng, 2012; Li and Zeng, 2015; Li and Chen, 2018).

2.4.4 Numerical Methods for Fractional Ordinary Differential Equations

Existence and Uniqueness theorems Ordinary differential equations of the Caputo type are mentioned in this section because, under suitable conditions, Riemann-Liouville derivatives can be converted into Caputo ones. The following theorems can be found in (Diethelm and Ford, 2002). Consider the initial value problem,

$$\begin{cases} {}_{C}D^{\alpha}_{0,t}u(t) = f(t,u(t)), & m-1<\alpha<m\in\mathbb{Z}^{+} \\ u^{(j)}(0)=u_0^j, & j=0,1,\cdots,m-1. \end{cases} \tag{2.93}$$

Theorem 1 *Assume that* $\mathcal{D} := [0,\chi^*]\times\left[u_0^0-\delta, u_0^0+\delta\right]$, *with some* $\chi^*>0$, *and some* $\delta>0$, *and let the function* $f:\mathcal{D}\to\mathbb{R}$ *be continuous. Furthermore, define* $\chi := min\{\chi^*, (\delta\Gamma(\alpha+1)/\|f\|_\infty)^{1/\alpha}\}$. *Then, there exists a function* $u:[0,\chi]\to\mathbb{R}$ *solving the initial value problem* (2.93).

Theorem 2 *Assume that* $\mathcal{D} := [0,\chi^*]\times\left[u_0^0-\delta, u_0^0+\delta\right]$, *with some* $\chi^*>0$, *and some* $\delta>0$. *Furthermore, let the function* $f:\mathcal{D}\to\mathbb{R}$ *be bounded on* $\mathcal{D}$ *and fulfil a Lipschitz condition with respect to the second variable, i.e.,*

$$|f(t,x)-f(t,y)| \le L|x-y| \tag{2.94}$$

with constant $L>0$ *independent of* t,x *and* y. *Then denoting* χ *as in theorem 1, there exists at most one function* $u:[0,\chi]\to\mathbb{R}$ *solving the initial value problem* (2.93).

The following are some numerical methods obtained by discretizing the Caputo derivative.

- **L1 methods**
  For $0 < \alpha < 1$, L1 scheme (2.89b) is used to discretize the Caputo derivative in equation (2.93), given by:

$$\sum_{j=0}^{n-1} b_{n-j-1}\left(u_{j+1}-u_j\right) = f(t_n,u_n) \tag{2.95}$$

  where $u_n \approx u(t_n)$, and $b_j = \frac{\Delta t^{-\alpha}}{\Gamma(2-\alpha)}\left[(j+1)^{1-\alpha} - j^{1-\alpha}\right]$.

- **Grunwald Letnikov formula**
  Using the Grunwald Letnikov approximation for the time-fractional derivative, the following is the method to discretize equation (2.93),

$$\frac{1}{\Delta t^{\alpha}} \sum_{j=0}^{n} \omega_{n-j}^{(\alpha)} \left[u_j - \sum_{k=0}^{m} \frac{u_0^k}{k!} t_j^k\right] = f(t_n,u_n), \quad m-1<\alpha<m. \tag{2.96}$$

  where $\omega_j^{(\alpha)} = (-1)^j \binom{\alpha}{j}$. The αth-order $(m-1<\alpha<m)$ Caputo derivative of a given function $f(t)$ can be understood as the $(m-\alpha)$order fractional integral of the function $f^{(m)}(t)$, according to the definition of the Caputo derivative. As a result, one can employ numerical techniques like in section 2.4.2 for integration to discretize the fractional derivatives. If we apply $D_{0,t}^{-\alpha}$ on both sides of equation (2.93), we can obtain the following equivalent equation

$$u(t) = \sum_{j=0}^{m-1} \frac{t^j}{j!} u_0^{(j)} + D_{0,t}^{-\alpha} f(t,u(t)), \quad m-1<\alpha<m. \tag{2.97}$$

- **Fractional forward Euler method**
  $\left[D_{0,t}^{-\alpha} f(t,u(t))\right]_{t=t_{n+1}}$ is approximated by the left fractional rectangular formula (2.83)

$$u_{n+1} = \sum_{j=0}^{m-1} \frac{t_{n+1}^j}{j!} u_0^{(j)} + \Delta t^{\alpha} \sum_{j=0}^{n} b_{j,n+1} f(t_j,u_j) \tag{2.98}$$

  where

$$b_{j,n+1} = \frac{1}{\Gamma(\alpha+1)}\left[(n-j+1)^{\alpha} - (n-j)^{\alpha}\right]$$

- **Fractional backward Euler method**
  $\left[D_{0,t}^{-\alpha} f(t,u(t))\right]_{t=t_{n+1}}$ is approximated by the right fractional rectangular formula (2.84)

$$u_{n+1} = \sum_{j=0}^{m-1} \frac{t_{n+1}^j}{j!} u_0^{(j)} + \Delta t^{\alpha} \sum_{j=0}^{n} b_{j,n+1} f(t_{j+1},u_{j+1}), \tag{2.99}$$

  where $b_{j,n+1}$ are as defined above.

- **Fractional weighted difference method**
  $\left[D_{0,t}^{-\alpha} f(t,u(t))\right]_{t=t_{n+1}}$ is approximated by the weight fractional rectangular formula (2.85)

$$u_{n+1} = \sum_{j=0}^{m-1} \frac{t_{n+1}^j}{j!} u_0^{(j)} + \Delta t^{\alpha} \sum_{j=0}^{n} b_{j,n+1} \left[\theta f(t_j,u_j) + (1-\theta) f(t_{j+1},u_{j+1})\right], \quad (2.100)$$

  where $b_{j,n+1}$ are as defined above.

2.4.5 Numerical Methods for Fractional Partial Differential Equations

Let $U(x,t)$ be a suitable smooth function such that it satisfies the diffusion equation given by,

$$\begin{aligned} {}_C D_{0,T}^{\alpha} U &= K_\alpha \partial_x^2 U + g(x,t), \qquad (x,t) \in (a,b) \times (0,T], \\ U(x,0) &= \phi_0(x), \qquad x \in (a,b), \\ U(a,t) &= U_a(t), U(b,t) = U_b(t), \qquad t \in (0,T]. \end{aligned} \quad (2.101)$$

- **Explicit Euler Type Method (Grunwald Letnikov Approximation)**
  The Caputo derivative is discretized using the Grunwald-Letnikov formula, and the spatial derivative is discretized using the central difference scheme. Let u_i^n denote the approximate value of $U(x_i,t_n)$ where $\Delta x = \frac{b-a}{N}$, $\Delta t = \frac{T}{n_T}$ and $x_i = a + i\Delta x$, $t_n = n\Delta t$. The method gives

$$\begin{aligned} \frac{1}{\Delta t^{\alpha}} \sum_{k=0}^{n} \omega_{n-k}^{(\alpha)} \left(u_i^k - u_i^0\right) =& K_\alpha \left(\frac{u_{i+1}^{n-1} - 2u_i^{n-1} + u_{i-1}^{n-1}}{(\Delta x)^2}\right) + g_i^n, \quad i = 1,2,\cdots,N-1, \\ u_i^0 =& \phi_0(x_i), \quad i = 0,1,2,\cdots,N, \\ u_0^n =& U_a(t_n), u_N^n = U_b(t_n), \end{aligned} \quad (2.102)$$

  where $\omega_k^{(\alpha)} = (-1)^k \binom{\alpha}{k}$. This method is stable if $\frac{K_\alpha (\Delta t)^\alpha}{(\Delta x)^2} \leq \frac{\alpha}{2}$.

- **Explicit Euler Type Method (L1 Approximation)**
  Here, the Caputo derivative is discretized using the L1 method and is given by,

$$\begin{aligned} \frac{1}{\Delta t^{\alpha}} \sum_{k=0}^{n-1} b_{n-k-1}^{(\alpha)} \left(u_i^{k+1} - u_i^k\right) =& K_\alpha \left(\frac{u_{i+1}^{n-1} - 2u_i^{n-1} + u_{i-1}^{n-1}}{(\Delta x)^2}\right) + g_i^n, \quad i = 1,2,\cdots,N-1, \\ u_i^0 =& \phi_0(x_i), \quad i = 0,1,2,\cdots,N, \\ u_0^n =& U_a(t_n), u_N^n = U_b(t_n), \end{aligned} \quad (2.103)$$

  where $b_k^{(\alpha)} = \frac{1}{\Gamma(2-\alpha)} \left((k+1)^{1-\alpha} - k^{1-\alpha}\right)$.

  This method is conditionally stable if $\frac{K_\alpha (\Delta t)^\alpha}{(\Delta x)^2} \leq \frac{1-2^{-\alpha}}{\Gamma(2-\alpha)}$ (Li and Zeng, 2015).

- **Implicit Euler Type Method (Grunwald Letnikov Approximation)**
  The implicit scheme using the Grunwald Letnikov approximation is given by,

$$\begin{aligned}\frac{1}{\Delta t^{\alpha}}\sum_{k=0}^{n}\omega_{n-k}^{(\alpha)}\left(u_i^k-u_i^0\right)=&K_\alpha\left(\frac{u_{i+1}^n-2u_i^n+u_{i-1}^n}{(\Delta x)^2}\right)+g_i^n,\quad i=1,2,\cdots,N-1,\\ u_i^0=&\phi_0(x_i),\quad i=0,1,2,\cdots,N,\\ u_0^n=&U_a(t_n),u_N^n=U_b(t_n),\end{aligned} \tag{2.104}$$

  where $\omega_k^{(\alpha)}=(-1)^k\binom{\alpha}{k}$. This method is unconditionally stable and is convergent of order $O(\Delta t+\Delta x^2)$.

- **Implicit Euler Type Method (L1 Approximation)**
  The implicit scheme using the L1 method is given by,

$$\begin{aligned}\frac{1}{\Delta t^{\alpha}}\sum_{k=0}^{n-1}b_{n-k-1}^{(\alpha)}\left(u_i^{k+1}-u_i^k\right)=&K_\alpha\left(\frac{u_{i+1}^n-2u_i^n+u_{i-1}^n}{(\Delta x)^2}\right)+g_i^n,\quad i=1,2,\cdots,N-1,\\ u_i^0=&\phi_0(x_i),\quad i=0,1,2,\cdots,N,\\ u_0^n=&U_a(t_n),u_N^n=U_b(t_n),\end{aligned} \tag{2.105}$$

  where $b_k^{(\alpha)}=\frac{1}{\Gamma(2-\alpha)}\left((k+1)^{1-\alpha}-k^{1-\alpha}\right)$.
  This method is unconditionally stable and is convergent of order $O(\Delta t^{2-\alpha}+\Delta x^2)$ (Li and Zeng, 2015).

Different integral approximations allow us to create a wider range of fractional numerical approximations. These approximations help us solve complex problems more accurately. For further exploration of these methods and to understand the stability analyses and the order of convergence, one can refer to the book by Li and Zeng (Li and Zeng, 2015).

Chapter 3

Spatiotemporal Linear Stability Analyses

3.1 Introduction

This chapter deals with the temporal and spatiotemporal linear stability analyses of viscoelastic, subdiffusive, plane Poiseuille flow obeying the Fractional Upper Convected Maxwell equation in the limit of low to moderate Reynolds number and Weissenberg number. Results are shown to identify the regions of topological transition of the advancing flow interface. In particular, we demonstrate how the exponent of the power-law scaling (t^α, with $0 < \alpha \leq 1$) in viscoelastic microscale models (Mason and Weitz, 1995) is related to the fractional order of the time-derivative, α, of the corresponding non-linear stress constitutive equation in the continuum (Adelman, 1976). This significantly differs from the existing studies in the sense that we analyse the linear stability of viscoelastic, subdiffusive channel flows through a combined temporal and spatiotemporal stability analysis (rather than only a temporal stability analysis of the classical (or integer order) viscoelastic channel flows (Khalid et al., 2021)) and the aim is to address the following intriguing questions: What is the critical flow/polymer relaxation condition for the onset of instability? And more crucially, what is the linear spatiotemporal, time asymptotic response of the flow at the critical value of the material parameters, leading to the topological transition of the advancing flow interface of the subdiffusive channel flows?

While the molecular theory of polymer dynamics has already established the correspondence between subdiffusive dynamics and linear viscoelastic relaxation of polymer melts and solutions, (Mason and Weitz, 1995), we ‘upscale’ these ideas at the continuum mechanical scale. Section 3.2 highlights how the exponent in the subdiffusive power-law timescale, t^α (Mason, Gang, and Weitz, 1996), is related to the fractional order of the time-derivative, α, of the corresponding non-linear stress constitutive equations in the continuum. Section 3.3 and 3.4 includes the linearization of the model and the numerical method used to find the temporal and absolute growth rate. Section 3.5 describes the validation of the model developed in section 3.2. The temporal and spatiotemporal stability of two specific cases of monomer diffusion in Rouse chain melts ($\alpha = 1/2$) (Rouse, 1953), and in Zimm chain solution ($\alpha = 2/3$) (Zimm, 1956) are reported in detail in section 3.6 and section 3.7, followed by some concluding remarks in section 3.8. The Rouse model predicts that the viscoelastic properties of the polymer chain can be described by a Generalized Maxwell model, where the elasticity is governed by a single relaxation time, which is independent of the number of Maxwell elements (or the so-called 'submolecules'). In contrast, Zimm's model predicts the ('shear rate and polymer concentration independent') viscosity of the polymer solution by calculating the hydrodynamic interaction of flexible polymers (an idea which was originally proposed by Kirkwood (Kirkwood, 1954)) by approximating the chains using a bead-spring setup.

3.2 Mathematical Model

We consider a viscoelastic fluid subject to shear deformation. Then, an infinitesimal elastic stress, τ_{xy} at time t arising from a small strain increment $d\gamma$ at an earlier time t' is given by,

$$d\tau_{xy} = G(t-t')\dot{\gamma}(t')dt', \tag{3.1}$$

where the relaxation modulus, $G(t)$, represents the influence of the dissipative processes of the surrounding concentrated fluid medium (Schiessel et al., 1995). Assuming linearity, the Boltzmann superposition principle may be utilized to construct the elastic stress at time t by summing up all of the infinitesimal contributions over the entire flow history, which is extended into the infinite past (Brader, 2010),

$$\tau_{xy} = \int_{-\infty}^{t} G(t-t')\dot{\gamma}(t')dt'. \tag{3.2}$$

In their seminal work on passive micro-rheology, Mason and co-workers (Mason and Weitz, 1995) have identified an approximate relation between the time-dependent memory kernel describing the viscous damping of the tracer particle at micro-scale (and which obeys the GLE, e. g., see equation (15) in (Mason, Gang, and Weitz, 1996)), $\zeta(t)$, and the stress relaxation modulus, $G(t)$, i. e.,

$$\zeta(t) = 6\pi a G(t), \tag{3.3}$$

where a is the radius of the tracer particle (assumed spherical). In the regime of linear viscoelasticity, one of the most commonly used three-parameter family of memory kernel is the generalized Rouse kernel for an equally weighted sum of negatively decaying exponential functions (McKinley, Yao, and Forest, 2009),

$$\zeta(t) = \frac{1}{N}\sum_{k=0}^{N-1} e^{-\left(\frac{k}{N}\right)^{\frac{1}{\alpha}}\left(\frac{t}{\lambda_0}\right)}, \tag{3.4}$$

for a number of kernels determining the length of the subdiffusive phase, N, the shortest memory time scale, λ_0, and a subdiffusive exponent, $\alpha \in (0\ 1]$. Since the polymeric liquids of our interest (Sircar and Wang, 2008; Sircar and Wang, 2010; Li, Sircar, and Wang, 2010; Sircar, Li, and Wang, 2010; Sircar, 2010; Sircar, Younger, and Bortz, 2015; Sircar et al., 2015; Sircar and Roberts, 2016; Sircar et al., 2016; Sircar and Bansal, 2019; Singh et al., 2020; Bansal, Chauhan, and Sircar, 2022; Bansal, Ghosh, and Sircar, 2023) show subdiffusive behavior on all length scales, we consider the case when $N \to \infty$ in the Prony series (3.4). For $t \gg \lambda_0$, this limiting behavior leads to the relation

$$\zeta(t) = \frac{\tilde{G}}{\Gamma(1-\alpha)}\left(\frac{t}{\lambda_0}\right)^{-\alpha}, \tag{3.5}$$

where $\Gamma(x)$ is the complete gamma function and $\tilde{G} = \Gamma(1+\alpha)\Gamma(1-\alpha)$, is a constant. In equation (3.5), we have used the fact that the Riemann sum on an infinite interval is given by,

$$\lim_{N\to\infty} \frac{1}{N}\sum_{k=0}^{N-1} f\left(\frac{k}{N}\right) = \int_0^\infty f(x)dx. \tag{3.6}$$

Using equations (3.2, 3.3, 3.5), one arrives at,

$$\tau_{xy} = \frac{\mathscr{A}\lambda_0^\alpha}{\Gamma(1-\alpha)}\int_{-\infty}^{t} dt'(t-t')^{-\alpha}\frac{d\gamma(t')}{dt'}, \tag{3.7}$$

where the constant, $\mathscr{A} = \dfrac{\tilde{G}}{6\pi a}$. We remark that $\mathscr{A}$ is no longer a constant (typically $\mathscr{A} = \mathscr{A}(t)$) when the concentration effects, such as the bond and entanglement effects, are considered (Kremer and Grest, 1990). The right-hand side of equation (3.7) represents a fractional integral corresponding to the Caputo formalism (Glockle and Nonnenmacher, 1991; Glockle and Nonnenmacher, 1994),

$${}_{-\infty}D_t^{-\beta} f(t) = \frac{1}{\Gamma(\beta)}\int_{-\infty}^{t} \frac{dt'}{(t-t')^{1-\beta}}\frac{df(t')}{dt'}. \tag{3.8}$$

Utilizing equations (3.7, 3.8), we arrive at the basic equation governing stress-strain relation in linear viscoelastic subdiffusive media,

$$\tau_{xy} = \mathscr{A}\lambda_0^\alpha \frac{d^{\alpha-1}}{dt^{\alpha-1}}\frac{d\gamma(t)}{dt} = \mathscr{A}\lambda_0^\alpha \frac{d^\alpha \gamma}{dt^\alpha}, \tag{3.9}$$

including the limiting cases of a purely elastic solid ($\alpha \to 0$ or a Hookean spring) and a purely viscous fluid ($\alpha = 1$ or a dashpot) (Scott-Blair, 1944). Through combinations of springs and dashpots, one arrives at standard linear viscoelastic models, including the Maxwell, Kelvin-Voigt, Zener, Poynting-Thomson and Burgers' model and others (Scott-Blair, 1947). The problem is that the corresponding differential equations have a relatively restricted class of solutions, which are too limited to provide an adequate description for the class of viscoelastic subdiffusive fluids. To overcome this shortcoming, one can relate the stress and strain through the fractional equation (3.9), which allows a smooth interpolation between a purely elastic behaviour and a purely viscous pattern. In the present analysis, we have selected the Fractional Upper Convected Maxwell equation to describe the nonlinear viscoelastic response of the subdiffusive media, derived next.

Figure 3.1a depicts the standard Maxwell model in which a spring and a dashpot are connected in series (Schiessel et al., 1995). We generalize this model by replacing these elements with their corresponding fractional elements: $(\alpha_i, \mathscr{A}_i, \lambda_i)$, $i = 1,2$ (figure 3.1b). Because of the sequential construction, the stress, τ, is the same for

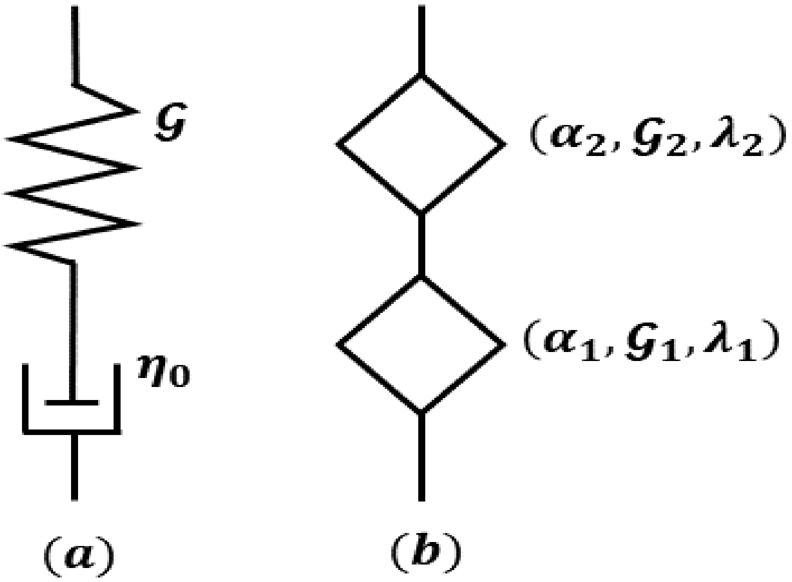

FIGURE 3.1: (a) The Maxwell element and (b) its fractional generalization.

both elements and their respective stress-strain relations are

$$\gamma_i = \mathscr{A}_i^{-1}\lambda_i^{-\alpha_i}\frac{d^{-\alpha_i}\tau_{xy}}{dt^{-\alpha_i}}, \quad \text{i = 1, 2,} \tag{3.10}$$

where both expressions follow from equation (3.9). Due to the construction of the Generalized Maxwell model, we have $\gamma(t) = \gamma_1(t) + \gamma_2(t)$, from which it follows,

$$\tau_{xy} + \frac{\mathscr{A}_1\lambda_1^{\alpha_1}}{\mathscr{A}_2\lambda_2^{\alpha_2}}\frac{d^{\alpha_1-\alpha_2}\tau_{xy}}{dt^{\alpha_1-\alpha_2}} = \mathscr{A}_1\lambda_1^{\alpha_1}\frac{d^{\alpha_1}\gamma}{dt^{\alpha_1}}. \tag{3.11}$$

Equation (3.11) can be simplified by setting $\lambda = (\mathscr{A}_1\lambda_1^{\alpha_1}/\mathscr{A}_2\lambda_2^{\alpha_2})^{1/(\alpha_1-\alpha_2)}$ and $E = \mathscr{A}_1(\lambda_1/\lambda)^{\alpha_1}$. Without loss of generality in the original spring and dashpot model of Maxwell, as outlined by Schiessel (Schiessel et al., 1995), we assume $\alpha_2 = 0$ and $\alpha = \alpha_1(> 0)$, and arrive at

$$\tau_{xy} + \lambda^{\alpha}\frac{d^{\alpha}\tau_{xy}}{dt^{\alpha}} = \eta_p\frac{d^{\alpha}\gamma}{dt^{\alpha}}, \tag{3.12}$$

where the constant, $\eta_p = E\lambda^{\alpha}$. We can extend equation (3.12) to three dimensions by replacing the elastic stress, τ_{xy}, with the stress tensor, $\boldsymbol{\tau}$, and the derivative, $\dfrac{d^{\alpha}\gamma}{dt^{\alpha}}$, with the rate of strain tensor, $\mathbf{D} = (\nabla\mathbf{v} + (\nabla\mathbf{v})^T)$ (where the operator $\nabla(\cdot) = \dfrac{\partial}{\partial\mathbf{x}}(\cdot)$), to arrive at

$$\boldsymbol{\tau} + \lambda^{\alpha}\frac{d^{\alpha}\boldsymbol{\tau}}{dt^{\alpha}} = \eta_p\mathbf{D}, \tag{3.13}$$

using the definition of fractional velocity, $\mathbf{v} = \dfrac{d^{\alpha}\mathbf{x}}{dt^{\alpha}}$ (Prodanov, 2018), which has a dimension of $\dfrac{H}{T^{\alpha}}$ (refer Section 3.3 for the discussion on non-dimensionalization).

Fractional velocities are defined as limits of the difference quotients of a fractional power and they generalize the notion of a local derivative (Prodanov, 2017). These derivatives are frequently used, for example, to model instantaneous interactions in Langevin dynamics (Prodanov, 2018).

Equation (3.13) is the rheological constitutive equation of the Fractional Maxwell model describing the linear viscoelastic media. The simplest way to combine rheological nonlinearity is to replace the (fractional) material time derivative in equation (3.13) with the (fractional) frame invariant, upper-convected time derivative (Macosko, 1994; Spagnolie, 2015), which leads us to the Fractional Upper Convected model, as follows,

$$\boldsymbol{\tau} + \lambda^{\alpha} \overset{\triangledown}{\tau} = \eta_p \mathbf{D}, \tag{3.14}$$

where the fractional upper-convected time derivative of the tensor $\boldsymbol{\tau}$ is defined as,

$$\overset{\triangledown}{\tau} = \frac{\partial^{\alpha} \boldsymbol{\tau}}{\partial t^{\alpha}} + \mathbf{v} \cdot \nabla \boldsymbol{\tau} - (\nabla \mathbf{v})^T \boldsymbol{\tau} - \boldsymbol{\tau} \nabla \mathbf{v}. \tag{3.15}$$

The fractional time derivative, $\frac{\partial^{\alpha}}{\partial t^{\alpha}}$, in equation (3.14, 3.15) is based on the Caputo definition (3.8).

The continuity and the momentum equations for an incompressible, subdiffusive flow (consistent with the stress constitutive relation (3.14)) are,

$$\nabla \cdot \mathbf{v} = 0, \qquad \rho \left[\frac{\partial^{\alpha} \mathbf{v}}{\partial t^{\alpha}} + \mathbf{v} \cdot \nabla \mathbf{v} \right] = -\nabla p + \eta_s \nabla \cdot \mathbf{D} + \nabla \cdot \tau, \tag{3.16}$$

where ρ is the density and p is the isotropic pressure. Equations (3.14, 3.16) represent the equations of motion describing the flow-instability of the subdiffusive viscoelastic fluids.

As a result of the dissipative processes, viscoelastic materials have memory, that is, their actual mechanical response is modulated by the past (Jiménez A. H., 2002). The fractional derivative operators account for the complete history to obtain the derivative at an instant. Unlike the classical Maxwell model (Sircar and Bansal, 2019; Bansal, Ghosh, and Sircar, 2021) which accounts for only the elastic (or stored) part of the deformation work, the Fractional Maxwell model accounts for both forms (stored and dissipated) of energy at any time point. Although Mckinley pointed out that the Fractional Maxwell model generally cannot capture polymer shear-thinning (Jaishankar and McKinley, 2014), the fractional version provides a better fit of the relaxation and creep behaviour for a significantly large class of viscoelastic materials using fewer parameters than the classical version (Jiménez A. H., 2002).

3.3 Linear Stability Analysis

The linearized stability analyses of the fully developed, planar Poiseuille flow inside an infinitely long channel of length L and width H (i. e., $0 \le x \le L$ and $0 \le y \le H$ such that $L/H \gg 1$, where x and y are the variables in the flow and the shear gradient direction, respectively) is studied. Figure 3.2 shows the configuration of planar Poiseuille flow.

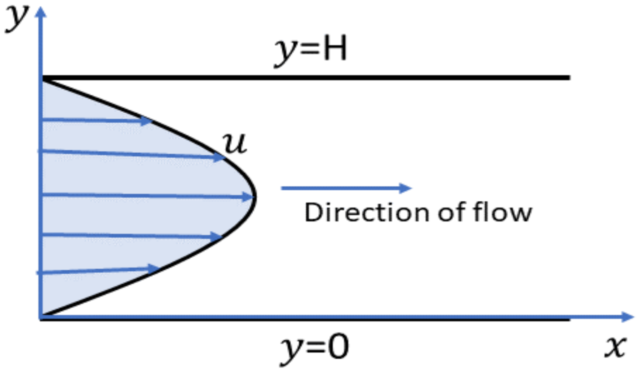

FIGURE 3.2: Poiseuille flow

At $y = 0$ and $y = H$, Poiseuille flow is limited within a channel surrounded by solid walls. Mean velocities and stress are not affected by the channel length variable x. However, pressure is affected by x. The mean velocity profile is a function of y and is naturally parabolic (Thomas, 1953). At the channel walls, the mean flow meets the 'no slip' boundary condition. Because the walls are motionless, the fluid velocities at the boundaries are zero. The boundary condition to the perturbation quantities similarly meets the no-slip boundary condition. It is frequently used as a model system for studying fluid dynamics in simple geometries as well as developing theoretical and computational approaches for more complex flow problems. Using the following scales for non-dimensionalizing the governing equations: the height of the channel H for length, the timescale T corresponding to maximum base flow velocity (i. e., $T = (H/\mathscr{U}_0)^{1/\alpha}$) for time and $\rho\mathscr{U}_0^2$ for pressure and stresses, we characterize equations (3.14, 3.16), rephrased as follows,

$$\nabla \cdot \mathbf{v} = 0, \tag{3.17a}$$

$$Re\left[\frac{\partial^\alpha \mathbf{v}}{\partial t^\alpha} + \mathbf{v}\cdot\nabla\mathbf{v}\right] = -\nabla p + \nu\nabla\cdot\mathbf{D} + (1-\nu)\nabla\cdot\mathbf{A}, \tag{3.17b}$$

$$\frac{\partial^\alpha \mathbf{A}}{\partial t^\alpha} + \mathbf{v}\cdot\nabla\mathbf{A} - (\nabla\mathbf{v})^T\mathbf{A} - \mathbf{A}\nabla\mathbf{v} = \frac{\mathbf{D}-\mathbf{A}}{We}, \tag{3.17c}$$

using the dimensionless groups, $Re = \dfrac{\rho\mathscr{U}_0 H}{\eta_0}$, $We = \dfrac{\lambda^\alpha\mathscr{U}_0}{H}$ and $\eta_s, \eta_p, \eta_0(= \eta_s + \eta_p)$ and $\nu(= \eta_s/\eta_0)$ are the solvent viscosity, the polymeric contribution to the shear viscosity, the total viscosity and the viscous contribution to the total viscosity of the fluid, respectively. In equation (3.17), the elastic stress, τ, is related to the polymer stress tensor, $\mathbf{A}$, as $\tau = (1-\nu)\eta_0\mathbf{A}$. The current analysis deploys fractional derivative of exponentials (Glockle and Nonnenmacher, 1991; Glockle and Nonnenmacher, 1994) given as,

$$\frac{d^\alpha(e^{iat})}{dt^\alpha} = (ia)^\alpha e^{iat}, \tag{3.18}$$

Let us denote the mean flow variables with capital letters and with a subscript '0'. We assume that the mean flow is two-dimensional, quasiparallel with its variation entirely in the shear gradient direction. Then, the (non-dimensional) plane Poiseuille flow velocity can be written as follows,

$$\mathbf{U}_0 = \left((y-y^2)\right)\mathbf{e_x}, \tag{3.19}$$

where $\mathbf{e_x}$ is the unit vector along the x-direction. The other mean flow variables satisfying equation (3.17), including the mean pressure, P_0, and the base state elastic stress tensor, $\mathbf{A}_0 = [A_{0_{ij}}]$, is given by,

$$\begin{aligned}
P_0 &= -2x - 8We(1-\nu)\left(y-y^2\right), && (3.20\text{a})\\
A_{0_{11}} &= 0, && (3.20\text{b})\\
A_{0_{12}} &= A_{0_{21}} = (1-2y), && (3.20\text{c})\\
A_{0_{22}} &= 2We\,(1-2y)^2, && (3.20\text{d})
\end{aligned}$$

and whose linearized stability analysis is presented next.

We restrict our stability analysis to the case when the disturbances are two-dimensional. Assuming an independent fate of each wavenumber, k (whose real part is chosen to be positive) and frequency, ω, it is natural to consider disturbances in the form of a normal mode expansion, such that the total velocity, pressure and stress are expressed in terms of their mean values and perturbations amplitudes (denoted by $(\mathring{\cdot})$), as follows,

$$\mathbf{r} = \mathbf{R}_0 + \varepsilon \mathring{r} e^{i(kx-\omega t)} \tag{3.21}$$

where $\varepsilon \ll 1$ and $\mathbf{r} = [\mathbf{v}\, p A_{11} A_{12} A_{22}]^T$, $\mathbf{R}_0 = [\mathbf{U}_0 P_0 A_{0_{11}} A_{0_{12}} A_{0_{22}}]^T$ and $\mathring{r} = [X_0 y(1-y) X_1 y(1-y) X_2 X_3 X_4 X_5]^T$ represent the total, the mean flow variables and the disturbance amplitudes, respectively. The disturbance amplitude, $\mathring{r}$, is chosen such that it satisfies the no-slip condition on the channel walls. Substituting the solution form (3.21) in equations (3.17a-3.17c) and retaining the $\mathcal{O}(\varepsilon)$ terms to arrive at the linearized equation governing the conservation of mass,

$$X_0\left[ik(y-y^2)\right] + X_1\left[1-2y\right] = 0, \tag{3.22}$$

the linearized equation describing the conservation of momentum in the $x-$direction,

$$\begin{aligned}
&X_0\left[(y-y^2)\left(Re(-i\omega)^\alpha + ikRe(y-y^2) - 2\nu(ik)^2\right) + 2\nu\right]\\
&+X_1\left[Re(1-2y)(y-y^2) - \nu(1-2y)(ik)\right] + ikX_2 - ik(1-\nu)X_3 = 0,
\end{aligned} \tag{3.23}$$

and the one governing the conservation of momentum in the $y-$direction,

$$\begin{aligned}
&X_0\left[-ik\nu\,(1-2y)\right] + X_1\left[(y-y^2)\,(Re(-i\omega)^\alpha + ikRe\right.\\
&\left.(y-y^2) - \nu(ik)^2\right) + 4\nu\left.\right] - (1-\nu)ikX_4 = 0.
\end{aligned} \tag{3.24}$$

The linearized equation for the elastic stress component A_{11},

$$\begin{aligned}
&X_0\left[\frac{-2}{We}(y-y^2)(ik)\right] + X_1\left[-2ik\,(1-2y)\,(y-y^2)\right]\\
&+X_3\left[(-i\omega)^\alpha + ik(y-y^2) + \frac{1}{We}\right] = 0,
\end{aligned} \tag{3.25}$$

for the component A_{12} (or A_{21}),

$$\begin{aligned} & X_0\left[-ik\,(1-2y)\,(y-y^2)-\frac{1}{We}\,(1-2y)\right] \\ & +X_1\left[-2(y-y^2)-2ikWe(1-2y)^2(y-y^2)-(1-2y)^2-\frac{1}{We}(y-y^2)(ik)\right] \\ & +X_3\,[-(1-2y)]+X_4\left[(-i\omega)^{\alpha}+ik(y-y^2)+\frac{1}{We}\right]=0, \end{aligned} \tag{3.26}$$

and for the component A^{22},

$$\begin{aligned} & X_0\left[-2\,(1-2y)^2\right]+X_1\left[-8We\,(1-2y)\,(y-y^2)-4We(1-2y)^3-\frac{2(1-2y)}{We}\right] \\ & +X_4\,[-2(1-2y)]+X_5\left[(-i\omega)^{\alpha}+ik(y-y^2)+\frac{1}{We}\right]=0. \end{aligned} \tag{3.27}$$

Equations (3.22-3.27) may be written in a matrix-vector format as follows,

$$\begin{bmatrix} ik(y-y^2) & 1-2y & 0 & 0 & 0 & 0 \\ M_1 & M_2 & ik & -ik(1-\nu) & 0 & 0 \\ \nu ik(2y-1) & M_3 & 0 & 0 & -ik(1-\nu) & 0 \\ \frac{2ik}{We}(y^2-y) & 2ik(1-2y)(y^2-y) & 0 & M_4 & 0 & 0 \\ M_5 & M_6 & 0 & -(1-2y) & M_4 & 0 \\ -2(1-2y)^2 & M_7 & 0 & 0 & -2(1-2y) & M_4 \end{bmatrix} \begin{bmatrix} X_0 \\ X_1 \\ X_2 \\ X_3 \\ X_4 \\ X_5 \end{bmatrix} = \begin{bmatrix} 0 \\ 0 \\ 0 \\ 0 \\ 0 \\ 0 \end{bmatrix}, \tag{3.28}$$

where the expressions M_i $(i=1,\dots 7)$ utilized above are given as,

$$\begin{aligned} M_1 &= (y-y^2)\left(Re(-i\omega)^{\alpha}+ikRe(y-y^2)-2\nu(ik)^2\right)+2\nu, \\ M_2 &= Re(1-2y)(y-y^2)-\nu(1-2y)(ik), \\ M_3 &= (y-y^2)\left(Re(-i\omega)^{\alpha}+ikRe(y-y^2)-\nu(ik)^2\right)+4\nu, \\ M_4 &= (-i\omega)^{\alpha}+ik(y-y^2)+\frac{1}{We}, \\ M_5 &= -ik\,(1-2y)\,(y-y^2)-\frac{1}{We}\,(1-2y), \\ M_6 &= -2(y-y^2)-2ikWe(1-2y)^2(y-y^2)-(1-2y)^2-\frac{1}{We}(y-y^2)(ik), \\ M_7 &= -8We\,(1-2y)\,(y-y^2)-4We(1-2y)^3-\frac{2(1-2y)}{We}. \end{aligned} \tag{3.29}$$

A nontrivial solution for the system (3.28), imposes a zero determinant condition on the coefficient matrix which leads to the dispersion relation, $D(k,\omega)=0$, given by,

$$\frac{1}{We}k^2 M_4\,(2ik\,(-1+\nu)\,(1-2y)\,(-1+y)\,y\,(1+(-2+ikWe\,(1-2y)$$

$$(-1+y))y)+M_4^2 We\left(\nu(1-2y)^2-M_3(-1+y)y\right)+M_4(-1+\nu)We$$
$$(M_5-2M_5y+ikM_6(-1+y)y))=0. \tag{3.30}$$

3.4 Numerical Method

In the ensuing description, we denote real/imaginary components with subscript r/i, respectively. The zeros of the dispersion relation (3.30) were explored within the complex $k-\omega$ plane inside the region $\omega_r \in [-1700, 0.2]$, $\omega_i \in [-5000, 100]$, $k_r \in [0, 5]$ and $k_i \in [-0.1, 0.2]$. For a real wavenumber k, the procedure for finding the most unstable mode (which is the largest positive imaginary component of any root of the dispersion relation or the temporal growth rate, ω_{Temp}, refer Section 3.6), consists of detecting the admissible saddle points ($\omega \in \mathbb{C}, k \in \mathbb{R}$) satisfying the equations (Huerre and Monkewitz, 1990),

$$D(k,\omega)=0, \tag{3.31a}$$
$$\frac{\partial \omega_i}{\partial k}=\frac{\partial D/\partial k}{\partial D/\partial \omega_i}=0, \tag{3.31b}$$

and then (among all the possible roots of equation (3.31)) identifying those roots with the largest positive imaginary component of the frequency. Equation (3.31) is solved using a multivariate Newton-Raphson algorithm (refer to (Sircar and Bansal, 2019; Bansal, Ghosh, and Sircar, 2021) for a detailed outline of this method).

Next, in the spatiotemporal analysis, eigenpairs with complex wavenumbers and frequencies are permitted in the solution of equation (3.31). The presence of absolute instability requires a specific condition related to the group velocity of the flow. This condition involves the vanishing of the group velocity at points called saddle points or branch points in the complex plane. However, the group velocity is always zero at saddle points, especially where two branches of wave numbers meet, regardless of whether they originate from the same or different halves of the plane. To address this issue, the concept of analytic continuation was introduced by Briggs (Briggs, 1964). This involves deforming the mathematical contours used for analysis in a way that maintains the separation of different branches. The deformation of these contours faces limitations when the branches originating from opposite halves of the plane intersect, leading to the appearance of saddle points known as pinch points. This is accompanied by the appearance of branch points called cusp points. These points have specific mathematical properties that Kupfer analyzed (Kupfer, Bers, and Ram, 1987). In a small neighbourhood around the pinch point, the dispersion relation can be approximated as a second-order algebraic form in the frequency domain and a first-order saddle point in the wave number domain. The behaviour of the wave number contours is then analyzed with respect to the cusp point. A ray is drawn from the cusp point, intersecting the image of the Fourier contour in the frequency domain. The number of intersections is counted to determine the stability characteristics. If the ray intersects an even number of times, the flow corresponds to an evanescent mode. If it intersects an odd number of times, the cusp point represents either an absolutely unstable system in the upper half of the frequency domain or a convectively unstable system in the lower half of the frequency domain. More details on this numerical method are given in Section 2.1.

Under the assumption that dispersion relation is a complex analytic function satisfying Cauchy-Riemann relations, the expressions are chosen preferentially to numerically evaluate the derivatives in equation (3.31b). Relaxation of the assumption (of analyticity) does not impact the numerical results but the evaluation of the complex derivatives in equation (3.31b) becomes cumbersome. The numerical continuation of the temporal growth rate (Section 3.6) and the absolute growth rate curves (Section 3.7) were realized within the range $Re \in [10^{-6}, 10^{2}]$, $We \in [0, 10^{3}]$ and at two specific values of $\nu = 0.05$ (the elastic stress-dominated case) and $\nu = 0.3$ (the viscous stress-dominated case), using a discrete step-size of $\triangle Re = 10^{-6}$ and $\triangle We = 10^{-4}$, respectively. While the (non-dimensional) physical domain spans within the range, $x \in (-\infty, \infty); y \in [0, 1]$, the temporal growth rate (ω_i^{Temp}) and the absolute growth rate (ω_i^{cusp}) of the perturbations are probed at four discrete, transverse spatial locations of the advancing interface: $y = 0.2, 0.9, 0.7, 0.5$. While the former two values of y are chosen qualitatively to probe the near-wall effects, the last value is selected to understand the development of the centerline instability.

3.5 Model Validation

The model and the numerical method outlined above are validated by reproducing the neutral stability curves for a plane Poiseuille of a classical Oldroyd-B fluid, as investigated by Atalik (Atalik and Keunings, 2002) ($\alpha = 1.0$ or the red curves in figure 3.3, in comparison with figure 6 in (Atalik and Keunings, 2002). The ‘dots’ on the curves are the only parameter values where the simulation occurred). The neutral stability curves for two fractional orders ($\alpha = 0.99$ (blue curves) and $\alpha = 0.95$ (green curves)) are also shown for comparison. The locus of neutrally stable points is found after selecting $\omega_i = 0$ in the dispersion relation (3.30) and solving for the unknowns (ω_r, k), at fixed values of Reynolds and elasticity number ($E = \dfrac{We}{Re}$).

Two conclusions can be deduced from figure 3.3. First, notice that the minimum value of the critical Reynolds number predicting a temporal instability increases, with increasing viscosity ratio, both for the classical case (a result identical to the one predicted by Atalik (Atalik and Keunings, 2002)) as well as the subdiffusive case. Second, observe that this minimum value of Re is significantly lower and appears at significantly larger values of E, for the subdiffusive fluid. These two observations indicate that the transition to instability is primarily driven by elasticity (rather than fluid inertia) for subdiffusive fluids. A more detailed outlook of the influence of elasticity is acquired by examining the temporal growth rates, described next.

3.6 Temporal Stability Analysis

First, we explore the linear stability of the system (3.28) by exclusively assigning ω to be a complex number. In earlier studies on wall-bounded viscoelastic flows, elasticity (characterized by the parameter, We) was found to have a destabilizing effect (for example, see (Khalid et al., 2021) and the references within). In this section, we

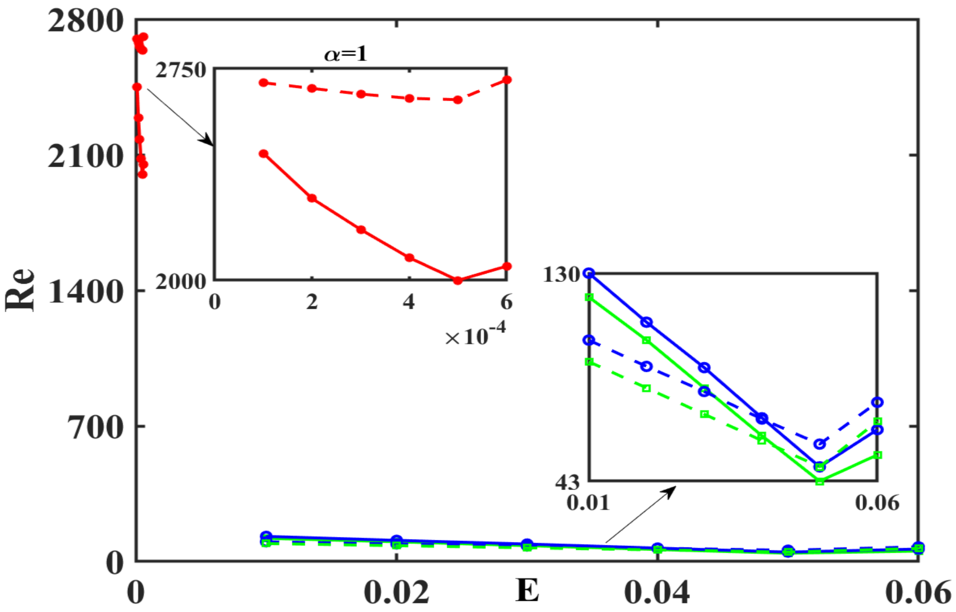

FIGURE 3.3: Neutral stability curves at the centerline ($y = 0$) for plane Poiseulle viscoelastic flow of a classical fluid (red curves, source: figure 6 in (Atalik and Keunings, 2002)) versus subdiffusive fluid at $\alpha = 0.99$ (blue curves), $\alpha = 0.95$ (green curves) and at viscosity ratio, $\nu = 0.01$ (solid curves), $\nu = 0.9$ (dashed curves), projected onto the $Re - E$ plane.

partially extend some of these ideas for the subdiffusive, two-dimensional Poiseuille flow within a selected range of parameters, Re, We, ν and especially for the case of the Rouse chain melts and the Zimm chain solution, which corresponds to the fractional order derivatives, $\alpha = 1/2, 2/3$, respectively. Figures 3.4 present the variation of the most unstable mode versus Re, and at fixed We and ν for viscoelastic Poiseuille flow.

Observe that the elastic stress-dominated case (or $\nu = 0.05$ case) is temporally more unstable (i. e., compare the maximum 'y' value on the ordinate axis of the figures on the left column versus those on the right column in figures 3.4). Also, observe especially for the Zimm's case , that not only the peak of the most unstable mode increases but also the range of Reynolds number exhibiting temporal instability increases with increasing values of We (i. e., notice the dashed green, blue and the red curves in figure 3.4). Also, analogous with the traditional (or integer order) viscoelastic channel flows, we find that for intermediate values of Reynolds number (or $1 \leq Re \leq 55$), elasticity is destabilizing (notice, from the dashed curves in figure insets in figures 3.4, that the most unstable mode is larger for larger values of We). These observations lead us to conclude that elasticity has a destabilizing impact within the intermediate range of Re. This destabilization mechanism is the result of a complex interaction between the inertial forces (typically operative at larger Reynolds number) and the normal stress anisotropy through elasticity (proportional to We) and can be explained via an energy formalism: the stretching of the polymers with increasing elasticity brings about a normal stress anisotropy, leading to an elastically loaded fluid, that is, when the polymers stretch, elastic energy is stored in the sheared fluid. This energy is transferred and released after the fluid element has been advected to other regions where the shear-induced stretching forces are smaller (Spagnolie, 2015). However, for sufficiently larger values of Re (or $Re > 55$), we find the emergence of the temporally stable state. The appearance of the temporally stable state at high fluid inertia is a hallmark of subdiffusive flows and the details of the same are elaborated in Section 3.7.

Regarding the near-wall effects, notice that Zimm's case is more unstable near wall (i. e., comparing the maximum 'y' value on the ordinate axis for $y = 0.2, 0.9$, figures 3.4a,b and 3.4g,h respectively) in comparison with the corresponding instability on channel centerline ($y = 0.5$ case, figures 3.4c,d). Further, within the intermediate range of Reynolds number (i. e., $1 \leq Re \leq 55$), elasticity is destabilizing near the walls (e. g., see the dashed curves in figure insets in figure 3.4a,b,g,h). All these near-wall effects can be understood via a mechanism similar to the one proposed by Rabaud (Rabaud, Couder, and Gerard, 1988) for wall-bounded Newtonian flows: the boundary effects induce a local perturbation on the advancing interface which (when coupled with elasticity) destabilizes the flow.

Finally, we find that the order of the fractional derivative, α has a strong correlation with the temporal stability of the channel flows. Comparing the values of ω_i^{Temp}, we deduce that the Zimm's model is temporally more unstable than the Rouse case. In a series of in silico studies, an investigation of the most unstable mode within the range, $\alpha \in [0.5\, 1.0]$, reveals: (a) the most unstable mode decreases with decreasing order of the fractional derivative, α, (b) the peak of the most unstable mode shifts to lower values of Re with decreasing values of α, and (c) in particular, the peak of the most unstable mode, for the Rouse model (i. e., the solid curves in figures 3.4), precipitates towards the limit $Re \to 0$. In other words, the transition pathway to flow turbulence in the Rouse polymer flows is characterized via elastic turbulence (appearing at vanishingly low values of Re and at moderate to high values of We) (Larson, 2000). To summarize, as α decreases, the nature of the transition pathway to flow turbulence changes from that of the elastoinertial turbulence (characterized by moderate values of Re and We) to elastic turbulence.

We recapitulate the interplay of the inertial forces (characterized by the parameter Re), the elastic forces (represented by the parameter We) as well as the boundary effects and the order of the fractional derivative on the progression of the temporal instability (exemplified by the most unstable mode) of the viscoelastic subdiffusive channel flows as follows: elasticity combined with reasonable fluid inertia has a destabilizing impact on the evolving flow front. The finite boundary is shown to have a destabilizing influence. Finally, the order of the subdiffusive timescale (alternatively, the order of the fractional derivative) impacts the nature of the transition pathway to turbulence (if any). In the next section, we outline a deeper characterization of these instabilities via spatiotemporal analysis.

3.7 Spatiotemporal Stability Analysis

The spatiotemporal analysis is typically relevant when one introduces an impulse excitation locally in a flow and observes how that disturbance evolves in time (Huerre and Monkewitz, 1990). More significantly, we evaluate the absolute growth rate (or ω_i^{Cusp}, details on computing these points are elaborated in Section 3.4) to identify the

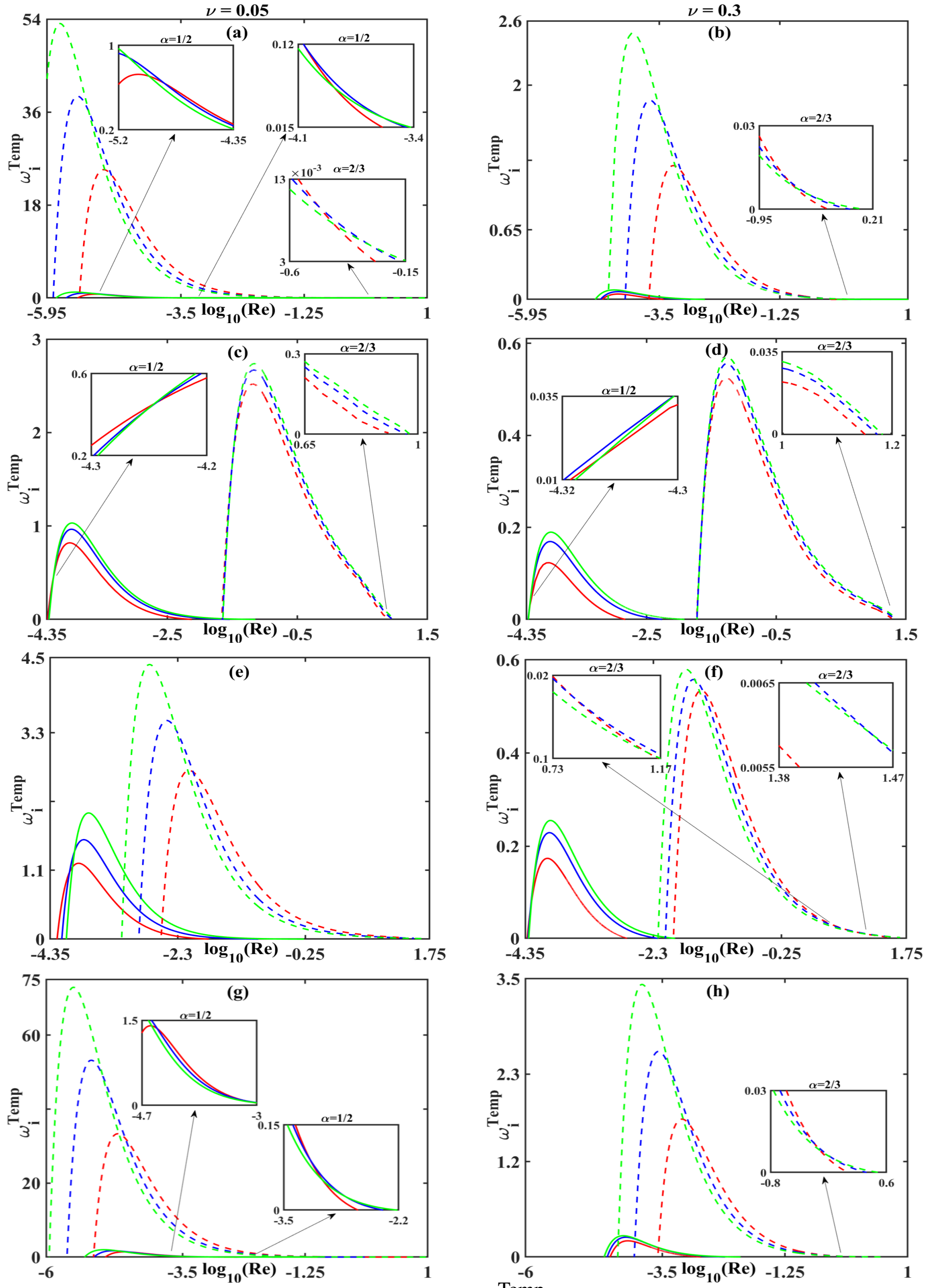

FIGURE 3.4: Most unstable mode, ω_i^{Temp} vs. Reynolds number for the Rouse model (solid curves) and for the Zimm's model (dashed curves), evaluated at $We = 15.0, 25.0, 35.0$ (red, blue and green curves, respectively), viscosity ratios, $\nu = 0.05$ (left column) and $\nu = 0.3$ (right column) and at transverse spatial locations: (a, b) $y = 0.2$, (c, d) $y = 0.5$, (e, f) $y = 0.7$ and (g, h) $y = 0.9$.

region of absolute instability. However, evanescent modes are also encountered in our analysis (Bansal, Ghosh, and Sircar, 2021). These modes do not merely depend on the sign of the absolute growth rate and have to be found via the sufficient conditions proposed by Briggs (Kupfer, Bers, and Ram, 1987) (refer Section 3.4). Evanescent modes are briefly referred in the description of the phase diagrams (figure 3.6).

Figure 3.5 represents the absolute growth rate curves versus Re, at three fixed values of Weissenberg number, $We = 15.0, 25.0, 35.0$, and at $\nu = 0.05$ (the elastic stress-dominated case) and $\nu = 0.3$ (the viscous stress-dominated case). For the selected values of We and for the elastic stress-dominated case, we find that the Rouse model exhibits a transition from absolute instability (or the parameter values where $\omega_i^{\text{Cusp}} > 0$) towards temporal stability (or the range of parameters where no curve is drawn in the plots for absolute growth rate curves) at a critical value of Reynolds number, $Re_c < 10^{-3}$, at $y = 0.2$ (figure 3.5a). This critical Reynolds number increases as one moves closer to the upper plate and along the transverse spatial location, y (i. e., compare the Re_c values from the inset in figures 3.5a,c,e,g). For the viscous stress-dominated case, the Rouse model indicates the following transition with increasing values of Re: convective instability (or the parameter values where $\omega_i^{\text{Cusp}} < 0$)→ absolute instability→ temporal stability. Again, the critical value of the Reynolds number at these transition points increases as one progressively moves towards the upper plate (refer to figures 3.5b,d,f,h). In contrast, the Zimm's model highlights a direct transition from absolute instability towards temporal stability, in the range of low to moderate values of Re and for both the elastic as well as the viscous stress-dominated case. However, both of these model reveals temporal stability in the limit of vanishingly small Reynolds number (or in the strongly elastic limit).

We remark that while some observations listed above follow from the well-established mechanisms seen in classical (or integer order) viscoelastic flows, namely the lack of symmetry in the flow-instability transition across the centerline (due to the anisotropy of the elastic stresses) as well as the appearance of absolute/convective instabilities at intermediate values of Re (generated due to the instability via the polymer elasticity), other observations are relatively novel, specifically the flow induced (temporal) stabilization at higher values of Re.

Next, we classify the nature of these instabilities by computing the boundaries of the temporally stable regions (**S**), evanescent modes (**E**), the convectively unstable (**C**) and the absolutely unstable regions (**A**) within a selected range of the flow-elasticity-viscosity parameter space, i. e., $Re \in [10^{-6}, 100]$, $We \in [0, 10^3]$ and $\nu \in \{0.05, 0.30\}$. While convective instability grows in amplitude as it is swept along by the flow, absolute instability occurs at fixed spatial locations, leading to surface transitions (or pinch-off) of the advancing interface (Huerre and Monkewitz, 1990). The flow stability phase diagram, projected onto the $Re - We$ parameter space (figure 3.6) reveal the presence of absolutely unstable and convectively unstable region at low to moderate values of Re and We ($Re \in [10^{-5}, 10]$ and $We \in [3, 350]$ for absolute instability, and $Re \in [10^{-5}, 10^{-2}]$ and $We \in [50, 150]$ for convective instability, respectively), as result of a complex tug-of-war between the inertial forces (proportional to Re) and the normal stress anisotropy through elasticity (proportional to We). To summarize, the parameter regions susceptible to topological transitions (or the parameter space which indicate absolute instability) in subdiffusive channel flows, are those driven by moderate inertia coupled with moderate to high elasticity.

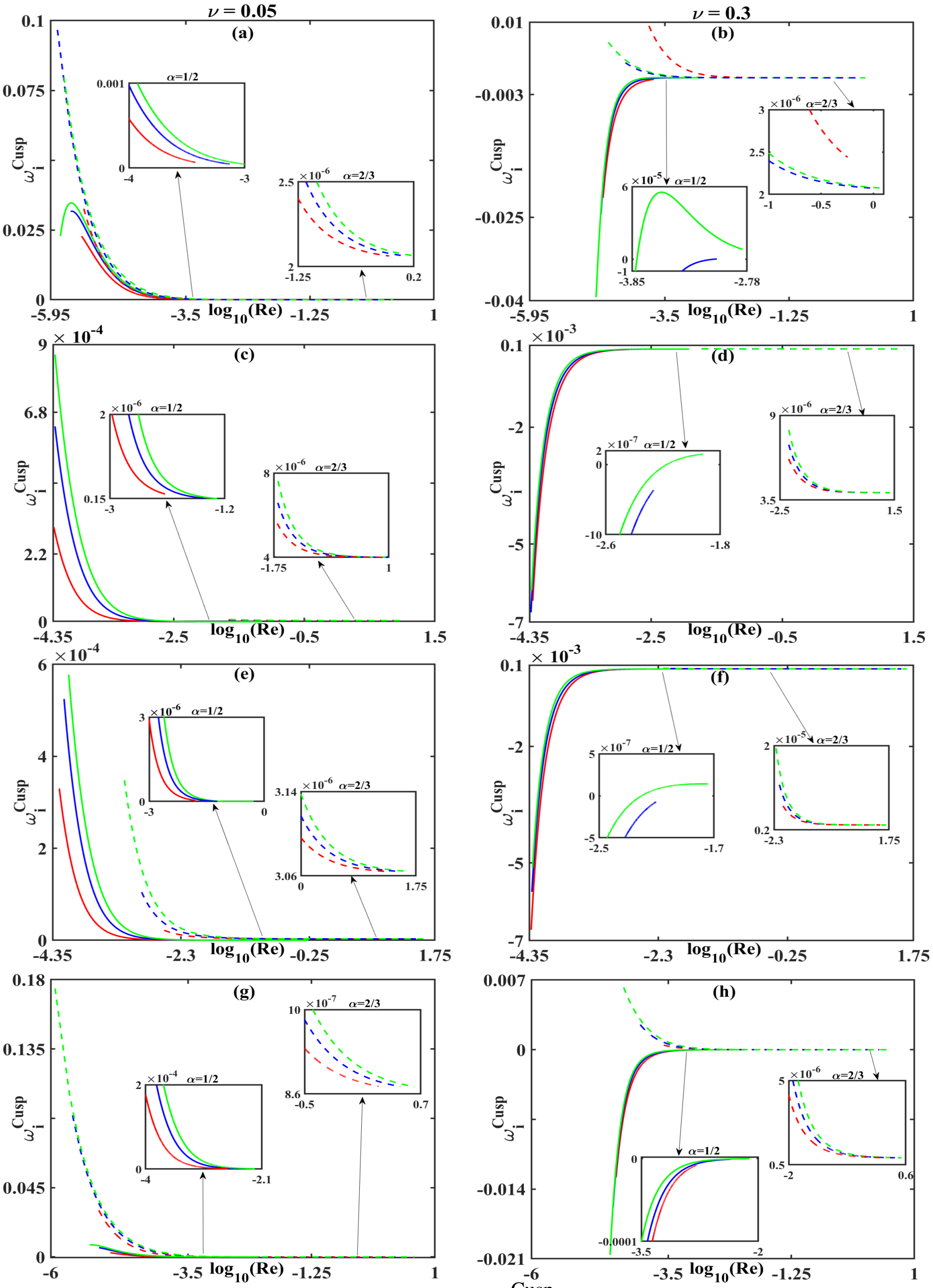

FIGURE 3.5: Absolute growth rate, ω_i^{Cusp} vs. Reynolds number for the Rouse model (solid curves) and for the Zimm's model (dashed curves), evaluated at $We = 15.0, 25.0, 35.0$ (red, blue and green curves, respectively), viscosity ratios, $\nu = 0.05$ (left column) and $\nu = 0.3$ (right column) and at transverse spatial locations: (a, b) $y = 0.2$, (c, d) $y = 0.5$, (e, f) $y = 0.7$ and (g, h) $y = 0.9$.

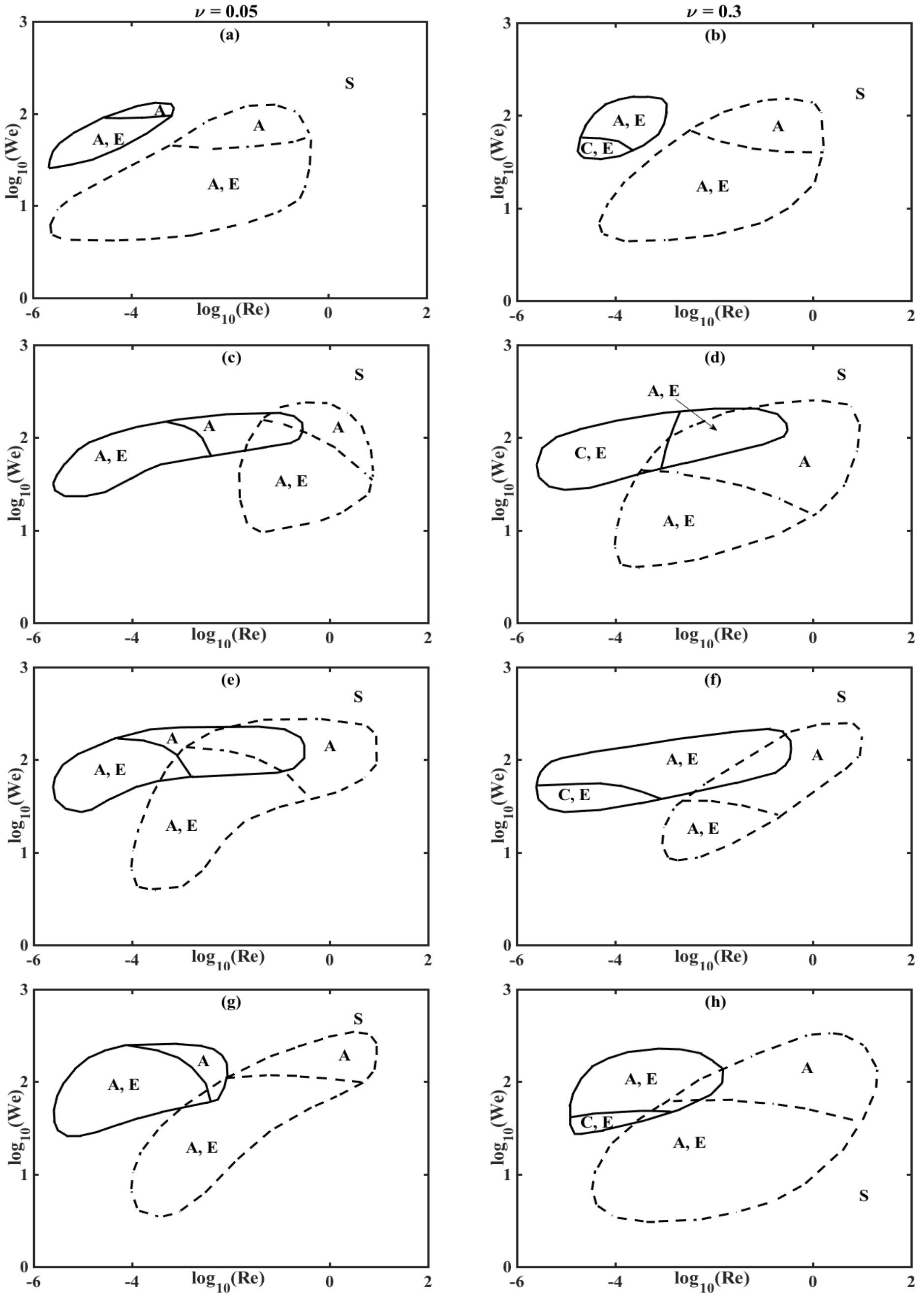

FIGURE 3.6: Viscoelastic subdiffusive stability phase diagram in the $Re - We$ parametric space for the Rouse model (solid curves) and for the Zimm's model (dashed curves), evaluated at transverse spatial locations: (a, b) $y = 0.2$, (c, d) $y = 0.5$, (e, f) $y = 0.7$ and (g, h) $y = 0.9$ and at fixed values of viscosity ratios, $\nu = 0.05$ (left column) and $\nu = 0.3$ (right column).

A notably ‘abnormal’ feature in the phase diagrams (3.6) is the presence of temporal stability at high inertia (i. e., $Re \geq 55$). While the in silico studies of the classical Oldroyd-B channel flows indicate the appearance of temporal instability for Reynolds number as low as $Re \sim 50$ (Khalid et al., 2021), temporal stability at high fluid inertia for viscoelastic flows is only recognized in experimental realizations (until now). For example, Riley (Riley, Hak, and Metcalfe, 1988) reported an elasticity-induced flow stabilization of viscoelastic fluids coated over compliant surfaces at a fairly high Reynolds number ($Re \sim 4000$). In a separate study involving ethanol gel fuels, elastic stabilization at a high shear rate was attributed due to an abnormally high second normal stress difference (Nandagopalan et al., 2018). Viscoelastic flow stabilization at higher values of *Re*, in tapered microchannels, was explained due to the presence of wall effects (Zarabadi, 2019). In another in vitro study, a biofilm deacidification created a non-homogeneous environment for molecular diffusion, leading to a ‘subdiffusive effect’ with hindered flow rates (Zarabadi, Charette, and Greener, 2018). These in vitro studies not only corroborate our numerical outcome, especially establishing the emergence of temporally stable region at high inertia, but also highlight the potential of fractional calculus in effectively capturing the flow-instability transition in subdiffusive flows.

3.8 Conclusion

This chapter addresses the temporal and the spatiotemporal linear stability analyses of viscoelastic, subdiffusive, plane Poiseuille flow in the limit of low to moderate Reynolds number and moderate to high Weissenberg number. Section 3.2, 3.3 and 3.4 presented the viscoelastic, subdiffusive channel flow model, the elements of linear stability analysis and the numerical method needed to solve the resulting dispersion relation. Section 3.5 validated the model for the classical planar Poiseuille flow obeying the Oldroyd-B stress constitutive equation (Atalik and Keunings, 2002). The temporal stability analysis in Section 3.6 indicates that with decreasing order of the fractional derivative: (a) the most unstable mode decreases, (b) the peak of the most unstable mode shifts to lower values of *Re*, and (c) in particular, the peak of the most unstable mode, for the Rouse model converges towards the limit $Re \to 0$. The spatiotemporal phase diagram in Section 3.7 indicates an abnormal region of temporal stability at high fluid inertia coupled with high elasticity, due to the presence of a non-homogeneous environment with hindered flow. Although we have shown how the exponent in the subdiffusive power-law scaling of the mean square displacement of the tracer particle in the microscale is related to the fractional order of the corresponding non-linear stress constitutive equations in the continuum, the arguments presented herein are ‘phenomenological’ in nature.

Chapter 4

Conformation Tensor via Non-Euclidean Metric

4.1 Introduction

In this chapter, we seek to enhance the physical realizability of the model proposed in Chapter 3. As such, Section 4.2 of this chapter meticulously derives an alternative formulation of the model presented in Chapter 3, utilizing the vorticity and stream-function framework. This novel approach employs a newly defined tensor, termed the "conformation tensor," which is physically more realizable. Previous approaches to analyze the polymer dynamics in dilute solutions have been to utilize the statistics of polymer forces (Dubief et al., 2005) and torques (Kim and Sureshkumar, 2013). However, a more appropriate quantity to probe the polymer deformation history is the conformation tensor, $\mathscr{C}$, a second-order positive definite tensor which is obtained by averaging overall molecular realizations, the dyad formed by the polymer end-to-end vector (Bird, Armstrong, and Hassager, 1987), which is related to the elasticity tensor $\mathbf{A}$ as $\mathscr{C} = We\mathbf{A} + \mathbf{I}$. The trace of $\mathscr{C}$ (denoted from here onwards as $\mathrm{tr}\mathscr{C}$) is commonly used in literature to analyze $\mathscr{C}$ since (i) it is equal to the sum of its principal stretches and is, therefore, a measure of the polymer deformation (Sureshkumar, Beris, and Handler, 1997), (ii) it is proportional to the elastic energy in purely Hookean constitutive models of the polymers (Beris and Edwards, 1994). However, $\mathrm{tr}\mathscr{C}$ is not a sufficiently complete descriptor of polymer deformation. For example, Berris (Beris and Edwards, 1994) found that the mean of $\mathrm{tr}\mathscr{C}$ can increase with increasing elasticity without a commensurate effect on the mean velocity profile. This behaviour arises because the mean stress deficit is not a function of any of the normal components of $\mathscr{C}$. This example highlights the importance of simultaneously considering all of the components of $\mathscr{C}$ in order to arrive at a complete picture of the polymer deformation and its effect on the velocity field. The fluctuating conformation tensor, $\mathscr{C}'$ (obtained by subtracting the mean conformation tensor, $\overline{\mathscr{C}}$ from instantaneous tensor $\mathscr{C}$) and its moments, provide one method to obtain relevant higher-order statistical descriptions of $\mathscr{C}$. However, this fluctuating tensor is not guaranteed to be physically realizable since (i) whenever $\mathrm{tr}\mathscr{C}' \leq 0$, this implies negative material deformation and this tensor loses positive-definiteness, and (ii) equally probable states of contraction ($\mathrm{tr}\mathscr{C} \in (0,1)$) and expansion ($\mathrm{tr}\mathscr{C} \in (1,\infty)$) would be described by fluctuations with very different magnitudes. A more appealing way to evaluate fluctuations in $\mathscr{C}$ is to use $\log\mathscr{C}$ because the logarithm of a positive definite matrix is a symmetric matrix and the set of symmetric matrices form a vector space (Bhatia, 2015). While

$\log\mathscr{C}$ has been an object of interest in some studies of viscoelastic flows (Fattal and Kupferman, 2004), two additional difficulties arise in using $\log\mathscr{C}$. First, the mean value of $\mathscr{C}$, or $\overline{\mathscr{C}}$, is not equal to $e^{\log\overline{\mathscr{C}}}$ implying that the effect of the polymer stress on the mean momentum balance requires all statistical moments of $\log\mathscr{C}$, even when the polymer stress is a linear function of $\mathscr{C}$. A second difficulty is that, in general, $e^{\log\overline{\mathscr{C}}+(\log\mathscr{C}')} \neq e^{\log\overline{\mathscr{C}}}\cdot e^{(\log\mathscr{C}')}$, which implies that there is no way to associate $\log\mathscr{C}'$ with a physical polymer deformation. Thus, this chapter is dedicated to the development of an alternate tensor from the polymer conformation tensor $\mathscr{C}$ as well as a formal way to visualize this new tensor for sub-diffusive flows. Section 4.3 delves into the introduction of the "structure tensor." Through this exploration, we unveil the description of three scalar invariants belonging to this structure tensor via the development of a geodesic on the Riemannian manifold. Section 4.4 includes the three scalar measures that encapsulate essential insights for quantitative analysis and interpretation. Section 4.5 embarks an outline of the weakly nonlinear perturbation analysis, followed by some concluding remarks in section 4.6.

4.2 Mathematical Model: Vorticity-Streamfunction Formulation

In this section, we outline the model governing the incompressible, sub-diffusive dynamics of a planar (2D) viscoelastic channel flow for polymer melts. The derivation of the model and the linear stability analysis for such flows is reported in chapter 3 (Chauhan, Bansal, and Sircar, 2023). For incompressible, two-dimensional flows with constant fluid properties, the equations (3.17) can be simplified by introducing the streamfunction ψ and vorticity Ω as dependent variables. Vorticity is a measure of the local rotation of a fluid element. It is defined as the curl of the fluid velocity vector. In two-dimensional flows, vorticity has only one non-zero component, which points out of the plane of the flow. Mathematically, it can be expressed as:

$$\Omega = (\nabla\times\mathbf{v})\cdot\hat{k} = \frac{\partial v}{\partial x} - \frac{\partial u}{\partial y} \tag{4.1}$$

The streamfunction ψ is a scalar function that is defined in such a way that its partial derivatives yield the horizontal and vertical velocity components and the continuity equation is identically satisfied. Given $\mathbf{v} = (u, v)$,

$$u = \frac{\partial\psi}{\partial y}, \qquad v = -\frac{\partial\psi}{\partial x} \tag{4.2}$$

We summarize the model (3.17) into the streamfunction-vorticity formulation and in terms of the conformation tensor $\mathscr{C}$. Consider the component form of equation (3.17b), given by,

$$Re\left[\frac{\partial^\alpha u}{\partial t^\alpha} + u\frac{\partial u}{\partial x} + v\frac{\partial u}{\partial y}\right] = \nu\left[\frac{\partial^2 u}{\partial x^2} + \frac{\partial^2 u}{\partial y^2}\right] + \frac{(1-\nu)}{We}\left[\frac{\partial\mathscr{C}_{11}}{\partial x} + \frac{\partial\mathscr{C}_{12}}{\partial y}\right], \tag{4.3a}$$

$$Re\left[\frac{\partial^\alpha v}{\partial t^\alpha} + u\frac{\partial v}{\partial x} + v\frac{\partial v}{\partial y}\right] = \nu\left[\frac{\partial^2 v}{\partial x^2} + \frac{\partial^2 v}{\partial y^2}\right] + \frac{(1-\nu)}{We}\left[\frac{\partial\mathscr{C}_{12}}{\partial x} + \frac{\partial\mathscr{C}_{22}}{\partial y}\right]. \tag{4.3b}$$

Differentiating equation (4.3b) partially with respect to x, and differentiating equation (4.3a) partially with respect to y, and subtracting (assume sufficient smoothness to permit changing the order of differentiation), we get,

$$\begin{aligned} &Re\left[\frac{\partial^\alpha}{\partial t^\alpha}\left(\frac{\partial v}{\partial x}-\frac{\partial u}{\partial y}\right)+\left(u\frac{\partial}{\partial x}+v\frac{\partial}{\partial y}\right)\left(\frac{\partial v}{\partial x}-\frac{\partial u}{\partial y}\right)\right] \\ &=\nu\left[\frac{\partial^2}{\partial x^2}\left(\frac{\partial v}{\partial x}-\frac{\partial u}{\partial y}\right)+\frac{\partial^2}{\partial y^2}\left(\frac{\partial v}{\partial x}-\frac{\partial u}{\partial y}\right)\right] \\ &+\frac{(1-\nu)}{We}\left[\frac{\partial^2\mathscr{C}_{12}}{\partial x^2}-\frac{\partial^2\mathscr{C}_{12}}{\partial y^2}+\frac{\partial^2}{\partial x\partial y}(\mathscr{C}_{22}-\mathscr{C}_{11})\right]. \end{aligned} \tag{4.4}$$

Using the definition of vorticity, we get the Poisson Equation,

$$\Omega=\frac{\partial v}{\partial x}-\frac{\partial u}{\partial y}=-\frac{\partial^2\psi}{\partial x^2}-\frac{\partial^2\psi}{\partial y^2}. \tag{4.5}$$

Changing $\mathbf{A}=\dfrac{\mathscr{C}-\mathbf{I}}{We}$ in equation (3.17c), we get,

$$\frac{\partial^\alpha}{\partial t^\alpha}\left(\frac{\mathscr{C}-\mathbf{I}}{We}\right)+\mathbf{v}\cdot\nabla\left(\frac{\mathscr{C}-\mathbf{I}}{We}\right)-(\nabla\mathbf{v})^T\left(\frac{\mathscr{C}-\mathbf{I}}{We}\right)-\left(\frac{\mathscr{C}-\mathbf{I}}{We}\right)\nabla\mathbf{v}=\frac{\mathbf{D}-\left(\dfrac{\mathscr{C}-\mathbf{I}}{We}\right)}{We}, \tag{4.6}$$

which implies

$$\frac{\partial^\alpha\mathscr{C}}{\partial t^\alpha}+\mathbf{v}\cdot\nabla\mathscr{C}-(\nabla\mathbf{v})^T\mathscr{C}+(\nabla\mathbf{v})^T-\mathscr{C}(\nabla\mathbf{v})+(\nabla\mathbf{v})=(\nabla\mathbf{v})+(\nabla\mathbf{v})^T-\left(\frac{\mathscr{C}-\mathbf{I}}{We}\right). \tag{4.7}$$

Using equations (4.4), (4.5) and (4.7), we obtain the model in vorticity-streamfunction form, as

$$Re\left[\frac{\partial^\alpha\Omega}{\partial t^\alpha}+\mathbf{v}\cdot\nabla\Omega\right]=\nu\nabla^2\Omega+\frac{(1-\nu)}{We}\nabla\times\nabla\cdot\mathscr{C}, \tag{4.8a}$$

$$\nabla^2\psi=-\Omega, \tag{4.8b}$$

$$\frac{\partial^\alpha\mathscr{C}}{\partial t^\alpha}+\mathbf{v}\cdot\nabla\mathscr{C}-(\nabla\mathbf{v})^T\mathscr{C}-\mathscr{C}\nabla\mathbf{v}=\frac{\boldsymbol{I}-\mathscr{C}}{We}, \tag{4.8c}$$

where $\dfrac{\partial^\alpha f(\mathbf{x},t)}{\partial t^\alpha}$ denotes the Caputo fractional derivative of order α (Podlubny, 1999) with respect to t defined by

$$\frac{\partial^\alpha f(\mathbf{x},t)}{\partial t^\alpha}=\frac{1}{\Gamma(1-\alpha)}\int_0^t\frac{dt'}{(t-t')^\alpha}\frac{\partial f(\mathbf{x},t')}{\partial t'},\qquad 0<\alpha<1, \tag{4.9}$$

and the operators $\nabla(\cdot)$ and $\nabla^2(\cdot)$ in equation (4.8a), are (integer order) gradient and Laplacian operators in $\mathbb{R}^2$. Note that equation (4.8c) represents the fractional version of the regular Oldroyd-B model for viscoelastic fluids (Sircar and Bansal, 2019) in terms of the conformation tensor $\mathscr{C}$ obtained from the equation for elasticity tensor $\mathbf{A}$ using the relation $\mathscr{C}=We\mathbf{A}+I$ (3.17).

From the perspective of continuum mechanics, $\mathscr{C}$, is the Finger tensor associated with polymer deformation (Beris and Edwards, 1994), such that

$$\mathscr{C} = \boldsymbol{F}\boldsymbol{F}^T, \tag{4.10}$$

where $\boldsymbol{F} = \boldsymbol{F}(t)$ is the instantaneous deformation gradient tensor. If the spatial coordinates in the micro-structure are given by $\boldsymbol{r} = \boldsymbol{r}(\boldsymbol{r}_0, t)$ where $\boldsymbol{r}_0$ are the coordinates at equilibrium, then $\boldsymbol{F} = \partial\boldsymbol{r}/\partial\boldsymbol{r}_0$. In other words, a vector $d\boldsymbol{r}_0$ deforms to $d\boldsymbol{r} = \boldsymbol{F}d\boldsymbol{r}_0$ under the deformation, $\boldsymbol{F}$.

4.3 Dynamics of Structure Tensor

Although the mathematical results outlined in this chapter are well-established results in advanced matrix analysis textbooks (Lang, 2001; Bhatia, 2015), to the author's best knowledge, they have not been used to evaluate the hydrodynamics of sub-diffusive flows. Here, we aim to (i) derive an appropriate tensor (or the so-called 'structure tensor') that describes the polymer deformation in a physically realizable manner, (ii) derive appropriate scalar measures associated with the structure tensor, and (iii) corroborate our theory developed in aim-(i) and (ii) through regular perturbation analysis and fully nonlinear simulations. The caveats in the conformation tensor outlined above (namely, the loss of positive definiteness in the arithmetic compilation of fluctuations and unequal measure for equally probable states representing contraction and expansion) enforce us to adopt a different framework to capture polymer deformation in sub-diffusive flows. We begin by denoting the general linear group of degree n, which is the set of all $n \times n$ invertible matrices, as $\boldsymbol{GL}_n$.

Definition 8 *Define the structure-preserving group action of $\boldsymbol{GL}_n$ on a set $\mathbf{V}_n \subseteq \mathbb{R}^{n\times n}$ as,*

$$[\boldsymbol{B}]_{\boldsymbol{A}} \equiv \boldsymbol{A}\boldsymbol{B}\boldsymbol{A}^T,$$

where $\boldsymbol{A} \in \boldsymbol{GL}_n$ and $\boldsymbol{B} \in \mathbf{V}_n$.

Using definition (8), we find that equation (4.10) reduces to

$$\mathscr{C} = [\boldsymbol{I}]_{\boldsymbol{F}}. \tag{4.11}$$

Let $\overline{\mathscr{C}}$ be the mean conformation tensor (or the conformation tensor associated with the flow at equilibrium, then we assume that $\mathscr{C}$ is similar to $\overline{\mathscr{C}}$ under the group action (8) for any rotation matrix $\boldsymbol{S} \in \boldsymbol{SO}_n \subseteq \boldsymbol{GL}_n$, where $\boldsymbol{SO}_n$ represents the $n \times n$ special orthogonal group of rotation matrices.

Similarly, define $\overline{\boldsymbol{F}} \in \boldsymbol{GL}_n$ as the deformation gradient tensor associated with the mean configuration such that,

$$\overline{\mathscr{C}} = \overline{\boldsymbol{F}}\overline{\boldsymbol{F}}^T. \tag{4.12}$$

We remark that $\overline{\boldsymbol{F}}$ is non-unique since it can be represented as

$$\overline{\boldsymbol{F}} = \overline{\mathscr{C}}^{1/2}\boldsymbol{S}, \tag{4.13}$$

for any $\boldsymbol{S} \in \boldsymbol{SO}_3$. $\overline{\mathscr{C}}^{1/2}$ is the unique matrix square-root, found exclusively in terms of $\overline{\mathscr{C}}$ and its invariants (i. e., its trace and determinants) using an application of the representation theorem (Bhatia, 2015). Since all we require is that the $\det \overline{\boldsymbol{F}} > 0$ (in order to maintain the positive definiteness of $\overline{\mathscr{C}}$), we choose $\boldsymbol{S} = \boldsymbol{I}$ in equation (4.13).

Given $\overline{\boldsymbol{F}}$ satisfying equation (4.13), we can decompose the instantaneous deformation gradient tensor $\boldsymbol{F}$ and $\overline{\boldsymbol{F}}$ by considering successive transformations on the vector $d\boldsymbol{r}_0$ as,

$$d\boldsymbol{r} = \boldsymbol{F} d\boldsymbol{r}_0 = \overline{\boldsymbol{F}} \mathscr{L} d\boldsymbol{r}_0, \tag{4.14}$$

where $\mathscr{L} = \overline{\boldsymbol{F}}^{-1} \boldsymbol{F}$ is the tensor describing fluctuations away from the mean configuration, denoted as fluctuating deformation gradient tensor. Alternatively, substituting $\boldsymbol{F} = \overline{\boldsymbol{F}} \mathscr{L}$ in equation (4.10) and utilizing definition (8), we arrive at the following definition,

Definition 9 (Structure tensor) *Define $\mathscr{G}$ such that*

$$\mathscr{C} = \overline{\boldsymbol{F}} \mathscr{G} \overline{\boldsymbol{F}}^T = [\mathscr{G}]_{\overline{\boldsymbol{F}}},$$

where $\mathscr{G} = \mathscr{L}\mathscr{L}^T$.

The fluctuating conformation tensor, $\mathscr{C}' (= \mathscr{C} - \overline{\mathscr{C}})$ is related to the structure tensor as follows,

$$\mathscr{C}' = [\mathscr{G} - \boldsymbol{I}]_{\overline{\boldsymbol{F}}}. \tag{4.15}$$

Using definition (9) in equation (4.8c) and pre multiplying (post multiplying) the resultant equation by $\overline{\boldsymbol{F}}^{-1}$ ($\overline{\boldsymbol{F}}^{-T}$) and noting that $\mathscr{G}$ is a symmetric tensor, we arrive at the following equation governing the dynamics of structure tensor,

$$\frac{\partial^\alpha \mathscr{G}}{\partial t^\alpha} + \mathbf{v} \cdot \nabla \mathscr{G} = \mathscr{G} \mathfrak{F}(\mathbf{v}) + \mathfrak{F}(\mathbf{v})^T \mathscr{G} - \mathscr{M} \tag{4.16}$$

which replaces equation (4.8c) in the viscoelastic sub-diffusive model (4.8). The functions, $\mathfrak{F}(\mathbf{v}) = \overline{\boldsymbol{F}}^T \nabla \mathbf{v} \overline{\boldsymbol{F}}^{-T} - \left(\overline{\boldsymbol{F}}^{-1} (\mathbf{v} \cdot \nabla) \overline{\boldsymbol{F}} \right)^T$, and $\mathscr{M} = \dfrac{1}{We} \left(\mathscr{G} - \left(\overline{\boldsymbol{F}}^T \overline{\boldsymbol{F}} \right)^{-1} \right)$.

4.4 Scalar Invariants via a Non-Euclidean Geodesic

The tensorial nature of $\mathscr{G}$ renders the quantification of the fluctuating conformation tensor, a difficult task. By utilizing $\mathrm{tr}\mathscr{G}$, Berris (Beris and Edwards, 1994) made an initial attempt to characterize polymer deformation in the Oldroyd-B model by defining a 'elastic potential energy'. Elastic energy was an insufficient descriptor in characterizing polymer deformation due to (a) its dependence on the choice of the particular constitutive model, and (b) elastic energy was found to be the same for a family of conformation tensors with identical trace but variable determinant. We instead evolve an approach to characterize deformation using the inherent structure of the tensor $\mathscr{G}$.

Any scalar characterization of $\mathscr{G}$ can be naively developed as a function of its three principle invariants, i.e., trace, dyadic product of eigenvalues and determinant. However, even for simple cases (such as the isotropic case) the invariants are bounded between 0 and 1 (1 and ∞) for compression with respect to $\overline{\mathscr{C}}$ (expansion with respect to $\overline{\mathscr{C}}$). This asymmetric characterization is undesirable. Further, the statistical moments of the invariants vary over several orders of magnitude, rendering these moments as uninformative predictors of polymer stretching. The above-mentioned problems arise because the set of $n \times n$ positive definite matrices (denoted with $\boldsymbol{PS}_n$ in subsequent discussion) do not form a vector space, and thus, the Euclidean notion of translation and distances are irrelevant. Instead, we exploit the Riemannian structure of $\boldsymbol{PS}_n$ to formulate alternative scalar measures of $\mathscr{G}$.

$\boldsymbol{PS}_n$ is a Hilbert space with inner product given by $\langle \boldsymbol{A}, \boldsymbol{B} \rangle := \mathrm{tr}\,(\boldsymbol{A}^T \boldsymbol{B})$, and has an induced norm $\|\boldsymbol{A}\|_{\boldsymbol{X}} = \left(\mathrm{tr}\left(\boldsymbol{X}^{-1}\boldsymbol{A}^T\boldsymbol{X}^{-1}\boldsymbol{A}\right)\right)^{1/2}$, where $\boldsymbol{X} \in \boldsymbol{PS}_n$. Furthermore, since $\boldsymbol{PS}_n$ is an open subset of the space of $n \times n$ real-valued matrices, it is a differentiable manifold. The tangent space at every point to this matrix manifold is the space of symmetric matrices. However, $\boldsymbol{PS}_n$ can be transformed into a Riemannian manifold by defining the geodesic via the inner product on the tangent space at every point. The next set of results forms the requisite machinery to formulate this geodesic, which will be needed to define the scalar invariants of $\mathscr{G}$.

Consider a parametrized curve on $\boldsymbol{PS}_n$ connecting points $\boldsymbol{X}, \boldsymbol{Y} \in \boldsymbol{PS}_n$. That is $P : [0,1] \to \boldsymbol{PS}_n$ with $P(0) = \boldsymbol{X}$ and $P(1) = \boldsymbol{Y}$. The distance, in the sense of the Riemannian metric, traversed on the manifold along the curve $P = P(r)$ is given by:

$$\ell_P(r) = \int_0^r \left\| \frac{dP(r')}{dr'} \right\|_{P(r')} dr'.$$

ℓ_P is then affine invariant.

Lemma 1 (Affine invariance (Bhatia, 2015)) *For every positive definite matrix* $\boldsymbol{A}$ *and differentiable path* P *on the Riemannian manifold of positive definite matrices, we have:*

$$\ell_P = \ell_{[P]_{\boldsymbol{A}}},$$

where $[\cdot]_{\boldsymbol{A}}$ *denotes an action under* $\boldsymbol{A}$ *of the form* $\boldsymbol{A}^T\boldsymbol{P}\boldsymbol{A}$.

Proof 1 *We use the definition of the norm* $\|\cdot\|$ *as stated above and the commutativity of the trace of the matrix product, to arrive at,*

$$\begin{aligned}
&\left\| \left(\boldsymbol{A}^T P(r) \boldsymbol{A}\right)^{-1/2} \left(\boldsymbol{A}^T P(r) \boldsymbol{A}\right)' \left(\boldsymbol{A}^T P(r) \boldsymbol{A}\right)^{-1/2} \right\|_{\boldsymbol{I}} \\
&= \left(\mathrm{tr}\left(\left(\boldsymbol{A}^T P(r) \boldsymbol{A}\right)^{-1} \left(\boldsymbol{A}^T P(r) \boldsymbol{A}\right)' \left(\boldsymbol{A}^T P(r) \boldsymbol{A}\right)^{-1} \left(\boldsymbol{A}^T P(r) \boldsymbol{A}\right)'\right)\right)^{1/2} \\
&= \left(\mathrm{tr}\,\boldsymbol{A}^{-1} (P)^{-1}(r) P'(r) (P)^{-1}(r) P'(r) \boldsymbol{A}\right)^{1/2} \\
&= \left(\mathrm{tr}\,(P)^{-1}(r) P'(r) (P)^{-1}(r) P'(r)\right)^{1/2} \\
&= \left\| (P)^{-1/2}(r) P'(r) (P)^{-1/2}(r) \right\|_{\boldsymbol{I}},
\end{aligned}$$

where we have used that $\|d\boldsymbol{X}\|_{\boldsymbol{X}} = \left\|\boldsymbol{X}^{-1/2} d\boldsymbol{X}\boldsymbol{X}^{-1/2}\right\|_{\boldsymbol{I}} = \left(tr\left(\boldsymbol{X}^{-1} d\boldsymbol{X}\right)^2\right)^{1/2}$. *The proof is completed by integrating both sides of this equality over* r *to obtain that:*

$$\ell_P = \int_0^r \left\| \frac{dP(r')}{dr'} \right\|_{P(r')} dr' = \int_0^r \left\| \frac{dP_{[A]}(r')}{dr'} \right\|_{P_{[A]}(r')} dr' = \ell_{[P]_{\boldsymbol{A}}}.$$

Using 1, we can define $d(\boldsymbol{X},\boldsymbol{Y})$, (or the geodesic distance between $\boldsymbol{X}$ and $\boldsymbol{Y}$) as the infimum of $\ell_P(1)$ over all possible curves P connecting $\boldsymbol{X}$ and $\boldsymbol{Y}$,

Definition 10

$$d(\boldsymbol{X},\boldsymbol{Y}) = \inf_P \{\ell_P(1) \,|\, P(r) \in \boldsymbol{PS}_n, P(0) = \boldsymbol{X}, P(1) = \boldsymbol{Y}.\}$$

Note that the Hopf-Rinow theorem guarantees the existence and uniqueness of such a geodesic. The next set of three results allows the construction of this geodesic.

Theorem 3 (Exponential metric increasing property (Lang, 2001)) *For any two real symmetric matrices $\boldsymbol{X}$ and $\boldsymbol{Y}$, we have that:*

$$\|\boldsymbol{X}-\boldsymbol{Y}\|_{\boldsymbol{I}} \leq d(e^{\boldsymbol{X}}, e^{\boldsymbol{Y}}), \tag{4.17}$$

Proof 2 *In order to demonstrate the proof, we wish to show the following inequality,*

$$\|\boldsymbol{X}-\boldsymbol{Y}\|_{\boldsymbol{I}} \leq \left\| e^{-\boldsymbol{A}/2}\left(De^{\boldsymbol{A}}(\boldsymbol{X}-\boldsymbol{Y})\right)e^{-\boldsymbol{A}/2} \right\|_{\boldsymbol{I}} \tag{4.18}$$

where $\boldsymbol{A}$ is any real symmetric matrix, $e^{-\boldsymbol{A}}$ is the exponential map evaluated at the point $\boldsymbol{A}$ in the Riemannian manifold of symmetric matrices, and $De^{\boldsymbol{A}}(\boldsymbol{X}-\boldsymbol{Y})$ is the derivative of the exponential map at the point $\boldsymbol{A}$ evaluated on the matrix $\boldsymbol{X}-\boldsymbol{Y}$ and defined as follows,

Definition 11

$$De^{\boldsymbol{H}}(\boldsymbol{K}) := \lim_{t\to 0} \frac{e^{\boldsymbol{H}+t\boldsymbol{K}} - e^{\boldsymbol{H}}}{t}.$$

for any matrices $\boldsymbol{H}$ and $\boldsymbol{K}$. Using the fact that for any real symmetric matrices $\boldsymbol{X}$ and $\boldsymbol{Y}$, the eigenvalues of $\boldsymbol{XY}$ are the same as those of $\boldsymbol{YX}$ and that $\|\boldsymbol{XY}\|_{\boldsymbol{I}} \leq \|\boldsymbol{YX}\|_{\boldsymbol{I}}$, inequality (4.18) can be transformed into the following inequality,

$$\|\boldsymbol{X}-\boldsymbol{Y}\|_{\boldsymbol{I}} \leq \left\| \left(De^{\boldsymbol{A}}(\boldsymbol{X}-\boldsymbol{Y})\right)e^{-\boldsymbol{A}} \right\|_{\boldsymbol{I}}, \tag{4.19}$$

and the exponential metric increasing property (4.17) follows from inequality (4.19), by integrating from $\boldsymbol{X}$ to the point $\boldsymbol{Y}$ along the geodesic (10).

Thus, in order to prove inequality (4.18) we shall equivalently show for a real symmetric matrix, $\boldsymbol{B} = (\boldsymbol{X}-\boldsymbol{Y})$ that,

$$\|\boldsymbol{B}\|_{\boldsymbol{I}} \leq \left\| e^{-\boldsymbol{A}/2}\left(De^{\boldsymbol{A}}(\boldsymbol{B})\right)e^{-\boldsymbol{A}/2} \right\|_{\boldsymbol{I}}, \tag{4.20}$$

and to show the proof of inequality (4.20), we deploy the following formula (abridged from equation (6.42) in (Bhatia, 2015)),

$$De^{\boldsymbol{A}}(\boldsymbol{B}) = \int_0^1 e^{t\boldsymbol{A}}\boldsymbol{B}e^{(1-t)\boldsymbol{A}}dt. \tag{4.21}$$

Note that the logarithmic mean of two positive numbers a, b is given by,

$$L(a,b) = \frac{a-b}{\log a - \log b} = \int_0^1 a^t b^{1-t} dt. \tag{4.22}$$

Further, for any positive definite matrix $\boldsymbol{R}$ and any real symmetric matrix $\boldsymbol{X}$, we have,

$$\left\| \boldsymbol{R}^{1/2} \boldsymbol{X} \boldsymbol{R}^{1/2} \right\|_{\boldsymbol{I}} \leq \left\| \int_0^1 \boldsymbol{R}^t \boldsymbol{X} \boldsymbol{R}^{1-t} dt \right\|_{\boldsymbol{I}}. \tag{4.23}$$

Inequality (4.23) can be obtained by writing $\boldsymbol{R}$ in an orthonormal basis such that it is a diagonal matrix with entries d_i. Then the matrix on the left-hand side of inequality (4.23) has entries of the form $\sqrt{d_i d_j} x_{ij}$ while the entries of the matrix on the right-hand side of inequality (4.23) is of the form $\left(\int_0^1 d_i^t d_j^{1-t} dt \right) x_{ij}$. Thus, inequality (4.23) follows from equation (4.22), as well as the fact that the logarithmic mean of two numbers a and b is bounded below by the geometric mean,

$$\sqrt{ab} \leq \frac{a-b}{\log a - \log b}. \tag{4.24}$$

Next, let $\boldsymbol{A}$ and $\boldsymbol{B}$ be real symmetric matrices and replacing $\boldsymbol{R} \leftrightarrow e^{\boldsymbol{A}}$ and $\boldsymbol{X} \leftrightarrow \left(e^{-\boldsymbol{A}/2} \boldsymbol{B} e^{-\boldsymbol{A}/2} \right)$ in inequality (4.23), we get,

$$\begin{aligned} \|\boldsymbol{B}\|_{\boldsymbol{I}} &\leq \left\| \int_0^1 e^{t\boldsymbol{A}} \left(e^{-\boldsymbol{A}/2} \boldsymbol{B} e^{-\boldsymbol{A}/2} \right) e^{(1-t)\boldsymbol{A}} dt \right\|_{\boldsymbol{I}} \\ &= \left\| e^{-\boldsymbol{A}/2} \int_0^1 e^{t\boldsymbol{A}} \boldsymbol{B} e^{(1-t)\boldsymbol{A}} dt\, e^{-\boldsymbol{A}/2} \right\|_{\boldsymbol{I}} \\ &= \left\| e^{-\boldsymbol{A}/2} \left(De^{\boldsymbol{A}}(\boldsymbol{B}) \right) e^{-\boldsymbol{A}/2} \right\|_{\boldsymbol{I}}, \end{aligned} \tag{4.25}$$

where the last equality follows from the formula (4.21). The result (4.20) follows from the inequality (4.25).

We note that the equality in equation (4.17) is achieved when $\boldsymbol{X}$ and $\boldsymbol{Y}$ commute, and in this case, we can parametrize the geodesic, as outlined in the next result.

Proposition 10 *Let $\boldsymbol{X} = e^{\mathscr{X}}$ and $\boldsymbol{Y} = e^{\mathscr{Y}}$ be positive definite matrices such that $\boldsymbol{X}\boldsymbol{Y} = \boldsymbol{Y}\boldsymbol{X}$. Then, the exponential function maps the line segment (Bhatia, 2015),*

$$(1-r)\mathscr{X} + r\mathscr{Y}, \quad 0 \leq r \leq 1,$$

in the Euclidean space of symmetric matrices to the geodesic between $\boldsymbol{X}$ and $\boldsymbol{Y}$ on the Riemannian manifold of positive definite matrices and

$$d(\boldsymbol{X},\boldsymbol{Y}) = \|\mathscr{X} - \mathscr{Y}\|_{\boldsymbol{I}}. \tag{4.26}$$

Proof 3 *It is enough to show that the path given by,*

$$P(r) = e^{((1-r)\mathscr{X}+r\mathscr{Y})}, \quad 0 \le r \le 1, \tag{4.27}$$

is the unique path of shortest length joining $\boldsymbol{X}$ *and* $\boldsymbol{Y}$ *in the space of symmetric matrices using the following metric,*

$$d(\boldsymbol{X},\boldsymbol{Y}) = \inf\{\ell_P | P \textit{ is a path from } \boldsymbol{X} \textit{ to } \boldsymbol{Y}.\} \tag{4.28}$$

Adopting the following parametrization of the path, $P(r) = \boldsymbol{X}^{1-r}\boldsymbol{Y}^r$ *as well as the commutativity of* $\boldsymbol{X}$ *and* $\boldsymbol{Y}$*, we have,*

$$P'(r) = (\mathscr{Y} - \mathscr{X})P(r). \tag{4.29}$$

Further, using the definition of ℓ_P *stated in (1), we have that,*

$$\ell_P = \int_0^1 \|\mathscr{X} - \mathscr{Y}\|_{\boldsymbol{I}}\, dr' = \|\mathscr{X} - \mathscr{Y}\|_{\boldsymbol{I}}. \tag{4.30}$$

Now, let $H(r)$*,* $a \le r \le b$ *be any path in the space of* $n \times n$ *symmetric matrices, and let* $Q(r) = e^{H(r)}$*. Then, by the chain rule,* $Q'(r) = D\left(e^{H(r)}\right)(H'(r))$ *(using 11). Consequently, we have that,*

$$\ell_{Q(r)} = \int_a^b \left\| \frac{dQ(r')}{dr'} \right\|_{Q(r')} dr' \ge \int_a^b \left\| \frac{dH(r')}{dr'} \right\|_{\boldsymbol{I}} dr'. \tag{4.31}$$

Applying the above result to ℓ_P *in equation (4.30), we immediately obtain that* $\|\mathscr{X} - \mathscr{Y}\|_{\boldsymbol{I}}$ *has to be the geodesic distance between* $\boldsymbol{X}$ *and* $\boldsymbol{Y}$*.*

Finally, using the affine-invariance property (1) of the Riemannian metric and noting that $\boldsymbol{I}$ commutes with every element of $\boldsymbol{PS}_n$, we arrive at the following result.

Theorem 4 *Let* $\boldsymbol{X}$ *and* $\boldsymbol{Y}$ *be positive definite matrices. There exists a unique geodesic* $\boldsymbol{X}\#_r\boldsymbol{Y}$ *on the Riemannian manifold of positive definite matrices that joins* $\boldsymbol{X}$ *and* $\boldsymbol{Y}$ *with the following parametrization (Bhatia, 2015),*

$$\boldsymbol{X}\#_r\boldsymbol{Y} = \boldsymbol{X}^{1/2}\left(\boldsymbol{X}^{-1/2}\boldsymbol{Y}\boldsymbol{X}^{-1/2}\right)^r \boldsymbol{X}^{1/2}, \tag{4.32}$$

which is natural in the sense that,

$$d(\boldsymbol{X},\boldsymbol{X}\#_r\boldsymbol{Y}) = r\,d(\boldsymbol{X},\boldsymbol{Y}), \tag{4.33}$$

for each $r \in \mathbb{R}$*. Furthermore, we have,*

$$d(\boldsymbol{X},\boldsymbol{Y}) = \left\|\log\left(\boldsymbol{X}^{-1/2}\boldsymbol{Y}X^{1/2}\right)\right\|_{\boldsymbol{I}} = \left[\sum_{i=1}^{3}\left(\log\sigma_i\left(\boldsymbol{X}^{-1}\boldsymbol{Y}\right)\right)^2\right]^{1/2}, \tag{4.34}$$

where σ_i *are the eigenvalues of the matrix* $\boldsymbol{X}^{-1}\boldsymbol{Y}$*.*

Proof 4 *Clearly, the matrices* $\boldsymbol{I}$ *and* $\boldsymbol{X}^{-1/2}\boldsymbol{Y}\boldsymbol{X}^{-1/2}$ *commute. Hence, the geodesic joining these points is naturally parameterized as:*

$$P_0(r) = \left(\boldsymbol{X}^{-1/2}\boldsymbol{Y}\boldsymbol{X}^{-1/2}\right)^r. \tag{4.35}$$

For each $\boldsymbol{A} \in GL_n$*, the transformation* $\Gamma_{\boldsymbol{A}}(P(r)) = \boldsymbol{A}^T P(r)\boldsymbol{A}$ *is an isometry (using Lemma 1). Hence, for* $\boldsymbol{A} = \boldsymbol{X}^{1/2}$*, applying the isometry* $\Gamma_{\boldsymbol{X}^{1/2}}$*, we obtain the path,*

$$P(r) = \boldsymbol{X}^{1/2}\left(P_0(r)\right)\boldsymbol{X}^{1/2} = \boldsymbol{X}^{1/2}\left(\boldsymbol{X}^{-1/2}\boldsymbol{Y}\boldsymbol{X}^{-1/2}\right)^r \boldsymbol{X}^{1/2}, \tag{4.36}$$

joining the points $\boldsymbol{X}^{1/2}\boldsymbol{I}\boldsymbol{X}^{1/2} = \boldsymbol{X}$ *and* $\boldsymbol{X}^{1/2}\boldsymbol{X}^{-1/2}\boldsymbol{Y}\boldsymbol{X}^{-1/2}\boldsymbol{X}^{1/2} = \boldsymbol{Y}$*. Because* $\boldsymbol{X}^{1/2}\boldsymbol{Y}\boldsymbol{X}^{1/2}$ *is an isometry, the path (4.36) is a geodesic joining* $\boldsymbol{X}$ *and* $\boldsymbol{Y}$*. Thus, equality (4.32) follows. Next, in order to prove the equality (4.33) we have that,*

$$\begin{aligned}
d(\boldsymbol{X}, \boldsymbol{X}\#_r\boldsymbol{Y}) &= d(\boldsymbol{X}, \boldsymbol{X}^{1/2}\left(\boldsymbol{X}^{-1/2}\boldsymbol{Y}\boldsymbol{X}^{-1/2}\right)^r \boldsymbol{X}^{1/2}) \\
&= d(\boldsymbol{X}^{-1/2}\boldsymbol{X}\boldsymbol{X}^{-1/2}, \boldsymbol{X}^{-1/2}\boldsymbol{X}^{1/2}\left(\boldsymbol{X}^{-1/2}\boldsymbol{Y}\boldsymbol{X}^{-1/2}\right)^r \boldsymbol{X}^{1/2}\boldsymbol{X}^{-1/2}) \\
&= d(\boldsymbol{I}, \left(\boldsymbol{X}^{-1/2}\boldsymbol{Y}\boldsymbol{X}^{-1/2}\right)^r) \\
&= \inf \int_0^1 \left\| \log(\boldsymbol{I}) - \log\left(\boldsymbol{X}^{-1/2}\boldsymbol{Y}\boldsymbol{X}^{-1/2}\right)^r \right\| dr \\
&= r \inf \int_0^1 \left\| \log\left(\boldsymbol{X}^{-1/2}\boldsymbol{Y}\boldsymbol{X}^{-1/2}\right) \right\| = r\, d(\boldsymbol{X}, \boldsymbol{Y}),
\end{aligned} \tag{4.37}$$

where the last equality arises as a consequence of (10) since,

$$\begin{aligned}
d(\boldsymbol{X}, \boldsymbol{Y}) &= d\left(\boldsymbol{I}, \boldsymbol{X}^{-1/2}\boldsymbol{Y}\boldsymbol{X}^{-1/2}\right) \\
&= \left\| \log \boldsymbol{I} - \log\left(\boldsymbol{X}^{-1/2}\boldsymbol{Y}\boldsymbol{X}^{-1/2}\right) \right\|_{\boldsymbol{I}} \\
&= \left\| \log\left(\boldsymbol{X}^{-1/2}\boldsymbol{Y}\boldsymbol{X}^{-1/2}\right) \right\|_{\boldsymbol{I}}.
\end{aligned} \tag{4.38}$$

Finally, from the definition of the Riemannian norm and basic linear algebra, we get that,

$$d(\boldsymbol{X}, \boldsymbol{Y}) = \left[\sum_{i=1}^{3} \left(\log \sigma_i\left(\boldsymbol{X}^{-1}\boldsymbol{Y}\right)\right)^2\right]^{1/2} = \left[\operatorname{tr}\log^2(\boldsymbol{X}^{-1/2}\boldsymbol{Y}\boldsymbol{X}^{-1/2})\right]^{1/2}, \tag{4.39}$$

where σ_i *are the eigenvalues of the matrix* $\boldsymbol{X}^{-1}\boldsymbol{Y}$*.*

We are now ready to introduce the scalar measures that can be used to quantify the structure tensor, $\mathscr{G}$. First, let us denote the matrix logarithm of $\mathscr{G}$ as $\mathscr{L}_{\mathscr{G}}$ (i. e., $\mathscr{G} = e^{\mathscr{L}_{\mathscr{G}}}$). This matrix logarithm exists, is unique (since $\mathscr{G}$ is positive definite) and has eigenvalues, which are the logarithm of the eigenvalues of $\mathscr{G}$.

4.4.1 Scalar Invariant 1: Volume Ratio

Let $\sigma_i(\mathscr{G})$ $(i = 1,2,3)$ be the eigenvalues of $\mathscr{G}$. Define the first scalar invariant as the volume ratio of fluctuations, δ_1, as

Definition 12

$$\delta_1 = \operatorname{tr} \mathscr{L}_{\mathscr{G}} = \log \det \mathscr{G} = \log \left(\frac{\det \mathscr{C}}{\det \overline{\mathscr{C}}} \right).$$

when $\delta_1 = 0$, the mean and the instantaneous conformation tensors have the same volume and when δ_1 is negative (positive), the instantaneous conformation tensor has a smaller (larger) volume than the mean volume.

4.4.2 Scalar Invariant 2: Shortest Distance from Mean

When $\mathscr{C} = \overline{\mathscr{C}}$, we have $\mathscr{G} = \mathbf{I}$. When $\mathscr{C} \neq \overline{\mathscr{C}}$, we wish to consider the shortest path between $\mathbf{I}$ and $\mathscr{G}$ as a measure of the magnitude of fluctuations. Using equation (4.39), we consider the squared geodesic distance related with this path,

Definition 13

$$\delta_2 = \operatorname{tr} \mathscr{L}_{\mathscr{G}}^2 = d^2(\mathbf{I},\mathscr{G}) = \sum_{i=1}^{3} (\log \sigma_i)^2 .$$

Using equation (4.39), we can verify that $d^2(\mathbf{I},\mathscr{G}) = d^2(\mathbf{I},\mathscr{G}^{-1})$, which implies that this squared geodesic treats both expansions and compressions identically. The affine invariance property (1) ensures that $d(\mathbf{I},\mathscr{G}) = d([\mathbf{I}]_{\mathbf{A}},[\mathscr{G}]_{\mathbf{A}})$. With $\mathbf{A} = \overline{\mathbf{F}}$, we obtain,

$$d^2(\mathbf{I},\mathscr{G}) = d^2(\overline{\mathscr{C}},[\mathscr{G}]_{\overline{F}}) = d^2(\overline{\mathscr{C}},\mathscr{C}) = d^2(\overline{\mathscr{C}}^{-1},\mathscr{C}^{-1}). \tag{4.40}$$

The last equality in equation (4.40) exhibits the fact that the metric introduced in equation (4.39), handles expansions and compressions on equal terms, unlike the regular Euclidean metric (or the Frobenius norm).

4.4.3 Scalar Invariant 3: Anisotropy Index

Following Hameduddin (Hameduddin, 2018), we define the anisotropy index, δ_3 as the squared geodesic distance between $\mathscr{G}$ and the closest isotropic tensor,

Definition 14

$$\delta_3 = \inf_a d^2(a\mathbf{I},\mathscr{G}) = \inf_a \operatorname{tr}(\mathscr{G} - (\log a)\mathbf{I})^2.$$

Through differentiation, we find that $a = \left(\prod_{i=1}^{3} \sigma_i \right)^{1/3} = (\det \mathscr{G})^{1/3}$ is the minimizing stationary point, which implies that,

$$\delta_3 = d^2((\det \mathscr{G})^{1/3}\mathbf{I},\mathscr{G}) = \delta_2 - \frac{1}{3}\delta_1^2. \tag{4.41}$$

Notice that $\delta_3 = 0$ if and only if $\delta_1^2 = 3\delta_2$, in which case $\mathscr{G}$ reduces to an isotropic tensor.

Finally, we surmise that equations (4.8a), (4.8b) and (4.16) along with definitions (9,12,13 and 14) form the complete set of equations governing the dynamics of viscoelastic sub-diffusive flows.

4.5 Perturbative Expansion for Weakly Non-linear Deformation

A weakly nonlinear expansion up to the Kth power of the velocity field is given by,

$$\Omega = \overline{\Omega} + \sum_{k=1}^{K} \varepsilon^k \Omega_k,$$

$$\psi = \overline{\psi} + \sum_{k=1}^{K} \varepsilon^k \psi_k, \tag{4.42}$$

where the superscript, $\overline{(\ )}$, denote the mean values and $\Omega_k(\boldsymbol{x},t)$, ψ_k, $(k \in [1,K])$ are the perturbed vorticities and stream-functions of the kth-order, respectively. A similar expansion for $\mathscr{G}$ is inappropriate because it is positive definite and there is no *a priori* guarantee on this property with regular arithmetic expansion. Instead, we adopt the geometric expansion by multiplicatively decomposing the fluctuating deformation gradient tensor into K separate components,

$$\mathscr{L}_{\text{Pert}} = \mathscr{L}_1 \mathscr{L}_2 \ldots \mathscr{L}_k \tag{4.43}$$

Using (9) as well as the matrix logarithm of $\mathscr{G}$ (=$\mathscr{L}_{\mathscr{G}}$), we can express the perturbed structure tensor at kth-stage of decomposition as,

$$\mathscr{G}_k^{\varepsilon^k} = \mathscr{L}_k \mathscr{L}_k^T = e^{\varepsilon^k \mathscr{L}_{\mathscr{G}_k}}, \tag{4.44}$$

where $\mathscr{L}_{\mathscr{G}_0} = \mathbf{0}$. From equation (4.43), we can associate a perturbed tensor,

$$\mathscr{L}_k = e^{\varepsilon^k \mathscr{L}_{\mathscr{G}_k}/2}. \tag{4.45}$$

At this stage, we remark that although we assume that each $\mathscr{L}_k$ is positive definite, the product of positive definite tensors, $\mathscr{L}_{\text{Pert}}$ (equation (4.43)) is not necessarily positive definite. However, since $\mathscr{L}_{\text{Pert}} \mathscr{L}_{\text{Pert}}^T = \mathscr{L}\mathscr{L}^T = \mathscr{G}$, we can show via a polar decomposition that $\mathscr{L}_{\text{Pert}} = \mathscr{L}\boldsymbol{R}$ for some rotation tensor, $\boldsymbol{R}$. Substituting equation (4.45) and (4.43) in equation (4.44), we arrive at the necessary expansion,

$$\begin{aligned}
\mathscr{G} &= e^{\varepsilon \mathscr{L}_{\mathscr{G}_1}/2} \ldots e^{\varepsilon^{K-1} \mathscr{L}_{\mathscr{G}_{K-1}}/2} e^{\varepsilon^K \mathscr{L}_{\mathscr{G}_K}} e^{\varepsilon^{K-1} \mathscr{L}_{\mathscr{G}_{K-1}}/2} \ldots e^{\varepsilon \mathscr{L}_{\mathscr{G}_1}/2}, \\
&= \boldsymbol{I} + \varepsilon \mathscr{L}_{\mathscr{G}_1} \\
&\quad + \varepsilon^2 \left(\frac{\mathscr{L}_{\mathscr{G}_1}^2}{2} + \mathscr{L}_{\mathscr{G}_2} \right) + \varepsilon^3 \left(\frac{\mathscr{L}_{\mathscr{G}_1}^3}{6} + \frac{1}{2} (\mathscr{L}_{\mathscr{G}_1} \mathscr{L}_{\mathscr{G}_2} + (\mathscr{L}_{\mathscr{G}_1} \mathscr{L}_{\mathscr{G}_2})^T) + \mathscr{L}_{\mathscr{G}_3} \right) + \ldots,
\end{aligned} \tag{4.46}$$

where the second equality in equation (4.46) makes use of the matrix exponential, $e^{\varepsilon^k \mathscr{L}_{\mathscr{G}_k}} = \sum\limits_{q=0}^{\infty} \varepsilon^{kq}\mathscr{L}_{\mathscr{G}_k}^{q}/q!$. Substituting expansions (4.42) and (4.46) in equations (4.8a), (4.8b) and (4.16), we arrive at the $\mathscr{O}(\varepsilon)$ model equations,

$$Re\left[\frac{\partial^\alpha \Omega_1}{\partial t^\alpha} + \overline{\mathbf{v}}\cdot\nabla\Omega_1 + \mathbf{v}_1\cdot\nabla\overline{\Omega}\right] = \nu\nabla^2\Omega_1 + \frac{1-\nu}{W_e}\nabla\times\nabla\cdot\left(\overline{\boldsymbol{F}}\mathscr{L}_{\mathscr{G}_1}\overline{\boldsymbol{F}}^T\right), \tag{4.47a}$$

$$\nabla^2\psi_1 = -\Omega_1, \tag{4.47b}$$

$$\frac{\partial^\alpha}{\partial t^\alpha}\mathscr{L}_{\mathscr{G}_1} + \overline{\mathbf{v}}\cdot\nabla\mathscr{L}_{\mathscr{G}_1} = 2\mathrm{sym}\left(\mathfrak{F}(\mathbf{v}_1) + \mathscr{L}_{\mathscr{G}_1}\mathfrak{F}(\overline{\mathbf{v}})\right) - \frac{1}{W_e}\mathscr{L}_{\mathscr{G}_1}, \tag{4.47c}$$

as well as the $\mathscr{O}(\varepsilon^2)$ model equations,

$$\begin{aligned} Re\Bigg[\frac{\partial^\alpha \Omega_2}{\partial t^\alpha} &+ \overline{\mathbf{v}}\cdot\nabla\Omega_2 + \mathbf{v}_2\cdot\nabla\overline{\Omega} \\ &+ \mathbf{v}_1\cdot\nabla\Omega_1\Bigg] = \nu\nabla^2\Omega_2 \\ &+ \frac{1-\nu}{W_e}\nabla\times\nabla\cdot\left(\overline{\boldsymbol{F}}\left(\frac{\mathscr{L}_{\mathscr{G}_1}^2}{2} + \mathscr{L}_{\mathscr{G}_2}\right)\overline{\boldsymbol{F}}^T\right), \end{aligned} \tag{4.48a}$$

$$\nabla^2\psi_2 = -\Omega_2, \tag{4.48b}$$

$$\begin{aligned} \frac{\partial^\alpha \mathscr{L}_{\mathscr{G}_2}}{\partial t^\alpha} + \overline{\mathbf{v}}\cdot\nabla\mathscr{L}_{\mathscr{G}_2} + \mathbf{v}_1\cdot\nabla\mathscr{L}_{\mathscr{G}_1} &= 2\,\mathrm{sym}\left(\mathfrak{F}(\mathbf{v}_2) + \mathscr{L}_{\mathscr{G}_2}\mathfrak{F}(\overline{\mathbf{v}})\right) + \frac{\mathscr{L}_{\mathscr{G}_1}^2}{2W_e} - \frac{\mathscr{L}_{\mathscr{G}_2}}{W_e} \\ &-\mathscr{L}_{\mathscr{G}_1}\mathrm{sym}\left(\mathfrak{F}(\overline{\mathbf{v}})\right)\mathscr{L}_{\mathscr{G}_1} + \mathscr{L}_{\mathscr{G}_1}\mathrm{asym}\left(\mathfrak{F}(\mathbf{v}_1)\right) \\ &-\mathrm{asym}\left(\mathfrak{F}(\mathbf{v}_1)\right)\mathscr{L}_{\mathscr{G}_1}, \end{aligned} \tag{4.48c}$$

where $\mathrm{sym}(\boldsymbol{A}) = (\boldsymbol{A}+\boldsymbol{A}^T)/2$, $\mathrm{asym}(\boldsymbol{A}) = (\boldsymbol{A}-\boldsymbol{A}^T)/2$ and $\mathbf{v}_i = (u_i, v_i) = (\frac{\partial\psi_i}{\partial y}, -\frac{\partial\psi_i}{\partial x})$.

4.5.1 Linear perturbations

As an illustration, we highlight the case of linear perturbative solutions for the 2D viscoelastic channel flow for polymer melts. A rectilinear coordinate system is used with x, y denoting the channel flow direction and the transverse direction, respectively. The origin of this coordinate system is chosen at the left end of the lower wall of the channel. The size of the domain is chosen to be $(x,y) \in \Gamma = [0,\,5]\times[0,\,1]$. The mean flow is assumed to be a plane Poiseuille flow with its variation entirely in the transverse direction, namely,

$$\mathbf{U}_0 = (y-y^2)\mathbf{e_x}, \tag{4.49}$$

where $\mathbf{e_x}$ is the unit vector along x-direction. The mean flow, $\mathbf{U}_0$, defines the mean vorticity, $\overline{\Omega} = 2y-1$, and the mean stream-function, $\overline{\psi} = \frac{y^2}{2} - \frac{y^3}{3}$. In this case, the initial conditions for the perturbed solution can be constructed via the superposition of the mean flow and the instability mode, as follows,

$$\begin{aligned}
\Omega|_{t=0} &\approx \overline{\Omega} + \varepsilon\Omega_1 = \overline{\Omega} + \varepsilon\mathscr{R}\{\widetilde{\Omega}(y)|_{t=0}e^{ikx}\},\\
\psi|_{t=0} &\approx \overline{\psi} + \varepsilon\psi_1 = \overline{\psi} + \varepsilon\mathscr{R}\{\widetilde{\psi}(y)|_{t=0}e^{ikx}\},\\
\mathscr{G}|_{t=0} &\approx \boldsymbol{I} + \varepsilon\mathscr{L}_{\mathscr{G}_1} = \boldsymbol{I} + \varepsilon\mathscr{R}\{\widetilde{\mathscr{L}_{\mathscr{G}}}(y)|_{t=0}e^{ikx}\},
\end{aligned}\tag{4.50}$$

where $(\Omega_1, \psi_1, \mathscr{L}_{\mathscr{G}_1})$ are the perturbations that are Fourier transformed in the x-direction. $\mathscr{R}\{\}$ denotes the real part of the complex valued function. The equations governing the initial conditions (4.50) are listed below. Assuming a normal mode expansion for the perturbed field, $\phi_1 = \widetilde{\phi(y)}e^{ikx}$ (where $\phi_1 = (\Omega_1, \psi_1, \mathscr{L}_{\mathscr{G}_1})$), equation (4.47) reduces to

$$Re\left((y-y^2)\widetilde{\Omega}(ik) - 2\widetilde{\psi}(ik)\right) = \nu\left(\widetilde{\Omega}(ik)^2 + \widetilde{\Omega}''\right) + \frac{1-\nu}{We}\Big(-k^2F_1F_2\widetilde{\mathscr{L}_{\mathscr{G}_{11}}} - k^2F_2^2\widetilde{\mathscr{L}_{\mathscr{G}_{12}}} - k^2F_1F_4\widetilde{\mathscr{L}_{\mathscr{G}_{12}}} - k^2F_2F_4\widetilde{\mathscr{L}_{\mathscr{G}_{22}}} - {F_1}''F_2\widetilde{\mathscr{L}_{\mathscr{G}_{11}}} - F_1{F_2}''\widetilde{\mathscr{L}_{\mathscr{G}_{11}}} - F_1F_2\widetilde{\mathscr{L}_{\mathscr{G}_{11}}}'' - F_2^{2''}\widetilde{\mathscr{L}_{\mathscr{G}_{12}}} - F_2^2\widetilde{\mathscr{L}_{\mathscr{G}_{12}}}'' - {F_1}''F_4\widetilde{\mathscr{L}_{\mathscr{G}_{12}}} - F_1{F_4}''\widetilde{\mathscr{L}_{\mathscr{G}_{12}}} - F_1F_4\widetilde{\mathscr{L}_{\mathscr{G}_{12}}}'' - {F_2}''F_4\widetilde{\mathscr{L}_{\mathscr{G}_{22}}} - F_2{F_4}''\widetilde{\mathscr{L}_{\mathscr{G}_{22}}} - F_2F_4\widetilde{\mathscr{L}_{\mathscr{G}_{22}}}'' - 2{F_1}'{F_2}'\widetilde{\mathscr{L}_{\mathscr{G}_{11}}} - 2{F_1}'F_2\widetilde{\mathscr{L}_{\mathscr{G}_{11}}}' - 2{F_1}'{F_4}'\widetilde{\mathscr{L}_{\mathscr{G}_{12}}} - 2{F_1}'F_4\widetilde{\mathscr{L}_{\mathscr{G}_{12}}}' - 2F_1{F_2}'\widetilde{\mathscr{L}_{\mathscr{G}_{11}}}' - 2F_1{F_4}'\widetilde{\mathscr{L}_{\mathscr{G}_{12}}}' - 2{F_2}'{F_4}'\widetilde{\mathscr{L}_{\mathscr{G}_{22}}} - 2{F_2}'F_4\widetilde{\mathscr{L}_{\mathscr{G}_{22}}}' - 4F_2{F_2}'\widetilde{\mathscr{L}_{\mathscr{G}_{12}}}' - 2F_2{F_4}'\widetilde{\mathscr{L}_{\mathscr{G}_{22}}}' + 2ikF_2{F_2}'\widetilde{\mathscr{L}_{\mathscr{G}_{11}}} + ikF_2^2\widetilde{\mathscr{L}_{\mathscr{G}_{11}}}' + 2ik{F_2}'F_4\widetilde{\mathscr{L}_{\mathscr{G}_{12}}} + 2ikF_2{F_4}'\widetilde{\mathscr{L}_{\mathscr{G}_{12}}} + 2ikF_2F_4\widetilde{\mathscr{L}_{\mathscr{G}_{12}}}' + 2ikF_4{F_4}'\widetilde{\mathscr{L}_{\mathscr{G}_{22}}} + ikF_4^2\widetilde{\mathscr{L}_{\mathscr{G}_{22}}}' - 2ikF_1{F_1}'\widetilde{\mathscr{L}_{\mathscr{G}_{11}}} - ikF_1^2\widetilde{\mathscr{L}_{\mathscr{G}_{11}}}' - 2ik{F_1}'F_2\widetilde{\mathscr{L}_{\mathscr{G}_{12}}} - 2ikF_1{F_2}'\widetilde{\mathscr{L}_{\mathscr{G}_{12}}} - 2ikF_1F_2\widetilde{\mathscr{L}_{\mathscr{G}_{12}}} - 2ikF_2{F_2}'\widetilde{\mathscr{L}_{\mathscr{G}_{22}}} - ikF_2^2\widetilde{\mathscr{L}_{\mathscr{G}_{22}}}'\Big),\tag{4.51a}$$

$$\widetilde{\psi}(ik)^2 + \widetilde{\psi}'' =- \widetilde{\Omega},\tag{4.51b}$$

$$(y-y^2)(ik)\widetilde{\mathscr{L}_{\mathscr{G}_{11}}} = \frac{2}{\sqrt{d}}\left(F_1F_4\widetilde{\psi}'(ik) - F_1F_2\widetilde{\psi}'' - F_2F_4\widetilde{\psi}(ik)^2 + F_2^2\widetilde{\psi}'(ik) - \widetilde{\mathscr{L}_{\mathscr{G}_{11}}}F_1F_2(1-2y) - F_2^2\widetilde{\mathscr{L}_{\mathscr{G}_{12}}}(1-2y) - \widetilde{\psi}(ik)\left(-F_4F_1' + F_2F_2'\right)\right) - \frac{\widetilde{\mathscr{L}_{\mathscr{G}_{11}}}}{We},\tag{4.51c}$$

$$(y-y^2)(ik)\widetilde{\mathscr{L}_{\mathscr{G}_{12}}} = \frac{1}{\sqrt{d}}\Big(-2F_1F_2\widetilde{\psi}'(ik) + F_1^2\widetilde{\psi}'' + F_2^2\widetilde{\psi}(ik)^2 + \widetilde{\mathscr{L}_{\mathscr{G}_{11}}}F_1^2(1-2y) + 2F_2F_4\widetilde{\psi}'(ik) - F_2^2\widetilde{\psi}'' - F_4^2\widetilde{\psi}(ik)^2 - \widetilde{\mathscr{L}_{\mathscr{G}_{22}}}F_2^2(1-2y) - \widetilde{\psi}(ik)\left(F_2F_1' - F_1F_2' - F_4F_2' + F_2F_4'\right)\Big) - \frac{\widetilde{\mathscr{L}_{\mathscr{G}_{12}}}}{We},\tag{4.51d}$$

$$(y-y^2)(ik)\widetilde{\mathscr{L}_{\mathscr{G}_{22}}} = \frac{2}{\sqrt{d}}\Big(\widetilde{\mathscr{L}_{\mathscr{G}_{12}}}F_1^2(1-2y) - F_2^2\widetilde{\psi}'(ik) + F_1F_2\widetilde{\psi}'' + F_2F_4\widetilde{\psi}(ik)^2 - F_1F_4\widetilde{\psi}'(ik) + \widetilde{\mathscr{L}_{\mathscr{G}_{22}}}F_1F_2(1-2y) - \widetilde{\psi}(ik)\left(F_2F_2' - F_1F_4'\right)\Big) - \frac{\widetilde{\mathscr{L}_{\mathscr{G}_{22}}}}{We},\tag{4.51e}$$

where we denote $\frac{d}{dy}() = ()'$ and

$$\overline{\boldsymbol{F}} = \begin{bmatrix} F_1 & F_2 \\ F_2 & F_4 \end{bmatrix} = \begin{bmatrix} \dfrac{1+\sqrt{s}}{\sqrt{2s+2\sqrt{s}}} & \dfrac{We(1-2y)}{\sqrt{2s+2\sqrt{s}}} \\ \dfrac{We(1-2y)}{\sqrt{2s+2\sqrt{s}}} & \dfrac{2s+\sqrt{s}-1}{\sqrt{2s+2\sqrt{s}}} \end{bmatrix}$$

where

$$s = 1 + We^2(1-2y)^2.$$

The solution to the boundary value problem (4.51) is found subject to the boundary conditions, $(\widetilde{\psi}(y), \widetilde{\psi'}(y)) = (0,0)$ at the rigid walls $y = 0, 1$, which is unique upto an integration constant for the stream-function perturbation (refer figure 4.1b for the solution).

An initial condition comprising of a small amplitude unstable mode will initially grow exponentially, as predicted by the linear theory. However, nonlinear effects eventually become significant since otherwise, the conformation tensor loses positive definiteness. Hence, our interest in studying linear perturbations is to find an estimate of the maximum time during which the perturbed solution can be well approximated by the linear theory, i. e., along the Euclidean manifold.

Consider an initial condition which is a perturbed base flow, $\mathscr{G}|_{t=0} = \boldsymbol{I} + \varepsilon \mathscr{L}_{\mathscr{G}}$. If we assume that the perturbed mode grows according to linear theory for some time and $\mathscr{G}$ evolves along Euclidean lines with growth rate $\omega > 0$, then $\mathscr{G}(t) = \boldsymbol{I} + \varepsilon \mathscr{L}_{\mathscr{G}} e^{\omega t}$. Suppose $\mathscr{L}_{\mathscr{G}}$ is not zero and is harmonic in the spatial direction, then $\mathscr{L}_{\mathscr{G}}$ has a strictly negative eigenvalue somewhere in the domain. This is because a harmonic perturbation leads to regions where the polymers are much more compressed than the maximum expansion, in a volumetric sense, since positive and negative additive perturbations to the mean conformation tensor, $\overline{\mathscr{C}}$, with equal magnitude are not of equal magnitude with respect to the natural norm on $\boldsymbol{PS}_3$. For positive-definiteness of $\mathscr{G}$, we require the eigenvalues, $1 + \varepsilon \sigma_i(\mathscr{L}_{\mathscr{G}}) e^{\omega t} > 0$, $(i = 1, 2, 3)$. Whenever $\sigma_i(\mathscr{L}_{\mathscr{G}}) < 0$, the dynamics induces a curvature on the evolution of the perturbed mode along $\boldsymbol{PS}_3$ before the time, t_m, when the eigenvalue of $\mathscr{G}$ crosses zero. Hence, at the point of crossing zero, this time is given by,

$$\omega t_m = -\left(\log \varepsilon + \log \max |\sigma_i(\mathscr{L}_{\mathscr{G}})|\right), \tag{4.52}$$

where $\max|\sigma_i(\mathscr{L}_{\mathscr{G}})|$ is the magnitude of the largest negative eigenvalue in the domain. Refer to chapter 3, on the instability of viscoelastic sub-diffusive channel flows (Chauhan, Bansal, and Sircar, 2023) to gain an insight on the procedure for finding, $\sigma_i(\mathscr{L}_{\mathscr{G}})$. Equation (4.52) serves as a guide for selecting the initial perturbation amplitude, ε, based on the time, t_m, i e., by reducing ε we can arbitrarily increase t_m to a desired value.

In order to compare the linear evolution of the unstable modes (equation (4.47) with initial conditions (4.50)) with the nonlinear modes (equations ((4.8a), (4.8b)

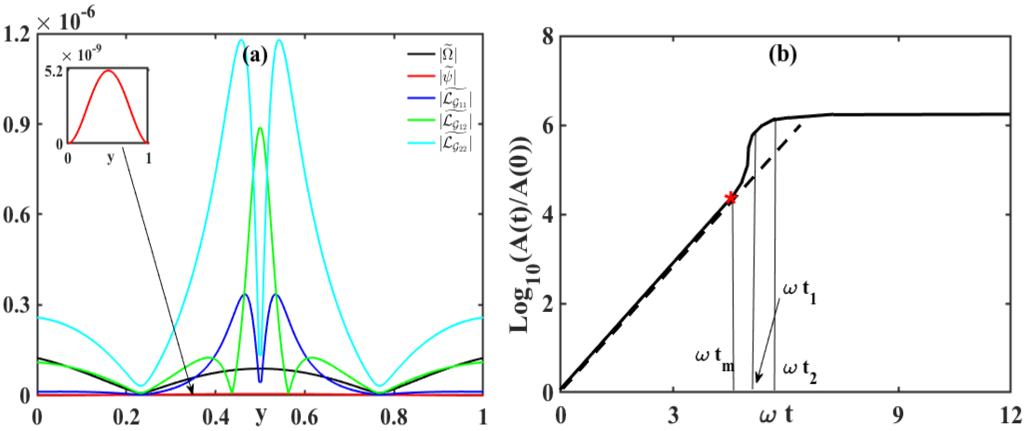

FIGURE 4.1: (a) Solution to the linearized system of equations (4.51) subject to the boundary values, $(\widetilde{\psi}(y), \widetilde{\psi'}(y)) = (0,0)$ at the rigid channel walls, $y = 0$ and $y = 1$, and (b) time evolution of A, as defined in equation (4.53) for parameter values, $We = 10.0, Re = 70.0, \nu = 0.3$ and $\alpha = 0.5$. The solid line represents the nonlinear evolution, $A(t)/A(0)$ (equations ((4.8a), (4.8b) and (4.16)) with initial conditions (4.50)) while the dashed line represents the growth of the solution predicted by the linear theory (4.47). The asterisk $(*)$ indicates the maximum time, t_m as defined in equation (4.52).

and (4.16)), the following quantity is utilized,

$$A(t) = \frac{1}{\ell_x \ell_y} \int_\Gamma d^2(\boldsymbol{I}, \mathcal{G}) d\Gamma, \tag{4.53}$$

which measures the perturbations away from the isotropic tensor, $\boldsymbol{I}$, in the volume-averaged sense (Hameduddin, 2018). (ℓ_x, ℓ_y) are the lengths of the domain in the flow direction and the transverse direction, respectively. The time evolution of the normalized function, $A(t)/A(0)$, for parameter values, $We = 10.0, Re = 70.0, \nu = 0.3, \alpha = 0.5, \varepsilon = 0.1, k = 0.01$ (refer equations ((4.8a), (4.8b) and (4.16) as well as the initial conditions (4.50)) is shown in figure 4.1b. We note that the evolution of $A(t)/A(0)$ matches with the one predicted by the linear theory (4.47), up to the maximum time, $\omega t_m \approx 4.6$ and then shows deviation from the linear growth in the form of an exponential growth upto time, $\omega t_1 \approx 5.2$, followed by an eventual saturation at $\omega t_2 \approx 6.0$. While the initial exponential deviation can be explained due to the exponential form (refer equation (4.46)) of the structure tensor, the mode saturation is the manifestation of nonlinear effects, which is absent in the linear theory.

4.6 Conclusion

In this chapter, we have developed a mathematically consistent decomposition of the conformation tensor, $\mathscr{C}$, into the structure tensor, $\mathcal{G}$ (9), for viscoelastic sub-diffusive flows, that resolves the difficulties associated with the traditional arithmetic decomposition. We characterized the fluctuations in $\mathcal{G}$ by using a geometry specifically constructed for $\boldsymbol{PS}_3$ and obtained three scalar measures: the volume ratio, δ_1 (12), the shortest distance from the mean conformation, δ_2 (13) and the anisotropy index,

δ_3 (14). The linear perturbation studies and the fully nonlinear simulations provided interesting insights about the instantaneous polymer conformation tensor that are not readily available from an arithmetic decomposition of $\mathscr{C}$, including (i) evaluation of a (perturbation amplitude-dependent) maximum time during which the linear perturbative solution can be well approximated by the weakly nonlinear solution, along the Euclidean manifold, (ii) a better measure to detect neighbourhoods where the mean conformation tensor tends to be significantly different in comparison to the instantaneous conformation tensor.

While the analysis presented here has delivered a general framework to provide a quantitative explanation of the previously published experimental findings (Riley, Hak, and Metcalfe, 1988; Nandagopalan et al., 2018; Zarabadi, Charette, and Greener, 2018; Zarabadi, 2019), the detailed physics of the flow-induced structure formation in viscoelastic sub-diffusive flows is given in chapter 6.

Chapter 5

Adaptive Implicit-Explicit Time Integration Method

5.1 Introduction

The growing number of applications of fractional derivatives in various fields of science and engineering indicates that there is a significant demand for better numerical algorithms. However, such algorithms are predominantly designed for one-dimensional problems (Murio, 2008) due to the severe memory restrictions imposed by these derivatives, a challenge which we alleviate in Section 5.2.1. The individual physics or scale components in fractional partial differential equations have very different properties that are reflected in their discretization; for example, in Fractional Advection Diffusion Reaction (FADR) systems (Jannelli, 2022), the discrete advection has a relatively slow (or 'nonstiff') dynamics while the diffusion is a fast (or 'stiff') evolving process. Implicit-Explicit integrators have been proposed as an attractive alternative (compared with the fully explicit or fully implicit time integration methods) where one combines the explicit (implicit) integration for the slow (fast) scale (Crouzeix, 1980). In an Implicit-Explicit scheme, the system of equations assumes the form (Ascher, Ruuth, and Wetton, 1995),

$$\frac{\partial^{\alpha}\Phi}{\partial t^{\alpha}} = \mathbf{f}(\Phi) + \eta\mathbf{g}(\Phi), \tag{5.1}$$

where the superscript, α, denotes order of the fractional derivative and η is a non-negative parameter. In Equation (5.1), the terms collected in $\mathbf{f}(\Phi)$ are on a slow time scale. Because they are (possibly) nonlinear, the implementation of a fully implicit integration scheme faces performance challenges, either from poor performance of iterative solvers or from a complex Jacobian matrix associated with the problem. Therefore, it makes sense to solve this term explicitly. The terms in $\mathbf{g}(\Phi)$, however, are on a fast time scale, and their explicit solution may require excessively small time steps in order to maintain numerical stability. Being usually linear in nature, they can be solved implicitly without further complications. The stability of such methods is still bounded by the Courant-Friedrichs-Lewy condition, but because the fast terms are treated implicitly, these conditions are less strict when compared to a fully explicit scheme of similar formal order of accuracy. A class of such a time-asymptotically stable Implicit-Explicit method is introduced in Section 5.2.

We have limited our focus on the development, analysis and applicability of a novel family of spatiotemporal discretization methods for the numerical solution of the 1D and 2D FADR systems. In our present knowledge, a detailed analysis of the numerical methods for the FADR equation in the finite difference framework is absent. Such analysis is available for the fraction diffusion equation (Brunner, Ling, and Yamamoto, 2010) and the advection-diffusion equation (Al-Khaled and Momani, 2005). The spatial approximation is discussed in section 5.3. Using the 1D linear FADR equation, the time-asymptotic stability analysis and the spectral analysis for the method are outlined in Sections 5.4 and 5.5. The numerical method is benchmarked using the test case for the 2D fraction diffusion equation, proposed by Brunner (Brunner, Ling, and Yamamoto, 2010), in Section 5.6, followed by a conclusion in section 5.7.

Let Σ be a bounded domain in $\mathbb{R}^2$ with sufficiently smooth boundary $\partial\Sigma$. We present the numerical method for an initial-boundary value problem for the time-dependent FADR equation with fractional time-derivative of order $\alpha \in (0, 1)$, as follows,

$$\begin{aligned}
&\frac{\partial^\alpha u(\mathbf{x},t)}{\partial t^\alpha} + K_1(\mathbf{x},t)\nabla\cdot u(\mathbf{x},t) = K_2(\mathbf{x},t)\nabla^2 u(\mathbf{x},t) + f(\mathbf{x},t), \quad \mathbf{x}\in\Sigma, \quad t\in(0,T),\\
&u(\mathbf{x},0) = u_0(\mathbf{x}), \quad \mathbf{x}\in\Sigma,\\
&\alpha_1 u(\mathbf{x},t) + \alpha_2\frac{\partial u(\mathbf{x},t)}{\partial n} = g_0(\mathbf{x},t), \quad \mathbf{x}\in\partial\Sigma, \quad t\in(0,T),
\end{aligned} \tag{5.2}$$

where $\frac{\partial^\alpha u(\mathbf{x},t)}{\partial t^\alpha}$ denotes the Caputo fractional derivative of order α (Podlubny, 1999) with respect to t defined by

$$\frac{\partial^\alpha u(\mathbf{x},t)}{\partial t^\alpha} = \frac{1}{\Gamma(1-\alpha)}\int_0^t \frac{dt'}{(t-t')^\alpha}\frac{\partial u(\mathbf{x},t')}{\partial t'}, \quad 0<\alpha<1, \tag{5.3}$$

and the operators $\nabla(\cdot)$ and $\nabla^2(\cdot)$ in equation (5.2), are the (integer order) gradient and the Laplacian operator in $\mathbb{R}^2$. $K_1(x,t), K_2(x,t)$ and $g_0(x,t)$ are continuous real valued functions, and, α_1, α_2 are constants in $\mathbb{R}$. The FADR equation is related with the non-Markovian continuous-time random walk and is a model for anomalous diffusional flow fields such as polymer melts (Chauhan, Bansal, and Sircar, 2023), flows of liquid crystals (Sircar and Wang, 2010) as well as biological flows including mucus (Sircar and Roberts, 2016) and cartilage (Sircar, Younger, and Bortz, 2015). In the next three sections, we propose the numerical method for the spatiotemporal discretization of equation (5.2).

5.2 Time Integration

The Caputo fractional time derivative in equations (5.2, 5.3) is discretized using the difference approximation, discussed in (Podlubny, 1999). Suppose the time interval [0, T] is discretized uniformly into n subintervals, define $t_k = k\Delta t$, $k = 0,1,\dots,n$, where $\Delta t = T/n$ is the time-step. Let $u(\mathbf{x}, t_k)$ be the exact value of a function $u(\mathbf{x},t)$ at time step t_k. Then, the fractional derivative can be approximated as follows,

$$\left.\frac{\partial^\alpha u(\mathbf{x},t)}{\partial t^\alpha}\right|_{t=t_{k+1}} \approx \frac{1}{\Gamma(1-\alpha)}\sum_{j=0}^{k}\frac{u(\mathbf{x}, t_{j+1}) - u(\mathbf{x}, t_j)}{\Delta t}\int_{j\Delta t}^{(j+1)\Delta t}\frac{dt'}{(t_{k+1}-t')^\alpha}$$

$$\begin{aligned}
&= \frac{1}{\Gamma(1-\alpha)} \sum_{j=0}^{k} \frac{u(\mathbf{x}, t_{j+1}) - u(\mathbf{x}, t_j)}{\Delta t} \int_{(k-j)\Delta t}^{(k-j+1)\Delta t} t'^{-\alpha} dt' \\
&= \frac{1}{\Gamma(1-\alpha)} \sum_{j=0}^{k} \frac{u(\mathbf{x}, t_{k+1-j}) - u(\mathbf{x}, t_{k-j})}{\Delta t} \int_{j\Delta t}^{(j+1)\Delta t} t'^{-\alpha} dt' \\
&= \frac{(\Delta t)^{1-\alpha}}{\Gamma(2-\alpha)} \sum_{j=0}^{k} \frac{u(\mathbf{x}, t_{k+1-j}) - u(\mathbf{x}, t_{k-j})}{\Delta t} r_j^{\alpha}, \qquad (5.4)
\end{aligned}$$

where the weight, $r_j^\alpha = \left[(j+1)^{1-\alpha} - j^{1-\alpha}\right]$. Following an earlier work which utilized a standard integer-order advection-reaction-diffusion (ADR) equations (Singh et al., 2020), we retain 'Implicit-Explicit method philosophy' by explicitly discretizing the advection and the reaction term (i. e., '$K_1 \nabla \cdot u(\mathbf{x},t)$' term and '$f(\mathbf{x},t)$' term, respectively in equation (5.2)), while the diffusive term (i. e., '$K_2(\mathbf{x},t)\nabla^2 u(\mathbf{x},t)$' term in equation (5.2)) is treated semi-implicitly, as follows,

$$K_2(\mathbf{x},t)\nabla^2 u(\mathbf{x},t) \approx \theta K_2(\mathbf{x},t)\nabla^2 u(\mathbf{x},t)|_{t_k} + (1-\theta) K_2(\mathbf{x},t)\nabla^2 u(\mathbf{x},t)|_{t_{k-1}}. \qquad (5.5)$$

This family of time integration method (referred to as the $\theta-$method in subsequent discussion), generalizes the computationally explicit L1-method by Brunner (Brunner, Ling, and Yamamoto, 2010) as well as the fully implicit method recently proposed by Jannelli (Jannelli, 2022).

5.2.1 Adaptive Time Stepping

When the simulation time is long, the size of 'memory' in the fractional derivative approximation becomes enormously large. However, according to the 'fading memory property ' (Diethelm and Freed, 2006), for long times, the solution of the FADR systems changes more slowly than the standard integer-order ADR processes. Hence, it makes sense to employ a large time step at longer times. Let $\widetilde{u(\cdot, t_k)}$ be the numerical approximation for $u(\cdot, t_k)$. To detect this change, we define a measure between the numerical solutions of two consecutive time steps by,

$$\Delta u_{t_k} = \frac{||\widetilde{u(\cdot, t_k)} - \widetilde{u(\cdot, t_{k-1})}||_{l^2}}{||\widetilde{u(\cdot, t_{k-1})}||_{l^2}}, \quad k = 1, \ldots, n. \qquad (5.6)$$

For some user-defined relaxation parameter δ, if $\Delta u_{t_k} < \delta$, then the time spacing is geometrically increased (i. e., $\Delta t \rightarrow 2\Delta t$), upto some prefixed value $\Delta t_{\max}$.

5.3 Spatial approximation

The gradients and Laplacian in equation (5.2) are spatially approximated using the upwind difference scheme and the second-order central difference scheme, respectively. Recall that the central difference scheme approximation of the convective terms in equation (5.2) does not model the flow-physics accurately (Singh et al., 2020). Furthermore, a first-order upwind scheme is too diffusive, thereby necessitating the use of higher-order upwind schemes. For example,

$$K_1(\mathbf{x},t)\frac{\partial u}{\partial x} \approx K_{1ij}\left(\frac{u^k_{i+1,j}-u^k_{i-1,j}}{2\Delta x}\right) + q(K_1^+ u_x^- + K_1^- u_x^+), \tag{5.7}$$

where

$$K_1^- = \min(K_{1ij},0) \quad K_1^+ = \max(K_{1ij},0),$$
$$u_x^- = \frac{u^k_{i-2,j}-3u^k_{i-1,j}+3u^k_{i,j}-u^k_{i+1,j}}{3\Delta x} \quad u_x^+ = \frac{u^k_{i-1,j}-3u^k_{i,j}+3u^k_{i+1,j}-u^k_{i+2,j}}{3\Delta x}, \tag{5.8}$$

where the parameter $q = 0.5$ represents the third-order accurate upwind formula (UD3), which is utilized for the interior stencil points. The use of ghost points is avoided by setting $q = 0$ for grid points immediately adjacent to the boundary, leading to a second-order accurate central difference scheme at these points. Since the focus is on the development of the time integration method, we retain the same spatial approximation outlined above in the subsequent test case.

5.4 Time-asymptotic Stability Analysis

The linear 1D FADR equation (5.2) (with $K_1 = c, K_2 = \gamma, f(x,t) = \lambda u(x,t)$ for $x \in (-\infty,\infty)$, where c,γ and λ are constants specifying the advection speed, coefficient of diffusion and coefficient of reaction, respectively) serves as a model for fractional partial differential equations replicating multi-scale processes.

First, we show that the solution of the linear 1D FADR equation, coupled with periodic boundary conditions and discretized using the numerical method outlined in Section 5.2-5.3, is time-asymptotically stable for a limited range of Courant-Friedrichs-Lewy number and Peclet numbers. The discretization of the linear 1D FADR equation, using the θ-method, is as follows,

$$\frac{(\Delta t)^{-\alpha}}{\Gamma(2-\alpha)}\left\{\sum_{j=1}^{n}\left(j^{(1-\alpha)}-(j-1)^{(1-\alpha)}\right)\left(u_i^{n-j+1}-u_i^{n-j}\right)\right\} + c\left(\frac{u^{n-1}_{i+1}-u^{n-1}_{i-1}}{2\Delta x}\right) +$$
$$qc\left(\frac{u^{n-1}_{i-2}-3u^{n-1}_{i-1}+3u^{n-1}_{i}-u^{n-1}_{i+1}}{3\Delta x}\right)$$
$$= \gamma\theta\frac{u^n_{i+1}-2u^n_i+u^n_{i-1}}{(\Delta x)^2} + \gamma(1-\theta)\frac{u^{n-1}_{i+1}-2u^{n-1}_i+u^{n-1}_{i-1}}{(\Delta x)^2} + \lambda u_i^{n-1}, \tag{5.9}$$

where n/i, denotes the temporal/spatial index and we set the parameter $q = 0.5$. Introducing the following non-dimensional parameters: the Courant-Friedrichs-Lewy number, N_c, Peclet number, Pe and Damköhler number, Da, where

$$N_c = \frac{c(\Delta t)^\alpha}{\Delta x}, \quad Pe = \frac{\gamma(\Delta t)^\alpha}{(\Delta x)^2}, \quad Da = \frac{\lambda(\Delta x)}{c}, \tag{5.10}$$

and rearranging the terms in equation (5.9), we arrive at the following equation,

$$\begin{aligned}
&(1+2Pe\theta\Gamma(2-\alpha))\,u_i^n - Pe\theta\Gamma(2-\alpha)u_{i+1}^n - Pe\theta\Gamma(2-\alpha)u_{i-1}^n = (1-qN_c\Gamma(2-\alpha)\\
&-2Pe(1-\theta)\Gamma(2-\alpha)+DaN_c\Gamma(2-\alpha))\,u_i^{n-1} + \Bigg(-N_c\frac{\Gamma(2-\alpha)}{2}+qN_c\frac{\Gamma(2-\alpha)}{3}\\
&+Pe(1-\theta)\Gamma(2-\alpha)\Bigg)u_{i+1}^{n-1} + \Bigg(N_c\frac{\Gamma(2-\alpha)}{2}+qN_c\Gamma(2-\alpha)+Pe(1-\theta)\Gamma(2-\alpha)\Bigg)\\
&u_{i-1}^{n-1} - qN_c\frac{\Gamma(2-\alpha)}{3}u_{i-2}^{n-1} + \sum_{j=2}^{n}\left(j^{(1-\alpha)}-(j-1)^{(1-\alpha)}\right)\left(u_i^{n-j+1}-u_i^{n-j}\right). \qquad (5.11)
\end{aligned}$$

If $\widetilde{u_i^n}$ be the (numerically) approximate solution of equation (5.11), then the round-off error, $\varepsilon_i^n = u_i^n - \widetilde{u_i^n} \quad (i = 0,\ldots,M)$, identically satisfies the same equation.

$$\begin{aligned}
&(1+2Pe\theta\Gamma(2-\alpha))\varepsilon_i^n - Pe\theta\Gamma(2-\alpha)\varepsilon_{i+1}^n - Pe\theta\Gamma(2-\alpha)\varepsilon_{i-1}^n = (1-qN_c\Gamma(2-\alpha)\\
&-2Pe(1-\theta)\Gamma(2-\alpha)+DaN_c\Gamma(2-\alpha))\varepsilon_i^{n-1} + \Bigg(-N_c\frac{\Gamma(2-\alpha)}{2}+qN_c\frac{\Gamma(2-\alpha)}{3}\\
&+Pe(1-\theta)\Gamma(2-\alpha)\Bigg)\varepsilon_{i+1}^{n-1} + \Bigg(N_c\frac{\Gamma(2-\alpha)}{2}+qN_c\Gamma(2-\alpha)+Pe(1-\theta)\Gamma(2-\alpha)\Bigg)\\
&\varepsilon_{i-1}^{n-1} - qN_c\frac{\Gamma(2-\alpha)}{3}\varepsilon_{i-2}^{n-1} - \sum_{j=2}^{n}(j^{(1-\alpha)}-(j-1)^{(1-\alpha)})(\varepsilon_i^{n-j+1}-\varepsilon_i^{n-j}) \qquad (5.12)
\end{aligned}$$

Due to periodic boundary conditions, we have,

$$\varepsilon_0^n = \varepsilon_M^n \quad n = 1,2,\ldots\ldots,T. \tag{5.13}$$

Assuming the round-off error has the following form,

$$\varepsilon_i^n = \xi_n e^{Ik(ih)}, \tag{5.14}$$

where $\xi_n = |\varepsilon_i^n|, I = \sqrt{-1}, h = \Delta x$ and $k = \frac{2\pi l}{L}$ (l: index, and L: Spatial domain length). We substitute the above relation in the equation (5.12) for the round-off error to arrive at the following form,

$$\begin{aligned}
&\Rightarrow (1+2Pe\theta\Gamma(2-\alpha))\xi_n e^{Ik(ih)} - Pe\theta\Gamma(2-\alpha)\xi_n e^{Ik(i+1)h} - Pe\theta\Gamma(2-\alpha)\xi_n e^{Ik(i-1)h}\\
&= \Bigg(1-qN_c\Gamma(2-\alpha)-2Pe(1-\theta)\Gamma(2-\alpha)+DaN_c\Gamma(2-\alpha)\Bigg)\xi_{n-1}e^{Ik(ih)} + \Bigg(-N_c\\
&\frac{\Gamma(2-\alpha)}{2}+qN_c\frac{\Gamma(2-\alpha)}{3}+Pe(1-\theta)\Gamma(2-\alpha)\Bigg)\xi_{n-1}e^{Ik(i+1)h} + \Bigg(N_c\frac{\Gamma(2-\alpha)}{2}+qN_c\\
&\Gamma(2-\alpha)+Pe(1-\theta)\Gamma(2-\alpha)\Bigg)\xi_{n-1}e^{Ik(i-1)h} - qN_c\frac{\Gamma(2-\alpha)}{3}\xi_{n-1}e^{Ik(i-2)h} -\\
&\sum_{j=2}^{n}(j^{(1-\alpha)}-(j-1)^{(1-\alpha)})(\xi_{n-j+1}-\xi_{n-j})e^{Ik(ih)} \qquad (5.15)
\end{aligned}$$

which

$$\mu_1 \xi_n = \mu_2 \xi_{n-1} + \sum_{j=2}^{n} r_j^{\alpha} \left(\xi_{n-j+1} - \xi_{n-j} \right), \tag{5.16}$$

where

$$\begin{aligned} \mu_1 &= 1 + 2Pe\theta\Gamma(2-\alpha)(1-\cos(kh)), \\ \mu_2 &= 1 - \left(N_c q \left(1 - \frac{2}{3}\cos(kh) \right) + 2Pe(1-\theta)(1-\cos(kh)) - DaN_c + IN_c \sin(kh) \right. \\ &\quad \left. - \frac{N_c q}{3} \left(2e^{-Ikh} - e^{-2Ikh} \right) \right) \Gamma(2-\alpha), \\ r_j^{\alpha} &= j^{(1-\alpha)} - (j-1)^{(1-\alpha)}. \end{aligned} \tag{5.17}$$

Next, we prove the result that the finite difference scheme (5.16-5.17) is time-asymptotically stable, in the form of the following theorem.

Theorem 5 *The approximate solution to the 1D linear FADR equation using the* θ*-method* (5.16) *with* $\alpha \in (0,1)$*, on the finite domain* $x \in [-L, L]$ *with periodic boundary conditions is time-asymptotically stable for all* $t \geq 0$.

Proof 5 *It suffices for us to show that the time-amplification factor,* ξ_n *(equation* (5.16)*), obeys the inequality,*

$$\xi_n \leq \xi_{n-1} \leq \xi_{n-2} \leq \ldots \leq \xi_1 \leq \xi_0. \tag{5.18}$$

- *For* $n = 1$ *in equation (5.16,5.17), we observe the* $\mu_1 \geq 1$ *while* $\mu_2 \leq 1$ *for sufficiently small* N_c*, and* Pe*, thereby leading us towards the conclusion that* $\xi_1 \leq \xi_0$.
- *Using induction hypothesis, we assume that* $\xi_{n-1} \leq \xi_{n-2} \leq \ldots \leq \xi_1 \leq \xi_0$*. Next we show that* $\xi_n \leq \xi_{n-1}$.
- *Since* $\mu_1 \geq 1$ *and* $\mu_2 \leq 1$*, equation* (5.16) *can be replaced with the following inequality,*

  $$\xi_n \leq \xi_{n-1} + \sum_{j=2}^{n} r_j^{\alpha} \left(\xi_{n-j+1} - \xi_{n-j} \right) \leq \xi_{n-1}. \tag{5.19}$$

  The second inequality in equation (5.19) *is because,*

  1. r_j^{α} *is positive and*
  2. $r_j^{\alpha} > r_{j+1}^{\alpha}$*, and*
  3. $\xi_{n-j+1} - \xi_{n-j} \leq 0$ *(via the induction hypothesis),*

  which completes the proof.

We emphasize that while the θ-method is not unconditionally stable, it is time-asymptotically stable for a restricted range of N_c and Pe.

5.5 Spectral Analysis

Although the θ-method is time-asymptotically stable, the presence of dispersion errors (through negative group velocity and large phase speed errors) would invalidate the long-time integration results (Sengupta, Sircar, and Dipankar, 2006). Hence, we couple the result in Section 5.4 along with the toolset of spectral analysis to deduce the relevant range of the parameters, N_c, Pe and Da, for an accurate representation of the numerical solution of the 1D FADR equation.

Using the spectral (Fourier) representation of the approximate solution of equation (5.11), we have $\widetilde{u_i^n} = \xi'_n e^{I(ikh)}$ $(I = \sqrt{-1}, k = \frac{2\pi l}{L})$. We define the numerical time-amplification factor, $G_{num} = \frac{\widetilde{u_i^n}}{\widetilde{u_i^{n-1}}} = \frac{\xi'_n}{\xi'_{n-1}}$. Dividing equation (5.11) with $\widetilde{u_i^{n-1}}$, we arrive at the equation governing G_{num},

$$\Big(1+2Pe\theta\Gamma(2-\alpha)(1-\cos(kh))\Big)G_{num} = \Big(1-qN_c\Gamma(2-\alpha)-2Pe(1-\theta)\Gamma(2-\alpha)$$
$$+DaN_c\Gamma(2-\alpha)\Big)-IN_c\Gamma(2-\alpha)\sin(kh)+\frac{2qN_c\Gamma(2-\alpha)}{3}\cos(kh)+\frac{2}{3}qN_c\Gamma(2-\alpha)$$
$$e^{-Ikh}+2Pe(1-\theta)\Gamma(2-\alpha)\cos(kh)-\frac{qN_c}{3}\Gamma(2-\alpha)e^{-2Ikh}-\sum_{j=2}^{n}\Big(j^{(1-\alpha)}-(j-1)^{(1-\alpha)}\Big)$$
$$\left(\frac{1}{G_{num}^{j-2}}-\frac{1}{G_{num}^{j-1}}\right) \tag{5.20}$$

$$(1+2Pe\theta\Gamma(2-\alpha)(1-\cos(kh)))\,G_{num}^{n} = \Bigg[1-qN_c\Gamma(2-\alpha)\left(1-\frac{4}{3}\cos(kh)+\right.$$
$$\left.\frac{1}{3}\cos(2kh)\right)-2Pe(1-\theta)\Gamma(2-\alpha)(1-\cos(kh))+DaN_c\Gamma(2-\alpha)-IN_c\Gamma(2-\alpha)$$
$$\left(\sin(kh)+\frac{2}{3}q\sin(kh)-\frac{q}{3}\sin(2kh)\right)\Bigg]G_{num}^{n-1}-\sum_{j=2}^{n}(j^{(1-\alpha)}-(j-1)^{(1-\alpha)})$$
$$\left(G_{num}^{n-j+1}-G_{num}^{n-j}\right). \tag{5.21}$$

Thus, we have,

$$C_0G_{num}^{n}+C_1G_{num}^{n-1}+\sum_{j=2}^{n}r_j^{\alpha}\left(G_{num}^{n-j+1}-G_{num}^{n-j}\right)=0, \tag{5.22}$$

where the coefficients,

$$\begin{aligned}
C_0 =& 1+2Pe\theta\Gamma(2-\alpha)(1-\cos(kh))\\
C_1 =& -1+qN_c\Gamma(2-\alpha)\left(1-\frac{4}{3}\cos(kh)+\frac{1}{3}\cos(2kh)\right)+2Pe(1-\theta)\Gamma(2-\alpha)(1-\\
&\cos(kh))-DaN_c\Gamma(2-\alpha)+IN_c\Gamma(2-\alpha)\left(\sin(kh)+\frac{2}{3}q\sin(kh)-\frac{q}{3}\sin(2kh)\right).
\end{aligned} \tag{5.23}$$

We remark that the order ‘n’ of the polynomial (5.22) is fixed at $n = 75$ in the subsequent analysis since our numerical studies have shown that an increase in the polynomial order by one shifts the contours of the spectral variables by less than 0.001%.

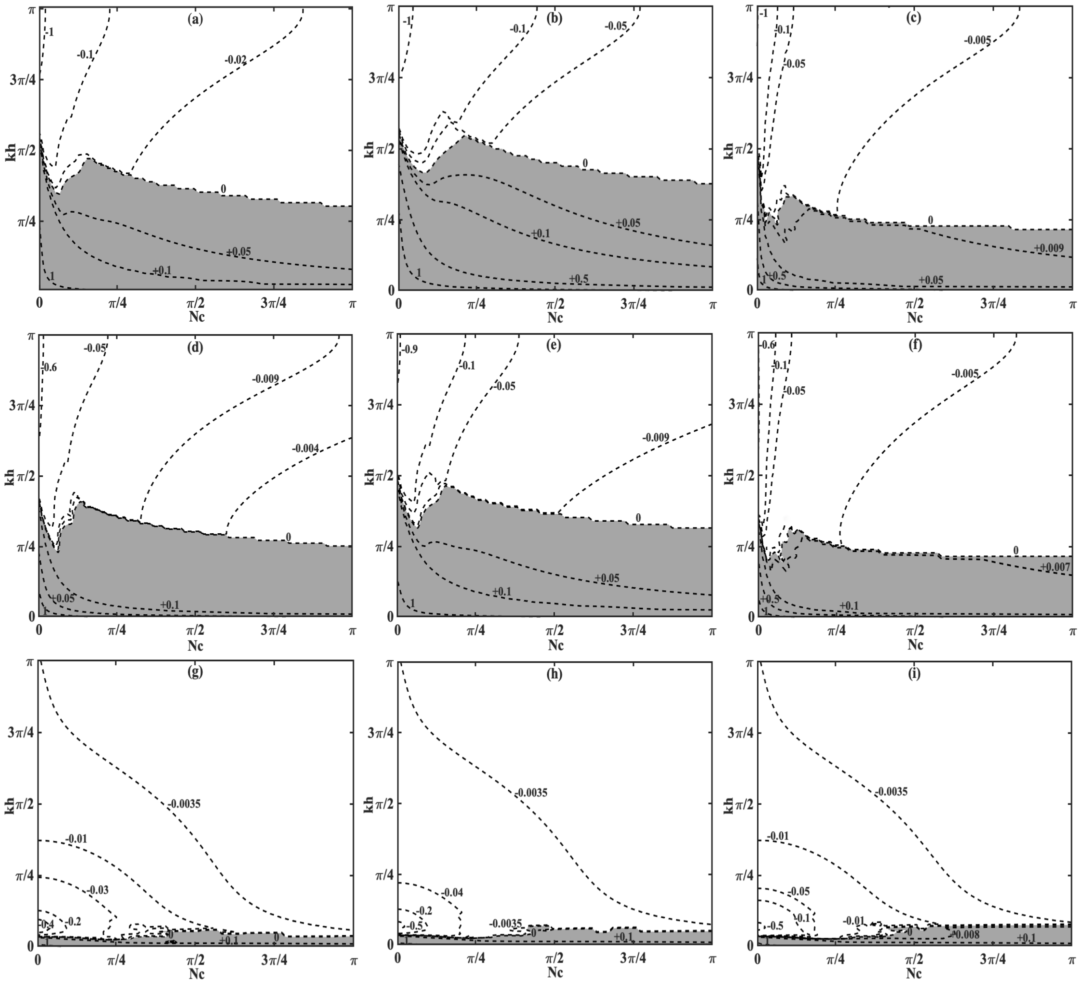

FIGURE 5.1: Group velocity ratio contours, V_g, at $\theta = 0.5$, $\alpha = 0.9$ and (a) $Pe = 0.001, Da = -0.01$, (b) $Pe = 0.001, Da = 0.0$, (c) $Pe = 0.001, Da = 0.01$, (d) $Pe = 0.01, Da = -0.01$, (e) $Pe = 0.01, Da = 0.0$, (f) $Pe = 0.01, Da = 0.01$, (g) $Pe = 1.0, Da = -0.01$, (h) $Pe = 1.0, Da = 0.0$ and (i) $Pe = 1.0, Da = 0.01$.

Next, transforming the exact solution of the linear 1D FADR equation, using Fourier-Laplace transform as $u(x,t) = \int\int \hat{U}(k,\omega)e^{I(kx-\omega t)}$, we arrive at the exact dispersion relation,

$$\omega_{exact} = \omega = I(\lambda - \gamma k^2 - cIk)^{\frac{1}{\alpha}}. \tag{5.24}$$

Similarly, we have a corresponding numerical dispersion relation for the approximate equation (5.11),

$$\omega_{num} = I(\lambda^N - \gamma^N k^2 - c^N Ik)^{\frac{1}{\alpha}}, \tag{5.25}$$

where the superscript ‘N’ denotes the corresponding numerical values of the parameters. Since

$$G_{num} = \frac{u(k,t+\Delta t)}{u(k,t)} = \frac{e^{I(kx-\omega_{num}(t+\Delta t))}}{e^{I(kx-\omega_{num}t)}} = e^{-I\omega_{num}\Delta t} = e^{I\beta}, \tag{5.26}$$

and the numerical phase speed is given by, $c_{num} = \frac{\omega_{num}}{k}$, we find that,

$$c_{num} = -\frac{\beta}{k\Delta t} = -\frac{1}{k\Delta t}\tan^{-1}\left(\frac{(G_{num})_{Imag}}{(G_{num})_{Re}}\right), \tag{5.27}$$

where the subscript ‘Imag’ / ‘Re’ denotes the imaginary/real values, respectively. Using the expression for the exact phase speed, $c_{exact} = \frac{\omega_{exact}}{k}$ and the non-dimensional parameters described in equation (5.11), we find the ratio of the phase speeds,

$$\frac{c_{num}}{c_{exact}} = \frac{-I\beta}{(DaN_c - (kh)^2Pe - I(kh)N_c)^{\frac{1}{\alpha}}}, \tag{5.28}$$

Finally, the expression for the numerical and the exact group velocities are given by,

$$\begin{aligned} V_{g_{num}} &= \left[\frac{\partial}{\partial k}(\omega_{num})\right]_{Re} = \left[\frac{\partial}{\partial k}\left(\frac{\beta}{\Delta t}\right)\right]_{Re} = \left[\frac{h}{\Delta t}\frac{d\beta}{d(kh)}\right]_{Re} \\ V_{g_{exact}} &= \left[\frac{\partial}{\partial k}(\omega_{exact})\right]_{Re} = \left[\frac{\partial}{\partial k}\left(I(\lambda-\gamma k^2-cIk)^{\frac{1}{\alpha}}\right)\right]_{Re} = \left[\frac{1}{\alpha}(c-2k\gamma I)(-I\omega)^{1-\alpha}\right]_{Re}. \end{aligned} \tag{5.29}$$

Hence,

$$\frac{(V_g)_{num}}{(V_g)_{exact}} = \left(\frac{\alpha}{\begin{array}{l} N_c\left(r^{1-\alpha}(\Delta t)^{1-\alpha}\cos(1-\alpha)\phi\right) \\ \quad +2kh\left(r^{1-\alpha}(\Delta t)^{1-\alpha}\sin(1-\alpha)\phi\right)Pe \end{array}}\right)\left(\frac{d\beta}{d(kh)}\right)\Bigg|_{Re}, \tag{5.30}$$

where $\omega = re^{I(\phi+\frac{\pi}{2})}$.

The contour plots for the group velocity ratio, $V_g = \left[\frac{V_{g,num}}{V_{g,exact}}\right]_{Re}$, for Peclet numbers, $Pe = 0.001, 0.01$ and 1.0, and Damköhler numbers, $Da = -0.01, 0.0$ and 0.01, are presented for two values of θ, namely, $\theta = 0.5$ (in figure 5.1) and $\theta = 1.0$ (in figure 5.2) in the (N_c, kh)-plane. The corresponding contour plots for the absolute phase speed error, $\Delta c = |1 - \frac{c_{num}}{c_{exact}}|$ are shown in figure 5.3 and figure 5.4 for $\theta = 0.5$ and $\theta = 1.0$, respectively. Regions of favourable spectral properties ($V_g > 0$ and $\Delta c \leq 0.1$) are highlighted with grey colour.

We outline the spectral properties, namely, the group velocity ratio and the absolute phase speed error, for a specific case of the fractional order, $\alpha = 0.9$. In general, we find that in the limit of vanishingly small values of kh, the numerical method has favourable spectral properties (i. e., $V_g > 0$ and $\Delta c \leq 0.1$ in the limit, $kh \to 0$). The region of positive group velocities ($V_g > 0$) indicates a region where the numerical solution travels in the correct direction and the numerical instabilities in the form

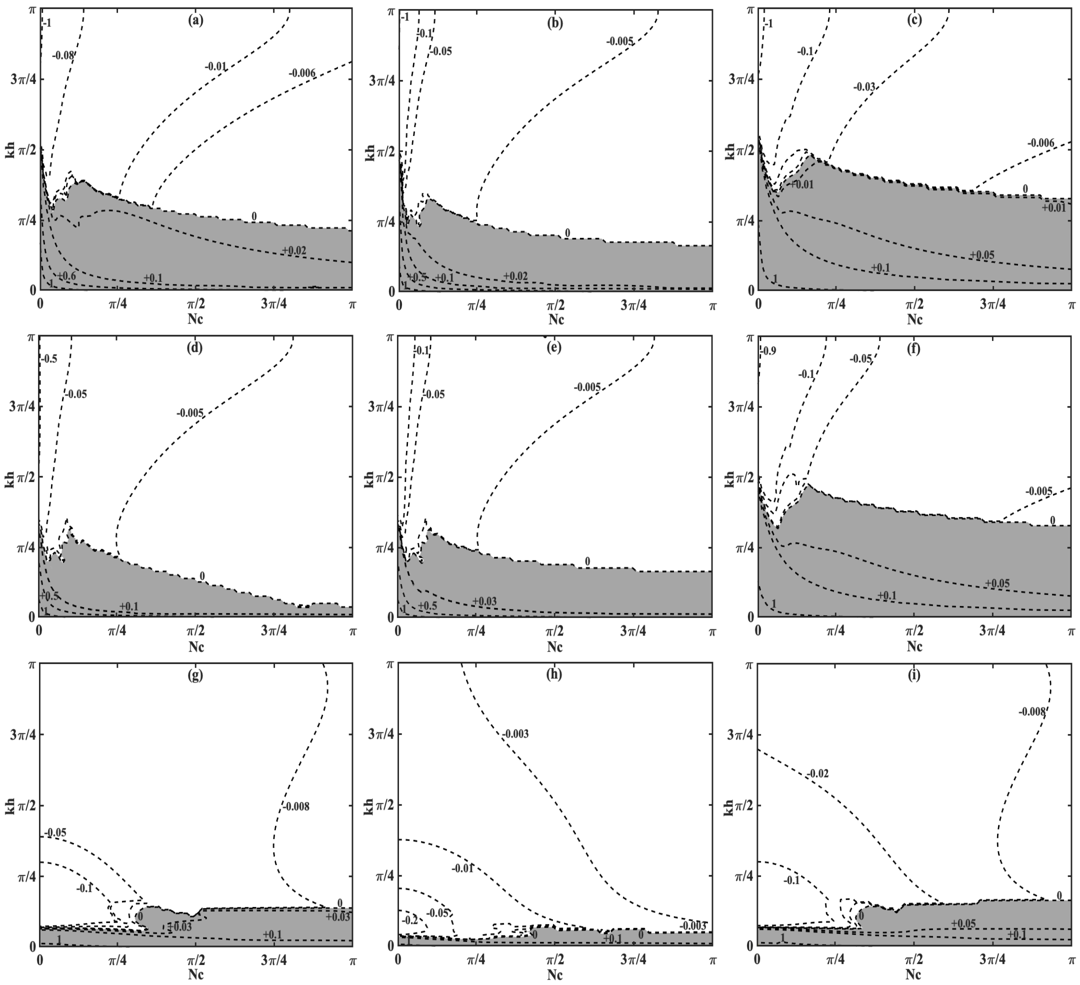

FIGURE 5.2: Group velocity ratio contours, V_g, at $\theta = 1.0$, $\alpha = 0.9$ and (a) $Pe = 0.001, Da = -0.01$, (b) $Pe = 0.001, Da = 0.0$, (c) $Pe = 0.001, Da = 0.01$, (d) $Pe = 0.01, Da = -0.01$, (e) $Pe = 0.01, Da = 0.0$, (f) $Pe = 0.01, Da = 0.01$, (g) $Pe = 1.0, Da = -0.01$, (h) $Pe = 1.0, Da = 0.0$ and (i) $Pe = 1.0, Da = 0.01$.

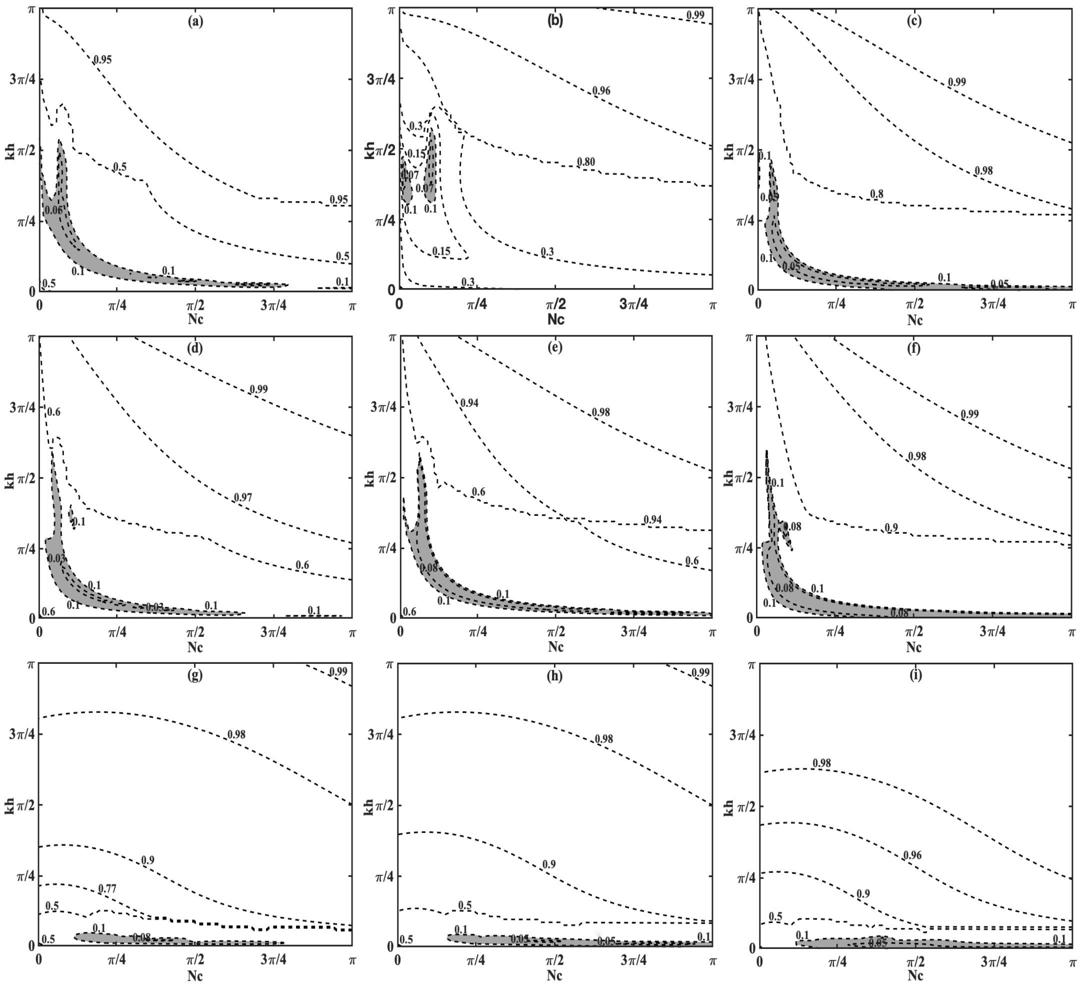

FIGURE 5.3: Absolute phase speed error contours, Δc at $\theta = 0.5$, $\alpha = 0.9$ and (a) $Pe = 0.001, Da = -0.01$, (b) $Pe = 0.001, Da = 0.0$, (c) $Pe = 0.001, Da = 0.01$, (d) $Pe = 0.01, Da = -0.01$, (e) $Pe = 0.01, Da = 0.0$, (f) $Pe = 0.01, Da = 0.01$, (g) $Pe = 1.0, Da = -0.01$, (h) $Pe = 1.0, Da = 0.0$ and (i) $Pe = 1.0, Da = 0.01$.

of q-waves are avoided (Singh et al., 2020). Figure 5.1 and 5.2 indicate that this favourable region is restricted to smaller values of kh with larger values of Pe as well as with smaller values of θ. While the former observation can be attributed to the fact that a stiff diffusive term (i. e., larger '$K_2(\mathbf{x},t)\nabla^2 u(\mathbf{x},t)$' term in equation (5.2) can be correctly approximated with smaller grid-size, h; the latter observation can be explained through a numerical stabilization due to the implicit treatment of fast time scale term (in this case, the diffusive term). Both of these observations are in congruence with the corresponding analysis of the integer order ADR equations (Singh et al., 2020). Similarly, the absolute phase error contours highlight spectrally favourable region ($\Delta c \leq 0.1$, equivalently the phase errors are restricted to 10% of the exact phase speed, see figures 5.3, 5.4) at lower values of Pe and at lower values of θ, indicating the fact that the phase errors in this numerical method can be reduced by introducing finer grids (Jin, Li, and Zhou, 2018; Jin, Li, and Zhou, 2019).

We summarize our discussion by indicating two sources of error that are particularly perplexing in the Direct Numerical Simulations of FADR equations. The first source of error is the existence of $q-$waves for those sets of numerical parameters for which the spatiotemporal discretization is time-asymptotically stable. In such a situation, the $q-$waves do not attenuate and have to be eliminated by deploying an explicit filter (Visbal and Gaitonde, 2002). Another aspect of spectral error is related to the Gibbs' phenomenon which occurs as a consequence of sharp discontinuity in the solution and which causes fictitious oscillations, a problem that can be remedied using high-accuracy dispersion relation preserving schemes (which has at least shown promise in integer order partial differential equations) (Sengupta, Sircar, and Dipankar, 2006).

5.6 Method Validation: 2D Fractional Diffusion Equation

Using the spectrally relevant parameter values discussed in section 5.5, the θ-method is verified by solving the 2D fractional diffusion equation ($K_1 = f = 0$ and $K_2 = 1$ in equation (5.2)), originally proposed by Brunner (Brunner, Ling, and Yamamoto, 2010), for the case of (a) zero Dirichlet boundary conditions ($\alpha_1 = 1, \alpha_2 = 0, g_0(\mathbf{x},t) = 0$) and (b) zero Neumann conditions ($\alpha_1 = 0, \alpha_2 = 1, g_0(\mathbf{x},t) = 0$), over the square domain, $(x,y) \in \Gamma = [-1,\, 1]^2$. The initial condition for the two test cases can be outlined as follows,

1. **Dirichlet case:** $u_0(x,y) = \cos\left(\frac{\pi}{2}x\right)\cos\left(\frac{\pi}{2}y\right)$,
2. **Neumann case:** $u_0(x,y) = \sin\left(\frac{\pi}{2}x\right)\sin\left(\frac{\pi}{2}y\right)$,

and the exact solution for both cases is given by

$$u_{exact}(x,y,t) = E_\alpha\left(-\frac{1}{4}\pi^2 t^\alpha\right) u_0(x,y), \tag{5.31}$$

where $E_\alpha(z) = \sum_{k=0}^{\infty} \frac{z^k}{\Gamma(\alpha k+1)}, \quad \alpha > 0$, is the one-parameter Mittag-Leffler function.

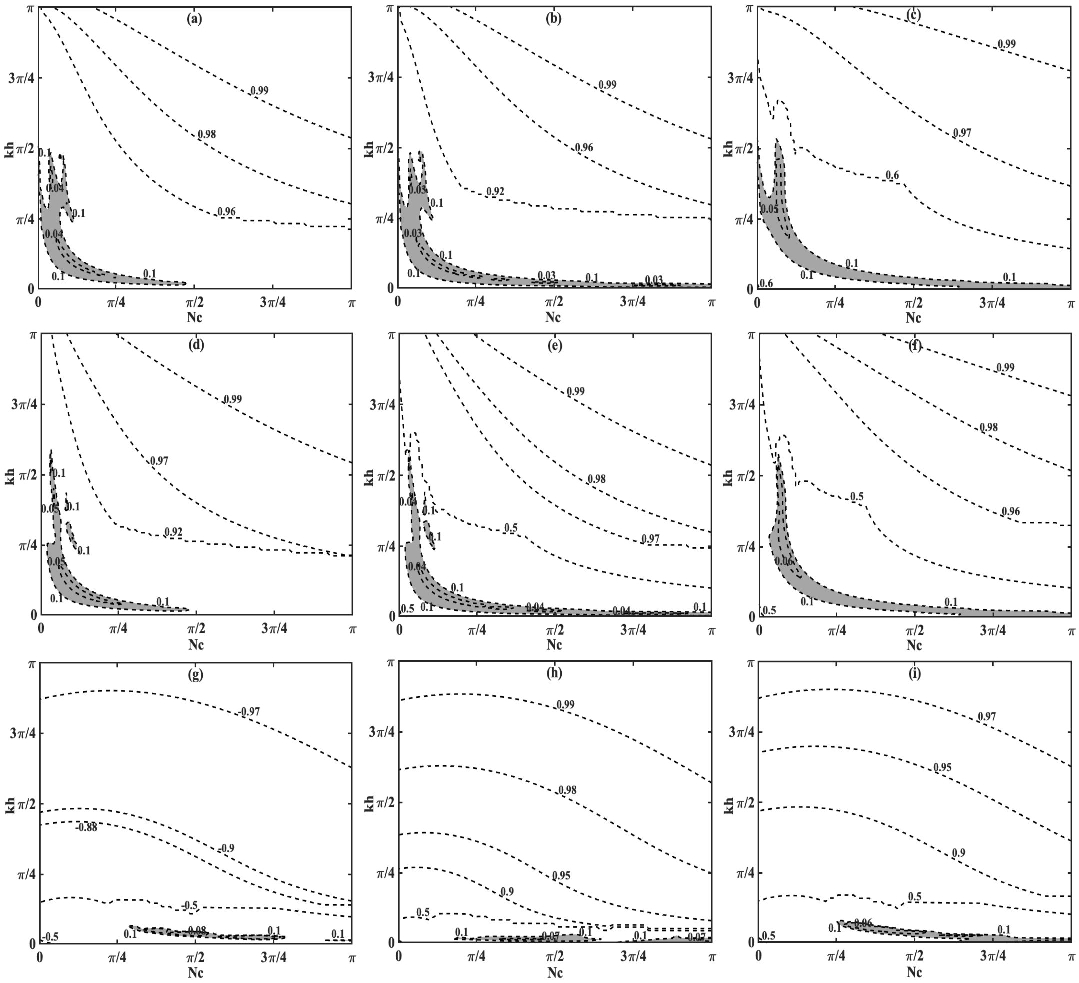

FIGURE 5.4: Absolute phase speed error contours, Δc at $\theta = 1.0$, $\alpha = 0.9$ and (a) $Pe = 0.001, Da = -0.01$, (b) $Pe = 0.001, Da = 0.0$, (c) $Pe = 0.001, Da = 0.01$, (d) $Pe = 0.01, Da = -0.01$, (e) $Pe = 0.01, Da = 0.0$, (f) $Pe = 0.01, Da = 0.01$, (g) $Pe = 1.0, Da = -0.01$, (h) $Pe = 1.0, Da = 0.0$ and (i) $Pe = 1.0, Da = 0.01$.

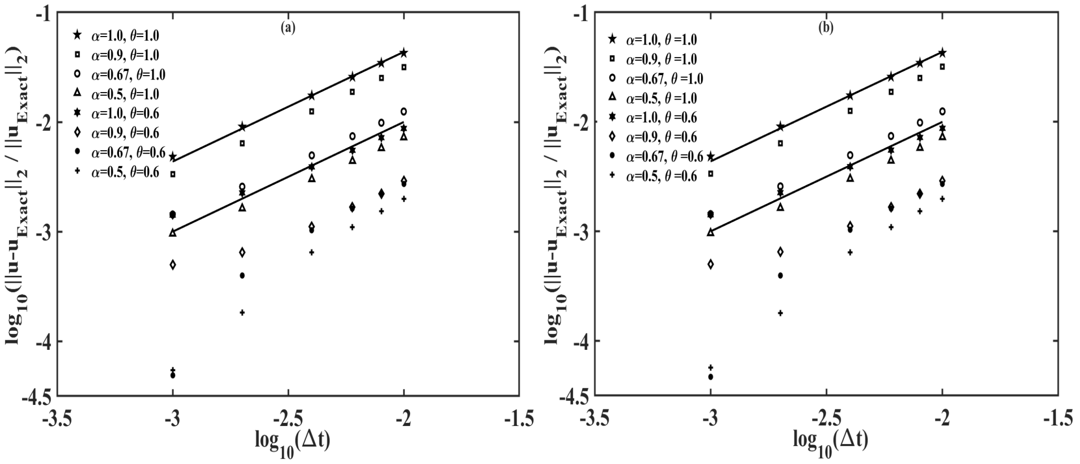

FIGURE 5.5: Relative error for the solution of the 2D fractional diffusion equation at simulation time $T = 0.35$, at $\alpha = 1.0, \theta = 1.0$ ($\star$); $\alpha = 0.9, \theta = 1.0$ ($\square$); $\alpha = 0.67, \theta = 1.0$ ($\circ$); $\alpha = 0.5, \theta = 1.0$ ($\triangle$); $\alpha = 1.0, \theta = 0.6$ ($*$); $\alpha = 0.9, \theta = 0.6$ ($\diamond$); $\alpha = 0.67, \theta = 0.6$ ($\bullet$); $\alpha = 0.5, \theta = 0.6$ ($+$); and for (a) Dirichlet boundary conditions, and (b) Neumann boundary conditions.

The domain, $\Sigma \cup \partial\Sigma$, is discretized using 51×51 points and the relative error in $l_2 - norm$, $\frac{\|\tilde{u}-u_{Exact}\|_2}{\|u_{Exact}\|_2}$, versus discretization time, Δt, is shown in figure 5.5. The total computation time is fixed at $T = 0.35$ for all cases. We note that the slope of the error curves at $\alpha = 1.0$ is one (highlighted with solid curves in figure 5.5a,b). This observation can be explained since at this value of α, the θ-method reduces to the standard, integer order, Euler method, which is first-order accurate. Further, note that the slope of the error curves for $\alpha < 1.0$ is sub-linear, indicating that for the fractional-order diffusion equation, the θ-method has a sub-linear order of accuracy.

5.7 Conclusion

This chapter addresses the development as well as the time-asymptotic and spectral stability of a novel class of numerical methods for the spatiotemporal discretization of fractional partial differential equations. The method, includes the time integration (section 5.2) and the spatial discretization (section 5.3). Using 1D linear FADR equation, the time-asymptotic stability and spectral analysis were outlined in section 5.4 and 5.5. The method was validated using the test case for the 2D fraction diffusion equation in section 5.6. Note that the focus of this chapter was on the development of the numerical method, hence, a comprehensive study on the mechanics of subdiffusive channel flow using the numerical method developed is reported in chapter 6.

Chapter 6

Rheodynamics of Channel Flows

6.1 Introduction

This chapter comprehensively explores through Direct Numerical Simulations of fully developed, planar Poiseuille flow within an infinitely extended channel characterized by dimensions L and H. The aspect ratio $L/H \gg 1$ establishes the foundation for this study, with x and y representing the flow and shear gradient directions respectively. There are three basic models used in the molecular theory for subdiffusive viscoelastic fluids: Rouse model ($\alpha = 1/2$), Zimm's model ($\alpha = 2/3$) and the Reptating chain model ($\alpha = 1/4$). The Rouse model assumes that a polymer chain can be approximated as a series of connected beads, with each bead representing a segment of the polymer. The movement of each bead is governed by the Langevin equation, which takes into account both a random force representing thermal fluctuations and a restoring force due to the elasticity of the polymer chain. Whilst the Rouse model applies to polymer melts, the Zimm model applies to polymer in solution where the hydrodynamic interaction is not screened. In a reptating chain model, the individual polymer chains become intertwined with one another due to their random motion. These entanglements significantly affect the movement of each polymer chain. This model focuses on how a polymer chain's motion is restricted by these entanglements and how the chain "reptates" through the network of other chains. Here, two specific cases of the fractional derivative are considered, namely, monomer diffusion in Rouse chain melts ($\alpha = 1/2$) (Rouse, 1953), and in Zimm chain solution ($\alpha = 2/3$) (Zimm, 1956). Section 6.2 lays the groundwork by detailing initial conditions, boundary specifications, and algorithmic details, including a numerical scheme designed to preserve the positive definiteness of the conformation tensor. In Section 6.3, we delve into numerical results obtained for viscous stress dominated case and elastic stress dominated case, followed by some concluding remarks in section 6.4.

6.2 Direct Numerical Simulation

We describe the incompressible, subdiffusive dynamics of a planar viscoelastic channel flow for polymer melts and present the numerical solution using the θ-method described in section 5.2. The model developed in streamfunction-vorticity formulation (4.8) is as follows,

$$Re\left[\frac{\partial^\alpha \Omega}{\partial t^\alpha} + \boldsymbol{v}\cdot\nabla\Omega\right] = \nu\nabla^2\Omega + \frac{(1-\nu)}{We}\nabla\times\nabla\cdot\mathscr{C}, \tag{6.1a}$$

$$\nabla^2\psi = -\Omega, \tag{6.1b}$$

$$\frac{\partial^\alpha \mathscr{C}}{\partial t^\alpha} + \boldsymbol{v}\cdot\nabla\mathscr{C} - (\nabla\boldsymbol{v})^T\mathscr{C} - \mathscr{C}\nabla\boldsymbol{v} = \frac{\boldsymbol{I}-\mathscr{C}}{We}, \tag{6.1c}$$

6.2.1 Initial and Boundary Conditions

Initial conditions: A rectilinear coordinate system is used with x, y denoting the channel flow direction and the transverse direction, respectively. The origin of this coordinate system is chosen at the left end of the lower wall of the channel. The mean flow is assumed to be a plane Poiseuille flow with its variation entirely in the transverse direction, namely,

$$\mathbf{U}_0 = (y-y^2)\mathbf{e_x}, \tag{6.2}$$

where $\mathbf{e_x}$ is the unit vector along x-direction. The mean flow, $\mathbf{U}_0$, defines the mean vorticity, $\Omega_0 = 2y-1$, and the mean stream-function, $\psi_0 = \frac{y^2}{2} - \frac{y^3}{3}$. The base state polymer conformation tensor, $\mathscr{C}_0 = [\mathscr{C}_{0ij}]$ is,

$$\begin{aligned}
&\mathscr{C}_{011} = 1,\\
&\mathscr{C}_{012} = \mathscr{C}_{021} = We(1-2y),\\
&\mathscr{C}_{022} = 2We^2(1-2y)^2+1.
\end{aligned} \tag{6.3}$$

The initial condition is composed of the mean flow superposed with a perturbed unstable mode, as follows,

$$\begin{aligned}
\Omega|_{t=0} &= \Omega_0 + \varepsilon\Omega_1 = \Omega_0 + \varepsilon\mathscr{R}\{\widetilde{\Omega}(y)|_{t=0}e^{ikx}\},\\
\psi|_{t=0} &= \psi_0 + \varepsilon\psi_1 = \psi_0 + \varepsilon\mathscr{R}\{\widetilde{\psi}(y)|_{t=0}e^{ikx}\},\\
\mathscr{C}|_{t=0} &= \mathscr{C}_0 + \varepsilon\mathscr{C}_1 = \mathscr{C}_0 + \varepsilon\mathscr{R}\{\widetilde{\mathscr{C}}(y)|_{t=0}e^{ikx}\},
\end{aligned} \tag{6.4}$$

where $(\Omega_1, \psi_1, \mathscr{C}_1)$ are the perturbations that are Fourier transformed in the x-direction. $\mathscr{R}\{\}$ denotes the real part of the complex valued function. The equations governing the initial conditions (6.4) can be obtained by assuming a normal mode expansion for the perturbed field, $\phi_1 = \widetilde{\phi(y)}e^{ikx}$ (where $\phi_1 = (\Omega_1, \psi_1, \mathscr{C}_1)$, equation (6.1) in $\mathscr{O}(\varepsilon)$ reduces to

$$\begin{aligned}
&Re\left((y-y^2)(ik)\widetilde{\Omega} - 2(ik)\widetilde{\psi}\right) - \nu\left((ik)^2\widetilde{\Omega} + \widetilde{\Omega}''\right)\\
&\qquad - (1-\nu)\left((ik)^2\widetilde{\mathscr{C}}_{12} - \widetilde{\mathscr{C}}''_{12} + (ik)\widetilde{\mathscr{C}}'_{22} - (ik)\widetilde{\mathscr{C}}'_{11}\right) = 0,
\end{aligned} \tag{6.5a}$$

$$\widetilde{\psi}(ik)^2 + \widetilde{\psi}'' + \widetilde{\Omega} = 0, \tag{6.5b}$$

$$(y-y^2)(ik)\widetilde{\mathscr{C}}_{11} - 2(ik)\widetilde{\psi}' + 2We(1-2y)(ik)^2\widetilde{\psi)} + \frac{\widetilde{\mathscr{C}}_{11}}{We} = 0, \tag{6.5c}$$

$$\begin{aligned}
&(y-y^2)(ik)\widetilde{\mathscr{C}}_{12} + 2We(ik)\widetilde{\psi} + (2We^2(1-2y)^2+1)(ik)^2\widetilde{\psi} - (1-2y)\widetilde{\mathscr{C}}_{11}\\
&\qquad - \widetilde{\psi}'' + \frac{\widetilde{\mathscr{C}}_{12}}{We} = 0,
\end{aligned} \tag{6.5d}$$

$$(y-y^2)(ik)\widetilde{\mathscr{C}}_{22} + 8We^2(1-2y)(ik)\widetilde{\psi} - 2(1-2y)\widetilde{\mathscr{C}}_{12} - 2We(1-2y)\widetilde{\psi}''$$

$$+2(2We^2(1-2y)^2+1)(ik)\widetilde{\psi}'+\frac{\widetilde{\mathscr{C}_{22}}}{We}=0. \qquad (6.5e)$$

where we denote $\frac{d}{dy}()=()'$. The solution to the boundary value problem is found subject to the boundary conditions, $(\widetilde{\psi}(y),\widetilde{\psi'}(y))=(0,0)$ at the rigid walls $y=0,1$, using a standard MATLAB boundary value solver.

Boundary conditions: In order to imitate an infinitely long channel, periodic boundary conditions are assumed at the flow inlet and outlet. No-slip (i. e., $u=v=0$) and zero tangential conditions (i. e., $\frac{\partial u}{\partial x}=\frac{\partial v}{\partial x}=0$) are imposed on the lower wall ($y=0$) and the upper wall ($y=1.0$) of the channel, respectively. Further, incompressibility constraint provides an additional condition on the walls: $\frac{\partial v}{\partial y}=0$. Since the flow is parallel to the channel walls, the walls may be treated as streamline. Thus, the streamfunction value, ψ, on the wall is set as a constant. That constant (which may be different on the lower and the upper wall) is found from the no-slip condition. Zero tangential condition implies that all tangential derivatives of streamfunction vanish on the wall. Thus, the boundary condition for vorticity is found from the Poisson equation (6.1b),

$$\frac{\partial^2\psi}{\partial y^2}|_{wall}=-\Omega_{wall}. \qquad (6.6)$$

Finally, the boundary conditions for the elastic stress tensor are constructed from equation (6.1c), coupled with the no-slip and zero tangential conditions, as follows,

$$\begin{aligned}
&\mathscr{C}_{11}=1,\\
&\frac{\mathscr{C}_{12}}{We}+\frac{\partial^\alpha\mathscr{C}_{12}}{\partial t^\alpha}-\frac{\partial u}{\partial y}=0,\\
&\frac{\mathscr{C}_{22}-1}{We}+\frac{\partial^\alpha\mathscr{C}_{22}}{\partial t^\alpha}-2\frac{\partial u}{\partial y}\mathscr{C}_{12}=0.
\end{aligned} \qquad (6.7)$$

6.2.2 Algorithmic Details

The size of the domain is chosen to be $(x,y)\in[0,\,5]\times[0,\,1]$. The domain is discretized using 76×51 points, such that the discrete points are equally spaced at $\Delta x=\frac{5}{75}$ and $\Delta y=\frac{1}{50}$ (excluding the boundary points, where the Dirichlet boundary conditions are imposed) in the $x-$ and the $y-$ directions, respectively. The variable in the θ-method is fixed at $\theta=1.0$. The minimum and the maximum time-step are chosen as $\Delta t_{min}=10^{-3}$ and $\Delta t_{max}=1.6\times10^{-2}$, respectively. The parameters in the initial conditions (6.4) are set at $\varepsilon=0.1, k=0.1$. The time-step in the simulation is increased adaptively using the technique outlined in Section 5.2.1. The Poisson equation (6.1b) is iteratively solved using the Gauss-Siedel iteration technique. Assuming $(N+1)$ (or $(M+1)$) points in the x (or y) direction, the size of the coefficient matrix is $N(M-1)\times N(M-1)$. Hence, due to size constraints, the numerical inversion of this coefficient matrix imposes severe memory restrictions. Instead, we note that the coefficient matrix has the following block tridiagonal structure with $(M-1)$ blocks,

$$\begin{pmatrix} D_1 & D_2 & 0 & \cdots & 0 \\ D_2 & \ddots & \ddots & & \vdots \\ 0 & \ddots & \ddots & \ddots & 0 \\ \vdots & & \ddots & \ddots & D_2 \\ 0 & \cdots & 0 & D_2 & D_1 \end{pmatrix} \tag{6.8}$$

where,

$$D_1 = \begin{pmatrix} R & r_1 & 0 & \cdots & 0 & r_1 \\ r_1 & \ddots & \ddots & & & 0 \\ 0 & \ddots & \ddots & \ddots & & \vdots \\ \vdots & & \ddots & \ddots & \ddots & 0 \\ 0 & & & \ddots & \ddots & r_1 \\ r1 & 0 & \cdots & 0 & r_1 & R \end{pmatrix} \tag{6.9}$$

D_1 and D_2 are $N \times N$ matrices, such that $D_2 = \text{Diag}\,(r_2)$ and $r_1 = (\Delta x)^{-2}, r_2 = (\Delta y)^{-2}$ and $R = -2(r_1 + r_2)$. Since the exact location of the non-zero entries is known, the invocation of the entire coefficient matrix in the Guass-Siedel iteration is avoided. The solution is updated by utilizing the non-zero entries of each row on a case-by-case basis. The row diagonal dominance of the matrix (6.8) ensures that the iteration converges in finite number of steps. Similarly, the vorticity equation (6.1a) involves another Laplacian term and its discretization involves a coefficient matrix identical to the form (6.8) $\left(\text{with } r_1 = -\nu\theta(dx)^{-2}, r_2 = -\nu\theta(dy)^{-2}, R = -2(r_1 + r_2) + \dfrac{Re(\Delta t)^{-\alpha}}{\Gamma(2-\alpha)}\right)$. Thus, the Laplacian term in equation (6.1a) is treated identically as above.

6.2.3 Numerical Evolution of the Conformation Tensor Equations

The advection term in the conformation tensor equation (6.1c) is second-order accurate in space with the exception of a few points where it is only first-order accurate. This change in order is due to the special treatment of the advection term in the conformation tensor that is needed to avoid the Hadamard instabilities resulting in the loss of symmetric, positive definite (SPD) property of the conformation tensor (Sureshkumar, Beris, and Handler, 1997). The special treatment is an efficient transformation of the slope-limiting approach of Vaithianathan *et al.* (Vaithianathan et al., 2006), which requires the evaluation of three schemes: forward, backward and centred stencils to approximate the advective flux at each grid point and at each time-step. The resultant scheme that maximizes the eigenvalues of the conformation tensor at the grid points, is then chosen. Further, following Dubief *et al.* (Dubief et al., 2005), we ensure that the polymer does not exceed its maximum extensibility by using a semi-implicit approach for the relaxation term in equation (6.1c).

6.3 Numerical Results

Next, the in silico studies for two specific cases of monomer diffusion in Rouse chain melts ($\alpha = 1/2$) (Rouse, 1953), and in Zimm chain solution ($\alpha = 2/3$) (Zimm, 1956) are discussed. The Rouse model predicts that the viscoelastic properties of the polymer chain can be described by a Generalized Maxwell model, where the elasticity is governed by a single relaxation time, which is independent of the number of Maxwell elements (or the so-called 'submolecules'). In contrast, the Zimm's model predicts the ('shear rate and polymer concentration independent') viscosity of the polymer solution by calculating the hydrodynamic interaction of flexible polymers (an idea which was originally proposed by Kirkwood (Kirkwood, 1954)) by approximating the chains using a bead-spring setup.

The instantaneous principle invariant of the conformation tensor, $\text{tr}\mathscr{C}$ as well as the new invariants (4.4) for a specific set of parameters values, $\nu = 0.3, Re = 70, We = 20$, and simulation time, $T = 7.15$, are presented for both the Zimm's case (left column) and the Rouse case (right column) in Figure 6.1. Figure 6.1a (as well as figure 6.1b) shows the logarithmic volume ratio, δ_1. We find that in figure 6.1a, we have predominantly negative values, indicating that the instantaneous volume is smaller than the volume of the mean conformation. Further, observe regions of very high values of δ_1 interspersed with regions of very low values, especially near the wall. This observation is the result of the slow diffusion of polymers in subdiffusive flows since there is no direct mechanism for smoothening out these 'elastic shocks' in the tensor field. Since these elastic shocks originate away from the flow inlet and outflow, we conclude that these structures predominantly form due to the flow interaction with the rigid walls. The measure, δ_1 does not distinguish between volume-preserving deformations. For example, δ_1 does not distinguish between $\mathscr{C}$ and $\det(\mathscr{C})\mathscr{C}_1$, for any tensor $\mathscr{C}_1$ with a unit determinant. In particular, $\delta_1 = 0$, does not imply $\mathscr{C} = \overline{\mathscr{C}}$. In order to identify regions where the instantaneous polymer conformation equals the mean conformation and quantify the deviation when it is not, we use the squared geodesic distance away from the mean along the Riemannian manifold, δ_2 (figure 6.1c and 6.1d). Figure 6.1c indicates that the conformation tensor field, $\mathscr{C}$, is significantly far away from $\overline{\mathscr{C}}$, near the wall. This deviation of δ_2, in the near wall region, can be explained via the 'memory effect', previously observed in regular Oldroyd-B fluids Sircar and Bansal, 2019. Finally, figure 6.1e,6.1f shows the instantaneous contours of the anisotropy index, δ_3. This index shows how close the shape of the instantaneous conformation tensor is to the shape of the mean conformation tensor, irrespective of volumetric changes. The visual resemblance of δ_2 and δ_3 suggests that deformations to the mean conformation are largely anisotropic near the wall. Next, we limit our focus on the contours of the first invariant, δ_1 (after noting in figure 6.1 that the contours of the other invariants are qualitatively similar) and for two different values of ν: $\nu = 0.3$ (elastic stress dominated case) and $\nu = 0.5$ (viscous stress dominated case).

6.3.1 Elastic Stress Dominated Case: $\nu < 0.5$

Flows with parameter values, $\nu < 0.5$ (or the elastic stress dominated case), are those associated with higher concentration of polymers per unit volume. The contours

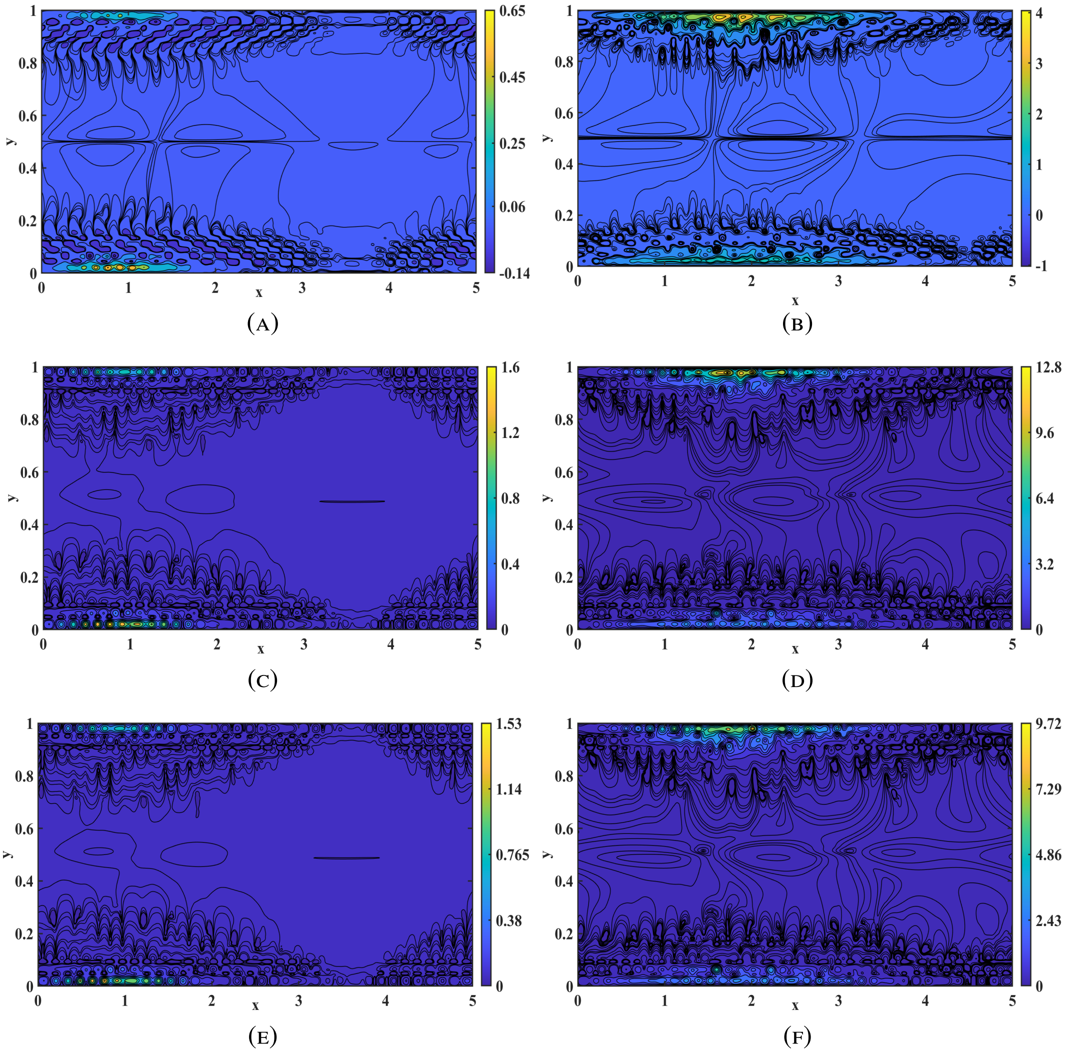

(A) (B)

(C) (D)

(E) (F)

FIGURE 6.1: Contours of instantaneous (a, b) volume ratio, δ_1, (c, d) shortest distance from the mean, δ_2, (e, f) anisotropy index, δ_3, for the Zimm's model (left column) and the Rouse model (right column) at simulation time, $T = 7.15$. Other parameters are fixed at $\nu = 0.3.Re = 70, We = 20$.

of the first invariant, δ_1, for the Zimm's model and the Rouse model, are shown in figures 6.2 and 6.3, respectively, at equal snapshots. At lower values of elastic relaxation (represented by the parameter, $We = 15$), the flow-macrostructure evolution in the Rouse model is slow, in comparison with the Zimm's model (i. e., comparing the contour values in the first two rows in figure 6.2 versus the first two rows in figure 6.3). A reversal of this trend occurs at higher values of elasticity (i. e., the third and the fourth rows in figures 6.2, 6.3 at $We = 20$). We attribute this observation due to the following reasoning. The Rouse model represents 'thicker' fluid, or fluids with slower diffusion than the Zimm's solution, due to the smaller fractional time derivative. Flows with smaller time derivatives (or the thicker polymer melt case) are those associated with higher concentration of polymers per unit volume (Bird, Armstrong, and Hassager, 1987). Physically, the formation of these 'spatiotemporal macrostructures' is associated with the entanglement of the polymer chains at microscale (Rubenstein and Colby, 2003), leading to localized, non-homogeneous regions with higher viscosity. Experiments (Fogelson and Neeves, 2015) have shown that non-Newtonian fluids with a higher polymer concentration have a greater tendency for the polymer strands to agglomerate (especially at higher elastic relaxation), or the so-called 'over-crowding effect' (Doi and Edwards, 1986).

Further, notice the disappearance of the structures at larger values of Re (i. e., notice the time-snippets at $Re = 1000$, the second and the fourth rows in figures 6.2 and 6.3). This observation can be attributed to the fact that the macrostructures are 'washed out' of the channel at higher flow velocities. In chapter 3, we had indicated the existence of 'temporally stable regions at high fluid inertia' through a spatiotemporal linear stability analysis (Chauhan, Bansal, and Sircar, 2023). Here, we associate temporally stable regions with regions devoid of flow structures.

6.3.2 Viscous Stress Dominated Case: $\nu \geq 0.5$

Observe that the 'flow structures' for the Zimm's model in the elastic stress-dominated case ($\nu = 0.5$, figure 6.4) are larger in size as well as in magnitude, in comparison with the Rouse model (figure 6.5), at equal simulation times. Even within the respective models, we find that the macrostructures are more prominent (both in size and magnitude) at higher values of elastic relaxation (i. e., at $We = 20$, third and fourth rows in figures 6.4 and 6.5). Again, note that the structure formation is conspicuously absent at larger values of Re (the second and the fourth rows in figure 6.4 and 6.5).

We summarize our discussion by noting that for the selected values of the parameters, ν, α, Re and We: (a) The elastic stress-dominated case ($\nu = 0.3$ case) is comparatively more unstable than the viscous stress dominated case, (b) The Rouse model is comparatively more unstable than the Zimm's model at low fluid inertia (or low values of Re) and higher elastic relaxation (or high values of We), and (c) Temporal stability is achieved at higher values of Re, irrespective of the model or the polymer concentration. Thus, our in silico studies not only corroborate the existence of the previously established temporally stable region at high fluid inertia (Chauhan, Bansal, and Sircar, 2023), but also highlight the potential of fractional partial differential equations in effectively capturing the flow-instability transition in subdiffusive flows.

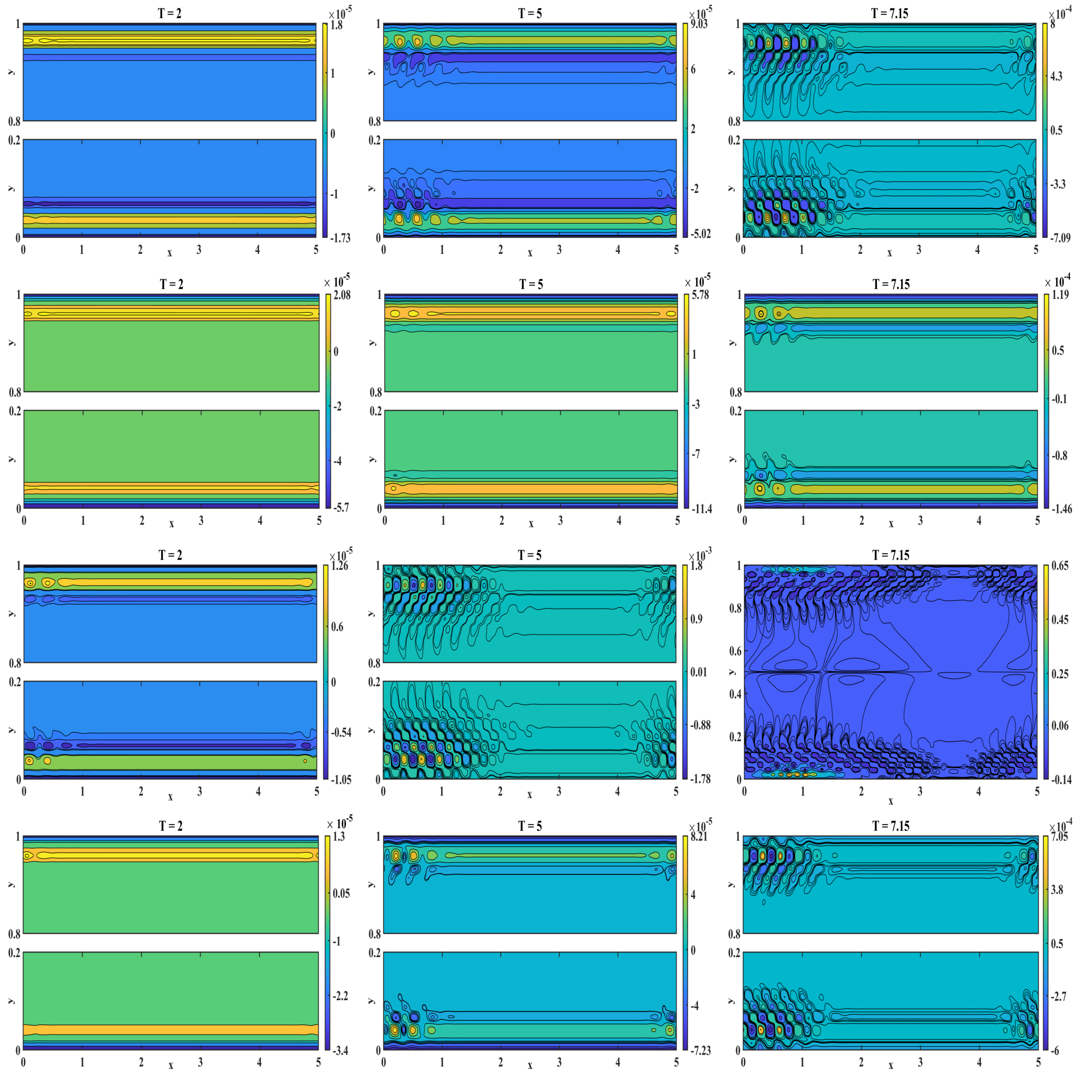

FIGURE 6.2: Contours of instantaneous volume ratio, δ_1, for the elastic stress dominated Zimm's model ($\nu = 0.3, \alpha = 2/3$). Other parameters set at $Re = 70, We = 15$ (first row), $Re = 1000, We = 15$ (second row), $Re = 70, We = 20$ (third row) and $Re = 1000, We = 20$ (fourth row). Plots shown with broken y-axis do not show any structure formation around the centerline.

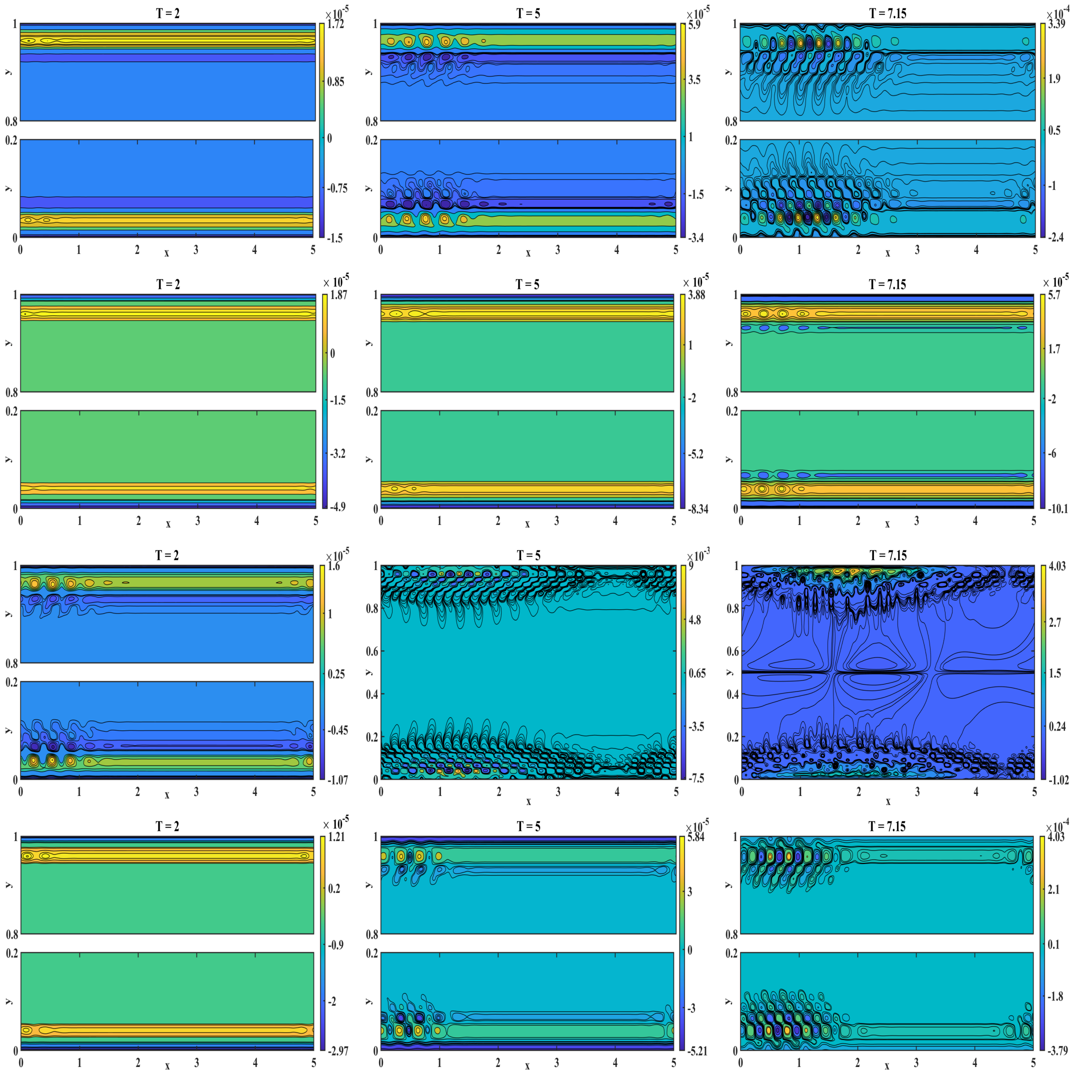

FIGURE 6.3: Contours of instantaneous volume ratio, δ_1, for the elastic stress dominated Rouse model ($\nu = 0.3, \alpha = 1/2$). Other parameters set at $Re = 70, We = 15$ (first row), $Re = 1000, We = 15$ (second row), $Re = 70, We = 20$ (third row) and $Re = 1000, We = 20$ (fourth row). Plots shown with broken y-axis do not show any structure formation around the centerline.

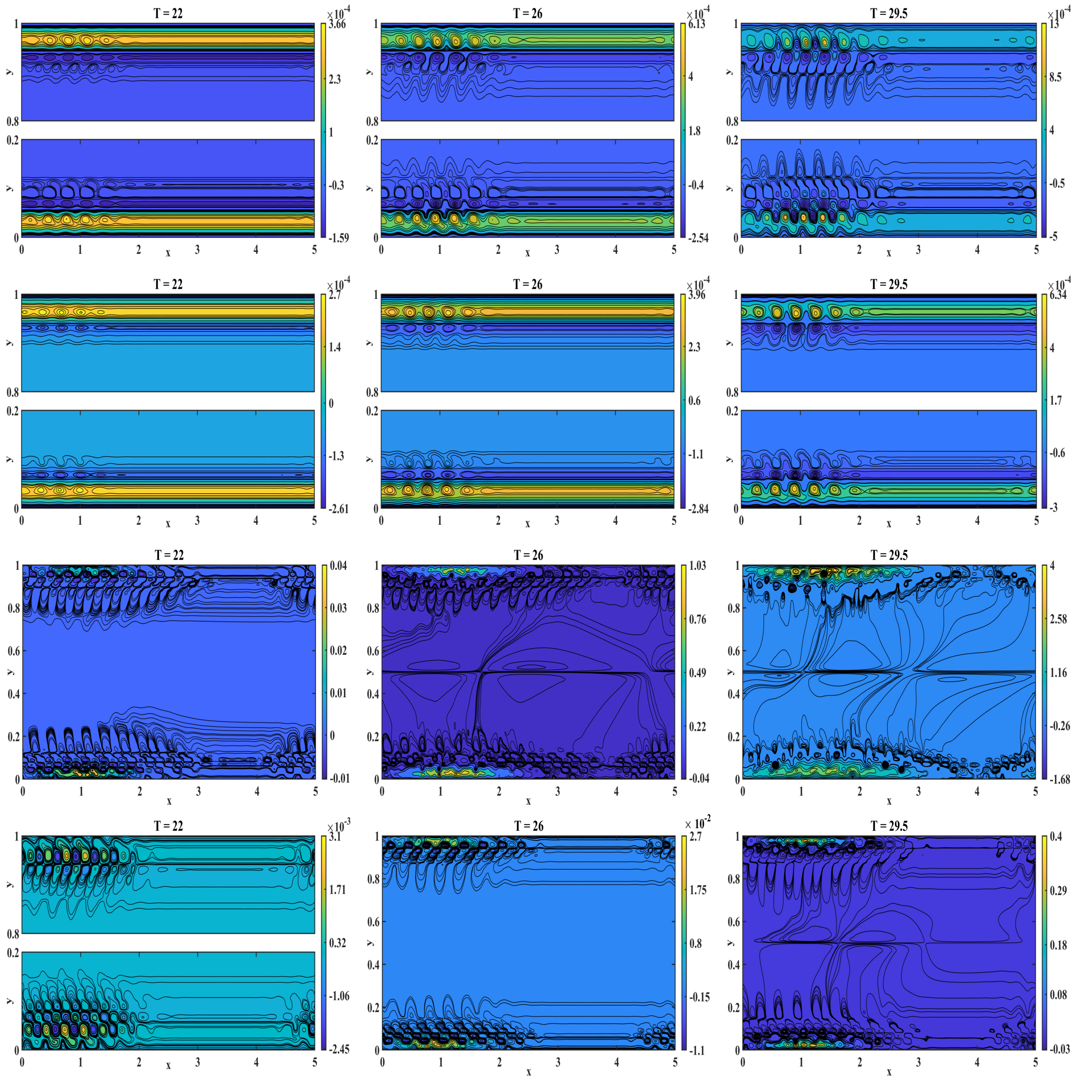

FIGURE 6.4: Contours of instantaneous volume ratio, δ_1, for the viscous stress dominated Zimm's model ($\nu = 0.5, \alpha = 2/3$). Other parameters set at $Re = 70, We = 15$ (first row), $Re = 1000, We = 15$ (second row), $Re = 70, We = 20$ (third row) and $Re = 1000, We = 20$ (fourth row). Plots shown with broken y-axis do not show any structure formation around the centerline.

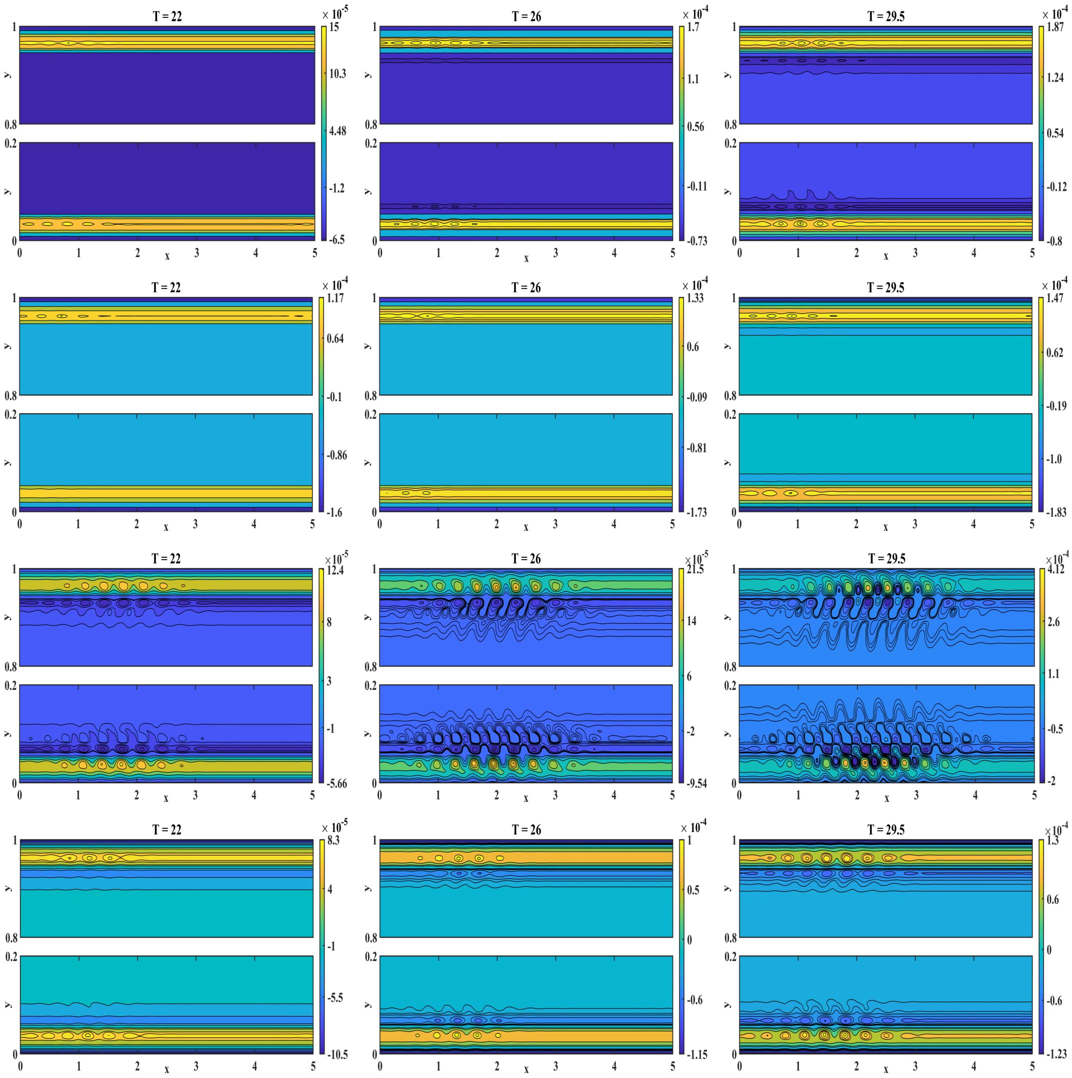

FIGURE 6.5: Contours of instantaneous volume ratio, δ_1, for the viscous stress dominated Rouse model ($\nu = 0.5, \alpha = 1/2$). Other parameters set at $Re = 70, We = 15$ (first row), $Re = 1000, We = 15$ (second row), $Re = 70, We = 20$ (third row) and $Re = 1000, We = 20$ (fourth row). Plots shown with broken y-axis do not show any structure formation around the centerline.

6.4 Conclusion

This chapter addresses the numerical simulation of the macroscopic model (6.1), which is upscaled from the microscale model for a non-Markovian continuous-time random walk for anomalous diffusional flow-fields relevant for ‘thick flows’ including polymer melts (Chauhan, Bansal, and Sircar, 2023), flows of liquid crystals (Sircar and Wang, 2010) as well as biological flows including mucus (Sircar et al., 2016) and cartilage (Sircar et al., 2015). Numerical simulations of channel flow at low to moderate Reynolds and Weissenberg numbers successfully reveal flow structures by enhancing the visualization of instantaneous elastic shock regions and detecting areas where the mean conformation tensor notably deviates from the instantaneous tensor, aligning with experimentally observed flow-instability transitions in subdiffusive flows.

Chapter 7

Conclusions: challenges faced and future problems

7.1 Introduction

Ideally, elastic springs and viscous dashpots are combined to create the traditional viscoelastic models of rheology, including the Oldroyd-B, Kelvin-Voigt, and Maxwell models. The conventional concept of derivatives with integer orders, or ordinary derivatives, forms the basis of these models. However, it has been found that these conventional models frequently lack the accuracy and predictive power, necessary to adequately capture the complex dynamic behaviour of polymers, particularly slow diffusion. Numerous tests demonstrate that the α_{th}-order fractional derivatives of applied strain, where $0 < \alpha < 1$, fit well with the relationship between the applied strain and the resulting stress determined from relaxation experiments. Fractional derivative models have been developed in response to these results. Over the last twenty years, fractional models have gained a solid reputation as being incredibly useful for precisely simulating subdiffusive viscoelastic materials (Koeller, 1984; Liu et al., 2008; Ferr'as et al., 2018). This capability was demonstrated in previous chapters when we saw how slow-diffusive mechanics of thick viscoelastic fluids are described by fractional models, shedding light on a variety of complex phenomena in these flows (Heymans and Bauwens, 1994; Schiessel et al., 1995).

The fractional models accurately represent numerous noteworthy occurrences including non-local, memory-dependent, and anomalous diffusion behaviours that arise in complex systems (Hoffmann and Prehl, 2008). Even though these models have several drawbacks, there are a number of scientific and technological issues where fractional derivative models can be used to understand flow behaviour better and create industry-specific technology. Additionally, these models are highly helpful in the medical domains for understanding blood flow, mucus flow, increased oil recovery, ecology, and so on. Several limitations for using fractional models are covered in section 7.2. Section 7.3 presents a variety of future issues motivated by the viscoelastic sub-diffusive flows. We present a range of fields in which fractional models can yield more insightful justifications and appropriate experiments. Furthermore, the methods developed in earlier chapters on the viscoelastic flows can be modified and customised to deal with particular problems and physical phenomena in a variety of problem domains.

7.2 Limitations

- There may be questions regarding the physical consistency of fractional models when they are used in physics and engineering. This is due to the fact that, without resorting to implausible interpretations, it is frequently difficult to draw a clear and meaningful connection between mathematical fractional operators and actual physical occurrences. Fractional derivatives, in contrast to integer-order derivatives, lack simple physical explanations. Because of this, scholars occasionally suggest interpretations that do not fairly depict the underlying physical behavior (Nigmatullin, 1992; Rutman, 1995), raising concerns about the viability of such models in particular situations.

- The appropriate and clear initialization of these models presents a significant difficulty when employing fractional models. Fractional models necessitate taking into account all historical data from negative infinity to the present, in contrast to typical integer-order models that depend on initial conditions at a particular time point. This basically means that in many real-world settings, initialising fractional models is computationally difficult and nearly impossible because they require an indefinite recollection of historical data. Therefore, handling the infinite-memory need can be a major challenge when utilising fractional models in real-world scenarios (Sabatier and Farges, 2018).

- The units of the parameters in fractional models frequently have no clear physical significance. Fractional model parameters may not have obvious, intuitive meanings in terms of actual phenomena, in contrast to classical models where parameters could represent physical quantities like mass or velocity. The inability to correlate these characteristics with particular physical attributes or mechanisms can result in a less intuitive understanding of the models in a physical setting (Sabatier, Farges, and Trigeassou, 2014; Sabatier et al., 2012).

- The complexity and diversity of methods to fractional calculus are reflected in more than thirty distinct definitions of the fractional differential operator (Oliveira and Tenreiro Machado, 2014a; Valério, Ortigueira, and Lopes, 2022). Fractional integration is a very new concept with vague mathematical definitions, but the same cannot be stated for fractional differentiation. One of the difficulties in applying fractional calculus in different contexts is the absence of a generally agreed definition for fractional derivatives. When working with fractional models, it is crucial to be very specific about the term being used because different definitions might cause differences in the behaviour and interpretation of fractional operators.

- It can be troublesome in some situations when a constant is given a nonzero derivative via the Riemann-Liouville fractional derivative. Additionally, the usage of the fractional Riemann-Liouville derivative for functions like exponential and Mittag-Leffler functions is limited because it exhibits a singularity at the origin for any arbitrary function that is constant at the origin. Higher regularity requirements for differentiability are necessary due to Caputo's derivative, which demands the first-order derivative to be computed before the fractional derivative can be determined. Consequently, although Caputo derivatives can only be defined for differentiable functions, Riemann-Liouville derivatives can be utilised for functions that have fractional derivatives of orders smaller than one (Oliveira and Tenreiro Machado, 2014b) but lack a first-order derivative.

- Fractional integration is defined in terms of a singular kernel in most cases. When solving or modelling fractional-order differential equations, this singularity may cause issues. Numerical computations with singular kernels can be difficult since handling these singularities calls for specific methods. Furthermore, singularities can influence the convergence and stability of numerical techniques, which increases the complexity of solving fractional differential equations when compared to integer-order ones (Sabatier, 2020; Caputo and Fabrizio, 2015).

Compared to classical PDEs, the models based on fractional differential equations are comparatively unknown. As a result, there are typically insufficient historical facts and established theories to address them. Because of this, using fractional models in real-world scientific and engineering applications may be challenging. Despite these difficulties, fractional derivatives have shown to be useful in a variety of fields, including biology, engineering, and physics. This emphasises how critical it is to confront and get over these computational challenges.

7.3 Future Problems

Fractional partial differential equations are versatile tools across diverse fields, capturing phenomena with non-local and memory-dependent behaviour (Uchaikin, 2013; Sun et al., 2018b). Applied in physics, fractional differential equations describe wave propagation in fractal media and model anomalous diffusion, sub-diffusion, and super-diffusion processes. In biology, they simulate long-range interactions in population dynamics, tumour growth, and cell migration. Finance employs fractional differential equations for risk management, portfolio optimization, and option pricing because they can simulate systems with memory effects. Engineering applications include modelling heat conduction, porous media fluid flow, and memory effects in structural mechanics. Fractional model adaptability addresses complex real-world problems, spanning fractional diffusion, wave equations, and specialized domains in physics, chemistry, biology, and engineering. Future research opportunities abound, offering a pathway to address challenges and advance understanding across a wide spectrum of scientific and engineering disciplines.

7.3.1 Microfluidic devices

Microfluidic devices, crucial in micro-electro-mechanical systems and microbiological sensors, consist of small-scale channels, chambers, and valves on glass, silicon, or polymer chips (Stone, Stroock, and Ajdari, 2004). These devices, with dimensions ranging from tens to hundreds of micrometres, offer precise control over fluid flow, impacting various fields like bioengineering, chemical transport, and heat management in electronics. At the core of microfluidic devices are electro-elastic instabilities (EEI), arising from the interplay between viscoelastic fluids and external electric fields at micro- and nano-levels. EEI encompasses electrohydrodynamics (EHD) and electrokinetic instabilities (EKI), each with distinct features shaping behaviours in applications from biotechnology to materials science. Efficient mixing is crucial, especially in clinical setups, where EEI-induced flow instabilities overcome laminar flow limitations, enhancing reactions.

Studies on classical viscoelastic fluids' EEIs extensively explore phenomena like chaotic flow fields and fluid mixing in microdevices (Sasmal, 2022). Recent investigations use fractional derivative-based models to explore anomalous diffusion, dynamics of slip flow, and the creation of multiple layers in microchannels that are electrically neutral. These types of models, such as temporal Caputo fractional derivative and fractional-order Oldroyd-B, provide insights into complex EEI phenomena that traditional differential equations struggle to capture (Feng et al., 2021; Liu, Zhang, and Jiang, 2021; Tian et al., 2022). Research by various authors demonstrates the pivotal role of fractional models in analyzing EEI in microfluidic devices. Incorporating fractional derivatives makes it possible to depict the characteristics of viscoelastic fluids and how they react to electric fields more accurately at micro- and nanoscales. This advancement contributes significantly to capture precise predictions and optimizations in diverse applications and promises a fruitful future research domain.

7.3.2 Nanofluids

Nanofluids, consisting of nanometer-scale particles in a fluid, have garnered attention for enhancing thermal conductivity, especially in viscoelastic nanofluids (Das et al., 2007). Slow diffusion is a common feature in viscoelastic nanofluids, and the addition of nanoparticles alters their diffusion properties, resulting in a slower diffusion rate (Guo et al., 2012; Aramideh, Vlachos, and Ardekani, 2019). Factors influencing this behaviour include nanoparticle type and concentration, as well as the viscoelastic nanofluid's particular rheological characteristics.

Enhancements in the modelling of viscoelastic nanofluids are provided via fractional derivatives. These derivatives efficiently capture non-local and memory-dependent activity, increasing the material's reaction to applied stresses and anticipating transient behaviour more precisely. They address anomalous diffusion that may occur in nanofluids and provide flexibility in modelling complex rheological properties, incorporating memory effects for better representation of deformation or flow responses. This approach aids in optimizing nanoparticle concentration and control in manufacturing processes, advancing scientific understanding, and opening up innovative applications in engineering fields such as biotechnology, tissue engineering, drug delivery systems, environmental cleanup, and enhanced oil recovery.

Although viscoelastic nanofluid research is still in its beginning stages, some computational investigations have examined heat transmission in nanoscale fluids using nonlinear fractional boundary layer equations. For example, research has been done (Cao et al., 2016b) on the heat transfer of nanofluids with fractional Maxwell viscoelastic characteristics over a moving plate and on unstable boundary layer flow. These works used time-dependent fractional derivatives and nonlinear fractional boundary layer equations to represent nanofluidic equations. An additional study examined heat transfer across a moving plate and incompressible, steady, and laminar fluid boundary flow while taking relaxation time parameters and distributed order time fractional operators (Liu et al., 2020b) into account. The modelling of viscoelastic nanofluids using fractional partial differential equations remains largely unexplored despite these discoveries, suggesting a promising field for further research.

7.3.3 Blood Flow

Blood, a complex fluid with unique rheological properties, exhibits non-Newtonian behaviour due to its composition of cells and plasma. It flows through vessels due to its viscosity and has some elasticity, allowing it to revert to its original shape after deformation. This viscoelastic nature (Thurston, 1972; Thurston, 1996) is crucial in various medical contexts, including cardiovascular diseases, respiratory diseases, cancer, and the design of medical devices. Understanding blood's viscoelastic behaviour is particularly relevant in hemorheology, aiding in the development of treatments for conditions like thrombosis and atherosclerosis (Dintenfass, 1964; Hell et al., 1989). Fractional derivatives play a vital role in modelling mathematical models with non-Newtonian and viscoelastic characteristics. Fractional derivatives provide more accurate modelling and analysis of blood movement inside vessels in the context of blood flow. It is possible for blood flow in capillaries and tiny vessels to display abnormal transport behaviour, and fractional derivatives are especially useful in describing such behaviour. Given the complex fractal-like geometries of blood vessels, fractional derivatives provide a natural framework for describing and analyzing systems with fractal properties, offering nuanced depictions of blood behaviour under different physiological and pathological conditions. Fractional models are particularly helpful in understanding atherosclerosis, a condition characterised by the buildup of fatty deposits on the arterial walls, which causes the vessels to narrow and obstruct normal blood flow. Atherosclerosis is intimately linked to conditions including diabetes, high blood pressure, smoking, oxidative stress, and ageing.

Researchers have employed mathematical modelling techniques utilizing fractional derivatives to study atherosclerosis in coronary arteries. While some models based on traditional equations captured atheroma plaque in simple geometries, fractional derivative models allow the incorporation of complex fractal-like geometries, memory, and slow diffusion (Cilla, Peña, and Martínez, 2013). Recent studies have employed fractional derivatives to analyze atherosclerosis and stenosed arteries, providing valuable insights beyond simple geometries (Yao et al., 2021). Studies using fractional models have explored various aspects of blood flow dynamics in conditions like atherosclerosis and stenosed arteries. For instance, researchers analyzed non-Newtonian magnetic blood flow in stenosed arteries and investigated chaotic dynamics in variable fractional order coronary artery models. These investigations contribute to the fundamental understanding of atherosclerosis and related health issues. Utilizing viscoelastic flow models based on fractional derivatives emerges as a viable path towards improving the knowledge of blood flow dynamics in diseases including carotid plaque, stenosis, and atherosclerosis (Zhou et al., 2022; Pérez Zerpa et al., 2015). Recent advancements have expanded on these insights, providing analyses that consider the viscoelasticity of blood flow. This approach holds the potential to offer valuable insights for addressing future challenges in the field of cardiovascular health and related medical conditions.

7.3.4 Plasma

Plasma, often referred to as the "fourth" state of matter, is a highly charged and energetic form of gas that arises when a regular gas is heated to extreme temperatures, causing ionization and the release of free electrons and ions (Goldston, 2020). Plasmas have special qualities that make them excellent electrical conductors, magnetic field generators, and thermally capable of extremely high temperatures. They play crucial roles in various high-energy phenomena in the universe, from stars and the sun to lightning on Earth. In addition to their natural occurrences, plasmas find applications in diverse fields, including astrophysical simulations, plasma TV screens, fluorescent lights, nuclear fusion, and plasma medicine. Complex plasmas with charged solid particles exhibit sub-diffusive behaviour influenced by magnetic fields. Sub-diffusion, characterized by constrained motion perpendicular to magnetic field lines, is observed in fusion experiments with irregular geometries. In the study of fusion plasmas, a super-diffusive framework is often applied, employing Lévy statistics and the fractional Fokker-Planck equation. Anomalous diffusion in plasmas under magnetic fields is modelled with fractional velocity derivatives and Langevin dynamics, providing insights into the transport of charged particles (Anderson, Moradi, and Rafiq, 2018).

Experimental studies on complex plasmas, particularly dusty plasmas, reveal sub-diffusive behaviour near melting points, showcasing caged motion and slower-than-usual particle movement (Kostadinova et al., 2021; Asgari, Muniandy, and Wong, 2011). The self-diffusion coefficient in these plasmas varies linearly with temperature. Fusion plasmas exhibit spatial non-locality and memory effects, leading to extensive particle displacements and anomalous transport in turbulent situations. Plasma turbulence, characterized by chaotic particle motion within plasmas, is explored using three-dimensional models. Anomalous transport in plasma turbulence is demonstrated through the movement of tracer particles, displaying a super-diffusive scaling pattern for their moments. Fractional derivatives emerge as a powerful tool for understanding physical phenomena in plasmas, providing a comprehensive theoretical framework for sub-diffusion, anomalous diffusion, and turbulence. Despite their potential, the application of fractional models in these contexts is an area that requires further exploration and research, presenting a promising avenue for future development.

7.3.5 Ecology

Fractional partial differential equations are significant in capturing numerous ecological phenomena due to their capacity to simulate memory effects, non-local interactions, and complicated spatial patterns (Kumar and Erturk, 2021; Ghanbari, 2021). These models are especially well-suited to ecological processes that display anomalous diffusion, like the dispersal of nutrients in soils, the spread of invasive species, and individual migration in heterogeneous landscapes. Fractional equations can be used to describe population dynamics with memory effects, in which conditions from the past affect the dynamics of the population today. This allows for the study of species that have been impacted by prior events. They are especially useful in explaining spatial patterns, aggregations, and fractal-like structures in populations, as well as the distribution of resources across landscapes (Rietkerk et al., 2004).

In the realm of biological models, fractional models are applied to understand interaction networks in food chains, particularly focusing on ecosystems involving phytoplankton, which play a crucial role in providing sustenance for marine life, generating oxygen, and contributing to atmospheric purification. The use of fractional derivatives in mathematical models efficiently handles the long-range temporal memory and space interactions inherent in biological systems.

Ecological systems often exhibit sub-diffusion, deviating from traditional diffusion patterns. Factors contributing to sub-diffusive behaviour include complex terrains, territorial behaviour of prey species, limited resources, and heightened awareness of predation risks (Sengupta, Kruppa, and Löwen, 2011). In order to accurately reflect the slower and more localised movement of prey, fractional derivatives must be included in the mathematical modelling of predator-prey systems with sub-diffusion. This method sheds light on the stability, distribution patterns, and spatial dynamics of predator-prey systems in diverse ecological contexts. The incorporation of fractional derivatives in ecological models is seen as a promising direction for future research, enabling the capture of various effects such as temporal memory, space interaction, and sub-diffusion in analogous ecological setups.

7.3.6 Mucus Layer

The mucus layer, a barrier of defence present in many parts of the body exposed to foreign chemicals either inside or outside the body, is essential to organ function and overall health. Mucus is a mixture of water, salts, glycoproteins, and other substances that have a heterogeneous polymer scaffold and viscoelastic characteristics. It serves critical functions in respiratory and gastrointestinal systems, protecting against foreign particles, controlling the movement of ions and nutrients, and providing lubrication. Specialized mucus types are generated in various body regions tailored to specific functions (Ernst et al., 2017). Health problems such as excessive mucus production in chronic bronchitis or unusually thick and sticky mucus in cystic fibrosis might result from disruptions in mucus production or composition. Understanding and regulating diffusive transfer across mucus layers are crucial for designing effective drug delivery systems. The diffusive transport within the mucus layer is a well-observed biological phenomenon that influences the movement of ions, bacteriophages, and other particles. Notably, bacteriophages with weak adhesive properties to mucus exhibit sub-diffusive motion, enhancing encounters with bacteria and showcasing a unique predator strategy. Gastric mucus in the digestive system acts as a barrier to diffusion, maintaining a significant pH gradient between the stomach lining and gastric lumen. Experimental studies and modelling have explored the behaviour of mucus, highlighting its significance in regulating the diffusion rate of small ions (Witten, Samad, and Ribbeck, 2018; Newby et al., 2018).

Fractional partial differential equations prove invaluable in modelling mucus layers, offering a comprehensive understanding of diffusion processes within them (Lewis, Missey, and Keener, 2021). These equations are in good accordance with the intricate dynamics of biological systems because they can predict anomalous diffusion, account for non-local interactions, and capture memory effects. Because fractional differential equations are flexible, mucus layer heterogeneity can be taken into account, providing a more realistic representation of particle behaviour in this critical biological context. Incorporating insights from fractional differential equations may offer a good fit for experimental data, enhancing our understanding of the unique characteristics of mucus and its role in biological environments.

7.3.7 Granular Flows

Granular materials exhibit intricate behaviours resulting from particle interactions, such as the surface waves, oscillons, caging effect, jamming, shear-banding, force-chain, segregation, and avalanche creation (Daerr and Douady, 1999; Goldhirsch, 2003; Reis, Ingale, and Shattuck, 2007; Fullmer and Hrenya, 2017; Zhou et al., 2020). The caging effect involves particles being temporarily trapped by neighbouring particles, causing erratic movement. Clustering and jamming refer to particle clustering and jamming in granular flows. Granular flows also display mixing and segregation behaviours. Anomalous diffusion in granular flows deviates from typical Brownian motion observed in gases and liquids. It occurs when granular particles move in a manner not predictable by standard diffusion equations, with the mean squared displacement adopting a power law with a different exponent from unity. Experimental investigations on driven granular systems have reported anomalous diffusion, observed through experiments and particle simulations (Marty and Dauchot, 2005).

The examination of diffusion characteristics in bi-disperse dry granular materials subjected to quasi-static cyclic shear has unveiled complex cage dynamics, which control sub-diffusion within the "slow relaxation" regime. An investigation into bi-disperse mixtures with concentration-dependent diffusivity identified two regimes, one exhibiting poly-disperse granular materials' anomalous scaling and another showing typical diffusive scaling (Christov and Stone, 2012). Anisotropic force networks in dense granular flows result in anisotropic diffusivity, where diffusivities along the average flow direction are roughly twice as large as those in the direction that is perpendicular. The particle motion can be sub-diffusive or super-diffusive due to varying shear rates and force networks.

While experimental and simulation evidence of sub-diffusion in granular materials is abundant, a comprehensive mathematical theory is lacking. Fractional differential equations offer a promising approach for understanding granular diffusion and describing complex granular behaviours. Fractional models contribute to a more accurate mathematical framework, fitting experimental data and extracting relevant parameters for various applications. The exploration of fractional granular rheology remains an untapped area, presenting an exciting avenue for future research.

7.4 Conclusion

While fractional models have proven invaluable in capturing complex phenomena with non-local and memory-dependent behaviour, their application is not without limitations. The complexity of these models can pose challenges in terms of computational demands and mathematical tractability. Furthermore, the extensive parameterization required for accurate representation may lack physical interpretability. Despite current limitations, the future holds exciting possibilities for refining and expanding the application of fractional models in these domains, offering deeper insights into the subdiffusive behaviour of viscoelastic fluids and advancing our comprehension of complex physical and biological systems.

Bibliography

Adelman, S. A. (1976). “Fokker–Planck equations for simple non-Markovian systems”. In: *J. Chem. Phys.* 64.1, pp. 124–130.

Akylas, T. R. (1982). “A nonlinear theory for the generation of water waves by wind”. In: *Studies in Appl. Math.* 67, pp. 1–24.

Akylas, T. R. and D. J. Benney (1980). “Direct resonance in nonlinear wave systems”. In: *Studies in Appl. Math.* 63.209-226.

Akylas, T. R. and D. J. Benney (1982). “The Evolution of Waves Near Direct-Resonance Conditions”. In: *Studies in Appl. Math.* 67, pp. 107–123.

Al-Khaled, Kamel and Shaher Momani (June 2005). “An approximate solution for a fractional diffusion-wave equation using the decomposition method”. In: *Applied Mathematics and Computation* 165.2, pp. 473–483.

Alexander, N. M. and W. V. Saarloos (2007). “An introductory essay on subcritical instabilities and the transition to turbulence in visco-elastic parallel shear flows”. In: *Physics Reports* 447.3, pp. 112–143.

An, Shujuan et al. (2022). “Electroosmotic and pressure-driven slip flow of fractional viscoelastic fluids in microchannels”. In: *Applied Mathematics and Computation* 425, p. 127073.

Anderson, Johan, Sara Moradi, and Tariq Rafiq (2018). “Non-Linear Langevin and Fractional Fokker–Planck Equations for Anomalous Diffusion by Lévy Stable Processes”. In: *Entropy* 20, p. 760.

Aramideh, Soroush, Pavlos P. Vlachos, and Arezoo M. Ardekani (2019). “Nanoparticle dispersion in porous media in viscoelastic polymer solutions”. In: *J. Non-Newton. Fluid Mech.* 268, pp. 75–80.

Aranha, J.A., D.K.P. Yue, and C.C. Mei (1982). “Nonlinear waves near a cut off frequency in an acoustic duct- a numerical study”. In: *J. Fluid Mech.* 121, pp. 465–485.

Ascher, Uri M., Steven J. Ruuth, and Brian T. R. Wetton (1995). “Implicit-explicit methods for time-dependent partial differential equations”. In: *SIAM Journal on Numerical Analysis* 32, pp. 797–823.

Asgari, H., S. V. Muniandy, and C. S. Wong (2011). “Stochastic dynamics of charge fluctuations in dusty plasma: A non-Markovian approach”. In: *Phys. Plasmas* 18, p. 083709.

Atalik, K. and R. Keunings (2002). “Non-linear temporal stability analysis of viscoelastic plane channel flows using a fully-spectral method”. In: *J. non-Newt. Fluid Mech.* 102, pp. 299–319.

Bagley, R. L. and P. J. Torvik (1983). “A Theoretical Basis for the Application of Fractional Calculus to Viscoelasticity”. In: *Journal of Rheology* 27, pp. 201–210.

Bagley, R. L. and P. J. Torvik (1986). “On the Fractional Calculus Model of Viscoelastic Behavior”. In: *Journal of Rheology* 30, pp. 133–155.

Bansal, D., T. Chauhan, and S. Sircar (2022). “Spatiotemporal linear stability of viscoelastic Saffman–Taylor flows”. In: *Phys. Fluids* 34.10.

Bansal, D., D. Ghosh, and S. Sircar (2021). “Spatiotemporal linear stability of viscoelastic free shear flows: Nonaffine response regime”. In: *Phys. Fluids* 33.054106.

Bansal, D., D. Ghosh, and S. Sircar (2023). “Selection Mechanism in Non-Newtonian Saffman-Taylor Fingers”. In: *SIAM J. Appl. Math.* 83.2, pp. 329–353.

Benny, D. J. and L. H. Gustavsson (1981). “A new mechanism for linear and nonlinear hydrodynamic instability”. In: *Studies in Appl. math* 64, pp. 185–209.

Beris, A. N. and B. J. Edwards (1994). *Thermodynamics of Flowing Systems: With Internal Microstructure*. Oxford University Press.

Bers, A. (1983). *Space-time evolution of plasma instabilities-absolute and convective*. Vol. 1. Handbook of Plasma Physics.

Bertram, R. (1977). “The development of fractional calculus 1695–1900”. In: *Historia Mathematica* 4.1, pp. 75–89.

Bhatia, R. (2015). *Positive Definite Matrices*. Princeton University Press.

Birajdar, Gunvant A. (2014). “Numerical Solution of Time Fractional Navier-Stokes Equation by Discrete Adomian decomposition method”. In: *Nonlinear Engineering* 3, pp. 21–26.

Bird, R., R. Armstrong, and O. Hassager (1987). *Dynamics of Polymeric Liquids*. Wiley.

Bird, R. Byron, ed. (1987). *Dynamics of polymeric liquids*. 2nd ed. New York: Wiley.

Brader, J. M. (2010). “Nonlinear rheology of colloidal dispersions”. In: *J. Phys.: Condens. Matter* 22.363101.

Briggs, R. J. (1964). *Electron-stream interaction with plasmas*. Cam bridge: MIT Press.

Brunner, Hermann, Leevan Ling, and Masahiro Yamamoto (Sept. 2010). “Numerical simulations of 2D fractional subdiffusion problems”. In: *Journal of Computational Physics* 229.18, pp. 6613–6622.

Burgers, JM (1935). “Mechanical considerations-model systems-phenomenological theories of relaxation and of viscosity”. In: *First report on viscosity and plasticity* 1.

Cao, Zhi et al. (2016a). “MHD flow and heat transfer of fractional Maxwell viscoelastic nanofluid over a moving plate”. In: *Journal of Molecular Liquids* 222, pp. 1121–1127.

Cao, Zhi et al. (2016b). “MHD flow and heat transfer of fractional Maxwell viscoelastic nanofluid over a moving plate”. In: *J. Mol. Liq.* 222, pp. 1121–1127.

Caputo, Michele and Mauro Fabrizio (Apr. 2015). “A new definition of fractional derivative without singular Kernel”. In: *Prog Fract Differ Appl* 1, pp. 73–85.

Carrera, Y. et al. (2017). “A fractional-order Maxwell model for non-Newtonian fluids”. In: *Physica A: Statistical Mechanics and its Applications* 482, pp. 276–285.

Causon, D. M. (2010). *Introductory finite difference methods for PDEs*. en.

Chaudhary, Indresh et al. (2021). “Linear instability of viscoelastic pipe flow”. In: *Journal of Fluid Mechanics* 908, A11.

Chauhan, Tanisha, Diksha Bansal, and Sarthok Sircar (July 2023). “Spatiotemporal linear stability of viscoelastic subdiffusive channel flows: a fractional calculus framework”. In: *Journal of Engineering Mathematics* 141.1, p. 8.

Chen, J. et al. (2014). “Numerical simulation for the three-dimension fractional sub-diffusion equation”. In: *Applied Mathematical Modelling* 38, pp. 3695–3705.

Chen, Yanli et al. (2021). “Analysis of blood flow characteristics in fractal vascular network based on the time fractional order”. In: *Physics of Fluids* 33.4, p. 041902.

Chhabra, R. P. (2010). “Non-Newtonian Fluids: An Introduction”. In: *Rheology of Complex Fluids*. New York, NY: Springer New York, pp. 3–34.

Choudhury, Moutushi Dutta et al. (2012). “Forced spreading and rheology of starch gel: Viscoelastic modeling with fractional calculus”. In: *Colloids and Surfaces A: Physicochemical and Engineering Aspects* 407, pp. 64–70.

Christov, Ivan C. and Howard A. Stone (2012). “Resolving a paradox of anomalous scalings in the diffusion of granular materials”. In: *Proc. Natl. Acad. Sci.* 109.40, pp. 16012–16017.

Cilla, M., E. Peña, and M. A. Martínez (2013). “Mathematical modelling of atheroma plaque formation and development in coronary arteries”. In: *J. R. Soc. Interface* 11, p. 20130866.

Clemmow, P.C. and J.P. Dougherty (1969). *Electronics of particles and plasmas*. Reading, Mass: Addison-Wesle.

Coffey, W. T., Yu. P. Kalmykov, and J. T. Waldron (2004). *The Langevin Equation: With Applications to Stochastic Problems in Physics, Chemistry and Electrical Engineering*. 2nd. Vol. 14. World Scientific Series in Contemporary Chemical Physics. World Scientific Publishing Company.

Craiem, Damian and Richard L Magin (2010). “Fractional order models of viscoelasticity as an alternative in the analysis of red blood cell (RBC) membrane mechanics”. In: *Physical Biology* 7, p. 013001.

Cremer, L. (1953). “Theorie der Luftschall-Di mpfung im l echteckkanal mit schluckender Wand and das sich dabei ergebende hSchste DS mpfungsmag”. In: *Acustica* 8, pp. 249–263.

Crighton, D.G. and M. Gaster (1976). “Stability of slowly-diverging jet flow”. In: *J. Fluid Mech* 77, pp. 397–413.

Crouzeix, Michel (1980). “Une méthode multipas implicite-explicite pour l’approximation des équations d’évolution paraboliques”. In: *Numerische Mathematik* 35, pp. 257–276.

Daerr, Adrian and Stéphane Douady (1999). “Two types of avalanche behaviour in granular media”. In: *Nature* 399, pp. 241–243.

Das, Sarit K et al. (2007). *Nanofluids: science and technology*. John Wiley & Sons.

De Espindola, J.J., João M. Da Silva Neto, and Eduardo M.O. Lopes (2005). “A generalised fractional derivative approach to viscoelastic material properties measurement”. In: *Applied Mathematics and Computation* 164, pp. 493–506.

Dehghan, Mehdi and Mostafa Abbaszadeh (2018). “A finite difference/finite element technique with error estimate for space fractional tempered diffusion-wave equation”. In: *Computers & Mathematics with Applications* 75, pp. 2903–2914.

Di Lorenzo, Salvatore et al. (2017). “Non-linear viscoelastic behavior of polymer melts interpreted by fractional viscoelastic model”. In: *Meccanica* 52, pp. 1843–1850.

Di Paola, M., A. Pirrotta, and A. Valenza (2011). “Visco-elastic behavior through fractional calculus: An easier method for best fitting experimental results”. In: *Mechanics of Materials* 43, pp. 799–806.

Di Paola, Mario et al. (2014). “On the influence of the initial ramp for a correct definition of the parameters of fractional viscoelastic materials”. In: *Mechanics of Materials* 69, pp. 63–70.

Diethelm, K. and A.D. Freed (Jan. 2006). “An efficient algorithm for the evaluation of convolution integrals”. In: *Computers & Mathematics with Applications* 51.1, pp. 51–72.

Diethelm, Kai and Neville J. Ford (2002). “Analysis of Fractional Differential Equations”. In: *Journal of Mathematical Analysis and Applications* 265.2, pp. 229–248. ISSN: 0022-247X.

Ding, Hengfei and Changpin Li (2018). “High-order numerical approximation formulas for Riemann–Liouville (Riesz) tempered fractional derivatives: Construction and application (II)”. In: *Applied Mathematics Letters* 86, pp. 208–214.

Ding, Xiang et al. (2017). “Unexpected viscoelastic deformation of tight sandstone: Insights and predictions from the fractional Maxwell model”. In: *Scientific Reports* 7.1, p. 11336.

Dintenfass, Leopold (1964). “Rheologic Approach To Thrombosis and Atherosclerosis”. In: *Angiology* 15.8, pp. 333–343.

Doi, M and S. F. Edwards (1986). “The theory of polymer dynamics, the Clarendon Press, Oxford University Press, New York, 1986, 391”. In: *Journal of Polymer Science Part C: Polymer Letters* 27.7, pp. 239–240.

Dubief, Y. et al. (2005). “New answers on the interaction between polymers and vortices in turbulent flows”. In: *Turbul. Combust. Former. Appl. Sci. Res.* 74.4, pp. 311–329.

Eldred, Lloyd B., William P. Baker, and Anthony N. Palazotto (1995). “Kelvin-Voigt versus fractional derivative model as constitutive relations for viscoelastic materials”. In: *AIAA Journal* 33, pp. 547–550.

Ercan, Ali and M. Levent Kavvas (2016). *Numerical Solution and Application of Time-Space Fractional Governing Equations of One-Dimensional Unsteady Open Channel Flow Process*. preprint. Rivers and Lakes/Mathematical applications.

Ernst, M. et al. (2017). “A Model for the Transient Subdiffusive Behavior of Particles in Mucus”. In: *Biophys. J.* 112.1, pp. 172–179.

Failla, Giuseppe and Massimiliano Zingales (2020). “Advanced materials modelling via fractional calculus: challenges and perspectives”. In: *Philosophical Transactions of the Royal Society A: Mathematical, Physical and Engineering Sciences* 378, p. 20200050.

Fattal, R. and R. Kupferman (2004). “Constitutive laws for the matrix-logarithm of the conformation tensor”. In: *J. non-Newt. Fluid Mech.* 123.2, pp. 281–285.

Feng, Chenqing et al. (2021). “The slip flow of generalized Maxwell fluids with time-distributed characteristics in a rotating microchannel”. In: *Appl. Math. Lett* 120, p. 107260.

Feng, L. B. et al. (2016). “Finite element method for space-time fractional diffusion equation”. In: *Numerical Algorithms* 72, pp. 749–767.

Feng, Libo, Fawang Liu, and Ian Turner (2019). “Finite difference/finite element method for a novel 2D multi-term time-fractional mixed sub-diffusion and diffusion-wave equation on convex domains”. In: *Communications in Nonlinear Science and Numerical Simulation* 70, pp. 354–371.

Ferr'as, L.L. et al. (2018). "Theoretical and numerical analysis of unsteady fractional viscoelastic flows in simple geometries". In: *Comput. Fluids* 174, pp. 14–33.

Ferrás, L.L. et al. (2018). "Theoretical and numerical analysis of unsteady fractional viscoelastic flows in simple geometries". In: *Computers & Fluids* 174, pp. 14–33.

Ferrás, Luís Lima et al. (2017). "A primer on experimental and computational rheology with fractional viscoelastic constitutive models". In: Zlín, Czech Republic, p. 020002.

Fetecau, C. et al. (2009). "Exact solutions for the flow of a generalized Oldroyd-B fluid induced by a constantly accelerating plate between two side walls perpendicular to the plate". In: *J. non-Newt. Fluid Mech.*, pp. 189–201.

Field, J.S., M.V. Swain, and N. Phan-Thien (1996). "An experimental investigation of the use of random squeezing to determine the complex modulus of viscoelastic fluids". In: *Journal of Non-Newtonian Fluid Mechanics* 65.2-3, pp. 177–194.

Flügge, Wilhelm (1975). "Viscoelastic Models". In: *Viscoelasticity*. Berlin, Heidelberg: Springer Berlin Heidelberg, pp. 4–33.

Fogelson, Aaron L. and Keith B. Neeves (Jan. 2015). "Fluid Mechanics of Blood Clot Formation". In: *Annual Review of Fluid Mechanics* 47.1, pp. 377–403.

Fricks, J. et al. (2009). "Time-Domain Methods for Diffusive Transport in Soft Matter". In: *SIAM J. Appl. Math.* 69.5, pp. 1277–1308.

Friedrich, C. (1991). "Relaxation and retardation functions of the Maxwell model with fractional derivatives". In: *Rheologica Acta* 30.2, pp. 151–158.

Friedrich, Chr., H. Schiessel, and A. Blumen (1999). "Constitutive behavior modeling and fractional derivatives". In: *Rheology Series*. Vol. 8. Elsevier, pp. 429–466.

Fullmer, William D. and Christine M. Hrenya (2017). "The Clustering Instability in Rapid Granular and Gas-Solid Flows". In: *Annu. Rev. Fluid Mech.* 49, pp. 485–510.

Gaster, M., E. Kit, and I. Wygnanski (1985). "Large scale structures in a forced tubulent mixing layer". In: *J. Fluid Mech.* 150, pp. 23–29.

Gemant, A. (1936). "A Method of Analyzing Experimental Results obtained from Elasto-viscous Bodies". In: *Physics* 7.8, pp. 311–317.

Gemant, A. (1938). "XLV. *On* fractional differentials". In: *The London, Edinburgh, and Dublin Philosophical Magazine and Journal of Science* 25.168, pp. 540–549.

Ghanbari, Behzad (2021). "On the modeling of an eco-epidemiological model using a new fractional operator". In: *Results Phys.* 21, p. 103799.

Gittes, F. et al. (1997). "Microscopic Viscoelasticity: Shear Moduli of Soft Materials Determined from Thermal Fluctuations". In: *Phys. Rev. Lett.* 79 (17), pp. 3286–3289.

Glockle, W. G. and T. F. Nonnenmacher (1991). "Fractional integral operators and Fox functions in the theory of viscoelasticity". In: *Macromolecules* 24.6426–6434.

Glockle, W. G. and T. F. Nonnenmacher (1994). "Fractional relaxation and the time-temperature superposition principle". In: *Rheo. Acta* 33.337–343.

Goldhirsch, Isaac (2003). "RAPID GRANULAR FLOWS". In: *Annu. Rev. Fluid Mech.* 35, pp. 267–293.

Goldston, Robert J (2020). *Introduction to plasma physics*. CRC Press.

Goychuk, I. and T. Pöschel (2020). "Hydrodynamic memory can boost enormously driven nonlinear diffusion and transport". In: *Phys. Rev. E* 102.1, p. 012139.

Goychuk, Igor (2012). "Viscoelastic Subdiffusion: Generalized Langevin Equation Approach". In: *Advances in Chemical Physics*. Ed. by Stuart A. Rice and Aaron R. Dinner. Hoboken, NJ, USA: John Wiley & Sons, Inc., pp. 187–253.

Goychuk, Igor, Vasyl O. Kharchenko, and Ralf Metzler (Nov. 2017). "Persistent Sinai-type diffusion in Gaussian random potentials with decaying spatial correlations". In: *Physical Review E* 96.5, p. 052134.

Goychuk, Igor and Thorsten Pöschel (Sept. 2021). "Fingerprints of viscoelastic subdiffusion in random environments: Revisiting some experimental data and their interpretations". In: *Physical Review E* 104.3, p. 034125.

Gritsenko, Dmitry and Roberto Paoli (2020). "Theoretical Analysis of Fractional Viscoelastic Flow in Circular Pipes: Parametric Study". In: *Applied Sciences* 10, p. 9080.

Guo, Hongyu et al. (2012). "Entanglement-Controlled Subdiffusion of Nanoparticles within Concentrated Polymer Solutions". In: *Phys. Rev. Lett.* 109, p. 055901.

Gustavsson, L. H. (1981). "Resonant growth of three-dimensional disturbances in plane Poiseuille flow". In: *J. Fluid Mech* 112.253-264.

Gustavsson, L. H. and L. S. Hultgren (1980). "A resonance mechanism in plane Couette flow". In: *J. Fluid Mech* 98, pp. 149–159.

Hameduddin, I. (2018). "Tackling viscoelastic turbulence". PhD thesis. John Hopkins University.

Hamid, Muhammad et al. (2019). "Numerical investigation of fractional-order unsteady natural convective radiating flow of nanofluid in a vertical channel". In: *AIMS Mathematics* 4, pp. 1416–1429.

Hanif, Hanifa (2022). "A computational approach for boundary layer flow and heat transfer of fractional Maxwell fluid". In: *Mathematics and Computers in Simulation* 191, pp. 1–13.

Hao, Zhaopeng et al. (2016). "A finite difference scheme for semilinear space-fractional diffusion equations with time delay". In: *Applied Mathematics and Computation* 275, pp. 238–254.

Hayat, T, S Nadeem, and S Asghar (2004). "Periodic unidirectional flows of a viscoelastic fluid with the fractional Maxwell model". In: *Applied Mathematics and Computation* 151, pp. 153–161.

Hell, K M et al. (1989). "Importance of blood viscoelasticity in arteriosclerosis". In: *Angiology* 40, pp. 539–546.

Hernández-Jiménez, A. et al. (2002). "Relaxation modulus in PMMA and PTFE fitting by fractional Maxwell model". In: *Polymer Testing* 21, pp. 325–331.

Heymans, N. and J.C. Bauwens (1994). "Fractal rheological models and fractional differential equations for viscoelastic behavior". In: *Rheola. Acta* 33, 210—219.

Hilfer, R (2000). *Applications of Fractional Calculus in Physics*. WORLD SCIENTIFIC.

Ho, C.M. and P. Huerre (1984). "Perturbed free shear layers". In: *Annu. Rev. Fluid Mech.* 16, pp. 365–424.

Hoffmann, Karl Heinz and Janett Prehl (2008). "Anomalous Transport on Disordered Fractals". In: *Anomalous Transport: Foundations and Applications*. Ed. by Günter Radons Rainer Klages and Igor M. Sokolov. Dordrecht, the Netherlands: John Wiley & Sons, pp. 397–427.

Hohenegger, C., R. Durr, and D.M. Senter (2017). “Mean first passage time in a thermally fluctuating viscoelastic fluid”. In: *Journal of Non-Newtonian Fluid Mechanics* 242, pp. 48–56.

Hohenegger, Christel and Scott A. McKinley (2018). “Reconstructing Complex Fluid Properties from the Behavior of Fluctuating Immersed Particles”. In: *SIAM Journal on Applied Mathematics* 78, pp. 2200–2226.

Huang, Jingting et al. (2022). “Numerical Study for the Performance of Viscoelastic Fluids on Displacing Oil Based on the Fractional-Order Maxwell Model”. In: *Polymers* 14.24, p. 5381.

Huerre, P. and P. A. Monkewitz (1990). “Local and global instabilities in spatially developing flows”. In: *Ann. Rev. Fluid Mech.* 22, pp. 473–537.

Hultgren, L. S. and L. H. Gustavsson (1981). “Algebraic growth of disturbances in a laminar boundary layer”. In: *Phys. Fluids* 24, pp. 1000–1004.

Hyder Ali Muttaqi Shah, S. and Haitao Qi (2010). “Starting solutions for a viscoelastic fluid with fractional Burgers’ model in an annular pipe”. In: *Nonlinear Analysis: Real World Applications* 11, pp. 547–554.

Jaber, Khaled K. and Rami S. Ahmad (2018). “Analytical solution of the time fractional Navier-Stokes equation”. In: *Ain Shams Engineering Journal* 9, pp. 1917–1927.

Jacob, J Sheela, J Hellan Priya, and A Karthika (2020). “APPLICATIONS OF FRACTIONAL CALCULUS IN SCIENCE AND ENGINEERING”. In: *JOURNAL OF CRITICAL REVIEWS* 7.13.

Jaishankar, A. and G. H. McKinley (2014). “A fractional K-BKZ constitutive formulation for describing the nonlinear rheology of multiscale complex fluids”. In: *J. Rheol.* 58.6, pp. 1751–1788.

Jamil, Muhammad, Constantin Fetecau, and Corina Fetecau (2012). “Unsteady flow of viscoelastic fluid between two cylinders using fractional Maxwell model”. In: *Acta Mechanica Sinica* 28.2, pp. 274–280.

Jannelli, Alessandra (Feb. 2022). “Adaptive numerical solutions of time-fractional advection–diffusion–reaction equations”. In: *Communications in Nonlinear Science and Numerical Simulation* 105, p. 106073.

Jia, Jiu-hong and Hong-xing Hua (2008). “Study of Oscillating Flow of Viscoelastic Fluid With the Fractional Maxwell Model”. In: *Journal of Fluids Engineering* 130, p. 041201.

Jiménez A. H. Santiago J.H., García A.M.and Gonzáles J.S. (2002). “Relaxation modulus in PMMA and PTFE fitting by fractional Maxwell model”. In: *Polym. Testing* 21, pp. 325–331.

Jin, Bangti, Buyang Li, and Zhi Zhou (Jan. 2018). “Numerical Analysis of Nonlinear Subdiffusion Equations”. In: *SIAM Journal on Numerical Analysis* 56.1, pp. 1–23.

Jin, Bangti, Buyang Li, and Zhi Zhou (Feb. 2019). “Subdiffusion with a time-dependent coefficient: Analysis and numerical solution”. In: *Mathematics of Computation* 88.319, pp. 2157–2186.

Khalid, M. et al. (2021). “The centre-mode instability of viscoelastic plane Poiseuille flow”. In: *J. Fluid Mech.* 915.A43.

Khan, M., S. Hyder Ali, and Haitao Qi (2009a). “Exact solutions of starting flows for a fractional Burgers’ fluid between coaxial cylinders”. In: *Nonlinear Analysis: Real World Applications* 10, pp. 1775–1783.

Khan, M., S. Hyder Ali, and Haitao Qi (2009b). “On accelerated flows of a viscoelastic fluid with the fractional Burgers’ model”. In: *Nonlinear Analysis: Real World Applications* 10, pp. 2286–2296.

Kim, K. and R. Sureshkumar (2013). “Spatiotemporal evolution of hairpin eddies, Reynolds stress and polymer torque in drag-reduced turbulent channel flows.” In: *Phys. Rev. E* 87.6, p. 063002.

Kirkwood, J. G. (1954). “The general theory of irreversible processes in solutions of macromolecules”. In: *J. Poly. Sci.* 12.1.

Kiss, Miklos Z, Tomy Varghese, and Timothy J Hall (2004). “Viscoelastic characterization of *in vitro* canine tissue”. In: *Physics in Medicine and Biology* 49, pp. 4207–4218.

Koch, W. (1986). “Direct resonance in Orr-Sommerfeld problems”. In: *Acta Mech.* 59, pp. 11–29.

Koeller, R. C. (1984). “Applications of Fractional Calculus to the Theory of Viscoelasticity”. In: *Journal of Applied Mechanics* 51.2, pp. 299–307.

Kohandel, M et al. (2005). “Frequency dependence of complex moduli of brain tissue using a fractional Zener model”. In: *Physics in Medicine and Biology* 50, pp. 2799–2805.

Kontou, E. and S. Katsourinis (2016). “Application of a fractional model for simulation of the viscoelastic functions of polymers”. In: *Journal of Applied Polymer Science* 133, p. 43505.

Kostadinova, E. G. et al. (2021). “Fractional Laplacian spectral approach to turbulence in a dusty plasma monolayer”. In: *Phys. Plasmas* 28.7, p. 073705.

Kou, S. C. and X. S. Xie (2004). “Generalized Langevin Equation with Fractional Gaussian Noise: Subdiffusion within a Single Protein Molecule”. In: *Phys. Rev. Lett.* 93.18, p. 180603.

Kremer, K. and G. S. Grest (1990). “Dynamics of entangled linear polymer melts: A molecular-dynamics simulation”. In: *J. Chem. Phys.* 92.8, pp. 5057–5086.

Kumar, Pushpendra and Vedat Suat Erturk (2021). “Environmental persistence influences infection dynamics for a butterfly pathogen via new generalised Caputo type fractional derivative”. In: *Chaos Solit. Fractals* 144, p. 110672. DOI: `10.1016/j.chaos.2021.110672`.

Kundu, Pijush K. (1972). “Small Disturbance Stability of Plane Poiseuille Flow of Oldroyd Fluid”. In: *The Physics of Fluids* 15.7, pp. 1207–1212.

Kupfer, K., A. Bers, and A. K. Ram (1987). “The cusp map in the complex-frequency plane for absolute instability”. In: *Phys. Fluids* 30.10, pp. 3075–3082.

Laghari, Muzaffar Hussain, Kashif Ali Abro, and Asif Ali Shaikh (2017). “Helical flows of fractional viscoelastic fluid in a circular pipe”. In: *International Journal of ADVANCED AND APPLIED SCIENCES* 4, pp. 97–105.

Lai, Samuel K. et al. (Jan. 2009). “Altering Mucus Rheology to “Solidify” Human Mucus at the Nanoscale”. In: *PLoS ONE* 4.1. Ed. by Laurent Kreplak, e4294.

Landau, L.D. and E.M. Lifshitz (1959). *Fluid Mechanics*. London: Permagon Press.

Lang, S. (2001). *Fundamentals of Differential Geometry*. Vol. 191. Springer.

Larson, R. G. (2000). “Turbulence without inertia”. In: *Nature* 405, pp. 27–28.

Laun, H. M. (1978). “Description of the non-linear shear behaviour of a low density polyethylene melt by means of an experimentally determined strain dependent memory function”. In: *Rheologica Acta* 17, pp. 1–15.

Laun, H. M. (1986). “Prediction of Elastic Strains of Polymer Melts in Shear and Elongation”. In: *Journal of Rheology* 30, pp. 459–501.

Lee, K. C. and B. A. Finlayson (1986). “Stability of plane poiseuille and couette flow of a Maxwell fluid”. In: *Journal of Non-Newtonian Fluid Mechanics* 21.1, pp. 65–78.

LeVeque, Randall J. (Jan. 2007). *Finite Difference Methods for Ordinary and Partial Differential Equations: Steady-State and Time-Dependent Problems*. Society for Industrial and Applied Mathematics.

Levine, A. J. and T. C. Lubensky (2001). “Response function of a sphere in a viscoelastic two-fluid medium”. In: *Phys. Rev. E* 63.4, p. 041510.

Lewandowski, R. and B. Chorążyczewski (2010). “Identification of the parameters of the Kelvin–Voigt and the Maxwell fractional models, used to modeling of viscoelastic dampers”. In: *Computers & Structures* 88.1-2, pp. 1–17.

Lewis, Owen L., Ella Missey, and James P. Keener (2021). “Principles of slowed hydrogen diffusion through a mucus layer”. In: *Phys. Rev. E* 104 (4), p. 044403.

Li, Changpin and An Chen (2018). “Numerical methods for fractional partial differential equations”. In: *International Journal of Computer Mathematics* 95, pp. 1048–1099.

Li, Changpin and Fanhai Zeng (2012). “FINITE DIFFERENCE METHODS FOR FRACTIONAL DIFFERENTIAL EQUATIONS”. In: *International Journal of Bifurcation and Chaos* 22, p. 1230014.

Li, Changpin and Fanhai Zeng (2015). *Numerical methods for fractional calculus*. Chapman & Hall/CRC numerical analysis and scientific computing. OCLC: ocn900624459. Boca Raton: CRC Press.

Li, J., S. Sircar, and Q. Wang (2010). “A Note on the Kinematics of Rigid Molecules in Linear Flow Fields and Kinetic Theory for Biaxial Liquid Crystal Polymers”. In: *e-LC Commun.)*

Li, Xianjuan and Chuanju Xu (2009). “A Space-Time Spectral Method for the Time Fractional Diffusion Equation”. In: *SIAM Journal on Numerical Analysis* 47, pp. 2108–2131.

Lifshitz, E. M. and L.P. Pitaevskii (1981). “Physical kinetics”. In: London: Pergamon. Chap. 6.

Lingwood, R. J. (1997). “Absolute instability of the Ekman layer and related rotating flows”. In: *J. Fluid Mech.* 331, pp. 405–428.

Liu, F. et al. (2007). “Stability and convergence of the difference methods for the space–time fractional advection–diffusion equation”. In: *Applied Mathematics and Computation* 191, pp. 12–20.

Liu, Lin et al. (2020a). “Flow and heat transfer of generalized Maxwell fluid over a moving plate with distributed order time fractional constitutive models”. In: *International Communications in Heat and Mass Transfer* 116, p. 104679.

Liu, Lin et al. (2020b). “Flow and heat transfer of generalized Maxwell fluid over a moving plate with distributed order time fractional constitutive models”. In: *Int. Commun. Heat Mass Transf.* 116, p. 104679.

Liu, Nan et al. (2018). “Time second-order finite difference/finite element algorithm for nonlinear time-fractional diffusion problem with fourth-order derivative term”. In: *Computers & Mathematics with Applications* 75, pp. 3521–3536.

Liu, Xiaolin and Dejian Li (2020). “A Nonlinear Damage Creep Model with Time-varying Viscoelasticity Based on Fractional Theory for Rock Materials”. In: *IOP Conference Series: Earth and Environmental Science* 570.3, p. 032012.

Liu, Y., H. Zhang, and X. Jiang (2021). “Fast evaluation for magnetohydrodynamic flow and heat transfer of fractional Oldroyd-B fluids between parallel plates”. In: *Z. Angew. Math. Mech.*

Liu, Yaozong et al. (2008). “Theoretical study of two-dimensional phononic crystals with viscoelasticity based on fractional derivative models”. In: *J. Phys. D: Appl. Phys.* 41.6, p. 065503.

Lu, Y. Charles (2006). “Fractional derivative viscoelastic model for frequency-dependent complex moduli of automotive elastomers”. In: *International Journal of Mechanics and Materials in Design* 3, pp. 329–336.

Macosko, C. W. (1994). *Rheology: Principles, Measurements, and Applications*. 1st ed. Wiley.

Magin, Richard L. (2010). “Fractional calculus models of complex dynamics in biological tissues”. In: *Computers & Mathematics with Applications* 59, pp. 1586–1593.

Mahdy, Amr, Nasser Sweilam, and Mohamed Khader (Jan. 2012). “Crank-Nicolson finite difference method for solving time-fractional diffusion equation”. In: *Journal of Fractional Calculus and Applications* 2, pp. 1–9.

Mahiuddin, Md. et al. (2018). “Development of fractional viscoelastic model for characterizing viscoelastic properties of food material during drying”. In: *Food Bioscience* 23, pp. 45–53.

Mainardi, F. (2010). *Fractional calculus and waves in linear viscoelasticity: an introduction to mathematical models*. OCLC: ocn619938514. London ; Hackensack, NJ.

Mainardi, Francesco (2018). *Fractional Calculus: Theory and Applications*. OCLC: 1154251152. Basel, Switzerland.

Majumdar, Simantini et al. (2017). “A study of the rheological properties of visco-elastic materials using fractional calculus”. In: *Colloids and Surfaces A: Physicochemical and Engineering Aspects* 516, pp. 181–189.

Maqbool, Khadija et al. (2016). “Analytical solutions for wall slip effects on magnetohydrodynamic oscillatory rotating plate and channel flows in porous media using a fractional Burgers viscoelastic model”. In: *The European Physical Journal Plus* 131, p. 140.

Marty, G. and O. Dauchot (2005). “Subdiffusion and Cage Effect in a Sheared Granular Material”. In: *Phys. Rev. Lett.* 94, p. 015701.

Mason, T. G., H. Gang, and D. A. Weitz (1996). “Rheology of complex fluids measured by dynamic light scattering”. In: *J. Mol. Struct.* 383, pp. 81–90.

Mason, T. G. and D. A. Weitz (1995). “Optical Measurements of Frequency-Dependent Linear Viscoelastic Moduli of Complex Fluids”. In: *Phys. Rev. Lett.* 74.7, pp. 1250–1253.

McKinley, S., L. Yao, and M. G. Forest (2009). “Transient anomalous diffusion of tracer particles in soft matter”. In: *J. Rheol.* 53.6, pp. 1487–1506.

Meerschaert, Mark M., Hans-Peter Scheffler, and Charles Tadjeran (2006). “Finite difference methods for two-dimensional fractional dispersion equation”. In: *Journal of Computational Physics* 211, pp. 249–261.

Meerschaert, Mark M. and Charles Tadjeran (2004). “Finite difference approximations for fractional advection–dispersion flow equations”. In: *Journal of Computational and Applied Mathematics* 172.1, pp. 65–77.

Meng, Yahui et al. (2021). “On the process of filtration of fractional viscoelastic liquid food”. In: *Communications in Theoretical Physics* 73, p. 045004.

Meral, F.C., T.J. Royston, and R. Magin (2010). “Fractional calculus in viscoelasticity: An experimental study”. In: *Communications in Nonlinear Science and Numerical Simulation* 15.4, pp. 939–945.

Merkine, L.O. (1977). “Convective and absolute instability of baroclinic eddies”. In: *Geophys. Astrophys. Fluid Dyn.* 9, pp. 29–57.

Meroz, Yasmine and Igor M. Sokolov (2015). “A toolbox for determining subdiffusive mechanisms”. In: *Physics Reports* 573, pp. 1–29.

Metzler, R. et al. (2014). “Anomalous diffusion models and their properties: non-stationarity, non-ergodicity, and ageing at the centenary of single particle tracking”. In: *Phys. Chem. Chem. Phys.* 16 (44), pp. 24128–24164.

Metzler, Ralf et al. (1995). “Relaxation in filled polymers: A fractional calculus approach”. In: *The Journal of Chemical Physics* 103, pp. 7180–7186.

Miller, Kenneth S. and Bertram Ross (1993). “An Introduction to the Fractional Calculus and Fractional Differential Equations”. In.

Ming, Chunying et al. (2016). “Analytical solutions of multi-term time fractional differential equations and application to unsteady flows of generalized viscoelastic fluid”. In: *Computers & Mathematics with Applications* 72, pp. 2084–2097.

Momani, Shaher and Zaid Odibat (2008). “Numerical solutions of the space-time fractional advection-dispersion equation”. In: *Numerical Methods for Partial Differential Equations* 24.6, pp. 1416–1429.

Morgado, R. et al. (2002). “Relation between Anomalous and Normal Diffusion in Systems with Memory”. In: *Phys. Rev. Lett.* 89.10, p. 100601.

Murio, Diego A. (Aug. 2008). “Implicit finite difference approximation for time fractional diffusion equations”. In: *Computers & Mathematics with Applications* 56.4, pp. 1138–1145.

Müller, Sebastian et al. (2011). “A nonlinear fractional viscoelastic material model for polymers”. In: *Computational Materials Science* 50.10, pp. 2938–2949.

Nandagopalan, P. et al. (2018). “Shear-flow rheology and viscoelastic instabilities of ethanol gel fuels”. In: *Exp. Thermal Fluid Sci.* 99, pp. 181–189.

Newby, Jay M. et al. (2018). “Technological strategies to estimate and control diffusive passage times through the mucus barrier in mucosal drug delivery”. In: *Adv. Drug Deliv. Rev.* 124, pp. 64–81.

Nigmatullin, R. R. (Mar. 1992). “Fractional integral and its physical interpretation”. In: *Theoretical and Mathematical Physics* 90.3, pp. 242–251. (Visited on 10/10/2023).

Nikan, O. and Z. Avazzadeh (2021). “Numerical simulation of fractional evolution model arising in viscoelastic mechanics”. In: *Applied Numerical Mathematics* 169, pp. 303–320.

Nonnenmacher, Theo F. (1991). “Fractional relaxation equations for viscoelasticity and related phenomena”. In: *Rheological Modelling: Thermodynamical and Statistical Approaches*. Ed. by José Casas-Vázquez and David Jou. Vol. 381. Springer Berlin Heidelberg, pp. 309–320.

Nutting, P.G. (1921). “A new general law of deformation”. In: *Journal of the Franklin Institute* 191.5, pp. 679–685.

Oliveira, Edmundo Capelas de and José António Tenreiro Machado (2014a). “A Review of Definitions for Fractional Derivatives and Integral”. In: *Math. Probl. Eng.* 2014, p. 238459.

Oliveira, Edmundo Capelas de and José António Tenreiro Machado (June 2014b). “A Review of Definitions for Fractional Derivatives and Integral”. In: *Mathematical Problems in Engineering* 2014. Ed. by Riccardo Caponetto. Publisher: Hindawi Publishing Corporation, p. 238459.

Palomares-Ruiz, J E et al. (2015). “Fractional viscoelastic models applied to biomechanical constitutive equations”. In: *Rev. Mex. Fis.*

Patnaik, Sansit, John P. Hollkamp, and Fabio Semperlotti (2020). “Applications of variable-order fractional operators: a review”. In: *Proceedings of the Royal Society A: Mathematical, Physical and Engineering Sciences* 476.2234, p. 20190498.

Perdikaris, Paris and George Em. Karniadakis (2014). “Fractional-Order Viscoelasticity in One-Dimensional Blood Flow Models”. In: *Annals of Biomedical Engineering* 42, pp. 1012–1023.

Phan-Thien, Nhan and Nam Mai-Duy (2017). *Understanding Viscoelasticity: An Introduction to Rheology*. Graduate Texts in Physics. Cham: Springer International Publishing.

Pierce, A. D. (1981). *Acoustics: An introduction to its physical principles and applications*. New York: McGraw-Hill.

Podlubny, Igor (1999). *Fractional differential equations: an introduction to fractional derivatives, fractional differential equations, to methods of their solution and some of their applications*. Mathematics in science and engineering v. 198. San Diego: Academic Press.

Podlubny, Igor, Richard L. Magin, and Iryna Trymorush (2017). “Niels Henrik Abel and the birth of fractional calculus”. In: *Fractional Calculus and Applied Analysis* 20.5, pp. 1068–1075.

Prakash, Amit, Doddabhadrappla Gowda Prakasha, and Pundikala Veeresha (2019). “A reliable algorithm for time-fractional Navier-Stokes equations via Laplace transform”. In: *Nonlinear Engineering* 8, pp. 695–701.

Prodanov, D. (2017). “Conditions for continuity of fractional velocity and existence of fractional Taylor expansions”. In: *Chaos Sol. Fractals* 102, pp. 236–244.

Prodanov, D. (2018). “Fractional Velocity as a Tool for the Study of Non-Linear Problems”. In: *Fractal Fract.* 2.1, pp. 2–23.

Pérez Zerpa, J.M. et al. (2015). “Modeling the arterial wall mechanics using a novel high-order viscoelastic fractional element”. In: *Appl. Math. Model.* 39.16, pp. 4767–4780.

Qi, Haitao and Hui Jin (2006). “Unsteady Rotating Flows of a Viscoelastic Fluid with the Fractional Maxwell Model Between Coaxial Cylinders”. In: *Acta Mechanica Sinica* 22.4, pp. 301–305.

Qi, Haitao and Mingyu Xu (2007). “Unsteady flow of viscoelastic fluid with fractional Maxwell model in a channel”. In: *Mechanics Research Communications* 34, pp. 210–212.

Qi, M. and M. Xu (2009). “Some unsteady unidirectional flows of a generalized Oldroyd-B fluid with fractional derivative”. In: *Appl. Math. Model* 33, pp. 4184–4191.

Rabaud, M., Y. Couder, and N. Gerard (1988). “Dynamics and stability of anomalous Saffman-Taylor fingers”. In: *Phys. Rev. A* 37, pp. 935–947.

Rasheed, Amer and Muhammad Shoaib Anwar (2018). “Simulations of variable concentration aspects in a fractional nonlinear viscoelastic fluid flow”. In: *Communications in Nonlinear Science and Numerical Simulation* 65, pp. 216–230.

Rasheed, Amer and Muhammad Shoaib Anwar (2019). “Interplay of chemical reacting species in a fractional viscoelastic fluid flow”. In: *Journal of Molecular Liquids* 273, pp. 576–588.

Reis, P. M., R. A. Ingale, and M. D. Shattuck (2007). “Caging Dynamics in a Granular Fluid”. In: *Phys. Rev. Lett.* 98, p. 188301.

Rietkerk, Max et al. (2004). “Self-Organized Patchiness and Catastrophic Shifts in Ecosystems”. In: *Science* 305.5692, pp. 1926–1929.

Riley, J. J., M. G. Hak, and R. W Metcalfe (1988). “Complaint coatings”. In: *Ann. Rev. Fluid Mech.* 20, pp. 393–420.

Rogosin, Sergei and Francesco Mainardi (2014). “George William Scott Blair – the pioneer of fractional calculus in rheology”. In: *Communications in Applied and Industrial Mathematics* 6.1.

Ross, Bertram (1977). “The development of fractional calculus 1695–1900”. In: *Historia Mathematica* 4, pp. 75–89.

Rouse, P. E. (1953). “A Theory of the Linear Viscoelastic Properties of Dilute Solutions of Coiling Polymers”. In: *J. Chem. Phys.* 21.7, pp. 1272–1280.

Rubenstein, M. and R. H. Colby (2003). *Polymer Physics*. New York: Oxford University Press.

Rubinstein, Michael and Ralph H. Colby (2003). *Polymer physics*. Oxford ; New York: Oxford University Press.

Rutman, R. S. (Dec. 1995). “On physical interpretations of fractional integration and differentiation”. In: *Theoretical and Mathematical Physics* 105.3, pp. 1509–1519. (Visited on 10/10/2023).

Sabatier, Jocelyn (May 2020). “Non-Singular Kernels for Modelling Power Law Type Long Memory Behaviours and Beyond”. In: *Cybernetics and Systems* 51.4, pp. 383–401. (Visited on 10/10/2023).

Sabatier, Jocelyn and Christophe Farges (2018). “Comments on the description and initialization of fractional partial differential equations using Riemann–Liouville’s and Caputo’s definitions”. In: *Journal of Computational and Applied Mathematics* 339. Modern Fractional Dynamic Systems and Applications, MFDSA 2017, pp. 30–39.

Sabatier, Jocelyn, Christophe Farges, and Jean-Claude Trigeassou (2014). “Fractional systems state space description: some wrong ideas and proposed solutions”. In: *Journal of Vibration and Control* 20.7, pp. 1076–1084.

Sabatier, Jocelyn et al. (2012). “On Observability and Pseudo State Estimation of Fractional Order Systems”. In: *European Journal of Control* 18.3, pp. 260–271.

Sahu, Kirti Chandra and Rama Govindarajan (2012). “Spatio-temporal linear stability of double-diffusive two-fluid channel flow”. In: *Physics of Fluids* 24, p. 054103.

Santamaría-Holek, I., D. Reguera, and J. M. Rubí (2001). “Diffusion in stationary flow from mesoscopic nonequilibrium thermodynamics”. In: *Physical Review E* 63, p. 051106.

Santamaría-Holek, I, J M Rubí, and A Pérez-Madrid (2005). “Mesoscopic thermodynamics of stationary non-equilibrium states”. In: *New Journal of Physics* 7, pp. 35–35.

Santamaría-Holek, I. et al. (2008). “Anomalous Diffusion in Microrheology: A Comparative Study”. In: *AIP Conference Proceedings*. Vol. 982. AIP, pp. 672–677.

Sasmal, C. (2022). “Fluid viscoelasticity suppresses chaotic convection and mixing due to electrokinetic instability”. In: *Phys. Fluids* 34, p. 082011.

Sasso, M., G. Palmieri, and D. Amodio (2011). “Application of fractional derivative models in linear viscoelastic problems”. In: *Mechanics of Time-Dependent Materials* 15, pp. 367–387.

Sayevand, K., J. Tenreiro Machado, and V. Moradi (2019). “A new non-standard finite difference method for analyzing the fractional Navier–Stokes equations”. In: *Computers & Mathematics with Applications* 78, pp. 1681–1694.

Schiessel, H and A Blumen (1993). “Hierarchical analogues to fractional relaxation equations”. In: *Journal of Physics A: Mathematical and General* 26, pp. 5057–5069.

Schiessel, H. and A. Blumen (1995). “Mesoscopic Pictures of the Sol-Gel Transition: Ladder Models and Fractal Networks”. In: *Macromolecules* 28.11, pp. 4013–4019.

Schiessel, H et al. (1995). “Generalized viscoelastic models: their fractional equations with solutions”. In: *Journal of Physics A: Mathematical and General* 28, pp. 6567–6584.

Schmid, P. and D. Henningson (2001). *Stability and Transition in Shear Flows*. Vol. 142.

Schnurr, B. et al. (1997). “Determining Microscopic Viscoelasticity in Flexible and Semiflexible Polymer Networks from Thermal Fluctuations”. In: *Macromolecules* 30, pp. 7781–7792.

Scott-Blair, G. W. (1944). “Analytical and Integrative Aspects of the Stress-Strain-Time Problem”. In: *J. Sci. Instr.* 21.5, pp. 80–84.

Scott-Blair, G. W. (1947). “The role of psychophysics in rheology”. In: *J. Coll. Sci.* 2.1, pp. 21–32.

Sengupta, Ankush, Tobias Kruppa, and Hartmut Löwen (2011). “Chemotactic predator-prey dynamics”. In: *Phys. Rev. E* 83, p. 031914.

Sengupta, T. K., S. K. Sircar, and A. Dipankar (Feb. 2006). “High Accuracy Schemes for DNS and Acoustics”. In: *Journal of Scientific Computing* 26.2, pp. 151–193.

Shaowei, W. and X. Mingyu (2006). “Exact solution on unsteady Couette flow of generalized Maxwell fluid with fractional derivative”. In: *Acta Mechanica* 187, pp. 103–112.

Sin, Chung-Sik et al. (2017). “Unsteady flow of viscoelastic fluid with the fractional K-BKZ model between two parallel plates”. In: *Applied Mathematical Modelling* 47, pp. 114–127.

Singh, S. et al. (Nov. 2020). “Implicit-explicit-compact methods for advection diffusion reaction equations”. In: *Computers & Fluids* 212, p. 104709.

Sircar, S. (2010). “A Hydrodynamical Kinetic Theory for Self-Propelled Ellipsoidal Suspensions”. In: *Int. J. Emerg. Multi. Flu. Sci.* 2.4.

Sircar, S. and D. Bansal (2019). “Spatiotemporal linear stability of viscoelastic free shear flows: Dilute regime”. In: *Phys. Fluids* 31.8, p. 084104.

Sircar, S., J. Li, and Q. Wang (2010). “Biaxial phases of bent-core liquid crystal polymers in shear flows”. In: *Comm. Math. Sci.* 8.3, pp. 697–720.

Sircar, S. and A. J. Roberts (2016). “Surface deformation and shear flow in ligand mediated cell adhesion”. In: *J. Math. Biol.* 73.4, pp. 1035–1052.

Sircar, S. and Q. Wang (2008). “Shear-induced mesostructures in biaxial liquid crystals”. In: *Phys. Rev. E* 78.6, p. 061702.

Sircar, S., J. G. Younger, and D. M. Bortz (2015). “Sticky surface: sphere–sphere adhesion dynamics”. In: *J. Biol. Dyna.* 9, pp. 79–89.

Sircar, S. et al. (2015). “Determining equilibrium osmolarity in poly (ethylene glycol)/chondrotin sulfate gels mimicking articular cartilage”. In: *J. Theo. Biol.* 364, pp. 397–406.

Sircar, S. et al. (2016). “Ligand-mediated adhesive mechanics of two static, deformed spheres”. In: *Eur. Phys. J. E* 39.10, pp. 1–9.

Sircar, Sarthok and Qi Wang (July 2010). “Transient rheological responses in sheared biaxial liquid crystals”. In: *Rheologica Acta* 49.7, pp. 699–717.

Sonin, N Ya (1869). “On differentiation with arbitrary index”. In: *Moscow Matem. Sbornik* 6.1, pp. 1–38.

Spagnolie, S. E. (2015). *Complex Fluids in Biological Systems: Experiment, Theory, and Computation*. Springer.

Stone, H.A., A.D. Stroock, and A. Ajdari (2004). “Engineering Flows in Small Devices: Microfluidics Toward a Lab-on-a-Chip”. In: *Annu. Rev. Fluid Mech.* 36.1, pp. 381–411.

Sturrock, P.A. (1958). “Kinematics of growing waves”. In: *Phys. Rev.* 112, pp. 1488–1503.

Su, Lijuan, Wenqia Wang, and Qiuyan Xu (2010). “Finite difference methods for fractional dispersion equations”. In: *Applied Mathematics and Computation* 216, pp. 3329–3334.

Su, Xianglong, Donggang Yao, and Wenxiang Xu (2020). “A new method for formulating linear viscoelastic models”. In: *International Journal of Engineering Science* 156, p. 103375.

Sun, HongGuang et al. (2018a). “A new collection of real world applications of fractional calculus in science and engineering”. In: *Communications in Nonlinear Science and Numerical Simulation* 64, pp. 213–231.

Sun, HongGuang et al. (2018b). “A new collection of real world applications of fractional calculus in science and engineering”. In: *Commun. Nonlinear Sci. Numer. Simul.* 64, pp. 213–231.

Sureshkumar, R. (2001). “Local linear stability characteristics of viscoelastic periodic channel flow”. In: *Journal of Non-Newtonian Fluid Mechanics* 97.2-3, pp. 125–148.

Sureshkumar, R., A. N. Beris, and R. Handler (1997). “Direct numerical simulation of the turbulent channel flow of a polymer solution”. In: *Phys. Fluids* 9.3, pp. 743–755.

Sureshkumar, R. and Antony N. Beris (1995). “Linear stability analysis of viscoelastic Poiseuille flow using an Arnoldi-based orthogonalization algorithm”. In: *Journal of Non-Newtonian Fluid Mechanics* 56.2, pp. 151–182.

Tackels, G. and M. J. Crochet (1973). “Stability of a plane Poiseuille flow of a finite linear viscoelastic fluid”. In: *The Physics of Fluids* 16.6, pp. 790–795.

Takeuchi, Yuki, Yoshihide Yoshimoto, and Reiji Suda (2017). “Second order accuracy finite difference methods for space-fractional partial differential equations”. In: *Journal of Computational and Applied Mathematics* 320, pp. 101–119.

Teh, C. H. and M. D. Morton (1977). “Stability of plane poiseuille flow of a highly elastic liquid”. In: *Journal of Non-newtonian Fluid Mechanics* 3, pp. 179–195.

Thacker, W.C. (1976). “Spatial growth of gulf stream meanders”. In: *Geophys. Fluid Dyn.* 7.27, pp. 1–95.

Thomas, L. H. (1953). “The Stability of Plane Poiseuille Flow”. In: *Phys. Rev.* 91 (4), pp. 780–783.

Thurston, George B (1972). “Viscoelasticity of human blood”. In: *Biophys. J.* 12, pp. 1205–1217.

Thurston, George B (1996). “Viscoelastic properties of blood and blood analogs”. In: *Advances in hemodynamics and hemorheology* 1, pp. 1–30.

Tian, Kai et al. (2022). “Two-dimensional electromagnetohydrodynamic (EMHD) flows of fractional viscoelastic fluids with electrokinetic effects”. In: *Nanomaterials (Basel)* 12, p. 3335.

Tlapa, G. and B. Bernstein (1970). “Stability of a Relaxation-Type Viscoelastic Fluid with Slight Elasticity”. In: *The Physics of Fluids* 13.3, pp. 565–568.

Tong, Dengke (2005). “Exact solutions for the flow of non-Newtonian fluid with fractional derivative in an annular pipe”. In: *Science in China Series G* 48, p. 485.

Tong, Dengke and Yusong Liu (2005). “Exact solutions for the unsteady rotational flow of non-Newtonian fluid in an annular pipe”. In: *International Journal of Engineering Science* 43, pp. 281–289.

Twiss, R. Q. (1952). “Propagation in electronion streams”. In: *Phys. Rev.* 88, pp. 1392–1407.

Uchaikin, Vladimir V (2013). *Fractional derivatives for physicists and engineers*. Vol. 2. Springer.

Vainstein, M. H., L. C. Lapas, and F. A. Oliveira (2008). *Anomalous Diffusion*. Tech. rep. arXiv:0805.0270.

Vaithianathan, T. et al. (2006). “An improved algorithm for simulating three-dimensional, viscoelastic turbulence”. In: *J. non-Newt. Fluid Mech.* 140.1, pp. 3–22.

Valério, Duarte, Manuel D. Ortigueira, and António M. Lopes (2022). “How Many Fractional Derivatives Are There?” In: *Mathematics* 10.5.

Valério, D., J. T. Machado, and V. Kiryakova (2014). “Some pioneers of the applications of fractional calculus”. In: *Fractional Calculus and Applied Analysis* 17.2, pp. 552–578.

Vieru, D., Corina Fetecau, and C. Fetecau (2008). “Flow of a viscoelastic fluid with the fractional Maxwell model between two side walls perpendicular to a plate”. In: *Applied Mathematics and Computation* 200.1, pp. 459–464.

Visbal, Miguel R and Datta V Gaitonde (Sept. 2002). “On the Use of Higher-Order Finite-Difference Schemes on Curvilinear and Deforming Meshes”. In: *Journal of Computational Physics* 181.1, pp. 155–185.

Wagner, Caroline E. et al. (2017). “Quantifying the consistency and rheology of liquid foods using fractional calculus”. In: *Food Hydrocolloids* 69, pp. 242–254.

Wang, Kaixin and Hong Wang (2011). “A fast characteristic finite difference method for fractional advection–diffusion equations”. In: *Advances in Water Resources* 34.7, pp. 810–816.

Wang, Kangle and Sanyang Liu (2016). “Analytical study of time-fractional Navier-Stokes equation by using transform methods”. In: *Advances in Difference Equations* 2016.1, p. 61.

Wang, Qinghe and Dengke Tong (2010). “The Flow Analysis of Viscoelastic Fluid with Fractional Order Derivative in Horizontal Well”. In: *Transport in Porous Media* 81.2, pp. 295–303.

Wang, Shaowei and Mingyu Xu (2009). “Axial Couette flow of two kinds of fractional viscoelastic fluids in an annulus”. In: *Nonlinear Analysis: Real World Applications* 10, pp. 1087–1096.

Wang, Xiaoping, Huanying Xu, and Haitao Qi (2020). “Numerical analysis for rotating electro-osmotic flow of fractional Maxwell fluids”. In: *Applied Mathematics Letters* 103, p. 106179.

Wenchang, Tan and Xu Mingyu (2002). “Plane surface suddenly set in motion in a viscoelastic fluid with fractional Maxwell model”. In: *Acta Mechanica Sinica* 18.4, pp. 342–349.

Wenchang, Tan, Pan Wenxiao, and Xu Mingyu (2003). “A note on unsteady ows of a viscoelastic uid with the fractional Maxwell model between two parallel plates”. In.

Wilson, H.J., Michael Ren ardy, and Yuriko Renardy (1999). “Structure of the spectrum in zero Reynolds number shear flow of the UCM and Oldroyd-B liquids”. In: *Journal of Non-newtonian Fluid Mechanics - J NON-NEWTONIAN FLUID MECH* 80, pp. 251–268.

Witten, Jacob, Tahoura Samad, and Katharina Ribbeck (2018). “Selective permeability of mucus barriers”. In: *Curr. Opin. Biotechnol.* 52, pp. 124–133.

Xie, Changping and Shaomei Fang (2019). “A second-order finite difference method for fractional diffusion equation with Dirichlet and fractional boundary conditions”. In: *Numerical Methods for Partial Differential Equations* 35, pp. 1383–1395.

Xu, Huanying, Xiaoyun Jiang, and Bo Yu (2017). “Numerical analysis of the space fractional Navier–Stokes equations”. In: *Applied Mathematics Letters* 69, pp. 94–100.

Yang, Di and Ke-Qin Zhu (2010). “Start-up flow of a viscoelastic fluid in a pipe with a fractional Maxwell’s model”. In: *Computers & Mathematics with Applications* 60, pp. 2231–2238.

Yang, Xiu and Xiaoyun Jiang (2019). “Numerical algorithm for two dimensional fractional Stokes’ first problem for a heated generalized second grade fluid with smooth and non-smooth solution”. In: *Computers & Mathematics with Applications* 78, pp. 1562–1571.

Yang, Yuyue et al. (2006). “High order schemes based on upwind schemes with modified coefficients”. In: *Journal of Computational and Applied Mathematics* 195, pp. 242–251.

Yao, Shao-Wen et al. (2021). “A mathematical modelling of a Atherosclerosis intimation with Atangana-Baleanu fractional derivative in terms of memory function”. In: *Results Phys.* 27, p. 104425.

Yeo, K. S., B. C. Khoo, and H. Z. Zhao (1996). “The absolute instability of boundary-layer flow over viscoelastic walls”. In: *Theoretical and Computational Fluid Dynamics* 8.4, pp. 237–252.

Yin, Youbing and Ke-Qin Zhu (2006). “Oscillating flow of a viscoelastic fluid in a pipe with the fractional Maxwell model”. In: *Applied Mathematics and Computation* 173.1, pp. 231–242.

Yu, Yue, Paris Perdikaris, and George Em Karniadakis (2016). “Fractional modeling of viscoelasticity in 3D cerebral arteries and aneurysms”. In: *Journal of Computational Physics* 323, pp. 219–242.

Yuste, S. B. and L. Acedo (2005). “An Explicit Finite Difference Method and a New von Neumann-Type Stability Analysis for Fractional Diffusion Equations”. In: *SIAM Journal on Numerical Analysis* 42, pp. 1862–1874.

Yuste, Santos B. and J. Quintana-Murillo (2016). “Fast, accurate and robust adaptive finite difference methods for fractional diffusion equations”. In: *Numerical Algorithms* 71, pp. 207–228.

Zarabadi, M (2019). “Development of a Robust Microfluidic Electrochemical Cell for Biofilm Study in Controlled Hydrodynamic Conditions”. PhD thesis. Univ. Laval.

Zarabadi, M. P., S. J. Charette, and J. Greener (2018). “Flow-Based Deacidification of Geobacter sulfurreducens Biofilms Depends on Nutrient Conditions: a Microfluidic Bioelectrochemical Study”. In: *Chem. Electrochem.* 5.23, pp. 3645–3653.

Zeng, Fanhai et al. (2013). “The Use of Finite Difference/Element Approaches for Solving the Time-Fractional Subdiffusion Equation”. In: *SIAM Journal on Scientific Computing* 35, A2976–A3000.

Zeng, Fanhai et al. (2015). “Numerical Algorithms for Time-Fractional Subdiffusion Equation with Second-Order Accuracy”. In: *SIAM Journal on Scientific Computing* 37, A55–A78.

Zhang, Jun and JinRong Wang (2018). “Numerical analysis for Navier–Stokes equations with time fractional derivatives”. In: *Applied Mathematics and Computation* 336, pp. 481–489.

Zhang, Mengchen et al. (2019). “A new time and spatial fractional heat conduction model for Maxwell nanofluid in porous medium”. In: *Computers & Mathematics with Applications* 78, pp. 1621–1636.

Zhang, Will, Adela Capilnasiu, and David Nordsletten (2021). “Comparative Analysis of Nonlinear Viscoelastic Models Across Common Biomechanical Experiments”. In: *Journal of Elasticity* 145.1-2, pp. 117–152.

Zhang, Will et al. (2020). “An efficient and accurate method for modeling nonlinear fractional viscoelastic biomaterials”. In: *Computer Methods in Applied Mechanics and Engineering* 362, p. 112834.

Zhang, Yang (2009). “A finite difference method for fractional partial differential equation”. In: *Applied Mathematics and Computation* 215.2, pp. 524–529.

Zhao, J. et al. (2016). “Unsteady natural convection boundary layer heat transfer of fractional Maxwell viscoelastic fluid over a vertical plate”. In: *Int. J. Heat Mass Trans.* 47, pp. 760–766.

Zheng, Liancun, Yaqing Liu, and Xinxin Zhang (2012). “Slip effects on MHD flow of a generalized Oldroyd-B fluid with fractional derivative”. In: *Nonlinear Analysis: Real World Applications* 13.2, pp. 513–523.

Zhou, Gordon G. D. et al. (2020). “Particle Size Segregation in Granular Mass Flows With Different Ambient Fluids”. In: *J. Geophys. Res. Solid Earth* 125, e2020JB019536.

Zhou, Yan et al. (2022). “The viscoelastic characteristics of in-vitro carotid plaque by Kelvin-Voigt fractional derivative modeling”. In: *J. Biomech.* 141, p. 111210.

Zimm, B. H. (1956). “Dynamics of Polymer Molecules in Dilute Solution: Viscoelasticity, Flow Birefringence and Dielectric Loss”. In: *J. Chem. Phys.* 24.2, pp. 269–278.

Zwanzig, R. and M. Bixon (1970). “Hydrodynamic Theory of the Velocity Correlation Function”. In: *Phys. Rev. A* 2.5, pp. 2005–2012.

List of Publications

1. D. Bansal, T. Chauhan, S. Sircar; Spatiotemporal linear stability of viscoelastic Saffman–Taylor flows. Physics of Fluids; 34 (10): 104105 (2022) https://doi.org/10.1063/5.0113987.

2. T. Chauhan, D. Bansal, S. Sircar; Spatiotemporal linear stability of viscoelastic subdiffusive channel flows: a fractional calculus framework. Journal of Engineering Mathematics 141, 8 (2023) https://doi.org/10.1007/s10665-023-10282-7.

3. T. Chauhan, M. Bhatt, S. Shrivastava, P. Shukla, and S. Sircar.; Rheodynamics of viscoelastic subdiffusive channel flows: low Weissenberg number regime. Physics of Fluids; 35 (12): 123121 (2023) https://doi.org/10.1063/5.0174598.

4. T. Chauhan, K . Kalyanaraman, S. Sircar; Quantifying macrostructures in viscoelastic subdiffusive flows. Journal of Mathematical Physics; 65 (7): 073101 (2024) https://doi.org/10.1063/5.0195666.

5. D. Ghosh, T. Chauhan, S. Sircar; Implicit-explicit time integration method for fractional advection-reaction-diffusion equations. ANZIAM Journal (2024) https://doi.org/10.1017/S1446181124000154.

6. M. Bhatt, T. Chauhan, R. Agrawal, M. Kumar, V. Kumar, S. Sircar; Elastoinertial stability analysis and structure formation in viscoelastic subdiffusive pipe flow. Physics of Fluids; 36 (12): 123111 (2024). https://doi.org/10.1063/5.0240113.